Technische Universität Dortmund – Fakultät Physik

Cluster-Surface Interaction of Mass Selected Ag Clusters with Graphite, Gold and C_{60} Functionalized Surfaces

Dissertation

Zur Erlangung des Doktorgrades der Naturwissenschaften vorgelegt von

Niklas Grönhagen

November 2011

Cluster-Surface Interaction of Mass Selected Ag Clusters with Graphite, Gold and C_{60} Functionalized Surfaces

Table of Contents

Introduction

Nano physics is a prime example for a scientific field that was not even known to exist until sophisticated machines were introduced to the scientific community, which were able to detect tiny structures and inherent properties of nanoscopic objects like atoms or molecules. Additional tools, developed in the early 50s, broadened the view of a realm that is more unique and complex than most people had imagined. A prominent example for such a machine is the scanning tunneling microscope (STM). It was first introduced to the scientific community by *Gerd Binnig* and *Heinrich Rohrer* [1–3] and won them together with *E. Ruska* the *Noble Price in Physics* in 1986.

The investigated nano scale objects of this thesis are for the most part small compounds called *clusters*, consisting of only 3 to 10^5 identical atoms [4]. These nano particles are traditionally investigated on their own as a beam in a vacuum chamber using varying spectroscopy or shape analyzing methods. The experiments of this thesis, however, used a more complex environment. By placing clusters on certain surfaces, newly emerging properties of the combined system could be analyzed.

Nanometer sized objects can be understood as being influenced by quantum and classical physics in equal parts. With the correct preparation of the system, it is possible to preserve some of the more unusual nanoscopic features in a macroscopic body, which opens up a wide field of possible applications. *Wei Lu* and *Charles M. Lieber*, for example, introduced a new method of creating electronics via a *bottom-up* approach [5] using nano particles as main components. *J. Bansmann et al.* proposed ways to possibly overcome the superparamagnetic limit in magnetic storage devices using nano particles while highlighting the need for an understanding of clusters on surfaces [6]. Clusters are not only useful for classical electronics. A number of problems concerning a prominent device, the quantum computer, seem solvable by using nano particles [7]. Clusters are involved in a wide variety of catalysts [8–11] where a thorough understanding of these nano particles can help to increase their functionality. Nano and in particular cluster physics is an ever expanding field. It enables not only the creation of new machines or the manipulation of materials but can also be used for passive devices like sensors [12–14]. Often, applications concentrate on nano particles on their own. However, in most cases they have to come in contact with a surface at one point. A particular approach in medical science uses nano particles to locally heat up body tissue [15,16] for different purposes, among others to destroy cancer cells.

Connected to these applications is an ever growing need for a deeper understanding of cluster-surface interactions. However, there are challenges for scientists of this field, which are especially a defining size dependence of cluster properties as well as an enormous sensitivity to environmental conditions. For an unobstructed view on the most fundamental cluster properties in combination with surfaces, a wide variety of combined approaches in well defined experimental setups is mandatory.

This thesis concentrates on cluster-surface interactions in multiple magnitudes. They range from weak interactions, which are realized by graphite surfaces, to strong interactions, which have been created using metal surfaces. Moderate interactions were achieved by the production of a multilayered system that facilitates the strong interaction of metal surfaces and the weak interaction of graphite. Silver and most recently copper cluster have been a central part of our experiments. They were deposited onto the mentioned surfaces with well defined masses and impact energies in an ultra high vacuum. Further parameters like thermal conditions and general cleanliness during sample preparation were handled with great care. In order to account for the mentioned challenges, this thesis will not only present multiple preparation, measurement and evaluation techniques but also complementary computer simulations of the investigated sample systems, which were conducted by our cooperation partners *T. Järvi* and *M. Moseler*.

1 Basics

In this chapter the theoretical foundation, the laboratory equipment and evaluation methods for the experiments will be presented. The interactions of clusters and surfaces form the basis of this entire work, theoretically and experimentally. An overview of the theoretical framework is given in the next sections. The devices used have the purpose of producing samples with specific parameters, creating the desired environmental conditions and allowing a detailed analysis of the clusters and surfaces. Information about that can be found in chapter 1.4 starting on page 28. The experimental procedures and evaluation methods are built around the special requirements for each experimental setup. A description can be found in chapter 1.5 starting on page 35.

1.1 Free Clusters

In the english language the term *cluster* traditionally refers to a *bunch* or *collection* without further specification [17]. The more modern *Dictionary of Chemistry* understands a *cluster compound* as a group of metals joined together by metal-metal bonds [18]. In cluster physics, however, clusters can consist of various atoms, molecules or even larger compounds of the same kind. There is no clear distinction of how many atoms are sufficient for a particle to become a cluster or how big it can get before it starts to be a macroscopic solid body. Historically molecular physics and solid state physics are two separate fields, which blend together in the case of a cluster. So the definition must incorporate both, which means that on the one hand the atom within a cluster can show clearly distinguished electronic orbitals in its bonds to neighboring atoms. On the other hand the properties of a macroscopic solid body might dominate, which leads to the formation of electronic band structures in metal clusters [19]. Of special interest are newly emerging properties, which are often related to one or both of the above fields but can nevertheless be absolutely unique.

This work focuses on metal clusters with a few ten to hundred atoms per cluster and their geometric as well as electronic properties. The fact that these clusters have been deposited onto a surface can have a great effect on their overall properties, especially due to the wide variety of unique substrates.

1.1.1 Structural Evolution

It is often helpful to imagine a cluster in the process of being build up from single atoms to get a grasp on its important properties. There is not a lot of variation in possible compositions in the case of very small particles like dimers and trimers, which only consist of 2 or 3 atoms, respectively. Despite being a frequent occurrence in many experiments due to their simple construction, they are not of special interest in this work. A dimer has a binding energy of about 1.6 eV [20]. Larger structures tend to reduce their internal energy further and are more complex regarding their geometric as well as electronic properties. Free clusters are usually fabricated in the gas phase and grow by aggregating. Under certain preparation conditions they reach energetic equilibrium. While most of them favor a compact, almost spherical shape, more complicated shapes are also observed in the cluster size evolution. Before

presenting more complex examples, two simple but important structural *motives*, geometric and electronically magic cluster sizes, are discussed.

1.1.1.1 Geometrically Magic Clusters

There need to be at least 13 atoms for an important geometrical aspect to emerge. With a compact shape, it is possible that one atom in the center is surrounded by neighboring ones. While the inner atoms contribute to the overall mass and electronic properties, the ones on the surface determine the interaction with its surroundings. By increasing the amount of atoms in the cluster compound, the ratio of inner atoms, which is proportional to the volume V, to surface A_S changes according to the following simple equations if the cluster is estimated to be a sphere:

$$V = \frac{4}{3}\pi r^3 \quad ; \quad A_S = 4\pi r^2 \quad \Rightarrow \quad \frac{A_s}{V} \sim \frac{1}{r} \tag{1.1}$$

Thus with a larger cluster a greater proportion of atoms is inside the structure and does therefore not interact with the environment. Normally a cluster tends to be spherical, but this is only approximately true. In general it acquires a geometric shape that helps to reduce the overall surface while energetically optimizing the chemical bonds. In many cases the amount of atoms does not allow a favorable arrangement, which decreases the stability of the cluster. Note that a cluster as a 3-dimensional body must adopt a highly symmetric shape in order to arrange each atom in a similar low-energy state with a maximum of surrounding bonding partners. At least for metals like sodium, silver or copper this favors a compact sphere-like shape because it allows an optimal surface to volume ratio. By that the amount of potential bondings is maximized.

However, for approximately spherical bodies like atoms there exists no closed packed arrangement for each layer in a cluster. Thus a spherical shape is only favorable in very few cases. As a compromise, so called icosahedra are formed fully or partly, which are compact on the one hand but allow a uniform distribution of atoms with equal bond lengths. So called *magic* geometric cluster sizes have an amount of atoms that allows them to adopt fully formed icosahedral shapes. The first five so called Mackay icosahedra [21] are illustrated in figure 1.1, the one with 13 atoms was mentioned before.

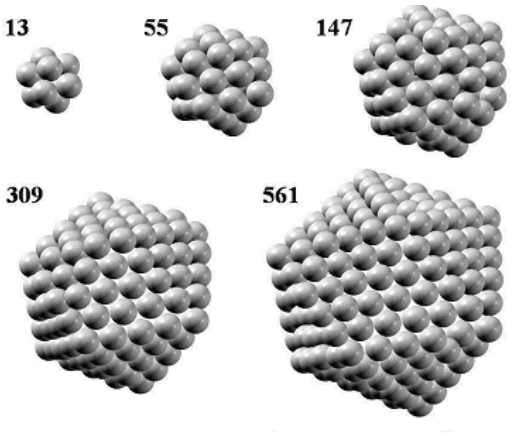

Figure 1.1: First five geometrically magic cluster sizes [4]. They are defined by their icosahedral shaped.

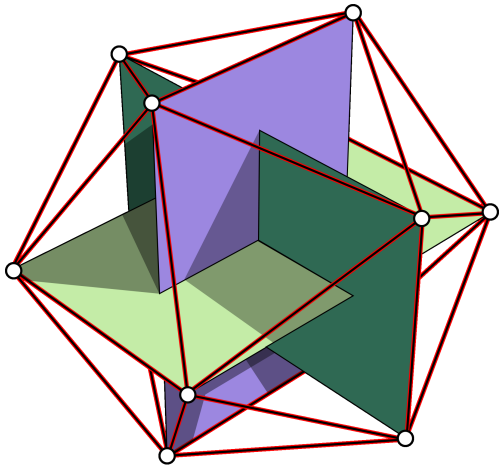

Figure 1.2: Mathematical construction of an icosahedron (see picture credits)

The enveloping shape of a geometrically magic cluster can be constructed by arranging rectangles with an edge length ratio of $(1+\sqrt{5})/2:1$ (*golden ratio*) as demonstrated in figure 1.2. The next magic cluster size can be formed when an additional layer of atoms is added. With the following formula a geometrically magic cluster with N_k atoms and k layers can be computed:

$$N_k = 1 + \sum_{i=1}^{k} (10 \cdot i^2 + 2) \tag{1.2}$$

Note that intermediate, partly formed icosahedral clusters, also exist but do not display the same stability because of the resulting asymmetrical shape. In consequence magic sizes cause the emergence of intermediate increases in stability when investigating the cluster sizes atom by atom. It is therefore of great interest how a geometrically magic cluster reacts if atoms are added or removed from it.

A first observation of the mentioned size evolution was archived by *O. Echt et. al.* [22] who investigated xenon clusters in the gas phase. Figure 1.3 demonstrates that geometrically magic cluster sizes display an increased frequency. Other maxima occur due to additional effects.

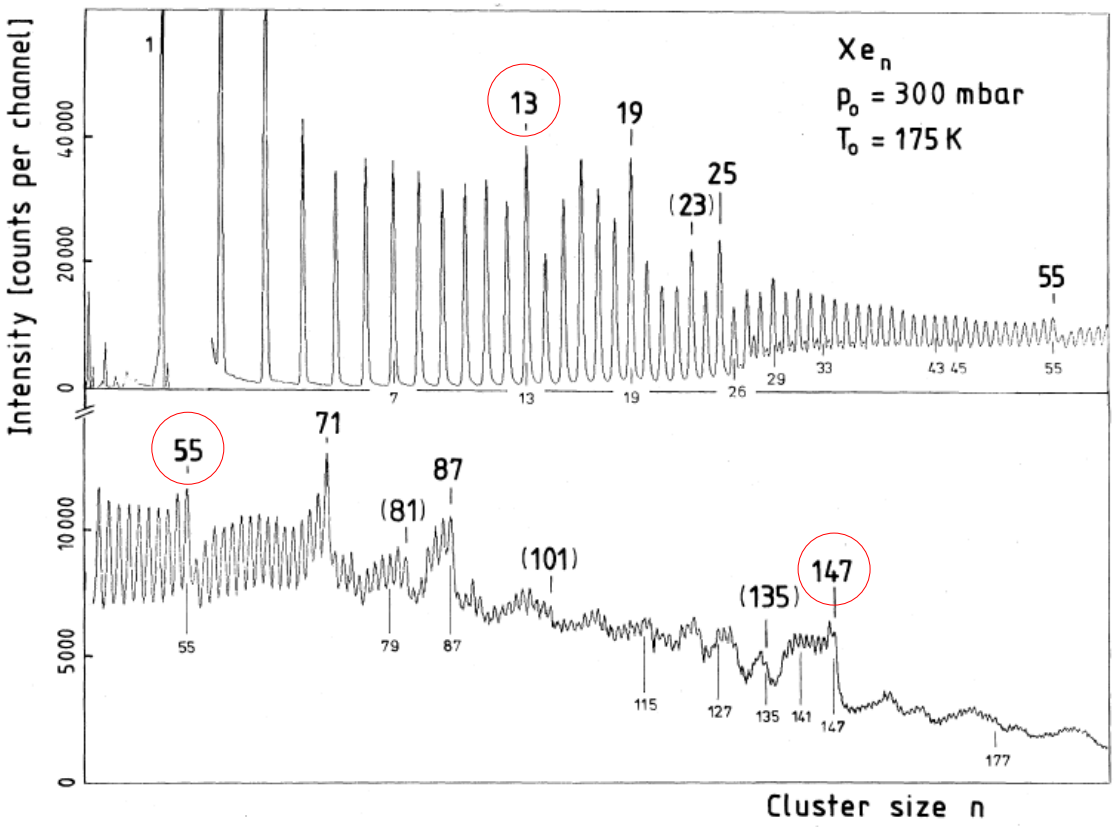

Figure 1.3: Mass spectrum of Xe clusters in the gas phase. Several sizes appear with an increased frequency which hints to a greater stability. Among these, marked with red circles, are the geometrically magic clusters [22].

1.1.1.2 Electronically Magic Clusters

Not only the geometric properties of a cluster determine its stability but also the electronic ones. This is especially the case when dealing with clusters that consist of metal atoms. As known in solid state physics for a long time, metallic bonds are not localized at a specific atom. Instead the orbitals merge to a continuum spanning over the entire compound, which leads to more sophisticated models for macroscopic metals. The so called *Jellium Model* [23] is often used, which replaces the positively charged atomic core by a uniform background charge. The electrons are regarded as being free to move in this *jellium*. If the cluster is comparably small, the compound acts like an enlarged atom with discrete orbitals, which distributes its electrons in energetically favorable ways.

An early experiment hinting to electronic similarities between clusters and single atoms was performed by *W. D. Knight et al.* [24]. The mass spectrum of alkali cluster beams mass selected by a *quadrupole mass analyzer* was investigated. As it turned out certain sizes in the spectrum showed a significant increase in intensity (N=8, 20, 40, 58, ...). Furthermore, the numbers of the more intense peaks were those expected from electrons in closed shells of a spherical potential. These observations lead to the conclusion that electronically magic cluster sizes existed. They encounter greater stability if they can form closed electronic shells and

thus have a greater abundance in the measured spectrum, which explains the larger peaks [25].

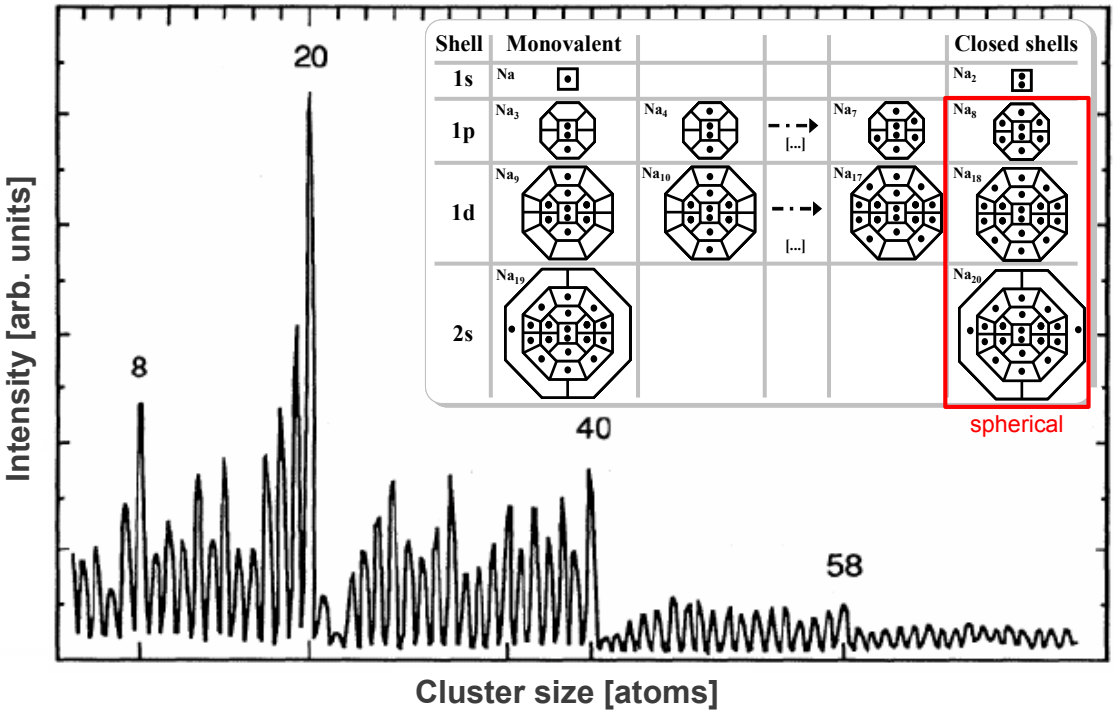

Figure 1.4: Measured mass spectrum of sodium clusters. Electronically magic clusters have an increased intensity [26]. In the upper right is an electronic shell model for sodium clusters [27]. Sizes marked with a red box have closed outer shells and are thus electronically particularly stable. This causes them to adopt a spherical shape.

A simple example for this behavior is sodium, which has only one valence electron. Clusters with N=8, 18, 20 atoms will now gain the equivalent to noble gas configuration because the outer shell is filled. Note that the following evolution is not equal to an atomic shell model. If the equivalent to noble gas configuration is possible for a sodium cluster, it will gain greater stability, which causes the particular cluster size to be preferred. Electronically the cluster's behavior can be compared to that of a small metallic droplet. The latter can be described by a smooth spherical confinement potential. In such a potential angular momentum occurs which allows the use of electronic shells. This causes each shell to have a quantum number n and angular momentum l. The pair (n,l) fills the shells in the following order: 1s, 1p, 1d, 2s, 1f etc. Each shell can then be filled with $2(2l+1)$ electrons, just like in a regular atom [28,29]. A spectrum of sodium clusters and a schematic visualization of the shell structure is depicted in figure 1.4. With this an additional geometric effect can be concluded. The mentioned confinement potential, which explains the occurrence of electronically magic numbers, hints to a spherical shape of the cluster at least for electronically magic cluster sizes. Deviations from magic numbers force the cluster to adopt either an oblate or prolate shape.

1.1.1.3 Examples for Cluster Structures

In this section examples for the properties of several free clusters of different elements will be presented. Sodium, as an example for an alkali metal, follows a simple growth pattern, which is strongly interconnected with geometric and magic sizes. Small structures between n=4-19 atoms can be generally predicted by *Jellium* models with the occurrence of some unusual intermediate shapes [30]. Larger structures in the range of n=20-57 atoms form closed shelled icosahedra interrupted by intermediate transitional shapes. Na_{20}^- to Na_{34}^- have a 19 atom double-icosahedral core stepwise decorated by a 15 atom equatorial belt. Between Na_{34}^- and Na_{44}^- the previously resulting structure is then capped by an anti *Mackay* overlay. With Na_{55}^- a Mackay overlay on a 13 atom icosahedral core is completed [31]. The special relevance of the intermediate icosahedral shapes has already been discussed. Copper and silver prove to be similar in behavior and structure to sodium because all three are free electron-like metals. This means that mainly their valence electrons contribute to their electronic properties [32], which partly explains their comparably simple size evolution. Because silver and copper have been used as cluster materials in the experiments of this work, the following sections will deal with them in more detail.

Lead like other group 14 (main group IVA) elements does not follow a simple evolution. Molecular dynamic simulations using a glue potential indicate that the majority of structures are hexagonally closed-packed or decahedral for n<40. Larger clusters, however, do not correspond to any structure commonly expected for clusters while still having high symmetry with the presence of magic numbers [33]. A study of *H.S. Lim et al.* concludes that face centered structures are favored over icosahedral structures for all clusters sizes [34]. Another noticeable effect is a strong charge dependence in the growth pattern of small clusters [35].

Tin, also being a group 14 element, shares many characteristic properties with lead. It is a metal that tracks a prolate growth pattern also found for Si_n and Ge_n clusters [36]. However, deviations occur for Si_n above n=14 and Ge_n above n=21. In the range between n~35-65 tin gradually adopts an almost spherical shape, while simultaneously passing through several intermediate structural families [37]. Smaller tin clusters can also have quite peculiar shapes. Sn_{12}^-, for example, is thought to have a slightly distorted empty icosahedral structure [38]. The stability of a tin cluster is not easy to determine. Unsupported Sn_n clusters do not melt but sublime in the size range of n=18-21 atoms [39]. This effect is also supported by *Alexandre A. Shvartsburg et al.* who showed a similar behavior for tin cluster ions with n=10-30 atoms. The melting points of the clusters is about 50 *K* above that of bulk metal, which is unusual because normally it is below that of the bulk. The group attributes this effect to the vastly different structure of tin clusters compared to the bulk [40]. An effect that is of great interest in cluster physics concerns the transition from non-metallic to metallic properties. *Cui et al.* inferred that such a transition occurs for Sn between Sn_{41}^- and Sn_{42}^- [38]. Tin clusters have also been analyzed theoretically, especially focusing on small tin cluster ions [41,42]. Further not discussed aspects like the formation of dimers of stable subunits show the complexity in the evolution of tin clusters [43].

Gold is another metal that shows a more complex behavior in terms of cluster shape. In the size range of n<14 it shows planar [44] and double-layered flat configurations [45,46]. For

n=16-18 hollow cages are observed [47]. Beside others tubular structures, fullerene-like hollow cages and fcc-like configurations emerge for larger cluster sizes [45,46,48–51]. Au_n clusters from n=29-35 have also been simulated using density functional theory and found to show a great number of different structures [52].

1.1.2 UPS as an Example for the Investigation of Free Clusters

There are only a few experimental methods that provide direct information on the cluster geometry. One tool, often used to get information on free clusters, is the so called *Ion Mobility Spectrometry* (IMS). Gas or vapor molecules are ionized before they are accelerated by an external electric field alongside a drift tube under elevated pressure [53]. Depending on their effective cross section, the ions gain deviating velocities. This causes different ions to reach the end of the drift tube at different times, which leads to a spectrum encompassing information on the ions [54]. Another useful method is *Trapped Ion Electron Diffraction* (TIED). The key goal is to achieve diffraction patterns from trapped cluster ions. A cluster beam is ionized in-situ and can thus be stored in a *Paul* trap [55]. In a next step the clusters are exposed to a high energy electron beam. This causes the emergence of a diffraction pattern, which is sufficient to provide information on the cluster's structure [56].

Other methods give more indirect information. The mass spectra themselves indicate stable geometries by dominant peaks (see figure 1.4), but experiments measuring the cluster's electronic structure can also be used to extract information on their geometric shape, in particular in combination with calculations. One particular method, which is used in the experiments of this work, is *Photoelectron Spectroscopy*. It has demonstrated its usefulness in the investigation of several kinds of metal clusters [30,31,57,58]. The underlying principle is based on the photoelectric effect which has been first observed by *Hertz* [59] and was later correctly described by *Einstein* [60]. UPS allows the investigation of the occupied states of a given sample. A photon of a specific energy is created, transpasses a certain distance in empty space and finally comes in contact with the specimen or cluster, which is to be investigated. The absorption of the photon causes the excitation of one of the specimen's electrons, which can then reach the surface and leave the compound if it gains enough kinetic energy. The energy increase of the electron is initially equal to that of the photon. However, it has to surpass the binding energy E_b of the material as well as the work function W of the sample so that the following equation applies:

$$E_{kin} = h\nu - E_b - W \tag{1.3}$$

The value ν stands for the frequency of the emitted light, while h is the Planck constant [61]. Note that the work function W is only relevant for solid bodies with the Fermi energy E_F being the reference. For small molecules the vacuum energy E_{Vac} is the reference so that in this case W in equation 1.3 is not relevant. Emitted electrons of different energies can be detected by an electrostatic analyzer, which uses their velocity to separate them spatially. The energy can then be attributed to them depending on their respective position. With known photonic energy and work function, the only unknown value remaining is the binding energy E_b, which holds information on the electronic structure of the investigated material. Figure 1.5

illustrates the measurement process, while figure 1.6 provides information on the electronic effects taking place. The spectrum that results from a measurement of multiple electrons with different energies is proportional to the combined density of states (JDOS) of initial and final electronic states [62]. Thus this method allows an experimenter to get a detailed analysis of the material's properties depending on the photon energy used and resolution of the detector. Note that electrons are detached by incoming photons not only with energy but also momentum conservation. Thus the resulting spectrum depends on the relative angle of the electron to the specimen. If a surface is present, changing the relative angle between sample and detector can therefore help to get a more complete picture of the electronic structure of a specific material.

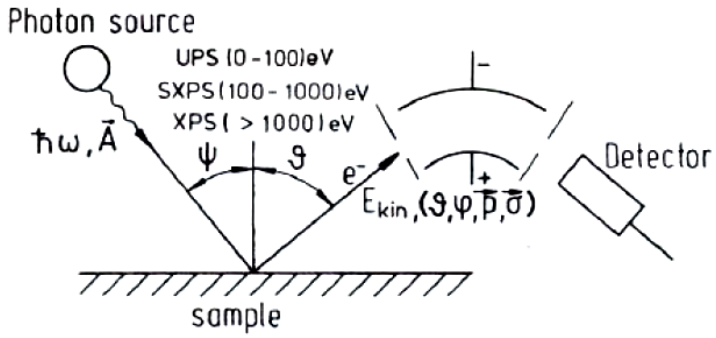

Figure 1.5: Schematic principle of an UPS measurement. Energies for SXPS and XPS are also depicted [63].

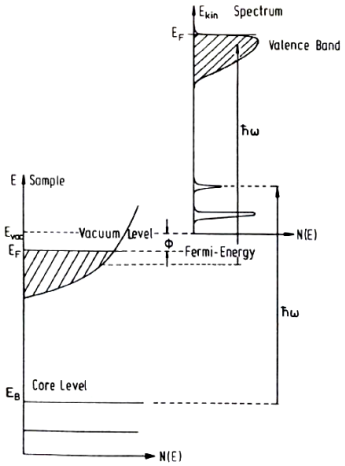

Figure 1.6: Principle of the energy transfer in the target material [63].

UPS (*Ultraviolet Photoelectron Spectroscopy*) uses photon energies from 10 *eV*-40 *eV*. This only allows the detachment of valence electrons, which limits the investigation of the atomic structure. However, due to the lower energy, it allows a greater resolution than competing methods.

(S)XPS, *(Soft) X-ray Photoelectron Spectroscopy*, works similarly to UPS with the difference that higher photon energies ranging from 160 *eV*-1500 *eV* are used so that the photons can reach deeper into the target material [63].

The existence of a substrate, which interacts only weakly with adsorbed particles, allows a cluster to keep its properties to a certain degree. Thus *Photoelectron Spectroscopy*, in particular UPS, can be used for these kind of sample systems.

Note that higher temperatures cause electrons to gain vibrational energy via electron-phonon interaction. This causes the respective spectra to lack structure due to a blurring effect [64]. Beside other reasons UPS experiments are therefore often conducted under low temperature conditions.

1.2 Cluster-Surface Interaction

The surface, on which the cluster is landed, normally has a complex morphology, which can lead to massive alterations of the shape and structure of a former free cluster. It is noteworthy that energy and shape of clusters on surfaces are strongly interconnected. The inter-atomic bondings depend on the proximity of cluster atoms to each other and the surface. This determines the subsequent internal energy of the compound. There exist stable configurations that are not always automatically adopted due to energy barriers which need to be surpassed. Only if a sufficient amount of energy is introduced to the system, be it during or after impact or due to heating, a new and more stable state can be adopted. These interactions are highly complex so that sophisticated experiments often in combination with computer simulations are needed to model them correctly. In order to understand these processes theoretically prior to detailed analyses, energies of both clusters and surfaces will be discussed on short and long time scales in this section. The energies involved can be separated into impact energy, which works on small time scales during the initial contact between surface and cluster, and binding energy, which is also of importance on longer timescales after the impact occurred.

In the following sections terms like temperature and pressure are used. Both work for macroscopic systems and loose their descriptive power in microscopic systems. It is even questionable if these terms still apply in the case of a cluster [65]. As being described by statistical processes, both quantities evade a simple description in the scales of a microscopic body. Thus there is no easy classification of the occurring effects. It gets more complicated if a macroscopic system like a surface interacts with a small cluster. Then the macroscopic system is correctly described by a temperature value but must be regarded as a donor of undirected kinetic energy to the microscopic system. The occurring effects range from melting to a total destruction of the clusters involved [66–68]. The experimental part of this work will mostly talk of temperatures if a cluster comes in contact with a macroscopic system.

1.2.1 Cluster Evolution on Surfaces

A typical system consisting of cluster and surface usually starts its evolution with the initial contact of both. The cluster's previous shape is that of a free cluster. Effects of the initial contact are strongly interconnected with the cluster's speed and size. Normally clusters impact with an energy in the order of 10 eV on a surface. A silver cluster consisting of 100 atoms would therefore have a speed of about 4×10^2 m/sec. With these non-relativistic speeds interactions between cluster and surface can be described by means of classical momentum and energy transfer. The influence of the cluster size is a more complicated matter because it involves, for example, the total or relative surface area, which can have a great impact on the cluster properties. The effects of the cluster's speed, however, are easier to quantify: The larger the speed, the larger is in consequence the impact energy. The initial cluster evolution normally happens on small time scales while simultaneously causing the most significant alterations.

In order to model the cluster correctly, the impact energy is not sufficient. After the cluster comes in contact with the surface, in many cases binding energy is released due to the forma-

tion of new bonds. The system evolves over a certain period of time, which can lead to many successive reorganization steps. During this time, it is also in contact with a specific surface so that an exchange of atoms may take place or an even more complete intermixing occurs. Multiple clusters on the same surface can interact with each other. Furthermore, kinks, layers or defects on the surface may have a great influence [69]. Finally, the surface may not consist of a pure substance but may be mixed purposely or not with foreign materials.

Both impact and binding energy are intertwined because both are part of the same overall process. While the former has descriptive power in a very short time scale, in most cases only a few picoseconds directly during deposition, the latter governs the interactions after that. Depending on the binding energy and the multitude of conditions mentioned above, processes like evaporation, diffusion, aggregation and alloying can occur [70]. The timescale of those ranges from seconds to days.

To understand concrete processes, a qualitative analysis of the energies involved is insufficient. The energy quantity must be regarded, too. In the case of low impact energies, the clusters are landed quite softly on the surface. This reduces the effects of rearrangements of the involved atoms in the cluster. Therefore information of the deposition is somewhat preserved. With a low deposition energy and sufficiently large cluster-surface interaction, thin films will form on a surface as observations show [71,72]. Increasing the deposition energy causes the formation of high quality adhering films [73–75]. In addition to that shallow implantations can occur. The temperatures and pressures produced by the impact can be varied by adjusting the kinetic energy of the clusters. Both parameters can be increased to a level that is unrivaled by many traditional methods [76–79]. If the clusters have a very high kinetic energy, the interaction between cluster and surface is so strong that incoming particles start to sputter. In most cases this means that atoms are dissolved from the surface while the clusters are completely destroyed [80–82]. The energy released from surface collisions may range from 10^{-2} *to* 10^{8} *eV*, thus it can cover 10 orders of magnitude [65].

To gain an understanding of the morphological changes of the cluster during impact, it is useful to take a closer look at a roughly spherical cluster. When it hits the surface, only very few atoms at the bottom are stopped abruptly while the rest remains at the initial velocity. This leads to a deformation of the cluster and, due to the bondings between its atoms, a shockwave propagates through the whole structure. This process can be understood by a local increase of potential energy, which is eventually released in form of kinetic energy. An example for that is the deposition of Al_N on a Cu surface, which leads to a size independent increase in temperature. With sufficient impact energy both surface and cluster melt, while the enormous increase in temperature and the occurring pressure leads to the formation of a crater [83]. *C. L. Cleveland* and *U. Landman* demonstrated that Ar_{561} clusters impacting on a NaCl(100) surface with a kinetic energy of 1050 *eV* create temperatures of 3000 *K* and pressures of 10^{4} *atm* [78].

Highly complex interactions can occur when a cluster initially comes in contact with a surface. Thus it is necessary to organize phenomena that are most frequently observed. These are [65]:

- **Soft landing**
  The particle does not move after impact, its kinetic energy is mostly absorbed by a buffer layer. There is only elastic deformation so that the structures of cluster and substrate are not altered. More detailed information on the theory can be found in chapter 1.2.2 on page 15. A description of the experimental procedure is presented in chapter 1.5.3 on page 42.
- **Ballistic deposition**
  The particle undergoes a plastic deformation during impact while the surface morphology is unchanged.
- **Fragmentation**
  The particle accumulates enough energy to not only deform but also decompose. This means that many internal bonds of the compound are broken while the fragmented remnants scatter over the surface. Size and position of those fragments strongly depend on impact energy, cluster size and the initial cluster material as well as surface properties.
- **Implantation**
  If the impact energy is large and the inter-atomic bonds of the particle are strong, the cluster can be buried below the surface after impact. The cluster stays intact for the most part without the formation of a crater or a prominent opening in the surface. The depth of the impact depends for the most part on the initial kinetic energy of the cluster. If the energy is large enough, the cluster can be completely buried below the surface.
- **Reflection**
  The particle touches the surface and is back-scattered due to an elastic deformation of cluster as well as surface. During impact, charge and energy information can be acquired.
- **Sputtering**
  Sputtering is observed when the kinetic energy of a particle is sufficiently large. During impact, the cluster scatters and its atoms as well as surface material are ejected. The impact energy and momentum of the cluster atoms is unevenly distributed, which leads to nonlinear collision cascades.
- **Crater formation**
  A particle that consists of more than 100 atoms can create enormous pressures when the impact energy is large enough. In contrast to implantation, surface material is forced to move away from the collision center. This results in a built up of material at the outer regions and a local melting. In consequence a crater is formed around the impacted cluster.
- **Radiation damage**
  The impact energy is large enough to displace cluster and surface material, but it is too

low to completely anneal the region in question. As a consequence vacancies and interstitials are produced. Even widespread amorphous zones can be created.

To get a grip on the relevant energies involved in any cluster-surface interaction, a classification of the cohesive energies of both cluster and surface can help. The equation

$$R = \frac{E_{coh}^{cl}}{E_{coh}^{s}} \qquad (10^{-2} \leq R \leq 10^{2}) \qquad (1.4)$$

shows the ratio R between the cohesive cluster energy E_{coh}^{cl} and the cohesive surface energy E_{coh}^{s} in the system. The variation of cluster-surface interactions under different conditions is obvious when the 4 orders of magnitude in the above energy ratio are regarded.

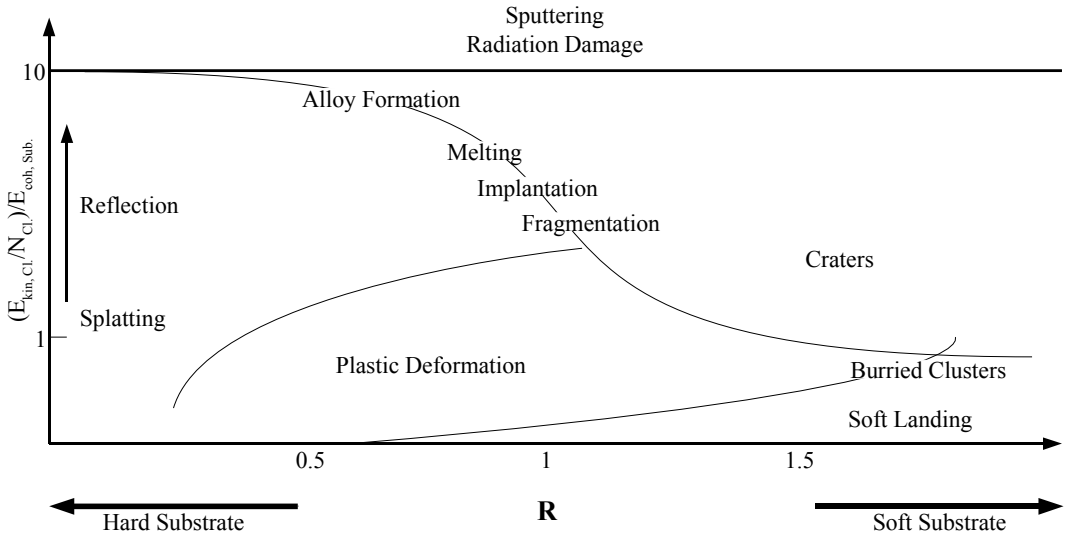

Figure 1.7: Mechanism diagram of cluster-surface interaction. R on the x-axis is the cluster energy ratio from equation 1.4 while the y-axis shows a normalized kinetic energy of the cluster (after [65] and [84])

With a low value of R, a deposited cluster can be subject to massive deformations while the surface remains unchanged. A large value of R causes the opposite effect. The surface is deformed while the cluster is not. The energy of the incoming particle is dispersed by the surface, which is of great importance for soft landing. Not only the individual cohesive energies of cluster and surface have to be regarded but also the bonding energy E_{coh}^{cl-s} between their respective atoms. In the case of soft landing, it is also necessary that the cluster stays intact long after impact, which is the case if $E_{coh}^{cl-s} \ll E_{coh}^{cl}$ is fulfilled. This means that the system will not favor a plastic deformation of the cluster [65].

Figure 1.7 shows a mechanism diagram that helps to classify the mentioned effects taking place during impact. Note that there are several combinations of impact energies and surface textures that result either in the formation of craters and reflection as well as a plastic deformation of the cluster. The cluster is only preserved under very specific circumstances. A soft landing process, necessary to retain an unaltered cluster, needs low energies and soft surfaces.

It has to be mentioned that the direct interaction between cluster and surface, which may release additional energy, is not included in the diagram. To preserve the cluster shape, the interaction between cluster and surface must be low.

Diffusion of clusters on a certain surface is another effect, which has to be taken into account. It describes the lateral mobility of a particle, like an atom or cluster, on the surface. Diffusion energy barriers determine the possibility and degree of said effect. Aggregates larger than single atoms usually experience a lower diffusion. Flat bodies like two-dimensional ad-atom islands have been shown to have a certain mobility on different surfaces [85–88]. Three-dimensional clusters can also show diffusion, especially in the presence of a weak cluster-surface interaction. Note that the cluster is not necessarily deformed or destroyed by that process. *Guerra et al.* propose that Sb_n and Au_n clusters up to 2300 atoms move by rotation over a graphite surface [89]. It is not yet clear to which degree other kinds of clusters behave accordingly. However, in many cases coalescence and agglomeration occurs independent of the intermediate processes [90].

1.2.2 Soft Landing

This topic will be dealt with in more detail because of the importance for most of the experiments described in this work. Keeping the cluster as well as the surface unaltered by deposition is the purpose of soft landing. This is a difficult task because collision induced plastic deformation as well as implantation or more destructive effects like fragmentation or sputtering have to be avoided. Energies lower than $10\,eV$ per cluster are required to reduce the chance that any of these effects occur.

Leaving the optimal arrangement of the surface aside for the moment, a simple model can help to clarify the event. If a small metal cluster (about 10 atoms) approaches a metal surface with $0\,eV$ kinetic energy, the cohesive energy between cluster and surface atoms will become important. Depending on the value of E_{coh}^{cl-s} (see above), the total energy of the system can be lowered. Another important aspect is the potential energy due to the initial shape of the cluster in the gas phase, which is the case before collision, in contrast to the final shape on the surface. Consequently the difference in energy will be released. Added to those values are the kinetic energy of the cluster, which is close to $0\,eV$ in this case, and the temperature of the surface, which has to be regarded as being the individual movements of atom in this order of magnitude. When the cluster comes in contact with the substrate, the particle will be accelerated towards it. Due to the low mass of a cluster and thus its low inertia compared to the forces at work, the entire transformation process happens at high speeds. While quantum effects will dominate as soon as cluster and surface atoms come close to each other, the relevant time scales are defined by the frequency of their mechanical contact. In a crystal this is best described by the Debye frequency (see section 3.1.2 on page 117), which leads to time scales of a few *ps* for interactions. The transformation of translational energy into internal energy heats the system up even before structural changes take place. When the cluster is in proper contact with the surface, the adsorption or binding energy, respectively, is released. Under conditions optimal for soft landing, the amount of energy is not sufficient to cause the bonds

of the cluster to break. Else the cluster is reshaped, maybe even from a 3-dimensional body to a flat one, which will eventually cover part of the surface. An example for this effect is Ag_7, which is shaped like a bipyramidal pentagon [91] while becoming a two-dimensional island on Pd(111) [92].

The behavior, described above, strongly depends on the cluster size. If larger clusters are regarded, deformation and implantation will happen with a reduced likelihood. This is due to the fact that a larger amount of atoms per cluster decreases its share of kinetic energy and thus making a deformation increasingly unlikely. Ignoring the multitude of surface and cluster materials for the moment, this is the case if the amount of atoms a cluster consists of is larger than around 100. For the cohesive energy ratio R from equation 1.4 on page 14 $R \approx 1$ must be fulfilled. This means that neither cluster nor surface are subject to significant deformations. A reduced cluster-surface interaction allows a lower amount of atoms per cluster for soft landing [65].

1.2.3 Investigating Clusters on Surfaces

Depending on the sample system, very different investigation methods have to be used in order to adopt to its special requirements. For the most part the magnitude of the cluster-surface interaction determines the method. While imaging processes like STM need a strong interaction in order not to move or collect clusters, this is not necessary for most types of spectroscopy. However, for the latter it is best if the interaction is weak so that the electronic structure is not altered or masked by the surface. Typically there exists any magnitude of interaction between those two extremes so that each experimental setup has to be adjusted to the measurement methods available.

This section will describe several methods suitable for the investigation of clusters on surfaces. The most frequently used *scanning tunneling microscopy* (STM) measurement process will be described as well as *scanning tunneling spectroscopy* (STS) as spectroscopy method. *Transmission electron microscopy* (TEM) is solely presented for comparison. *Molecular dynamic* (MD) simulations have been conducted by groups associated with us and were used in some investigations so that the basic principle will be described.

1.2.3.1 STM - Scanning Tunneling Microscopy

Quite complex scanning tunneling microscopes are in use today but to describe them in detail would be far too elaborate at this point. Thus only the basic principle will be explained in this chapter, which remained unchanged since the beginning.

In classical physics an electric current always needs a conducting medium to transpass a specific distance. This is, however, not the case in quantum physics. The *Schrödinger Equation* allows a finite electrical current between two electrodes, even if an isolator like vacuum prevents any classical transfer. This is described by so called quantum tunneling [93]:

$$I \propto e^{-2\sqrt{\frac{2m}{\hbar^2}(\Phi - E)}d} \tag{1.5}$$

The electrical current I exponentially decreases with the distance d, which is equal to the size of the classical gap for the case that the electron energy E is much smaller than the work function Φ of the respective material. The constants m and $h=2\pi\hbar$ are the electron mass and the *Planck constant*, respectively [61]. Note that $E<<\Phi$ must be fulfilled for equation 1.5 in order to justify certain simplifications. A realistic system is three dimensional while the potentials at works are neither infinite nor simple, as often assumed in simplified models.

The great sensitivity of the tunneling current towards changes in distance together with the fact that there is no mechanical contact between both electrodes, are very important for a functioning scanning tunneling microscope. In a practical sense quantum tunneling is used by replacing one electrode by a tungsten tunneling tip and the other by the sample that is to be investigated. An electrical current is only possible if both materials are conducting so that normally metals or at least metal coatings are used for tip and sample. To investigate a particular surface, not only does it need to have conducting properties but must also be flat on an atomic level so that a tip can be moved alongside it without collisions. The tip on the other hand must converge at an atomic level so that only few atoms contribute to the tunneling current. However, due to the great distance sensitivity of this method, several atoms can be nearby the sample while the majority of the current will still flow through the outer most atom. For a proper measurement, UHV conditions are crucial to prevent unwanted adsorbats, and low temperatures hinder thermal drift effects [94–96].

To investigate surfaces, the normal mode of operation is the *mode of constant current*. In this case the distance between tip and sample is varied by piezo electric elements until the current has reached a preset value. Aside from electronic effects, the distance d in equation 1.5 is therefore always set to a constant value. By determining the tip's displacement, a relief of the sample's surface can be measured (see figures 1.8 and 1.9).

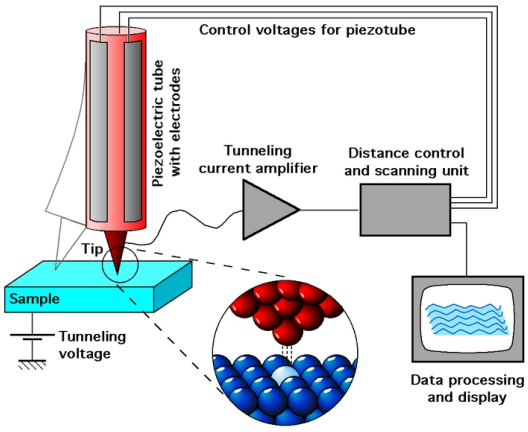

Figure 1.8: Schematic depiction of an STM apparatus (see picture credits)

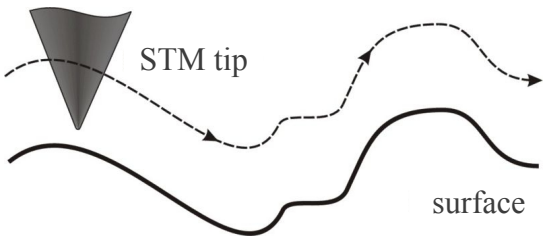

Figure 1.9: The STM tip keeps a constant distance to the surface (see picture credits)

Not only geometric structures on the sample's surface can have influence on the measurement but also changes in the electronic properties of the materials. A certain amount of electrons can be detached from either sample or tip, depending on the sum of all electronic states that can be reached at a specific voltage. Note that not only electrons at a specific energy must be regarded but also those closer to the *Fermi* level. A more detailed description can be found in section 1.2.3.2. The density of states that is the summation of all states in an energy interval, is best described by the band structure of the metal in question. A greater amount of electrons causes an increase of the measured tunneling current so that the feedback control system changes the distance accordingly. As a consequence changes in the electronic structure can overlap the height information as illustrated in figure 1.10. Thus an STM image is not a simple depiction of the sample's surface.

The tip can cause additional problems in certain experiments. Because it must be thought as being a three dimensional body, not only the outer most part can interact with a structure on a surface but also the sides. If an object has a height much greater than its width, the lateral information is nearly completely lost. This is due to the fact that during scanning the tip approaches the object and atoms at the flank create the tunneling current. The tip is therefore retracted which creates the illusion of a surface structure where actually is none. Thus the tip's shape is always imaged as well as figure 1.11 demonstrates. Mathematically this phenomenon can be described as a convolution of surface structure and tip. However, the height information of a sufficiently simple object is unchanged despite of possible additional electronic effects.

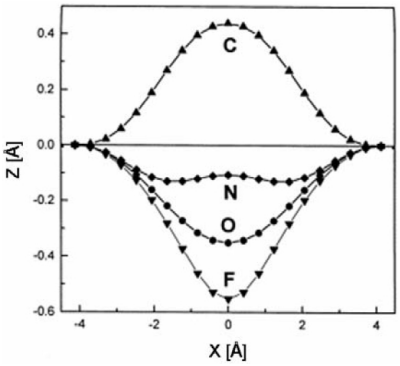

Figure 1.10: STM line profiles for several adsorbates [97]. Depending on the electronic structure, the height information is altered.

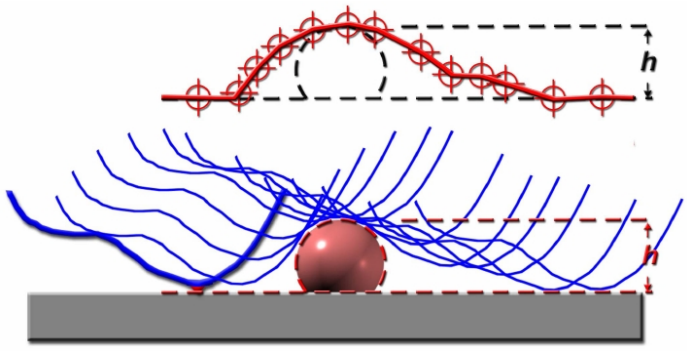

Figure 1.11: Schematic depiction of a round cluster (bottom, red) measured by an arbitrarily shaped tip (bottom, blue). The cluster is imaged as depicted on the top by the red encompassing line.

A standard STM apparatus is able to work in two more modes of operation. There is the *mode of constant height* in which the tip's distance to the sample is kept constant while changes in tunneling current are measured. An advantage of this method is the ability to move the tip much more quickly over the surface because a feedback loop can be avoided. There is, however, an increased risk of collisions. As a third option the STM apparatus can be used for STS, which is a spectroscopy method. It will be described in more detail in the next section.

1.2.3.2 STS - Scanning Tunneling Spectroscopy

A special feature of the STM apparatus is its spectroscopy option. The investigated materials must have some conductivity to enable the process, similar to STM. In most practical applications metals or semiconductors are used.

In contrast to a standard STM measurement the tunneling current is not kept constant by adapting the z-position of the tip, but the x-, y- and z-coordinates are set to a fixed value. This could be right above a cluster on the surface or a prominent structure, which is to be investigated. While the tip is not moving, the tunneling bias is continuously changed in a preset range in combination with a measurement of the tunneling current. Electrons surpassing the tunneling barrier are either coming from occupied states or going into unoccupied states of the material in question, depending on the direction of the current. With a greater positive voltage applied to the sample, more electrons from deeper orbitals of the tip are detached and are consequently added to the tunneling current as demonstrated in figure 1.12. In the case of a metal, discrete orbitals are replaced by a continuous band structure. Now the measured current correlates to the amount of all electronic states from which electrons are detachable by the applied bias. Thus the change in current or mathematically speaking the derivative of the bias-current function correlates to the density of states at a certain energy.

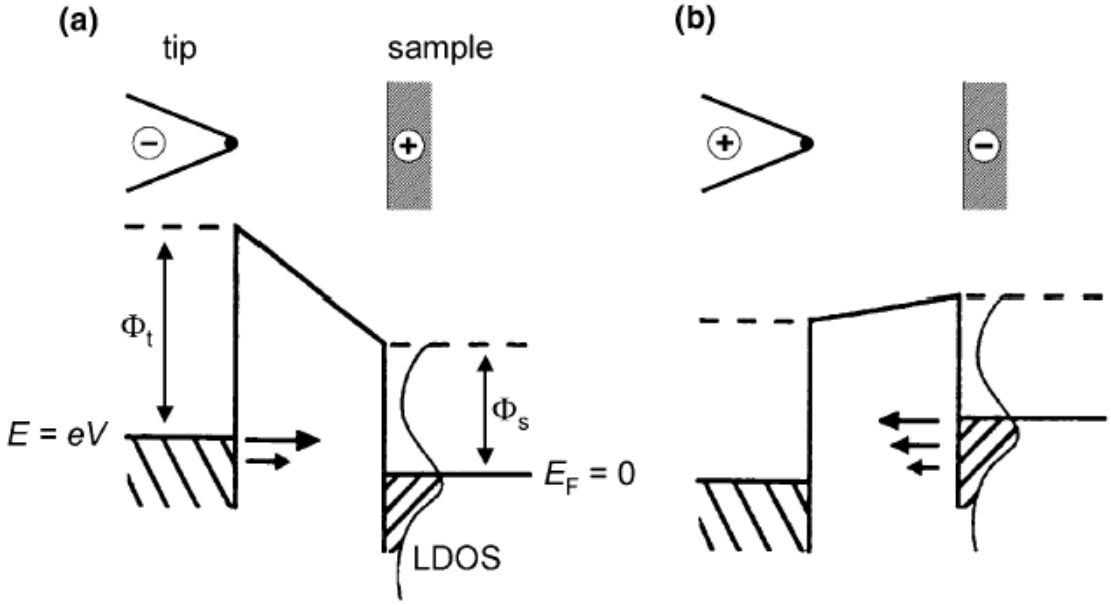

Figure 1.12: Schematic depiction of the sample-tip system for positive and negative voltages. If the tip is negatively charged (a), electrons from occupied states of the tip are transmitted into unoccupied states of the sample. The opposite is true if the tip is positively charged and the sample negatively (b). Now the occupied states of the sample can be investigated [62].

In summary STS can be used to investigate tiny structures on a surface because the tunneling tip restricts the electrons to overcome the tunneling barrier in a wider area. The fact that the outer most end of the tip ideally consists of just a single atom, allows the investigation of structures well below 1 nm^2. STS enables in contrast to UPS (see section 1.1.2 on page 9) not

only the investigation of occupied states but also of unoccupied states due to the fact that positive and negative voltages are applicable [93].

1.2.3.3 TEM – Transmission Electron Microscopy

A transmission electron microscope can be understood as a device which essentially consists of electronic lenses. These are used to manipulate electrons for imaging purposes. Electrons can contain information on the surface structure if they transpass it. They can be measured using a sufficient detector before evaluating the data using special computer systems. An advantage to optical microscopy is the dependence of an electron's wavelength on its velocity. Thus electrons with a high kinetic energy are able to resolve smaller structures than photons in the visible spectrum. Thus much better resolutions can be obtained compared to optical microscopy. However, lens aberrations set a limit to the achievable resolution. With sufficiently high electron energies, structures in the order of 0.05 *nm* can be imaged. The device is, however, only able to operate under vacuum conditions for which several pumping stages are necessary.

Because electrons easily interact with matter, only thin specimen of 10 *nm*-100 *nm* thickness can be imaged properly. The thickness can be increased if the atomic number of the atoms, which the sample consists of, is low. Another important factor concerning the possible thickness is the electron energy. It normally ranges from 80 *keV*-400 *keV* while a smaller value requires a thinner specimen. However, when a lower resolution is acceptable, the thickness of the specimen in question can be increased.

TEM is mentioned in this chapter despite not being used in the experiments. It poses, however, a competition to STM in its capability to image objects. It has been used quite successfully in depicting surface structures and even clusters on an atomic level [98,99].

1.2.3.4 Molecular Dynamic Simulation

A key tool for cluster physics is the computer simulation of the cluster's behavior on an atomic level. This is due to the fact that the underlying questions do not stem from unknown physical behaviors of the particles but from their complex interaction. While experimental results are still necessary to confirm and improve computed results, much of the data can nowadays be gathered by using powerful computers. Of course there are still some effects, particularly on long time scales, that cannot be simulated in a reasonable time frame. For a simulation to be accurate, time steps smaller than 10 *fs* are necessary. Because each step is in itself a complex computation, time frames up to several *ns* can be considered being the limit for this type of simulation. However, even in experiments with longer time scales, so called molecular dynamic simulation can help to model the initial state or intermediate arrangements.

Molecular dynamic simulation can be understood as a simulation method that is mainly initialized with an arrangement of atoms and their overall temperature. The latter can be described as an initial random momentum of the atoms. Further aspects like initial kinetic energy can also be involved. Due to the complexity of the system, certain models are used to simplify the computation, especially of the potentials involved. Thus the choice of fitting models strongly depends on the experimental outcome of cluster-surface collisions. The more

detailed the information gets the more accurate the simulations will be. In MD simulations, the relevant spatial order of magnitude is around a few *nm*, which leads to additional complications. Because temperature often plays a major role in such systems, all experimental as well as simulated outcomes must be regarded as not being representative on their own. Every interaction can only be described statistically. Only a sufficiently large number of particles with the same initial conditions provide enough information to be able to include statistical effects and reveal underlying physical principles. This is automatically the case in most experiments, which normally deal with a large number of particles. A simulation, however, has to run the same computation once for each particle. Thus statistics are always limited if the simulation should finish in a reasonable time [65,100].

A more specialized version of a computer simulation is *density functional theory* (DFT). It encompasses quantum mechanical models to solve the many body problem raised by solid state physics. Mathematically functionals of the local electron density are used as input parameters, hence the name of the method. This avoids solving the entire Schrödinger equation for the many body system, which would be an impossible task for systems surpassing even a small number of electrons [101]. The exact approach and numerous details will not be described at this point for neither MD nor DFT simulations are emphases of this work but serve as complementary tools. They were performed by the cooperation partners *T. Järvi* and *M. Moseler* in Freiburg.

1.3 Materials

In an experimental setup the arrangement of used materials has a great influence on their interaction and thus behavior. Cluster as well as surface materials can be chosen from almost any atom in solid state, which includes gases at low temperatures. Obviously the complexity of any interaction increases with the number of electrons involved in a bonding so that larger, especially metallic atoms, tend to form more complex compounds. Noble gases, for example, lack electrons contributing to inter-atomic bondings and thus display a comparably simple *van-der-Waals* interaction [102–104]. Another aspect determining the arrangement of atoms is their size. This is important if different kinds of materials are in direct contact with each other. Geometrically or energetically a simple, highly ordered lattice structure may be impossible. This and further geometric effects cause the emergence of reconstruction patterns [105–107].

For both clusters and surfaces, the aspects mentioned above are essential. However, for a more detailed discussion, it is useful to describe them separately because they have quite different requirements in an experimental sense.

1.3.1 Cluster Materials

The choice of a cluster material has a strong influence on its behavior. The cluster size does not only depend on the amount of atoms it consists of but also on the atom's radius and bond length. The cluster mass, which influences the velocity and momentum it gets during acceler-

ation, is determined by the atomic mass of the chosen material. Most important, however, are the material's electronic properties, which have a great influence on many aspects of the resulting cluster. They determine shape, size, melting point and various interactions with a given surface.

Most commonly used for cluster materials are metals of a single element because they are easy to handle experimentally, form greater compounds voluntarily and deliver a comprehensible electronic structure. The latter is characterized by a non-metallic distribution of electrons in the atomic shell structure for smaller clusters and a partly or fully formed band structure for larger ones. This phenomenon is of special interest because it delivers information on the very basic question about the evolution of metallic properties. It is possible to create alloys of several clusters and investigate their properties. This is, however, often avoided if experiments aim at basic research because the larger complexity of new compounds is difficult to handle in theoretical approaches like simulations. In addition to that very basic phenomena, that are to be investigated, may be superimposed by side effects.

It is also possible to use quite exotic materials for clusters. Not only metals but about all nonmetals can be used to form a cluster. Noble gases have been mentioned before [22,108–110]. Carbon atoms form special clusters that are called fullerenes (see section 1.3.2.3 on page 26). Even two atomic gases like oxygen can become clusters [111]. Small metalloid atoms like Boron have also been used [112]. Furthermore the great variety of chemical compounds can also form clusters. This blurs, however, the boundary between cluster physics and chemistry. In addition to that inter-atomic interactions become increasingly complex and thus more difficult to understand or even simulate. Thus these materials are more often used for technical purposes than for theoretical ones. In this work, however, very basic cluster properties are to be investigated which demand the simple atomic structures found in metals.

1.3.1.1 Copper

Copper is commonly used as a cluster material in the laboratory but was only recently introduced to our experiments. It is a reddish-orange transitional metal with an atomic number of 29 and an atomic mass of 63.55 *amu* [113]. In contact with oxygen it can form a great variation of oxides [114]. However, when in air, it normally forms a layer of brown-black copper oxide, which gives the metal its commonly known color. The oxidized layer isolates lower layers from contact with air so that they remain in their pure unaltered form. Both aspects are important in an experimental sense. On the one hand the high reactivity of copper is a well known obstacle in any cluster experiment. Sufficient UHV conditions are mandatory to prevent oxidation or reaction with other foreign materials. An image of a copper target can be found in figure 1.24 on page 36.

Due to the fact that both copper and silver count as noble metals, the electronic properties of copper will be described exemplary. This can be done because both metals are quite similar in their electronic structure. They have a single valence electron in the s-shell, which mainly contributes to the electronic properties. Note that this allows the emergence of electronically magic number. This marks a similarity to the previously mentioned sodium. As transitional metals, copper and silver posses electrons in d-states, which are usually difficult to describe because they have partly localized and partly itinerant character. However, both have a fully

filled d-shell, which makes them easier to handle theoretically than other transitional metals. This causes them to be useful for UPS, which is the most commonly used experimental method to gather information on the electronic properties of clusters in this work. Until today photoemission spectra of copper and copper compounds have been measured multiple times. In [115–117] a selection of several examples can be found.

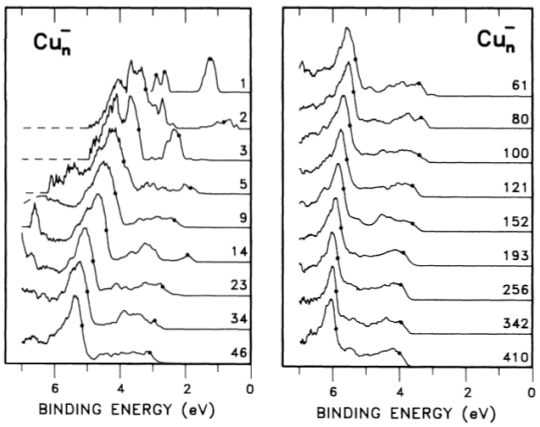

Figure 1.13: UPS spectra of negatively charged Cu_n^- clusters [118]. 4s and 3d band energies are marked as small dots.

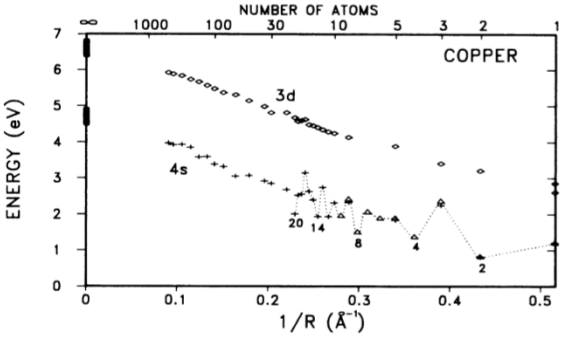

Figure 1.14: 4*s* (open triangles) and 3*d* (open dots) band energies as a function of the inverse cluster radius *1/R* [118].

O. Cheshnovsky et al. provided quite detailed information on the evolution of the electronic properties of size selected copper clusters [118]. They argued that the first small peak below the vacuum level in the photoemission spectrum of copper (see figure 1.13) can be attributed to the 4*s* state and the most prominent peak to the onset of 3*d* states. However, these onsets move away from the vacuum level with increasing cluster size and approach the Fermi level for $n \to \infty$ as illustrated in figure 1.14 (cf. the dynamic final state effect in section 4.1.4 on page 143). Note that the 4*s* states can be attributed to delocalized valence electrons, which are very sensitive to changes in cluster shape and surface area. Thus the corresponding peaks do not move away smoothly from the Fermi level but show intermediate deviations. The 3*d* onset on the other hand delivers a monotone evolution. This is caused by the more core-like nature of the corresponding electrons so that they are only slightly influenced by the cluster geometry. There is also a sharpening of the 3*d* peak, which can be attributed to an increased density of states also observed in bulk copper [118,119].

1.3.1.2 Silver

Silver is the most commonly used cluster metal in the following experiments. It is a lustrous white transitional metal with an atomic number of 47 and an average atomic weight of 107.87 *amu*. An image of a silver target used in our experiments is shown in figure 1.24 on page 36. The mass of a single atom in a typical cluster is not easy to determine because natural silver comes in the form of two stable isotopes, ^{107}Ag and ^{109}Ag, which are nearly identical in occurrence (^{107}Ag: 51,8 %) [113,120]. When silver is used as a target material in an experiment, both isotopes are normally mixed together so that the atoms in a resulting cluster have

two different masses in equal parts. This is, however, unproblematic because isotopes do not have any significant influence on the atom's electronic properties. In addition to that the cluster mass, at least for bigger clusters, can be estimated from the abundance of both isotopes. An advantage for experimenters is silver's low tendency to form oxides in air or to react with rest gases in vacuum chambers.

1.3.2 Surface Materials

In contrast to cluster materials, surface materials are not the main focus of interest. Their properties are only interesting in combination with the cluster that they have contact with. Depending on the surface material, numerous changes to the cluster can occur as mentioned before in section 1.2 on page 11. Aside from interactions, a surface must serve as a layer for clusters, which means that it has to be uniform and void of defects. This restricts the amount of possible surface materials. Only substances that come with well known preparation methods are usable. For once metals can be easily flattened and it is possible to fashion them into almost any shape. Some metals show low vapor pressures so that they are quite suited for vacuum conditions [121], and many can be heated to high temperatures, which increases options for preparation. In addition to that a theoretical approach towards understanding an interaction is simplified if both cluster and surface consist of the same material.

For some purposes other surface materials are preferred. While metals can still serve as an underlayment, the actual surface may be exchanged by a nonmetal. This is due to the fact that interactions between metals are normally so strong that the initial shape of a cluster is lost after coming in contact with the surface. Therefore buffer layers like C_{60} are used. In other cases, like UPS, the electronic structures of cluster and surface are too similar to distinguish them from each other. Then materials with a less prominent electronic structure like graphite are used.

1.3.2.1 Gold

Gold is a transitional metal with an atomic number of 79 and an atomic mass of 196.97 *amu* [113], which results in a high density compared to other metals. It has only one naturally occurring isotope so that a potential gold surface consists of only one kind of atom. An advantageous property of gold is its ductility, which is greater than that of any other metal. This helps to fashion thin and smooth surfaces for samples. The crystalline structure of gold is face cubic centered (fcc). A cut alongside the plane of the Miller indices (111) results in an Au(111) surface [122]. Figure 1.15 illustrates the concrete structure of Au(111).

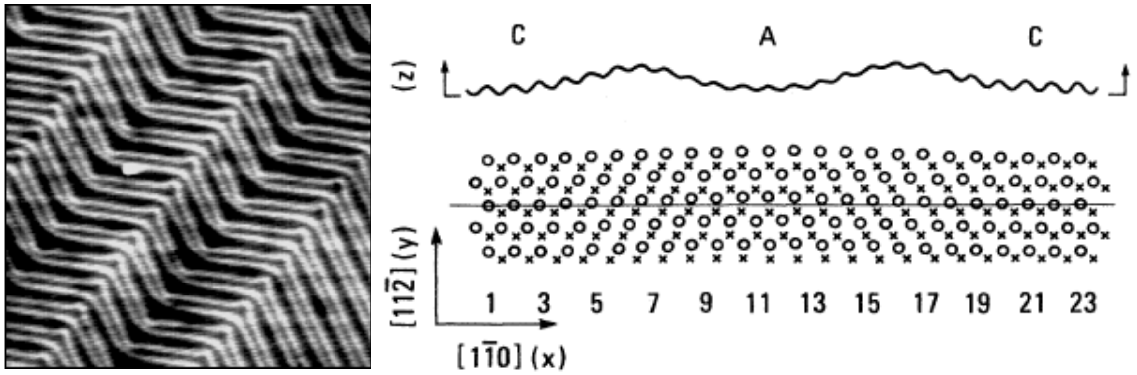

Figure 1.15: On the left is an STM image of a $(23\pm1)\times\sqrt{3}$ reconstructed Au(111) surface. This type of surface arrangement is also known as herringbone reconstruction because the ridges, visible as white lines, resemble a herringbone pattern [123]. On the right a schematic of Au(111) is shown. Empty circles illustrate Au atoms of the reconstructed top layer, while crosses represent Au atoms of the layer below; the capital letter C shows where a hcp structure can be observed while the capital letter A indicates a region with fcc structure [124,125].

In most experiments this epitaxial Au(111) is used for surfaces. It is created by evaporating gold onto a mica underlayment. Under fitting environmental conditions, a uniform oriented lattice emerges [126]. It is smooth and for the most part defect free on an atomic level. Au(111) shows a $(23\pm1)\times\sqrt{3}$ reconstruction in its crystalline structure on its surface [125], which is unique for a metal with an fcc structure [127]. This is due to missing bonding partners at the top layer. Consequently it is not energetically favorable for Au(111) to keep the lattice structure but to rearrange the top most atoms. Now the regular ABC stacking order of a fcc structure is frequently interrupted by an ABA stacking order (hcp structure).

1.3.2.2 HOPG (Highly Ordered Pyrolytic Graphite)

While graphite is the most common modification of carbon in nature, HOPG is a rare exception due to its highly ordered structure and smooth surface. It is composed of layers, which are bound in between by covalent bondings resulting from a sp^2 hybridization. Such a layer shows a hcp lattice structure with an ABAB stacking order. The layers themselves are, however, only bound by van-der-Waals interaction to each other, which are much weaker than the covalent bondings. A direct comparison of the binding energies clarifies this effect. The covalent bondings within a layer have a binding energy of 3.4 *eV* while the layers themselves are only bound with 0.07 *eV*. Thus stable single layers emerge, which are easily removed from each other. In addition to that the covalent bondings are with 0.142 *nm* shorter than the distance between the layers, which is 0.335 *nm* [128] (see figures 1.16 and 1.17).

The trigonal orientation of the orbitals of a carbon atom prevents not only the formation of carbon rings but also leaves one of four valence electrons unpaired. Each carbon atom can now contribute one free, so called π-electron, to a band of delocalized electrons. As a consequence HOPG is an anisotropic conductor: Its in-plane resistivity resembles with $\rho=9.6\times10^{-6}\,\Omega m$ that of a metal. This connection to metallic behavior is also reflected by a very metal-like temperature dependence of the conductivity. The resistivity between the lay-

ers is due to a lack of any effective electron transportation mechanism with $\rho = 4.1 \times 10^{-5}\,\Omega m$ significantly higher [129–132].

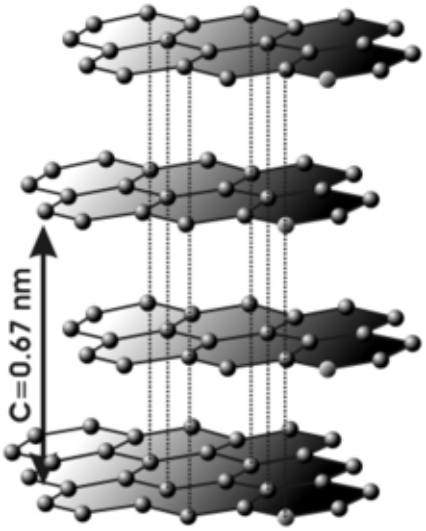

Figure 1.16: Layers of HOPG shown in pseudo 3D. (see picture credits)

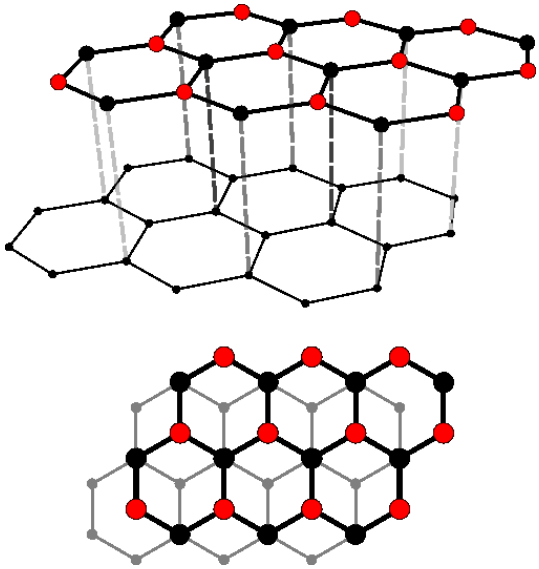

Figure 1.17: Layers of HOPG shown in pseudo 3D and top view. Atoms marked red have a greater distance to atoms in neighboring layers. (see picture credits)

Thus HOPG can be used for STM experiments, which need an electrical conducting surface. At the same time the non-metallic nature of graphite and the low tendency to form bonds between the layer, ensures a weak interaction between HOPG and any particle on its surface.

1.3.2.3 C_{60} and other Fullerenes

Fullerenes are special kinds of molecules, which are completely composed of carbon atoms. They qualify as so called network clusters [32]. They are beside graphite and diamond one of the three most prominent carbon modifications. The existence of fullerenes is predicted since 1970, when *E. Osawa* showed that they could theoretically be formed [133]. Until 1985 they remained a theoretical possibility, which changed when *R.E. Smalley et al.* and *H.W. Kroto* proved their existence experimentally [134]. They can be characterized by their special shape, which always consists of a carbon shell with a hollow interior. This includes closed objects like spheres or ellipsoids as well as tubes, which have two open ends. The hollowed out shape causes them to occupy a greater volume than the individual sizes of the carbon atoms, they consist of, would suggest. The lattice structure has to be ordered in such a way that the atoms, they consist of, can be distributed uniformly. There is no theoretical limit for the size of a fullerene. However, smaller ones are more stable than their larger counterparts.

C_{60} is a spherical, cage like fullerene, which consists of 60 carbon atoms [28] and has a diameter of about 1 *nm*. It can be constructed out of 20 hexagons and 12 pentagons, which are characterized by a carbon atom at each of their edges. However, 2 pentagons never come in

contact with each other, which is known as the *isolated pentagon rule* (IPR). The C_{60} molecule is the smallest IPR fullerene. The size as well as the high symmetry contributes to its stability, which is the highest amongst fullerenes. First observations of C_{60} in a solid state were made by *Krätschmer et al.* in 1990 [135].

As figures 1.18 and 1.19 illustrate, each carbon atom is in direct contact with 3 neighbors due to covalent bondings. This is similar to HOPG, which is just like C_{60} sp^2 hybridized. In direct analogy each carbon atom of C_{60} contributes a free and delocalized π-electron to the molecule. As a consequence this fullerene shows surprisingly high electrical conductivity.

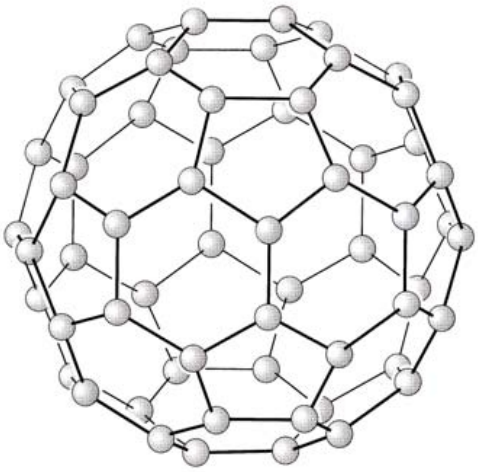

Figure 1.18: schematic depiction of a C_{60} molecule. Each pentagon of the surface is surrounded by 5 hexagons [28].

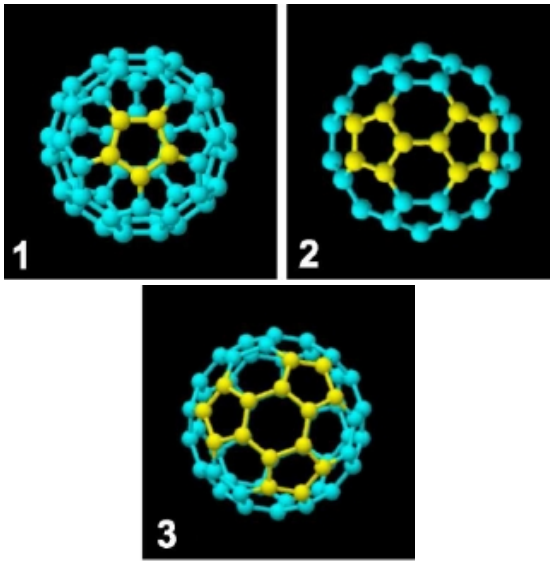

Figure 1.19: Depiction of three possible orientation of C_{60}-fullerenes on an arbitrary surface in top view. The highlighted parts can be revealed in STM measurements due to their deviating electronic behaviors [136].

C_{60} is particularly beneficial when used as a buffer layer. Because most materials used as an underlayment, such as Au(111) or HOPG, are either detrimental to the integrity of a cluster or do not adhere it to the surface. Both materials are comparably easy to prepare so that they can be used as an underlayment for C_{60}. With an approximate distance of 1 *nm* from the surface, due to the size of the molecule, each interaction with the surface is weakened. With additional C_{60} layers the distance is increased and thus the interaction further reduced. An important property of C_{60} is its ability to keep clusters in place when STM measurements are conducted. Furthermore fullerenes do not display a strong interaction between each other so that incoming particles can locally and temporarily shift the fullerenes and thus loose their kinetic energy without being deformed. This phenomenon is used in the soft landing procedure and will be discussed in chapter 1.5.3 on page 42.

C_{60} on HOPG or Au(111), the most commonly used surface materials in the experiments, has been shown to shift its orientation spontaneously. The fullerenes rotate independently from each other but the magnitude correlates to the temperature they are exposed to. How-

ever, at 77 K, which is the most common experimental condition, this effect is negligible. Note that in some cases higher temperatures were involved so that this effect may non the less be of importance.

1.4 Surface Science Facility

Each experimental setup depends on the devices used and their composition as well as the available time frame. The entirety of all machines and components will be summarized as *Surface Science Facility*. This encompasses the *Cluster Machine* and a surface science apparatus provided by the *Omicron Nanotechnology GmbH* [137] composed of *Preparation* as well as the *Analysis Chamber* and facilitating devices like pumps and pressure gauges. Construction and related experiments were conducted within the context of the project *SPP 1153* of the *Deutsche Forschungsgemeinschaft*. An overview of the relevant devices will be given in the following chapters, focusing on the parts that have been used most extensively while only briefly covering the rest.

1.4.1 Preparation and Analysis Chamber

The Preparation Chamber of the Surface Science Facility can be understood as its center piece. It is connected to every other chamber as well as the *Cluster Machine* and enables the manipulation of sample systems. UHV conditions are ensured by three pumping stages. In a first step a pressure of about 10^{-3} *mbar* is generated with a *Rotary Vane Pump*, which transports large amounts of gas by using fast rotating vanes. The resulting pressure is low enough for a *Turbomolecular Pump* to work. It increases the outwards oriented momentum of gas particles by using an array of rotating metallic lamellas. Statistically the particles are then more likely to leave the chamber than to return to it. Together both pumps can lead to pressures as low as 10^{-8} *mbar*. Adsorbates inside the chamber, primarily water, prevent a further decrease in pressure. Thus Preparation Chamber as well as Analysis Chamber are heated to 150°*C* from time to time using a baking tent. As a consequence a final pressure as low as 10^{-11} *mbar* can be archived. In most cases, however, the pressure is stable around 5×10^{-10} *mbar*. After baking, the Turbomolecular Pumps can be separated from the main chamber by valves so that shutting them down, which is necessary to prevent vibrations during STM experiments, does not affect the pressures inside the Preparation Chamber. After that an *Ion Pump*, which is located underneath the Preparation Chamber, preserves vacuum conditions. It uses a high voltage to ionize stray atoms and molecules, which are then incorporated in titanium plates and thus removed from the vacuum chamber. In addition to that a *Titanium Sublimation Pump* supports this effort by frequently evaporating titanium into the chamber and thus absorbing foreign material. All pumps are described in more detail in [138].

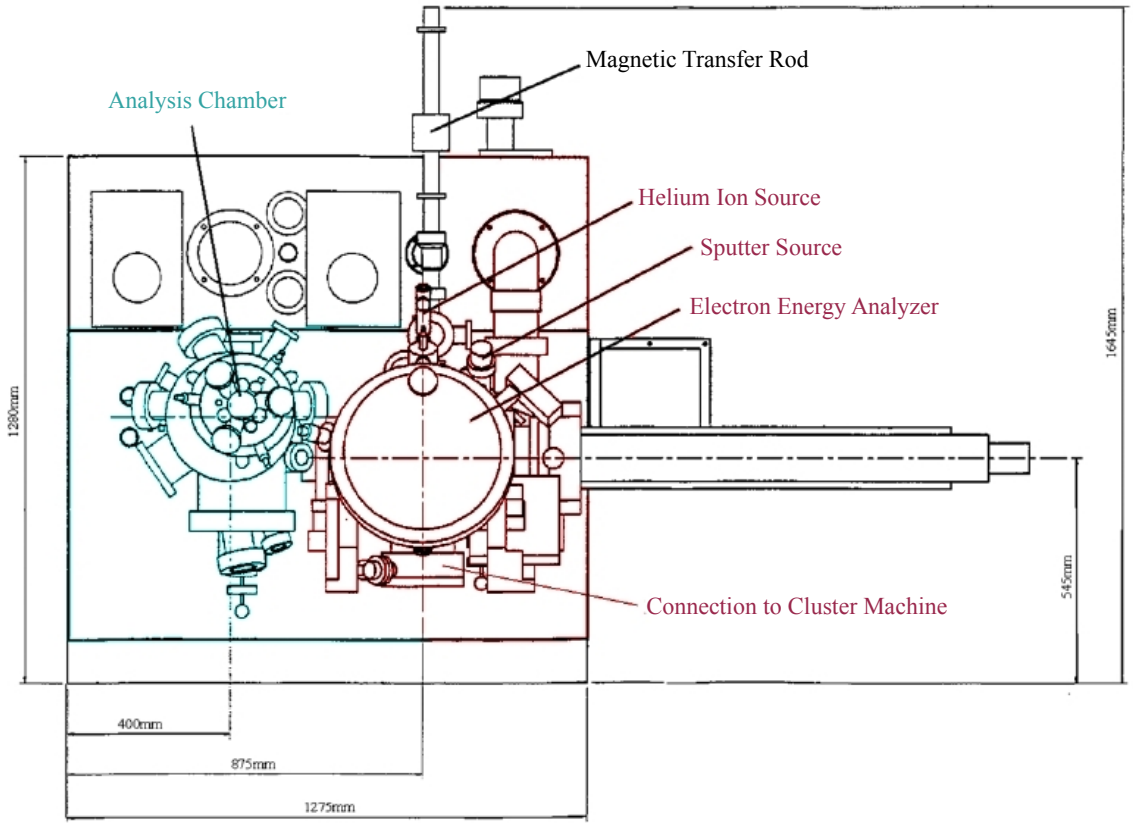

Figure 1.20: Top view of the Preparation Chamber (red) with connected Analysis Chamber (green) and associated parts (gray). The Cluster Machine is a separate device and is connected to the Preparation Chamber by a single flange and valve.

A newly prepared sample can be inserted into the chamber via a load lock, which can be isolated from it by a valve. This enables the opening and closing of the lock without endangering the vacuum conditions of the Preparation Chamber. A magnetic transfer rod (see figure 1.20) enables the experimenter to hold the sample and place it inside the Preparation Chamber. There it is transferred to the main manipulator, which is arranged alongside the chamber's main axis. It is a vital piece of equipment because it can move the sample back and forth as well as tilting it to different angles by rotating the manipulator. This enables the use of several devices like evaporators or the Cluster Machine by placing the sample in front of them. A transfer of the sample into the Analysis Chamber is also possible. Another features of the manipulator is its ability to heat a sample up to at least 600°C while checking the temperature with the help of an inbuilt thermocouple. It can also be cooled with liquid gases. By using liquid helium, temperatures as low as 10 K can be achieved while an inbuilt heater allows a continuous temperature variation. For the measurement of low temperatures a silicon diode is used instead of the thermocouple due to its higher accuracy.

Noble gases like helium, argon and neon can be inserted into the Preparation Chamber for different purposes. Argon is necessary to supply a sputter gun. Argon and neon can be adsorbed onto samples when its temperature is low enough. It has to be noted that even the gas

lines are usually baked out before they are used. However, tiny amounts of foreign gas can enter the chamber non the less and therefore affect the vacuum condition negatively.

The sputter gun is used to ionize and accelerate argon atoms towards a sample. The ions impact with high kinetic energy and successively remove the top most layers of surface material.

An inbuilt C_{60} evaporator [139] allows the creation of C_{60} buffer layers on different sample systems. The amount of material can be precisely adjusted so that coverages between less than 1 to more than 3 monolayers can easily be achieved. Another evaporator enables the deposition of several metals onto a sample. The desired substance must be inserted into a crucible while the chamber is not under vacuum conditions. So changing the metal requires a greater effort. In most cases lead and more recently silver have been used as evaporation material.

The Analysis Chamber is connected to the Preparation Chamber and separated from it by a valve. It encompasses the entire STM apparatus and several sample holders. The chamber is void of any mechanical pump but Ion Pump and Titanium Sublimation Pump are present. It is less exposed to undesirable vacuum conditions because there is neither a connection to a lock or the cluster machine nor does any contamination due to inserted gas occur. This enables an enduring pressure around 5×10^{-11} *mbar*. Thus samples can be stored effectively for a long time without the risk of severe contamination. Note that a sample inside the STM apparatus is subjected to a much lower pressure due to the small volume of its interior and the surrounding cryostat, which adsorb foreign material when cooled with liquid gas.

1.4.2 Cluster Machine

The main part of the Cluster Machine is composed of three chambers. The first is the *Cluster Source*, which contains the target that delivers clusters of multiple sizes by gas aggregation. The second, the C*ryo Chamber*, provides a low temperature environment in order to adsorb argon gas and foreign materials. The third chamber is the *Mass Selector*, which enables the experimenter to isolate a desired cluster mass. Each chamber is put under high vacuum conditions of at least 10^{-6} *mbar* by using two essential pumping stages. A Rotary Vane Pump in combination with a Turbomolecular Pump is attached to each chamber so that the final vacuum conditions can be achieved. A basic depiction of the Cluster Machine and its interior can be found in figure 1.21.

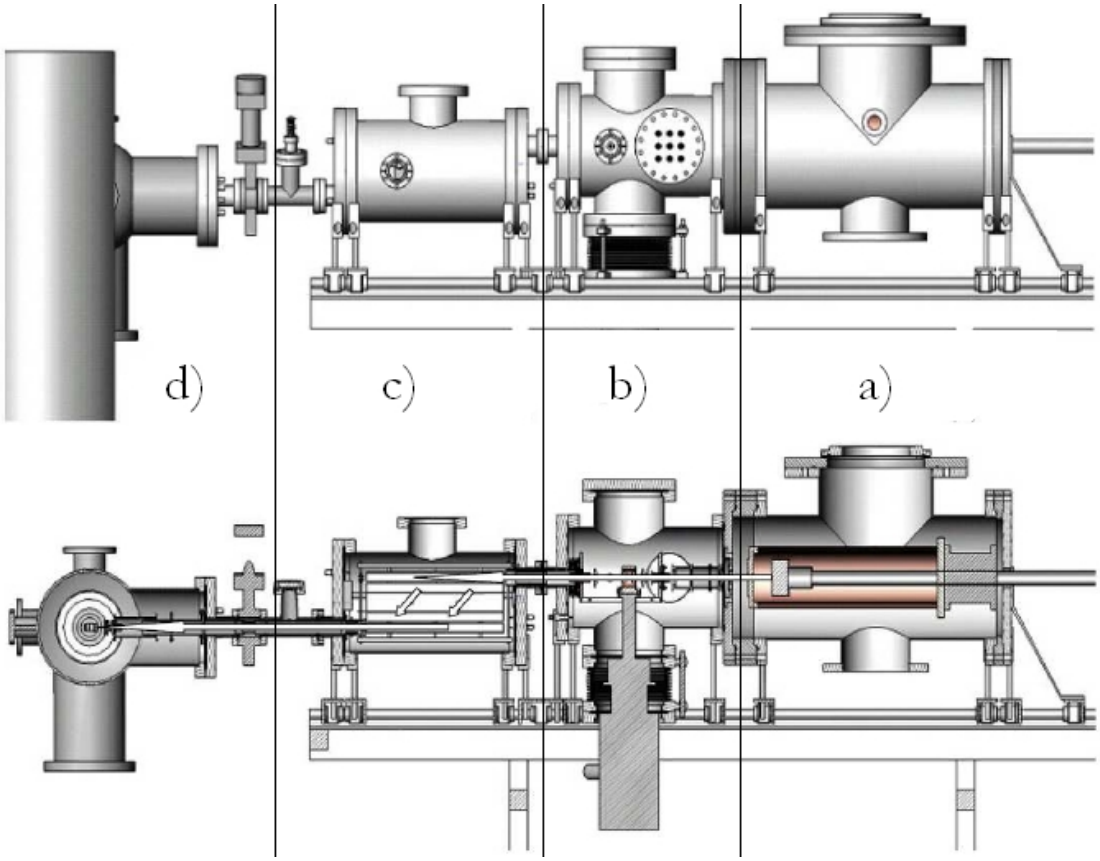

Figure 1.21: Cluster machine as seen from outside (top) and schematic depiction of the interior (bottom). Clusters are produced in the Cluster Source (a), transpass the Cryo Chamber (b) and reach the Mass Selector (c). The connected Preparation Chamber (d) is also depicted.

1.4.2.1 Cluster Source

The first chamber contains the target, which provides the cluster material. It is placed in a special holder where it can be externally cooled and adjusted by moving the holder back and forth, a slight tilting is also possible. In addition to that there are conductions in order to externally provide gas to the target. The clusters are produced by a *Magnetron Sputter Gas Aggregation Source* [140], which essentially ionizes the target material by using argon and helium gas from the conductions. To create the necessary plasma, a high voltage of 1200 V provides an electric field. In combination with a magnetic field stemming from a permanent magnet, the electrons in the plasma are forced in cycloid tracks while the ionized gas atoms consequently sputter the target and produce the typical ring on its surface visible in figure 1.24 on page 36. Subsequent collisions with the gas atoms reduce the velocity of single target atoms sufficiently for them to coalesce as illustrated in figure 1.22.

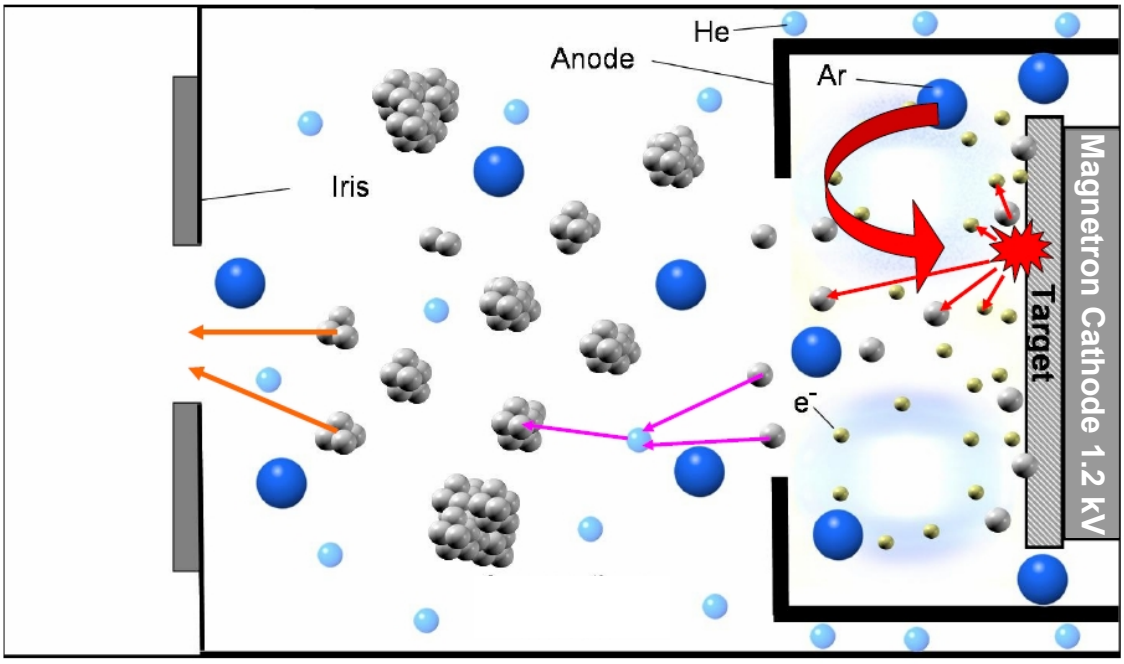

Figure 1.22: Schematic depiction of the cluster formation in the Cluster Source. Electrons near the cathode ionize argon atoms and are forced in cycloid paths. Single atoms leave the immediate proximity of the target and get into the main body of the Cluster Source. There they coalesce to clusters by interacting with helium and argon atoms (pink arrows in the center). Subsequently they leave the chamber in a multitude of sizes (orange arrows on the left).

An external cooling of the target using liquid nitrogen facilitates the cluster condensation while simultaneously improving the heat transport away from the target, which prevents it from overheating. Varying the distance of the target from the closest electrodes influences the distribution of cluster sizes. This is a commonly used method to preselect clusters. Electric fields, produced by several electrodes, accelerate and guide the charged clusters through the first chamber into the second one.

1.4.2.2 Cryo Chamber

In the second chamber, the Cryo Chamber, remaining argon gas and other unwanted atoms or molecules are removed by a Turbomolecular Pump. In addition to that argon atoms frequently have direct contact with a component of the chamber that is cooled to about 10 K using a cryo pump [141]. This causes the atoms to adsorb at the mentioned component so that they are removed from the vacuum. After the experiment, the cooling is switched off and the entire material is desorbed again.

The clusters are focused and aligned in the desired direction using multiple electrodes. Their voltages can be individually varied from 0 V to -1500 V. Clusters are then guided through the chamber into the next one.

1.4.2.3 Mass Selector

The third chamber contains a *Time of Flight Mass Selector* [142]. Here UHV conditions are present (10^{-9} *mbar*) due to a separate baking of the chamber, which normally takes place a few days before the deposition starts. The clusters are assumed to carry just one elementary charge, because no fractional cluster masses are observed at least for small clusters. By applying a short electric pulse to them, clusters of several sizes are accelerated differently due to their deviating mass-to-charge ratio. Another pulse decelerates the clusters after they moved unhindered in vacuum for a short period of time. Now all clusters are separated spatially due to their previously deviating velocities. Because the clusters retain their lateral kinetic energy during the entire process, those at the correct position or with the chosen mass, respectively, move out of the main Cluster Machine into the attached Preparation Chamber. The exact timing and pulse length determine the resulting cluster mass. Following this basic concept, voltages and pulse frequency are chosen in a way that optimizes resolution and throughput. A more detailed description of the process can be found in [123,142]. Figure 1.23 shows the interior of the Mass Selector and illustrates the basic mass selecting process.

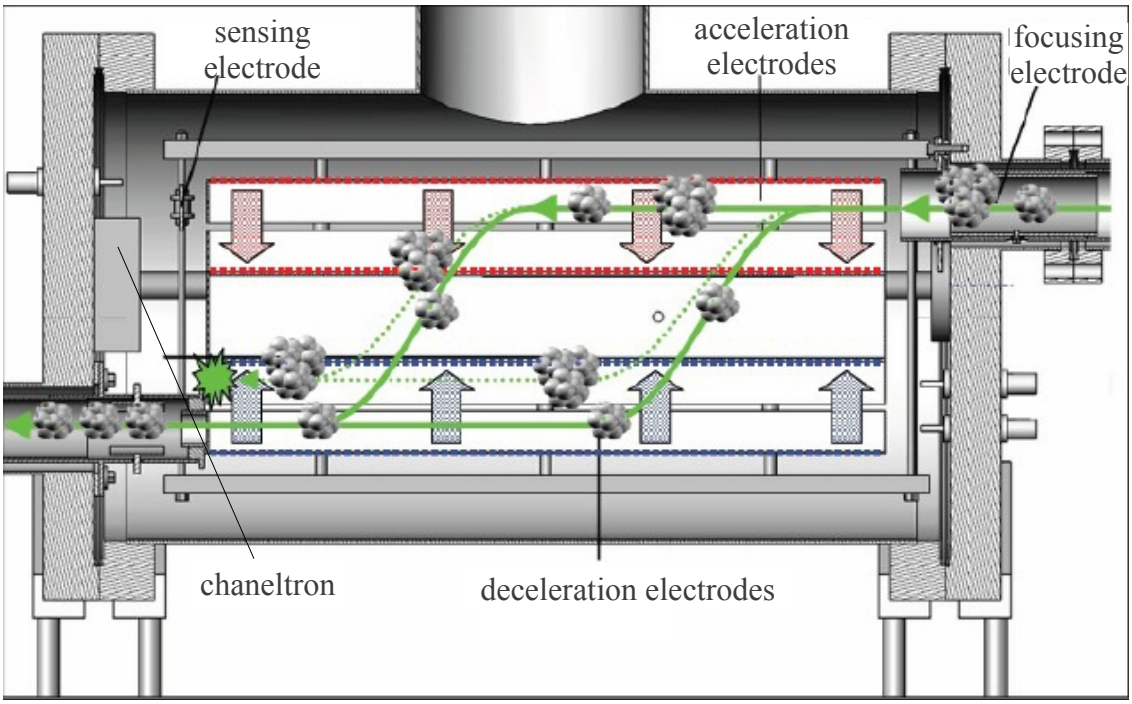

Figure 1.23: Schematic depiction of the interior of the Mass Selector. Incoming clusters (right), displaying a wide variety of sizes, are accelerated differently by an electric pulse due to their deviating mass-to-charge ratio (upper red arrow). After drifting through vacuum for a preset time, the clusters are decelerated with an opposing pulse (lower blue arrows). In a last step only clusters of a specific mass are correctly positioned to leave the chamber [143].

In this chamber is also a part called *Faraday Cup* 1 (FC1). It is temporarily used for adjusting the Cluster Machine. A second Faraday cup, called *Faraday Cup* 2 (FC2), is of much greater importance and its function will be discussed in following sections.

1.4.3 Software

The Surface Science Facility as well as the Cluster Machine come with essential programs, which are necessary to operate them. The following descriptions aim at giving an overview of features and problems that the software entails.

The STM is controlled and its data is gathered by a software called *Scala SPM SO* 2.2 provided by the *Omicron Nanotechnology GmbH*. The software runs on a specialized Unix based system. The most important features used here are an automatic approach mechanism for the STM tip, its scanning functionality and basic evaluation tools for quick analyses.

The Cluster Machine is controlled by two separate *Labview* scripts [144]. The first script initializes the pulse voltages of the mass selector as well as the waiting time interval t_w. The second one is more extensive in its ability to set necessary parameters like initial cluster mass, mass steps and final cluster mass. It is also able to set the bias of the second *Faraday Cup* (FC2, see section 1.5.1 on page 35) in order to control the amount of incoming clusters.

During the course of this thesis, several additional pieces of software have been developed in order to increase the functionality of the Surface Science Facility. This part only provides a rough overview of the software in use.

Many programs have been coded using *Perl* as a script language [145]. They focus on solving localized problems, which are either too time intensive for a manual approach or are needed for a lack of alternatives.

1. *Cluster Evaluation Software* (CES): This Perl script uses *gtk*2 [146] as a graphical user interface to visualize STM images for further evaluation. Using this software, it is possible to select a cluster by a mouse click. An automatic calculation of relative as well as absolute height, position and width of the cluster is conducted. Several other more specialized options are available. They will be mentioned in the appropriate section if necessary. The gathered information can then be exported to a text file in *ASCII* format.
2. *CSA Mass Spectrum Analyzer* (CMSA): This is a Perl script that helps to identify peaks in a mass spectrum provided by the Cluster Machine. An example of an analyzed mass spectrum can be found in figure 1.28 on page 38. The software identifies the highest peaks with the preset estimated distance (e.g. the atomic mass of Ag is 107.87 *amu*). Peak index and position are plotted and can be checked for errors (for example missing peaks). In addition to that the average peak distance together with its offset is calculated. One resulting graph is presented in figure 1.28 on page 38. A text file in *ASCII* format is created.
3. *STS Evaluation Software* (SES): This is a Perl script for processing raw data. Preparation and comparison of STS data requires several evaluation steps. The software identifies spectra of the same image that belong to each other and averages them. In addition to that similar spectra are sorted and arranged for a clear depiction. The tool works automatically but a visual inspection of the data is still necessary. An *ASCII* text file is created.

4. *UPS Evaluation Software* (UES): This Perl script is similar to the *STS Evaluation Software*. It is, however, adapted to raw UPS data, which are normalized and bundled for further evaluation. The software generates a text file in *ASCII* format, which contains all necessary information. A more advanced version has recently been coded by *D. Engemann* and is described in more detail in section 4.1.2 on page 135.
5. *Labview Script for Voltage-Current Curves*: This script is coded in *Labview* and works in combination with the Cluster Machine. It enables the user to automatically identify the respective cluster current belonging to a specific bias. The detailed use and results can be seen in chapter 1.5.3 on page 42.

There are two other Perl scripts, which are not mentioned here because they are described in detail in the respective chapters. The first one is a simulation of the limited resolution of the Cluster Machine and the respective cluster sizes. The application of this script can be found in section 2.2.3 on page 85. The other script provides an alternative evaluation method for histograms and can be found in section 2.2.2 on page 82.

1.5 Experimental Procedure

This section deals with devices used to perform the experiments. These included a wide range of machines and tools. Only the most important ones will be mentioned. Furthermore preparations that were necessary to conduct the experiments will be part of the following chapters.

Working parameters of the machines like pressures and temperatures displayed by measuring devices were cross checked or calibrated by additional experiments, which could stand on their own or were part of another setup. In addition to that newly introduced devices had to be adjusted and their working parameters identified before any experiment could take place.

1.5.1 Preparation of the Cluster Machine

It is essential that the Cluster Machine is free of evaporated and subsequently adsorbed metal from a preceding target before the device can be used again. While only little target material reaches the sample, most of it will remain inside the Cluster Source. Thus a visible metal layer is created on all parts that are close to the target or near the most intense, initial cluster beam. This can cause several negative side effects. Even a thin metal layer on isolating parts can cause short circuits. With a longer run-time of the machine, the layer thickens and thus its conductivity increases.

Additionally the target has a limited lifetime. This is due to the significant amount of material that is sputtered off as long as the machine is running. Subsequently a ring of lacking metal is present in the target as visible in figures 1.24 and 1.25. After sputtering the target for a sufficiently long time, the inner part might be carved out so that it will drop out of its holder. In this case the machine would not work any more and the chamber had to be opened. Another effect of an aging target and the subsequent contamination of the chamber is its increasing inability to produce smaller clusters in a usable manner.

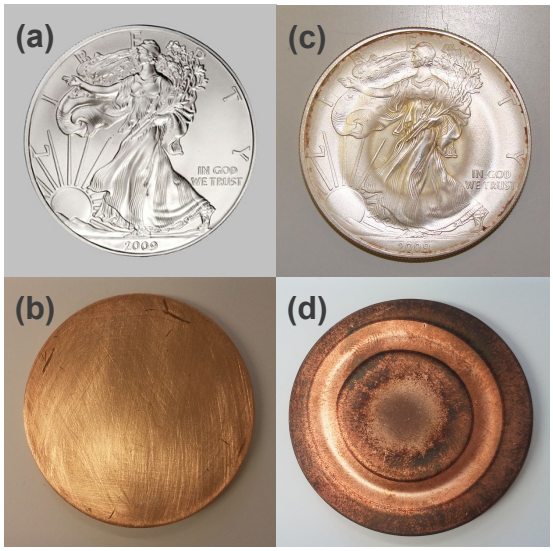

Figure 1.24: *American Eagle Dollar* used as silver target; diameter 40.7 *mm* (a) (see picture credits). Copper target with a diameter of 40.7 mm (b). The silver (c) and copper (d) targets are depicted after sputtering them for several hours.

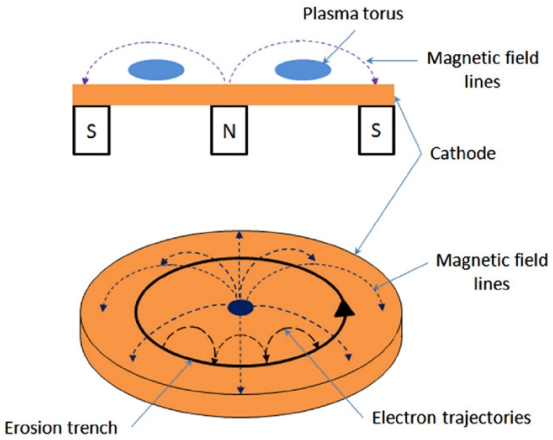

Figure 1.25: Schematic depiction of a copper target during sputtering [90]. The typical eroded trench is also visible in figure 1.24 (c,d).

Most of the parts in question are removable so that a cleaning can take place outside the chamber. With the help of fine sandpaper and similar techniques the unwanted material can be removed before putting the cleaned parts back into the chamber. Therefore a cleaning procedure is necessary as soon as the target approaches the end of its lifetime.

Before any deposition can take place, the Cluster Machine has to be adjusted. In section 1.4.2 on page 30 it is shown that the device can be regarded as an array of electrodes, which form electronic lenses. While clusters are created by the Magnetron Sputter Source, the particles have to reach the mass selector and after that the sample. Unfortunately each time the Cluster Source has been opened, new settings are necessary to guide the cluster beam successfully through the machine.

To achieve this goal an analogue picoamperemeter is used to detect currents at different electrodes as soon as the source is switched on. The adjusting normally starts at electrodes in closest proximity to the source because the current is usually most intense in this area. It is therefore possible to easily detect the charges reaching the particular electrode, which enables the experimenter to maximize the current by changing the applied voltage of all previous electrodes. This procedure can be repeated until the Mass Selector is reached. For the last section between mass selector and sample the Faraday Cup 2 (FC2) inside the Preparation Chamber is used to detect a usually minute cluster current of only a few picoampere. Unfortunately the Faraday cup has to be moved frequently during experiments in order to not collide with the manipulator. Therefore it has to be newly adjusted before each deposition is due. For that the light of an intense light source is used, which passes though a window collinear with the cluster ion beam. The resulting light spot allows the positioning of the Faraday cup.

After maximizing the cluster current by varying the voltages of the electrodes, the desired cluster sizes can be identified. A computer, which is connected to detection and controller devices, enables the manipulation and analysis of the cluster current. A more detailed description of the software can be found in section 1.4.3 on page 34. In short the computer is used to set the pulse frequency of the mass selector, which directly translates into a cluster mass as long as the atomic mass of the target material is known. Meanwhile the cluster current is detected and can be displayed as a function of the cluster mass. This leads to a graph, which shows individual cluster sizes as peaks.

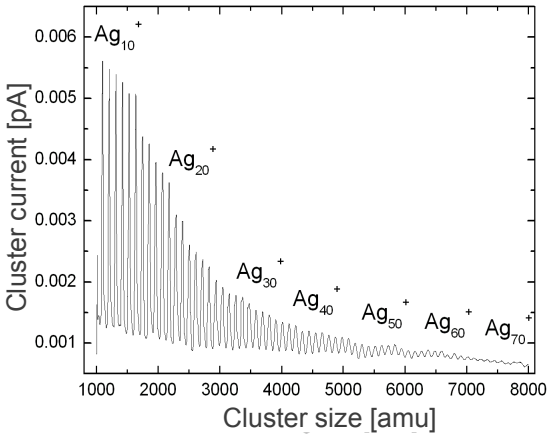

Figure 1.26: Cluster sizes as peaks in the cluster current intensity during continuously reducing the mass selector's frequency and thus increasing the selected cluster mass. The resolution of the Cluster Machine is proportional to the cluster mass so that peaks start to merge at one point and seize to be identifiable [123].

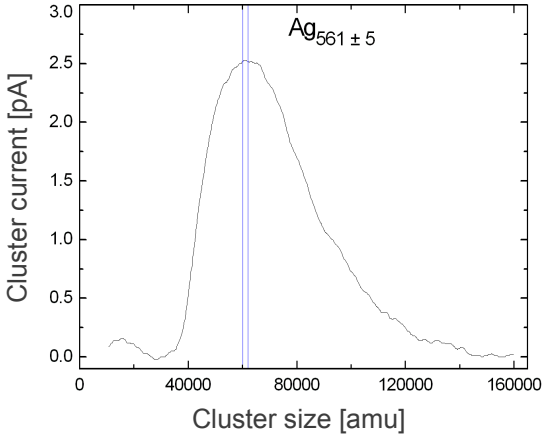

Figure 1.27: Cluster sizes measured over a wide range. Single peaks are no more visible due the given resolution. Now a calibration related intensity distribution is detectable, which overlaps with single cluster peaks. If, for example, Ag_{561} is to be measured, the peak distance is necessary to extrapolate the correct peak number [123].

The appearance of the graph can be explained by taking a quick look at the mass selector. Cluster sizes are discrete because the mass can only change in steps of atoms. Thus a properly working mass selector can separate individual sizes by choosing the correct pulse length. The limited resolution of the machine will then broaden the theoretically sharp peaks for each cluster size. A graph like the one in figure 1.26 appears as a consequence. Note that the broadening of the peaks, which is equivalent to the resolution, increases with increasing cluster size. Therefore the peaks disappear at some point and only a relatively even curve remains. This fact is reflected in figure 1.27, which shows cluster sizes over a much wider range. Single peaks are no more detectable but a variation in intensity is non the less present. The latter can be attributed to the working parameters of the cluster machine, which cause certain cluster sizes to exist in greater abundance.

The fact that at some point no more peaks are identifiable does not prevent the deposition of larger clusters. It is possible to find the cluster mass by extrapolating the peak distance of smaller clusters. With a properly adjusted Cluster Machine, the distance between peaks is identical and independent of the cluster mass. Theoretically the peak distance should be equal to one atomic mass of the target material. This may be true to a certain degree but additional

effects alter this value. Most important in this context is the change in biases of the machine after the cleaning process. It is now most likely that the cluster beam travels under a different angle though the mass selector. To address this issue, the exact position of each detectable cluster peak must be identified. The measured cluster size can then be plotted against the expected cluster size.

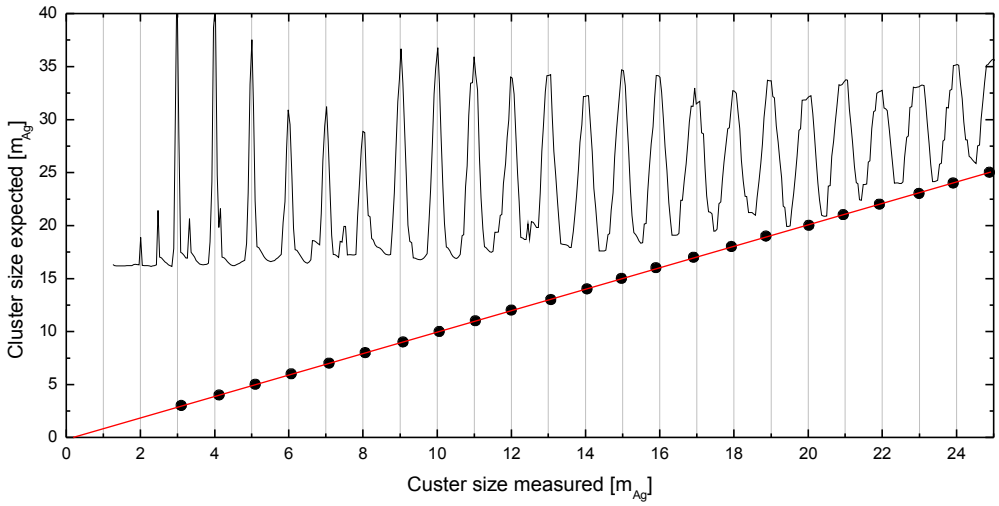

Figure 1.28: The measured cluster size plotted against the suspected cluster size (black dots) in units of silver masses (m_{Ag}=107.87 *amu*). The respective peaks are shown above for illustration with an arbitrary y-axis scale.

The resulting plot can be seen in figure 1.28. The values can be fitted by a linear function, which enables the identification of clusters sizes beyond the position where the peaks disappear.

During our experiments this procedure proved to be problematic. Normally the peaks had to be identified quasi manually using a software tool like Origin. Especially when multiple cluster sizes were deposited in a row using the new *Movable Focus Lens* (see next section), this time consuming process hindered the experiment. Therefore a Perl script has been coded that identifies the peak position automatically and provides information on the correct mass setting for the desired cluster size. Several tests proved its functionality. This and other software is described in section 1.4.3 on page 34.

1.5.2 Movable Focus Lens

To compare different experimental results, it is of great importance to keep all environmental conditions fixed, as far as that is possible. In most cases this is a futile attempt if an experiment is to be reproduced. This can only be done to a certain degree while high quality devices help to come close to said goal. Also important is a good documentation of the whole procedure in combination with multiple experimenters, who can cross check parameters. If incon-

sistencies in the data reveal themselves at a later point, this can help to sort out errors or confirm new and unusual physical effects. Another approach to keep experimental conditions fixed is to do as many experiments at once as possible. This does not only reduce the total effort that is put into an experiment but ensures also that nearly all experimental conditions are identical for each *sub experiment*. The new device, described in this section, was designed with that in mind. The following paragraphs will describe the function, working parameters and practical results of the Movable Focus Lens (MFL).

Most of the preparation steps of a certain sample take place before deposition. As mentioned in section 1.5.5.1 on page 47, many steps are necessary to get a sample, which is ready to be used as a substrate for clusters. To nullify the effect of slightly different environmental conditions as well as varying amounts of C_{60} layers, unwanted adsorbates and vibration vise behavior of the sample, it is best to use the same sample for as many experiments as possible. This has been tried before with mixed results. The size of the cluster deposition spot proved to be one obstacle in this endeavor. While the scannable area of the sample takes up 5×5 *mm*, the spot itself is around 3 *mm* in diameter. This allows only multiple deposition spots if the cluster beam aims at the rim of the sample. Theoretically it should have been possible to place up to 4 spots on a single sample. Practically this was compromised by the relatively large distance between the last electrode and the sample itself where the bias is normally applied. We estimated said distance to be a few centimeters. The successive investigation of the resulting deposition spots showed that their positions were massively altered. The reason for that is probably the geometry of the manipulator that holds the sample. When a bias is applied between the last electrode of the ion optics and the manipulator, the resulting electrical field is most likely deformed. The clusters will then follow those field lines and reach places on the sample that are not meant for them. In addition to that the deposition spots are deformed and possibly not separated from each other any more.

These obstacles have to be overcome. For that a device was built that reduces the size of the deposition spot. It also works as the final electrode by being mounted in front of the previous one and reduces thereby the distance between ion optics and sample to only a few millimeters (varying from experiment to experiment). The focus lens is made of stainless steel, which is the usual choice of construction material in a vacuum chamber. It is movable and enables therefore the positioning of the essential cup, which is mounted in front of it, to be very close to the sample despite the restrictions given by the geometrical setup inside the preparation chamber.

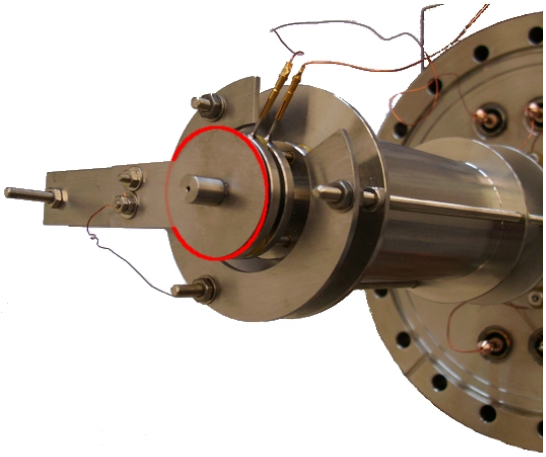

Figure 1.29: Photograph of the new Movable Focus Lens (red circle) attached to the ion optics

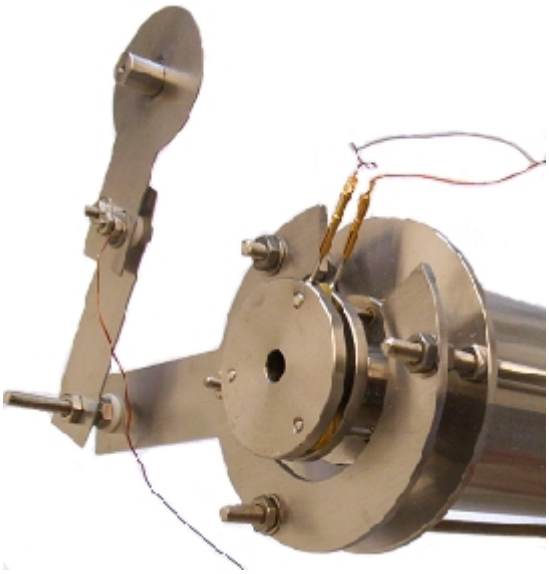

Figure 1.30: Movable Focus Lens with the cup hinged aside.

The mentioned cup is depicted in figures 1.29 and 1.30. It provides a plane surface facing the sample. This surface ensures that electrical field lines are approximately parallel between ion optics and sample. The total diameter of the cup is 5 *mm*. A borehole in the middle, which is 1 *mm* in diameter, enables the clusters to reach the sample. The typical distance to the sample surface is about 3 *mm*.

A bias can be applied to the device to enable an additional focusing of the incoming cluster beam. In order to estimate the effectiveness of the lens, the diameter of the resulting deposition spot has been computed. This was accomplished by comparing the total amount of deposited cluster material to the cluster coverage density in the deposition center. Note that this only works under the assumption that the clusters are evenly distributed in the mentioned spot. In a particular deposition of Ag_{86} clusters a coverage C of 10 *pAmin* for the entire deposition was measured. To compute the diameter d of the deposition spot, the cluster current, measured with the Faraday cup 2, is used (see section 1.5.6.1 on page 48). STM images revealed that a coverage density of D=77.1/(100×100 nm^2) ±10 % existed in the deposition center. Under the assumption that the spot has a circular shape, the following equation applies:

$$d = 2\cdot\sqrt{\frac{C}{\pi\cdot D}} \approx 2\cdot\sqrt{\frac{10\cdot 60\cdot 10^{-12}\,Asec}{\pi\cdot 1.602\cdot 10^{-19}\,Asec\cdot(77.1\pm 7.7)/(10^{-8}\,mm^2)}} \approx (0.79\pm 0.04)\,mm \tag{1.6}$$

Note that the real spot should be slightly bigger due to a reduction of intensity towards the rim. It is conceivable that the spot is identical in size to the previously mentioned bore hole. Thus a reduction of the cluster spot from 3 *mm* to 1 *mm* is most likely achieved. This is possible without any loss of intensity by carefully adjusting the applied voltage. Thus only about 1/*9th* of the previous deposition time is needed to get the same cluster coverage density.

The new deposition parameters increase the experimental options considerably. With the new Movable Focus Lens it is possible to deposit at least 9 spots on the $5 \times 5\ mm^2$ area, which is scannable by STM. Furthermore the spots can be positioned with an accuracy of about $0.1\ mm$.

Several experiments have been set up, which not only provided new data concerning cluster properties but also proved the functionality of the new device. There have been investigations with STM and UPS, which show clearly that the deposition spots are precisely positioned and well separated. In one UPS experiment in particular the d-band intensities of 8 Ag_n deposition spots on HOPG were measured (see figure 1.31). This was done by setting the energy to 4-6 *eV* below the Fermi level while simultaneously moving the manipulator and thus changing the sample position relative to the detector. This resulted in a profile of the d-band intensities alongside the z-coordinate. All three measurements at different x-positions of the manipulator are shown in figure 1.31. The peaks, associated with the respective deposition spots, can be clearly seen. Note that the given data lacks the necessary accuracy to identify exact spot positions. The width of the peaks is strongly influenced by the limited spatial resolution of the UPS experiment (see section 4.1 on page 131). However, the d-band intensities show non the less a good match with the preset positions of the deposited cluster sizes.

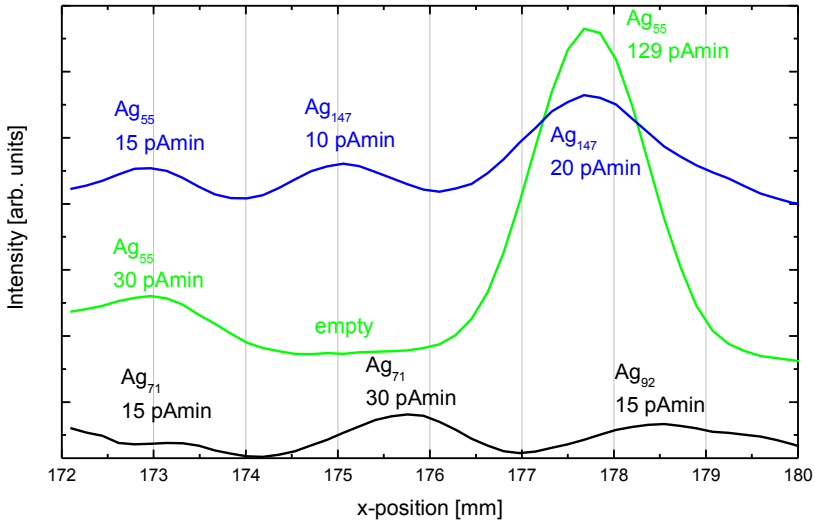

Figure 1.31: Three graphs of $Ag_n/C_{60}/Au(111)$ schematically arranged on the y-axis corresponding to the z-position on the sample; d-band intensities measured depending on the sample position. The deposition process aimed at producing 8 uniformly distributed and well separated deposition spots surrounding an empty center (similar to that of figure 4.9 on page 137).

Furthermore the deposition time in combination with the respective ion current allows the comparison of cluster coverage densities with and without the MFL. Investigations of $Ag_{55}/C_{60}/Au(111)$ deposited without MFL with 51 *pAmin* showed a coverage density of

$D = 56/(100 \times 100\ nm^2)$. Thus, using the MFL, the cluster coverage density is increased by a factor of about *7*, which is in good accordance with the observed reduction of the deposition spot diameter.

In conclusion the new Movable Focus Lens works as well as planned. The ability to position deposition spots precisely in combination with the reduced spot diameter enabled us to conduct several new types of experiments. The increased cluster coverage density and therefore reduced deposition time allowed us to deposit at least 9 spots in one experimental run on one and the same sample. These could be positioned in such a way that we were able to investigate them in STM as well as in UPS easily.

1.5.3 Deposition

To ensure that clusters stay intact after deposition, a soft landing procedure as described in section 1.2.2 on page 15 is used. The specific properties of the sample system play an essential role for the process to work. It must be able to absorb the energy of incoming clusters by elastic deformation without being deformed itself. A suitable material is therefore C_{60}. Several layers of these fullerenes are placed on top of Au(111) or HOPG. Other underlayments are also possible but were not used in the following experiments. All surface materials are described in more detail in section 1.3.2 on page 24.

Another important aspect of soft landing is the reduction of impact energy by applying an adjusted bias. This is possible because the clusters, which reach the sample, normally carry a single positive elementary charge.

When applying a bias to the manipulator, which holds the sample, not only the average speed of the clusters is changed. The bias also influences the total amount of cluster material reaching the sample. Therefore a balancing of both effects is necessary so that a soft landing is ensured without reducing the ion current too much. For that the cluster velocities have to be investigated more closely.

The velocity is observed to be distributed Gauss-like. This is not directly measurable with the detector in use (*Keithley Picoammerter*). However, the desired information can be derived from the ion current by making use of the fact that the resulting curve is equivalent to the integrated kinetic energy curve of the clusters.

Several of these voltage-current curves are depicted in figures 1.32 and 1.33. They are usually gathered for each cluster size prior to a deposition. To ensure a soft landing, the impact energy has to be as low as possible without loosing too much current. At the point, where the slope of the voltage-current curve reaches a maximum value, the derived curve (several are shown in figure 1.2) has a maximum in the Gauss distribution, which roughly corresponds to the average kinetic energy of all clusters. If the bias was set to this particular voltage, about half of the clusters would reach the sample.

Normally the voltage is further decreased by 3 *V* so that about 70 % of the clusters reach the sample. The mentioned 3 *V* translate into 3 *eV* average energy per cluster because the en-

tire Gauss distribution is shifted by that value. Strictly speaking this is not true because not all clusters arrive at the sample. However, normally it is sufficient to apply this simplification.

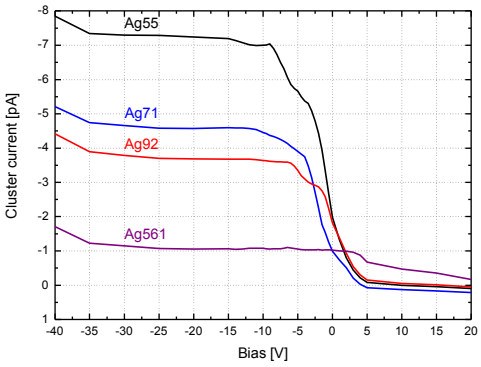

Figure 1.32: Voltage-current curves for Ag_{55} to Ag_{561} clusters providing basic information on their initial kinetic energy. Note that larger clusters are decelerated less due to their greater inertia.

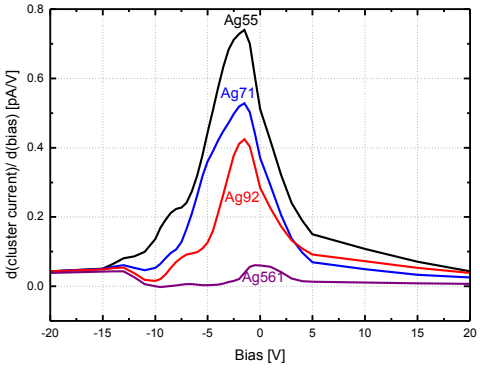

Figure 1.33: Derived voltage-current curves of figure 1.32 showing the kinetic energy distribution of incoming clusters. The curves have been smoothed in order to illustrate the similarity to Gauss distributions.

For most experiments 3 *eV* was the standard average deposition energy because it provided a low enough impact energy on the one hand and sustained a high enough cluster current on the other. However, in some cases different energies were chosen. Voltages above approximately 3 *V* simply cause a shift of the entire Gauss distribution. This is not the case if the kinetic energy is set to values below 3 *eV*. Then large parts of the Gauss curve are cut off, which means that a substantial amount of clusters does not reach the sample. This effect becomes more severe the lower the average deposition energy is. It is now possible though to determine the centroid of the new, cut-off distribution. This way the average energy of the clusters reaching the sample can be determined non the less. A more detailed analysis of this effect will follow in the appropriate experiment in chapter 3 on page 106.

1.5.4 Cooling and Annealing the Sample

Temperature as a measure of kinetic energy per atom can be used to add energy to a system in a precisely defined, however statistically distributed amount. While cooling is usually used to prevent unwanted movements and alterations of adsorbed particles on a surface, annealing enables the controlled influx of additional energy. Annealing is of great importance for all following experiments. Exposing clusters to room temperature is the easiest way to do so. The sample is simply put in a holder close to the STM apparatus for a certain amount of time. Providing temperatures deviating from that involves the use of the manipulator and its cooling as well as heating capabilities. Those will be described in the following paragraphs.

For cooling purposes two kinds of liquid gases are in use. The first and most frequently used cooling material is liquid N_2. Under atmospheric pressure N_2 keeps a temperature of 77.36 *K* [113]. For practical purposes the short term LN_2 for *Liquid* N_2 is used in experimental descriptions and sometimes in order to inform about the specific temperature at which an experiment is kept. Furthermore whenever a temperature of 77 *K* is mentioned, it is only a close estimate because the sample in questions is always in contact with other parts of the environment that often have room temperature so that heat transport can take place.

Another liquid gas used for cooling is liquid helium, for short LHe. It has an evaporation temperature of 4.22 *K* under atmospheric conditions [113]. Analogous to LN_2 a sample in contact with LHe will be kept at 4 *K* whenever the liquid gas is allowed to evaporate. However, in contrast to nitrogen, helium is a much more valuable gas. To prevent it from evaporating into the environment, the gas is reused with the help of a circulatory setup. The handling of liquid helium is further complicated by the fact that it must not come in contact with parts of the apparatus that are at room temperature before it has reached the sample. This would cause the liquid to evaporate instantly so that it cannot reach its destiny in liquid form and thus any cooling is prevented. These circumstances make it less interesting for an experimenter to use LHe in a practical sense, despite its ability to cool a sample much further down than LN_2. Thus the latter is more often used for cooling purposes in experiments if extremely low temperatures are not required. Furthermore lower temperatures have the disadvantage of causing additional adsorption of foreign material onto a sample.

Heating is done by applying an adjustable voltage to a filament in close proximity to the sample. Not only temperatures above room temperature can be precisely adjusted this way, but also those below. This is possible because cooling the sample with LHe during heating will result in an intermediate temperature. While the amount of gas cannot be controlled easily, a controller unit simultaneously measures the temperature via a diode, which enables it to adjust the heating accordingly.

1.5.4.1 Temperature Adjustment

The temperature displayed by the silicon diode, which is attached to the sample holder construction, does not measure exactly where the sample is located. Thus the real temperature of the sample is always higher than shown. However, the magnitude of this effect can be identified by observing the behavior of adsorbed gas on the sample by means of UPS.

To observe the evolution of an adsorbing Xe film using UPS, an energy range at the position of the main Xe peak at -7.04 *eV* below the Fermi level was chosen for a scan. As depicted in figure 1.34 the first monolayer of Xe produces a prominent electronic spectrum with clearly visible peaks. The surface material, in this case HOPG, lacks these peaks.

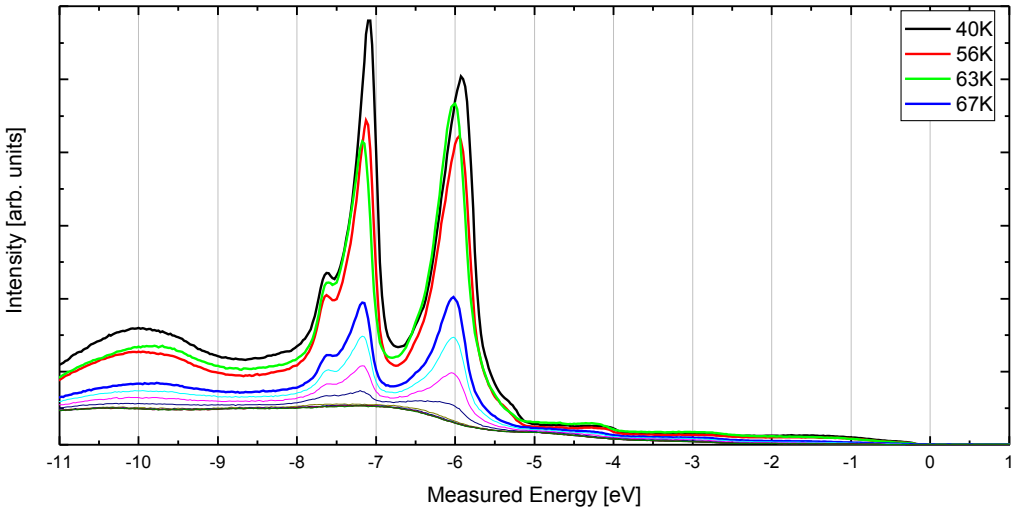

Figure 1.34: UPS spectra of desorbing Xe on HOPG. Temperatures are only given for the more prominent spectra. Energy shifts of the peaks were caused by partly defect electronics at that time.

While monitoring the sample, its temperature was reduced by 0.5 *K/min*, starting at 100 *K*. At some point a Xe film adsorbed, which was clearly visible in the measured UPS spectrum. Due to the emergence of the peak, the measured curve displayed a positive slope until it approached a constant maximum (see figure 1.35).

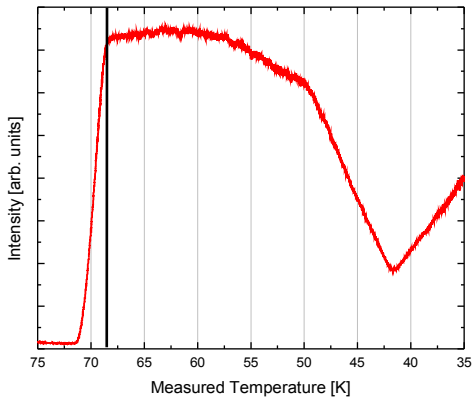

Figure 1.35: Temperature depended evolution of the main Xe peak. At 68.5 *K* the main peak disappears, which indicates the desorption of the Xe layer.

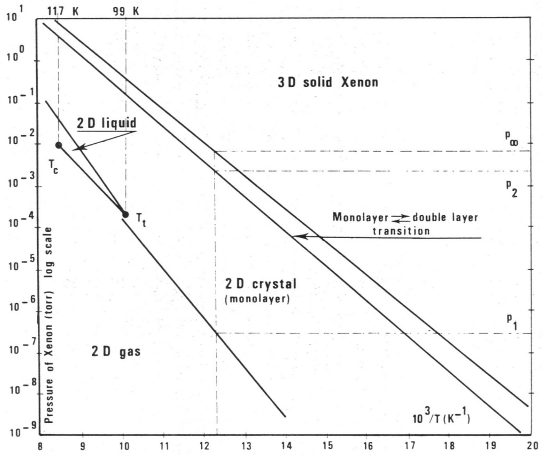

Figure 1.36: Various Xe phases adsorbed on graphite with their respective stability regions [147]. Of interest is the transition from 2D gas to 2D crystal.

The temperature was then gradually reduced from 75 *K* to 40 *K* over a course of 18 *min*. At first adsorption was observable due to the Xe gas inside the chamber starting at 68.5 *K*. At a

certain point the first monolayer was saturated which resulted in no further intensity increase in the spectrum. Finally at 50 *K* the second monolayer of Xe started to adsorb, which masked the main Xe peak of the first monolayer. Finally more prominent structures of additional Xe layers emerged for temperatures lower than about 42 *K*.

The long time intervals between temperature change ensured a sufficient equilibrium in order to keep a good correlation between measured temperature and observed desorption. In a next step the theoretical temperature for Xe evaporation had to be identified. Note that the desorption temperature of a gas heavily depends on pressure conditions [147]. With a pressure of 7.1×10^{-8} *mbar* inside the STM chamber, a temperature of 77 *K* was estimated for the sample surface using the adsorption conditions displayed in figure 1.36. This was about 8 *K* higher than measured. These results are only rough estimations that could not be validated otherwise. They show, however, that the sample temperature is displayed lower than measured. For the evaluation of most experiments, this deviation is of little importance. However, in some cases it is necessary to take this effect into account in a detailed analysis.

1.5.5 Sample Preparation

In our experiments quite different sample systems have been used. Not all will be described in detail at this point because most are specially designed for a certain kind of experiment. Thus a more detailed description will follow in the respective experimental chapters. At this point a more general description, which encompasses all used sample systems, will be given.

The preparation of an experiment normally starts with choosing a sample plate, which is roughly rectangular in shape with a size of 18×15 mm^2 and a thickness of 1 mm^2. It has an eyelet on one side to grab it with a wobble stick inside a vacuum chamber.

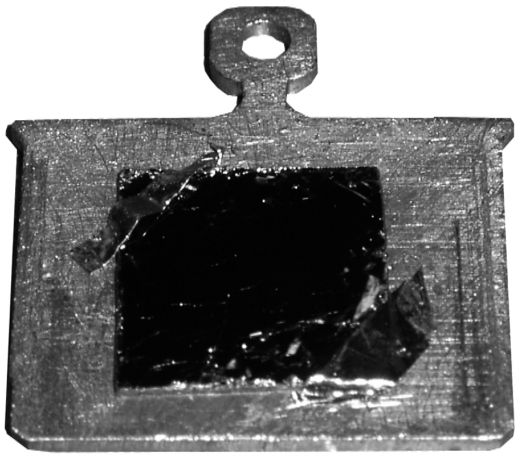

Figure 1.37: Photograph of a typical HOPG sample.

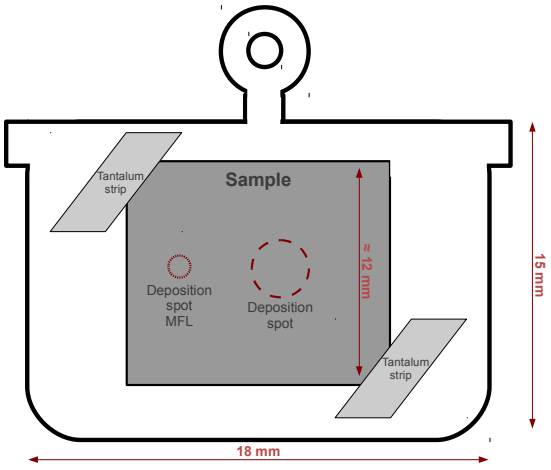

Figure 1.38: Schematic depiction of a sample. As examples both deposition spot sizes with and without *Movable Focus Lens* (MFL) are shown.

The preferred material for the sample plate is molybdenum because it has a low tendency to emit foreign material into the vacuum chamber even if it is heated to high temperatures.

The sample itself, in our case usually HOPG or Au(111), is put onto the plate and hold in place by small stripes of tantalum, which are electro welded to the plate. At this point it is important to make sure that a good contact between sample and plate is guaranteed. If this is not the case, an STM measurement could be compromised due to a lack of electrical conductivity. In addition to that vibrations might occur because part of the sample may resonate in an unwanted frequency. Furthermore a good thermal contact is necessary for all experiments that require low temperatures so that an effective cooling can take place. During each preparation step outside the vacuum chamber, a contamination of the whole sample system has to be avoided. This means that rubber gloves must be worn and tools as well as the workspace have to be cleaned with isopropyl alcohol or acetone. It is crucial to avoid any damage to the surface of a sample because even small scratches may hinder a proper investigation of that region when sensitive measurements are conducted.

After the sample is transferred into the preparation chamber of the Surface Science Facility, all samples have to be heated to at least $100°C$ in order to remove adsorbed water from their surfaces.

1.5.5.1 Au(111) and HOGP Sample Preparation

As mentioned in section 1.3.2.1 on page 24, gold as a surface material has many advantages like inertness and ductility. Due to its favorable crystalline structure it is used in many experiments conducted by us. In many cases it is functionalized with C_{60} in order to create a buffer layer on top of it.

To create an Au(111) surface, gold has to be evaporated on a fitting underlayment. This is done for two reasons. First, gold will automatically form the desired (111) crystalline structure as soon as it covers the surface. Second, very thin layers can be created this way, which uses up less material, while simultaneously providing a large uniform surface area. As an underlayment mica is used. It is a non-conducting, transparent mineral with some flexibility. Au(111)/mica normally comes in foils of $50 \times 100\ mm^2$. These have to be treated with care because touching or exposing them to dust could cause damage to the sensitive surface. To create a sample, a piece of roughly $10 \times 10\ nm^2$ is cut out of the foil and electro welded on the molybdenum sample holder.

Finally the sample is transferred into the preparation chamber (see section 1.4.1 on page 28) and heated to about $250°C$-$350°C$ in order to remove water and unwanted foreign material. After that the sample is sputtered with Ar ions in order to remove the top layers. This ensures that even unwanted adsorbates, which do not disappear during heating, are removed. To recover the surface from damages due to sputtering, it is heated to about 250-300$°C$. Further steps like the evaporation of C_{60} or other materials are now possible.

HOPG (see section 1.3.2.2 on page 25) comes in tiny blocks with a few centimeters in width. In our case bigger quadratic plates with a diameter of up to $12 \times 12\ mm^2$ and a thickness of $1\ mm$ have been used. For the last step of surface preparation a stripe of strong adhesive tape is used to remove the top most layers of the HOPG plate. This procedure has to be repeated until a clean and smooth surface is created. After that the plate is mounted onto a sample holder. The whole sample is then transferred into the STM chamber where it is heated to

about 600℃ for 1 *h*. This removes water and adsorbates from the surface. After that the sample is ready for deposition.

1.5.5.2 Evaporating C60

To enable soft landing and in order to reduce the interaction between cluster and underlying surface, C_{60} fullerenes (see section 1.3.2.3 on page 26) have been used in many occasions as a buffer material. They are evaporated inside the Preparation Chamber (see section 1.4.1 on page 28) from a small crucible. By heating the crucible electrically different temperatures can be archived and controlled by a *Type K Thermocouple*. The evaporation rate is controlled by keeping the thermovoltage constant at 17.15 *mV* (420°*C*). When the desired temperature is reached, a shutter is opened, which releases the C_{60} fullerenes into the preparation chamber so that they can land on a previously positioned sample.

The number of monolayers is set by varying the amount of evaporated C_{60}. This is done by choosing a specific duration, which has been identified in previous experiments. If only one monolayer C_{60} should cover the surface, the sample can be heated to about 250°*C* for 30 *min* after the shutter has been closed. This process causes the C_{60} fullerenes to form a uniform monolayer. However, multiple monolayers cannot be evaporated at once if a multitude of separated and clearly identifiable islands shall be created. During the heating the fullerenes would simply move to the rim areas or form very large coherent layers, which are difficult to identify. Instead additional layers are evaporated onto an existing, already heated and thus uniform C_{60} surface. Then a subsequent heating is unnecessary because the fullerenes of the second and additional monolayers form small, uniform islands on their own.

1.5.6 Experimental Data Collection

In this chapter a quick overview of the data gathering procedures is given in order to clarify the context in which the respective conclusions are drawn. Many practical steps that will be mentioned in the following sections are part of an often repeated routine. While the precise steps are too numerous to be presented in detail, key issues will be explained.

1.5.6.1 Computing Cluster Current

The second *Faraday Cup* (*FC*2) is used to measure a current stemming from clusters produced by the cluster machine. To get a grasp of the total amount of cluster that can be associated with this current, a few assumptions have to be made. First, the clusters are thought to carry a single elementary charge. Thus it can be assumed that the measured current *I* allows a direct computation of the amount of charges in a time interval by the relation

$$I = \frac{N \cdot e}{t} \quad \Rightarrow \quad N = \frac{I \cdot t}{e} \tag{1.7}$$

with *e* being the elementary charge [61] and *t* the time in seconds. The value *N* coincides with the amount of clusters due to their single elementary charge.

In consequence the cluster current is always measured over a certain time period and the amount is given by the product of those two values in units of *pAmin*. As shown in equation 1.7, the total amount of clusters can be computed easily with this.

1.5.6.2 STM

The STM measurement conducted in the context of this work used an *Omicron LT STM* apparatus [137]. In this particular setup, the scannable size of the sample is restricted to $5 \times 5\ mm^2$ around the center of the sample plate. The tip is approached towards the sample surface with piezo electric elements while optically controlling the distance. Even surfaces show a reflection of the tip and allow a visual inspection of the actual gap. For the remaining distance (in the order of several micrometers) a feedback loop is used to approach the tip until the systems detects a tunneling current.

STM data comes in the form of images that can be adjusted in terms of size and resolution. In addition to that a forward and a backward direction are scanned alternately. Normally the images have a size of 100 nm^2 to 200 nm^2. The speed at which a scan can be conducted heavily depends on the tip's stability and sample quality. Under unfortunate conditions a typical measurement can take up to 1 *h* but in most cases half the time is achievable. Because of a frequent and often sudden deterioration in the quality of the scan, the process has to be monitored constantly. If a change in tip state takes place that affects the scan negatively, most of the tunneling parameters have to be readjusted until the problem is solved.

The raw data can either be evaluated by a program called WsXM [148], which encompasses several functions to study the morphology of the STM image, or a self developed program called CES (see chapter 1.4.3 on page 34) can be used, which is able to count clusters as well as cavities and compute their heights (depth) and several other properties. Both pieces of software are used on a regular basis.

After scanning, the images are transferred to a desktop PC. Raw images often show a significant slope in one direction, which is due to a tilting of the scanned region or entire sample relative to the tip. To correct this, WsXM is used to flatten the image either automatically or by selecting several areas that serve as reference zones. After that the images are usually converted to a format readable by the self developed program CES. The clusters are then identified, their properties computed and an ASCII file, that entails all necessary information, is created.

With the help of the program Origin, a list of cluster properties is extracted and can be evaluated by different means. For the most part histograms are created from individual cluster heights. Their enveloping curves resemble Gauss curves whose maximum can be interpreted as being the average cluster height while the broadening arises from deviations and errors of the measurement process. Other functions are used less often and will only be mentioned in the appropriate context.

In many of the following experimental chapters STM images are presented. Their color coding can be understood in the following way: Each pixel can be attributed to a certain measured height. The pixel that corresponds to the maximum height in the scanned area is de-

picted in white. The pixel that can be associated with the minimum height is depicted in black. Every height between those two extremes has a color that transitions from black over red to white. The exact nuances depend on how close the height of the pixel is to the absolute height maximum or minimum. Because there are several ways to distribute the colors, it is not possible to assign them to any particular height. This can only be done by analyzing the corresponding data, the images themselves can solely be used for a qualitative evaluation (see figure 1.39). STM images can also be displayed by deriving each line so that a pseudo 3D representation emerges.

In some cases profiles of clusters and surfaces are presented. These are achieved by facilitating a function of WsXM that allows drawing a line across an STM image. Along that path the profile is created, which is automatically scaled to range from the minimum to the maximum value of the selected data set (see figure 1.40).

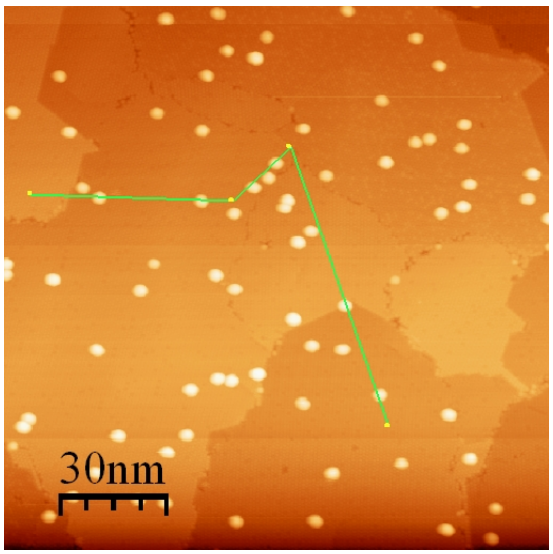

Figure 1.39: Typical STM image with profile path marked green (taken from deposition d263/ Ag_{80})

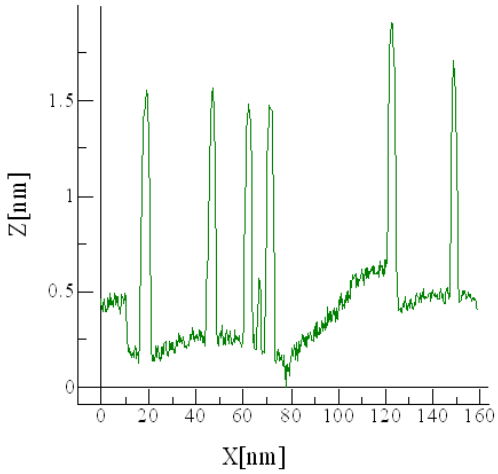

Figure 1.40: Profile of the entire marked path in figure 1.39.

Normally the STM has to be calibrated to work properly at a given temperature. Therefore STM calibration files exist for room temperature, 77 *K* (liquid N_2 temperature) and 5 *K* (liquid He temperature). These files correctly describe the heights of e.g. atomic steps and other structures at low scan speeds. However, detailed analysis of C_{60} layers on HOPG revealed that this calibration had to be altered in the case of nm-sized structures scanned at 77 K and with typical speed used for cluster images [123]. Clusters on the surface are in consequence imaged 11% larger than they actually are. So all height values have to be multiplied by a factor of 0.89 in order to correct them. Usually this is done automatically by the CES software when the cluster height is identified. Images can be corrected using a script that essentially does the same thing, though for each pixel. Note that heights can also be shifted slightly due to a different electronic behavior of surface and cluster. This and the validity of the previously mentioned factor have been confirmed experimentally as shown in figure 3.27 on page 124.

1.5.6.3 STS

Data collected by STS must be evaluated with the difficulties in measurement in mind. Ideally an STS spectrum of a cluster would encompass detailed information on the cluster's electronic properties but deficiencies of the method complicate matters. This section gives an overview of all necessary measurement as well as evaluation steps.

The whole process starts with an STM image, which is small enough in size to encompasses a maximum of three clusters. The clusters are scanned with a significantly reduced speed. When the scan reaches the assumed center of a cluster, the STS mode of the STM device is chosen to take several spectra of the cluster as well as spectra of the substrate as a reference. It is noteworthy that some clusters are collected or destroyed by the tip during this process. Thus it is mandatory to stop the scan when the tip has on the one hand transpassed the cluster's center but has on the other hand not reached its exteriors. In this state the STS spectra should be gathered. This way a possible alteration of the cluster's integrity can be monitored. Note that low temperatures, normally around 5 *K* (liquid helium), must be used in order to prevent thermal drift effects. The latter, if too prominent, can compromise the entire measurement by altering the position of the tip in an unknown fashion.

All of the about 100 substrate spectra, which have been measured in a row, have to be averaged. This is, however, often complicated by faulty spectra, which have been compromised by random currents probably caused by changes in the relative position between tip and sample due to vibrations. These have to be sorted out while the remaining spectra deliver a good estimate for the material's electronic structure. Finally each cluster can be associated with three types of spectra:

1. Substrate spectra gathered before the cluster is reached.
2. Cluster spectra that entail the desired information.
3. Further substrate spectra gathered after the cluster has been scanned.

At this point a smoothing of the gathered curves is mandatory in order to recognize their evolution. Note that in reality not only the electronic structure of cluster or substrate is investigated but also the one of the tip itself. So every change in tip state threatens to compromise the measurement. To get information on the severity of this effect, both substrate reference spectra can be used to identify differences. If they show profound changes, the tip state has obviously been altered during the process. Only clusters that were subject to the same tip state can be compared directly. Normally only very few, not more than 4, clusters experience the same tunneling conditions. Furthermore not all of these sets contain useful information. In many cases a severe tip influence can deteriorate the quality of the respective spectrum. A cluster that is contaminated by foreign material can also deliver problematic data. Finally a great hindrance lies in the fact that the tip has to be positioned over the very center of the cluster. This is hardly controllable, despite having tremendous effects on the resulting spectrum.

1.5.6.4 UPS

To evaluate UPS spectra, the information gathered by the experimental setup (see section 1.1.2 on page 9) is first transferred from the UPS computer to a desktop PC. The information of each spectrum is saved into a single ASCII file. The first row contains information on the energy, while the according electron count can be found in the second. The program UES is used to normalize and bundle the data.

For normalization a value must be manually chosen that determines the energy at which all spectra should display the same electron count. The new electron count is unimportant for any further analysis so that arbitrary but identical values suffice. In a last step all spectra, until now in multiple files, are bundled in a single ASCII file. Normalization and bundling is done by the software UES. With the help of the program Origin, the ASCII file can be read and its content can be displayed.

Clusters on HOPG demand a special evaluation method that has a great impact on the preceding design of the experimental setup. Note that electrons, which are emitted from a large area of the sample, reach the detector all at once so that the spectra of clusters and the underlying surface are overlapping and are thus indistinguishable. But if the surface is measured independently from the clusters, i.e. before deposition, the respective spectrum can be subtracted. This way the sole sum of all cluster spectra remains, at least theoretically. This is of course only possible if the interaction between clusters and surface is weak so that they can be regarded as being independent from each other. Consequently, when using this evaluation method, only sample systems with weak cluster-surface interaction were investigated in the respective experiments. Additionally the fraction of the substrate covered by clusters has to be very small, which is mostly the case if coalescence is avoided.

2 Experimental Results for Moderate Cluster-Surface Interaction

The experiments, which are presented in this chapter, deal with clusters on surfaces in multiple configurations. The previously described methods and laboratory tools were used to fashion several types of samples and bring them in contact with mass selected clusters from the cluster machine. The experiments are ordered by the theoretically predicted interactions the clusters would encounter after depositing them onto a surface. Thus the three main topics are **moderate**, **strong** and **weak** cluster-surface interaction. While this distinction is in itself not precise due to the wide variety of sample systems, it enables a rough classification of the phenomena observed.

As mentioned in section 1.2 on page 11, the cluster-surface interaction is mainly governed by potentials that must be overcome by cluster atoms in order to decay or rearrange. This can be understood as a competition of binding energy within the cluster and binding energy between cluster and surface. The former must be surpassed for the latter to be released. If this results in a net surplus of energy, the cluster can change its shape and organize in a more energetically favorable arrangement. Note that cluster-surface interaction also encompasses diffusion barriers for clusters on the surface. This effect is somewhat independent of binding energies and is caused by the lateral electronic or geometric properties of the sample. A low diffusion barrier allows the cluster to be moved easily alongside the surface while a large barrier keeps it in place.

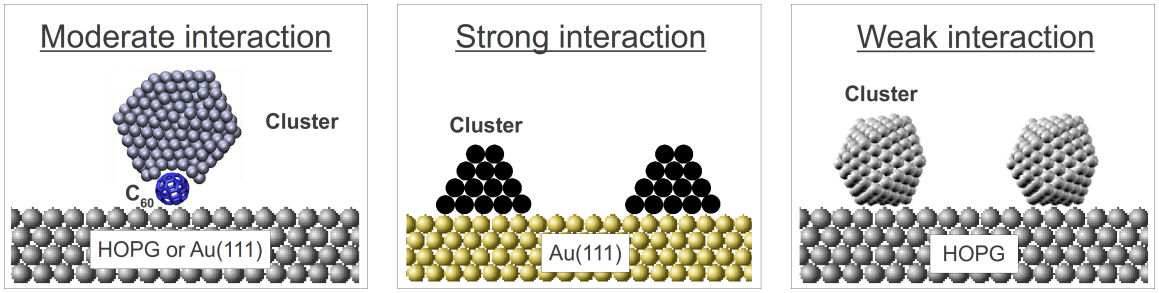

Figure 2.1: Schematic depiction of moderate, weak and strong cluster-surface interaction. In the case of moderate interaction the cluster is possibly deformed but overall intact (cluster shape calculated by *M. Moseler*). When a strong interaction is present, the cluster is destroyed and an island forms. In the case of a weak interaction the cluster is at most slightly deformed but beyond that unchanged. In the images atoms are not true to scale.

In the following chapters most experiments fall in the category of **moderate** cluster-surface interaction. Because it allows an overview of many relevant effects, moderate interaction will be presented before the other experimental results. On the one hand a moderate interaction encompasses configurations that do not cause the cluster to change its shape dramatically and thus keep the initial atomic arrangement for the most part. Thus only a low binding energy is present. This distinguishes the moderate from the strong cluster-surface interaction. On the other hand this interaction is strong enough in terms of diffusion to keep the cluster motionless at temperatures lower than about 77 *K* and enables the experimenter to image the

surface with STM, which distinguishes it from a weak interaction. In the following experiments a moderate interaction is accomplished by a metallic surface like Au(111) functionalized with a buffer layer of C_{60}. Note that the weak interaction between a cluster and C_{60} is significantly increased by the presence of an Au(111) underlayment. The energy barrier for a rearrangement of the cluster lies between 1 *eV* and 2.4 *eV* for 1 ML and 2 ML/C_{60}/Au(111), respectively [149]. With additional layers of C_{60} the barrier is increased and the cluster-surface interaction thus reduced. In addition to that C_{60} delivers a comparably large diffusion barrier due to the uneven surface of a C_{60} layer.

As mentioned before, **strong** cluster-surface interaction is put into effect if the cluster changes its shape or decays for temperatures around 77 *K*. Experimentally a strong interaction is accomplished by depositing silver clusters directly onto Au(111). The system can be easily investigated using STM. The energy barrier for a rearrangement of the cluster is smaller than 0.4 *eV* (computed by *T. Järvi*). The exact value can be much lower depending on the criteria for cluster alteration. Diffusion barriers are difficult to quantify. However, they can be very low. *P. Blandin* and *C. Massobrio* calculated an energy lower than 0.1 *eV* for the diffusion barrier of Ag on Pt(111) using molecular dynamic simulations [150].

Finally **weak** cluster-surface interaction takes place if the cluster is neither reshaped nor firmly fixated on the surface. The energy barrier for a rearrangement of a cluster is for the most part independent of the surface, which causes it to behave similarly to a free particle. Experimentally a weak interaction is accomplished by using HOPG as an underlayment. In our case UPS was used for investigation. Note that the exact value of the binding energy between cluster and HOPG surface strongly depends on the material and size of the cluster. However, it can be estimated to vary between 0.25-0.8 *eV* [151–153] for the configurations of the following experiments. A low diffusion barrier is also present for metal atoms [153].

The strength of cluster-surface interaction normally coincides with a specific surface material and method of measurement. There are, however, further possibilities of bringing the experiments in a certain order. For example the observed phenomena, like formation of islands or coalescence, would be suitable criteria. In order to account for this fact, the final chapter of this work will deal with a discussion of all observed phenomena.

2.1 Ag_{55}-Ag_{138} on 1 and 2 ML C_{60}/Au(111)

Several experiments have been conducted to investigate the overall behavior of Ag clusters on a C_{60}/Au(111) surface. This sample system is described in more detail in section 1.5.5.1 on page 47. Note that the amount of adsorbed C_{60} was varied for different experiments. In some cases less than 1 ML was chosen so that free areas of bare Au(111) remained. In others up to 1.5 ML C_{60} covered the surface so that additional islands of 2 ML C_{60} formed. Figures 2.2 and 2.3 show an Au(111) surface covered with varying amounts of C_{60}.

The sample's temperature was kept constant at 77 *K* in all cases during deposition as well as measurement. The process of cluster deposition is explained in section 1.5.3 on page 42.

All clusters had an average kinetic energy of 3 *eV*. Only slight variations of the mentioned procedure occurred. These were often necessary rearrangements of the experimental setup due to complications. They will only be mentioned in the appropriate place if they have been of any consequence to the final experimental results.

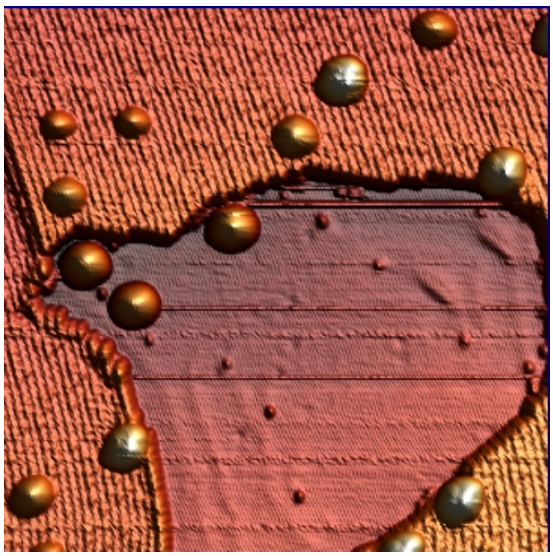

Figure 2.2: Bare Au(111) (center) surrounded by a C_{60} layer. Several clusters are also visible. Image size: 60×60 nm^2.

Figure 2.3: Islands of 2.ML C_{60} on top of C_{60}/Au(111). Image size: 292×292 nm^2.

As mentioned before, this sample system can be associated with moderate cluster-surface interaction. Although the inter-atomic bonds of the cluster dominate compared to the interaction with the surface, electronic effects can non the less be observed. Changes in the electronic structure of the target material can influence STM measurements which has been observed in several occasions with respect to other surface materials [97].

The following experiments have been done in succession to earlier studies conducted by *S. Duffe* [123]. They aimed at gaining a deeper understanding of rearrangement and decay processes. Most of the experiments described in this section can also be found in the diploma work of *N. Miroslawski* [154].

2.1.1 Ag_{55} and Ag_{95} on 1 ML C_{60}/Au(111)

This experiment served mainly three purposes. First, the heights of Ag_{55} and Ag_{95} on C_{60}/Au(111) were to be compared. Earlier experiments often lacked a sufficient comparability of the measured heights. The main reason for that was the fact that each new sample was fashioned under slightly different environmental conditions. For example the temperature or the contamination with foreign material could not thought to be identical. As a consequence it was aimed to deposit two cluster sizes onto a single sample to ensure the exact same conditions for their evolution. It was then possible to evaluate if the environmental conditions of different samples would affect the outcome in any significant way.

Second, the shape and size of the deposition spot were to be measured. This proved to be an important step to get a grasp on the alterations of the cluster beam by the electron optics. In addition to that it was necessary to identify the exact area at which the clusters landed in comparison to the coordinates of the manipulator. The relative positions of Ag_{55} and Ag_{95} were useful in order to see if there were any deviations from the expected coordinates.

Third, the experiment had to determine if and how the two emerging spots were separated and if and how they could be distinguished sufficiently to find areas, which were not compromised by the other cluster size. It was also not entirely sure if both cluster sizes would interact in any way during or directly after deposition, especially in areas with a high cluster coverage.

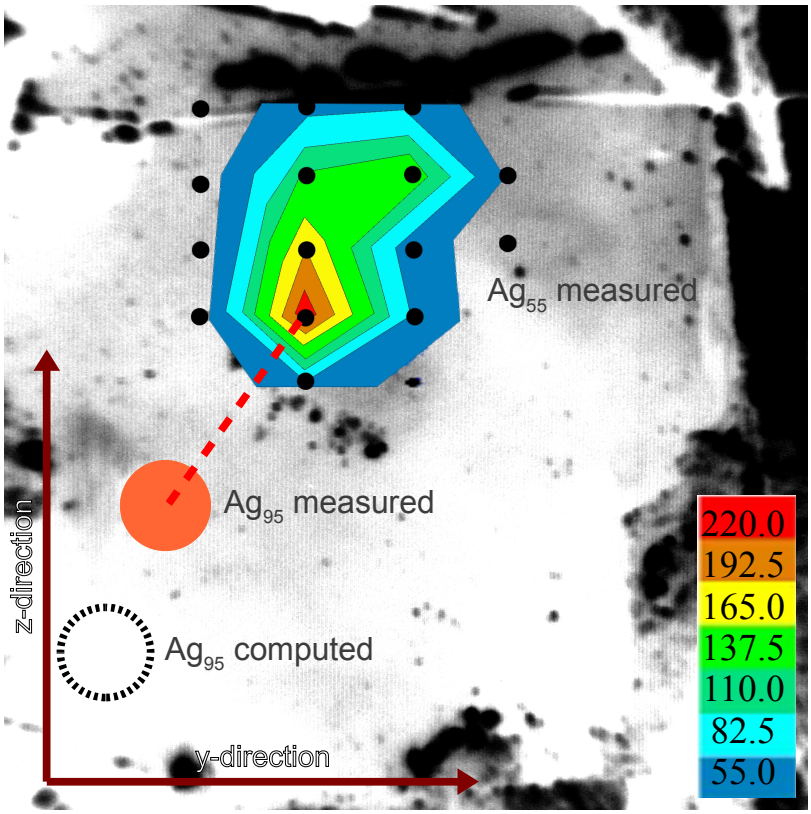

Figure 2.4: Photograph of the Au(111)/mica sample scaled and inverted together with a measured Ag_{55} deposition spot distribution (top). The numbers on the right show the amount of identified clusters in a single 200×200 nm^2 image. The suspected deposition center of Ag_{95} is depicted in the lower left together with the computed spot. Along the red dashed line several positions were scanned (see figure 2.9). Image size: 6.1×6.1 mm^2.

Preparation and deposition were done under standard conditions. Deposition started with Ag_{55}, followed by a mapping and measurement of the spot. Ag_{95} was deposited 12 *d* later. To get a sufficient separation of both spots, their positions were chosen with near maximal distance. Figure 2.4 illustrates the chosen spot positions. Note that the depicted directions resemble the coordinates of the manipulator. The Ag_{55} spot was positioned close to one rim of the sample with a large value on the z-axis. The Ag_{95} spot can be described by a smaller

z-value while simultaneously being slightly shifted back on the y-axis so that it was positioned in one corner of the sample. The manipulator coordinates revealed a theoretical relative distance of the spots of 3.5 *mm*.

First investigations of the sample showed that the Ag_{55} deposition spot was indeed at the desired position. Ag_{95}, however, deviated from that and was found to be shifted on the z-axis of the manipulator. Later experiments revealed similar alterations of the position depending on the relative coordinates. The precision of the manipulator and the correctness of the deposition parameters could also be verified by these additional experiments. A remaining and conclusive explanation for this phenomenon is the uneven geometry of the manipulator near the sample it holds. When a particular voltage is applied to the device, the electric field lines between metallic parts of the manipulator and ion optics can not thought to be straight. Thus an ion beam at the rim of the sample comes quite close to uneven electric fields which leads to a change in its path or even a warping of the emerging cluster spot.

After mapping Ag_{55}, a height of 1.24 *nm* was determined for this cluster size. This is significantly smaller than the 1.38 *nm* measured by *S. Duffe* in a preceding experiment [123]. However, the respective deposition temperature was with 165 *K* larger, which might have caused alterations of the clusters. In addition to that the cluster count was about a factor 3 smaller than in this experiment.

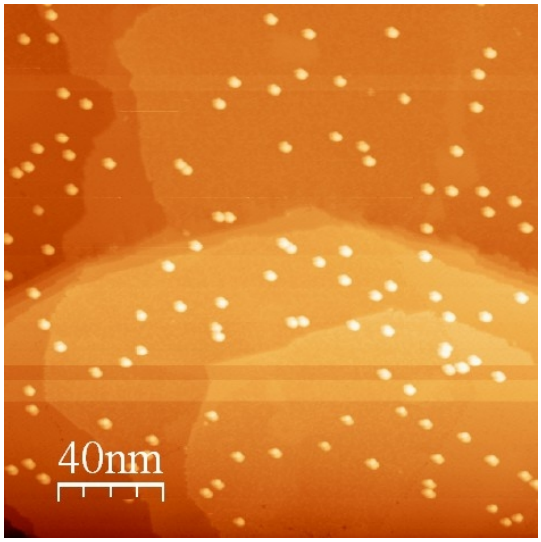

Figure 2.5: STM image of Ag_{55} clusters on 1 ML C_{60}/Au(111).

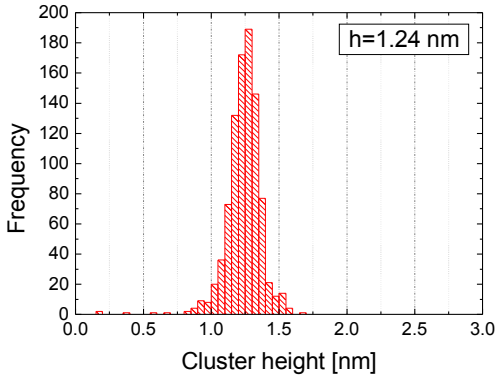

Figure 2.6: Height histogram of clusters from the Ag_{55} deposition center.

Successive measurements of the Ag_{95} center region revealed an average cluster height of 1.47 *nm*. As expected this value is larger than that for Ag_{55}, because of the greater size of Ag_{95}. The latter was, however, not mapped completely due to time constraints. At this point it was not yet clear if both cluster sizes were separated. However, the comparably low error of

both Ag_{55} and Ag_{95} in combination with very Gauss-like enveloping curves indicated that each deposition spot only consisted of one size.

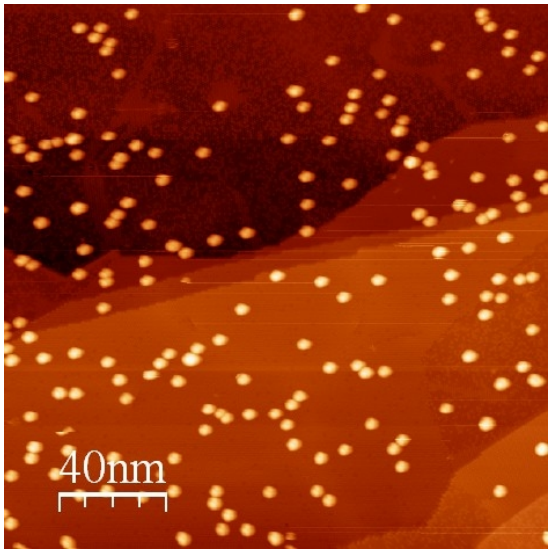

Figure 2.7: STM image of Ag_{95} clusters on 1 ML C_{60}/Au(111).

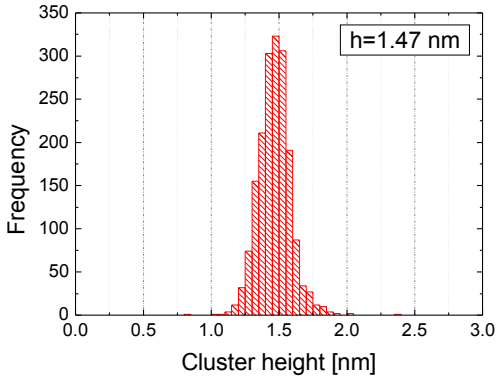

Figure 2.8: Height histogram of clusters from the Ag_{95} deposition center.

At this point the focus of the experiment shifted from measuring heights to analyzing the possible overlapping of both sizes. For that the maxima of the Ag_{55} and Ag_{95} deposition spots were used as reference points for a straight line that ran between them across the sample. Uniformly spaced positions on that line were chosen to conduct STM scans. The heights of the clusters in these regions were identified and histograms generated. As it turned out the amount of clusters never reached 0 at any point, which means that both deposition spots overlapped. Consequently the images half way the distance between both deposition centers were used for a histogram, which was expected to entail a mixture of both sizes. Because the average height of Ag_{55} and Ag_{95} deviated 0.23 *nm* from each other, which is about half the observed standard deviation of the enveloping Gauss curves, the formation of a shoulder either on the right or the left side of the distribution was expected. The latter solely depends on the ratio of both cluster sizes in the relevant images.

As the histogram of the transition region reveals (see figure 2.9), a shoulder is indeed visible. To validate the above analysis, the transition was simulated by adding up enveloping curves of Ag_{55} and Ag_{95} histograms from their respective deposition centers. Only the ratio between those two was adjusted.

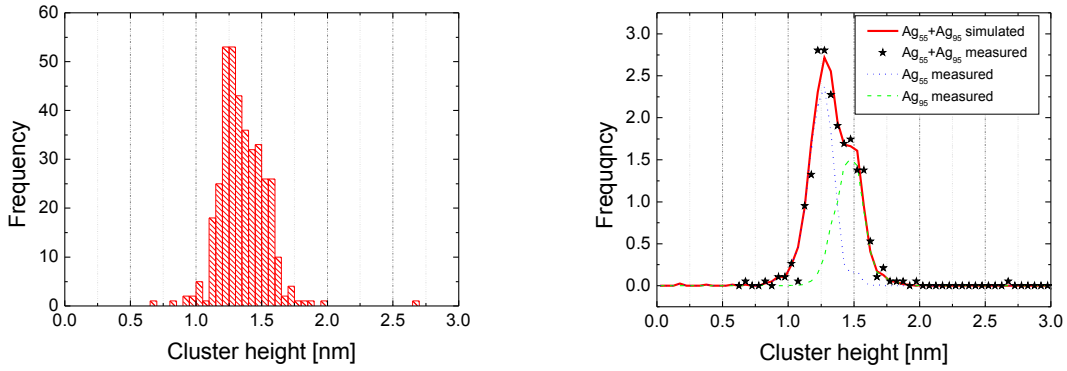

Figure 2.9: On the left is a histogram of cluster heights taken from a transitional area between the Ag_{55} and Ag_{95} deposition. On the right are measured and normalized enveloping curves of Ag_{55} (blue, dotted) and Ag_{95} (green, dashed) cluster histograms. The summed curves are depicted as a red line. Respective histogram values from clusters of the transition region are depicted as black stars.

Figure 2.9 confirms the notion that both cluster sizes could be clearly distinguished. Consequently the deposition maxima were not compromised by the other cluster size. In addition to that an interaction between Ag_{55} and Ag_{95} in the transition area can be ruled out.

2.1.2 Ag_{55}, Ag_{88} and Ag_{138} on 1 ML C_{60}/Au(111)

After depositing two separate deposition spots onto a single sample, we aimed at placing three spots on a sample. As mentioned before, inaccuracies in the positioning could not be ruled out. Consequently three cluster sizes with very different expected heights were chosen. Even with overlapping spots, mixed cluster sizes could still be distinguished due to their deviating histograms. To attain a reference to previous experiments, the first size was chosen to be Ag_{55}. Ag_{88} was chosen because it was slightly smaller in size than the electronically magic Ag_{92}. It was theorized that a sudden height change might occur when the cluster approaches a magic size. Finally the electronically magic Ag_{138} was chosen because it had not been deposited up to this point and helped in closing certain gaps in the overall measured cluster size distribution.

The positions for each deposition spot were arranged in a certain pattern comparable to that of figure 2.4 on page 56. As it turned out an exact positioning was again not possible. Especially the deposition spots near the sample's rim were as expected shifted from their desired position. As a consequence only clusters from the rim region of the Ag_{138} spot were in reach of the STM apparatus.

After identifying each deposition spot and scanning a sufficient amount of images, a direct comparison of the cluster sizes to each other and to previously measured cluster sizes was possible (see figures 2.10-2.13).

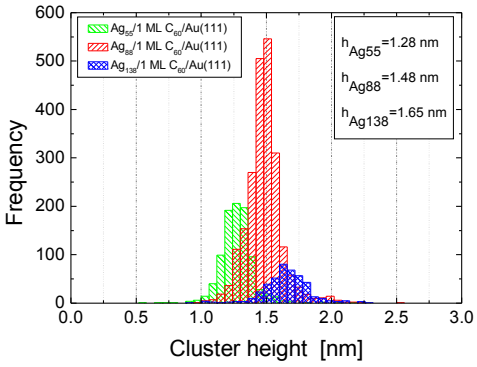

Figure 2.10: Histograms of Ag_{55}, Ag_{88} and Ag_{138} on C_{60}/Au(111) on the same sample. The deviating frequency is due to differences in scannable cluster coverage.

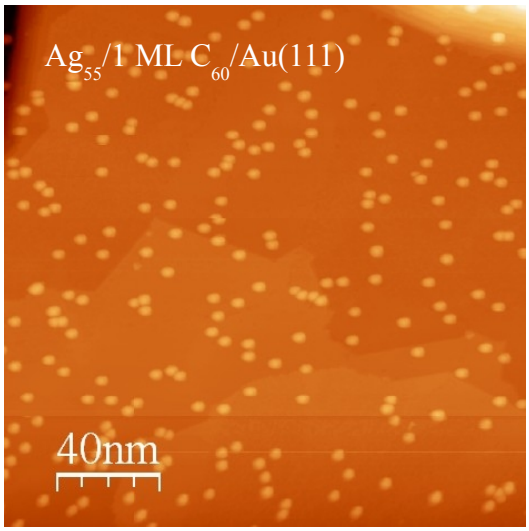

Figure 2.11: STM image of Ag_{55} on 1 ML C_{60}/Au(111).

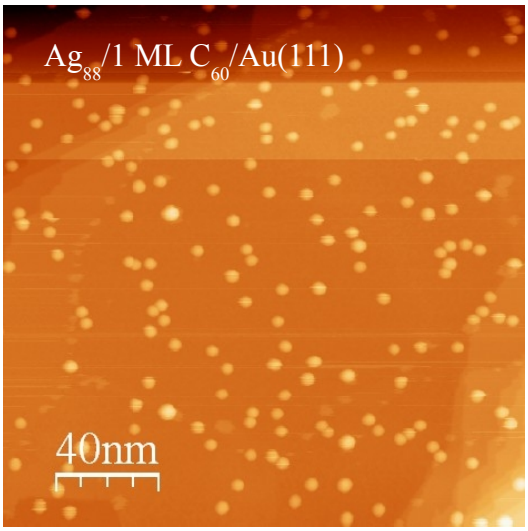

Figure 2.12: STM image of Ag_{88} on 1 ML C_{60}/Au(111).

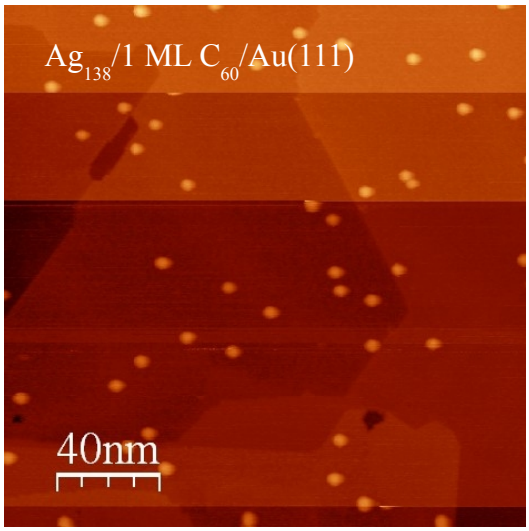

Figure 2.13: STM image of Ag_{138} on 1 ML C_{60}/Au(111). Note the low cluster coverage.

As mentioned before, the Ag_{138} spot was just barely reachable so that a lesser total amount of individual clusters was available per image. This lead to a reduced count rate. Ag_{55} shows a lesser overall count rate than Ag_{88} because it was measured before and thus a low cluster count was sufficient for a comparison to earlier results. Obviously the average height of Ag_{55} clusters comes with 1.28 *nm* quite close to previous measurements. As it turns out Ag_{88} has an average height of 1.48 *nm* and thus does not differ significantly from the height of Ag_{95}. Ag_{138} and similar cluster sizes were not measured before so that a direct comparison to other experimental results is not possible. It is, however, with an average height of *1.65 nm* similar to the computed height of $0.32 \cdot N^{1/3}$ *nm* (N being the number of atoms) of a spherical cluster.

This experiment proved again the possibility of separating several deposition spots, but this time complications were apparent. In addition to that it was proven that cluster height measurements were quite reproducible. In that context earlier measurements of Ag_{80} (deposited at 165 *K*) [123] showed with 1.31 *nm* a much lower height than Ag_{88}. Thus a comparably swift change in cluster height was conceivable between those two sizes.

2.1.3 Ag_{82}, Ag_{84} and Ag_{86} on 1.5 ML C_{60}/Au(111)

In the context of previous experiments, it was aimed to investigate the region from Ag_{82} to Ag_{88} in more detail. Therefore the intermediate cluster sizes Ag_{82}, Ag_{84} and Ag_{86} were deposited onto the same sample. The additional size Ag_{110} was accidentally deposited outside the scannable sample area and was therefore not part of the experiment. Furthermore the amount of evaporated C_{60} was increased to 1.5 ML during sample preparation in order to obtain additional 2nd monolayer islands of C_{60} on the surface.

Despite the difference in the amount of evaporated C_{60}, the preparation and deposition procedure was identical to earlier experiments. The deposition spots were again distributed evenly on the the scannable sample area. Difficulties in spot adjustment were reproduced as well so that several spots shifted. Consequently the center of the Ag_{86} spot was outside the scannable sample area which resulted in a reduced total amount of counted clusters.

Clusters were counted separately depending on the C_{60} layer they were found on. Due to the lesser relative area of 2nd monolayers C_{60}, the respective total cluster count of the 2nd ML was reduced compared to that of the first layer. The height of the clusters was found to be independent of the C_{60} monolayer.

Figures 2.14 and 2.15 show the respective STM images for both 1st and 2nd monolayer C_{60}. Figures 2.16 and 2.17 show STM image and histogram for Ag_{86} on 1 ML C_{60}. Note that the frequency for 2nd monolayer clusters was not sufficient for Ag_{86} to deliver any meaningful information. This was due to the fact that only rim areas of the deposition spot could be investigated and that C_{60} island occurred less frequent that far from the sample's center. Thus 2nd layer Ag_{86} is not displayed at this point. It is, however, conceivable that Ag_{86} would not behave differently to the other two cluster sizes.

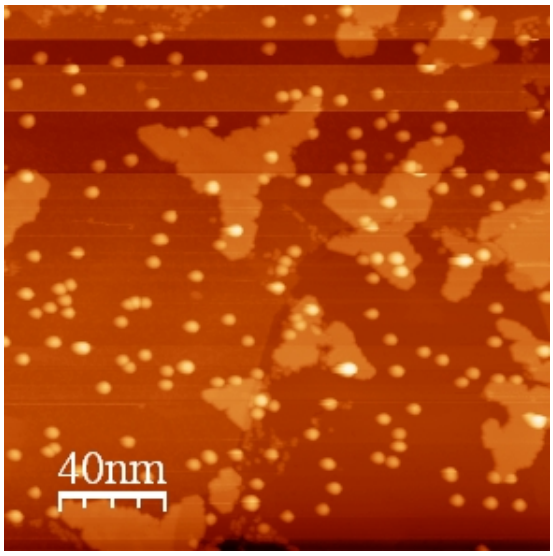

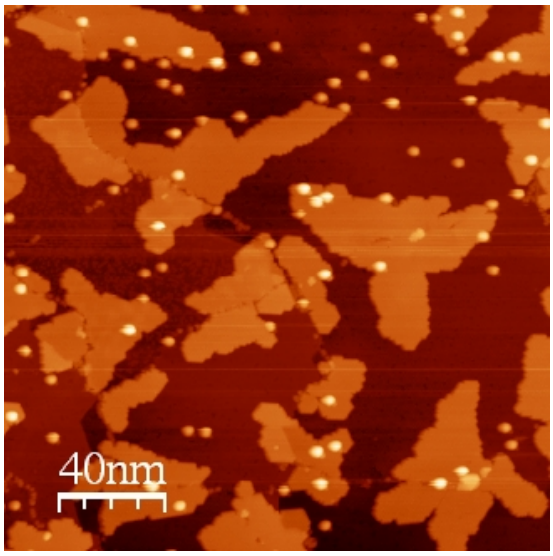

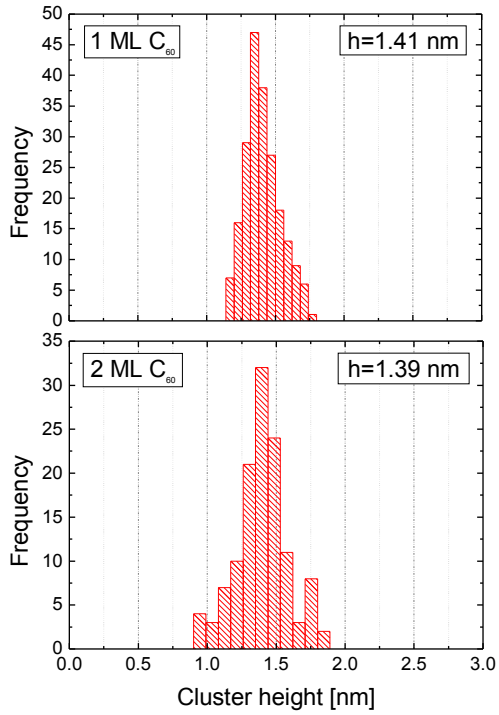

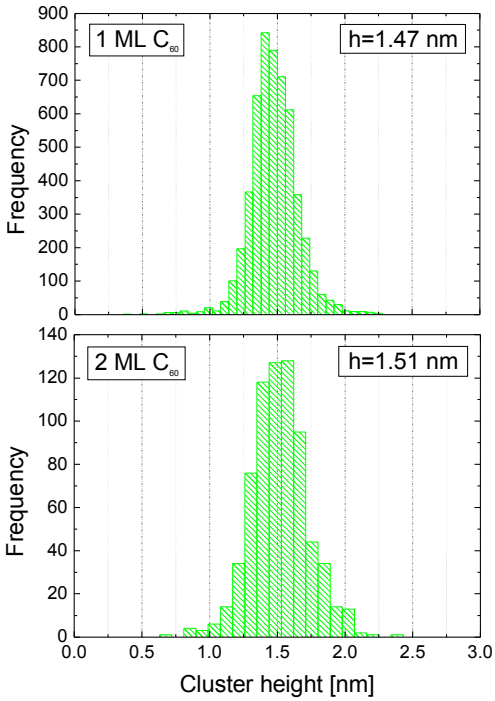

Figure 2.14: STM image and respective height histograms of Ag_{82}/1.5 ML C_{60}/Au(111). Both monolayers have been evaluated separately.

Figure 2.15: STM image and respective height histograms of Ag_{84}/1.5 ML C_{60}/Au(111). Both monolayers have been evaluated separately.

By comparing the heights of the measured cluster sizes, a quite significant shift can be observed. In this case Ag_{82} shows with 1.41 *nm* the lowest height while Ag_{84} is with 1.47 *nm* higher than all the others. Ag_{86} displays an intermediate value with 1.44 *nm*. This is unexpected because no clear increase in height is visible. On the contrary, first it rises to a maximum for Ag_{84}, just to decrease again for Ag_{86}. However, errors in measurement cannot be excluded.

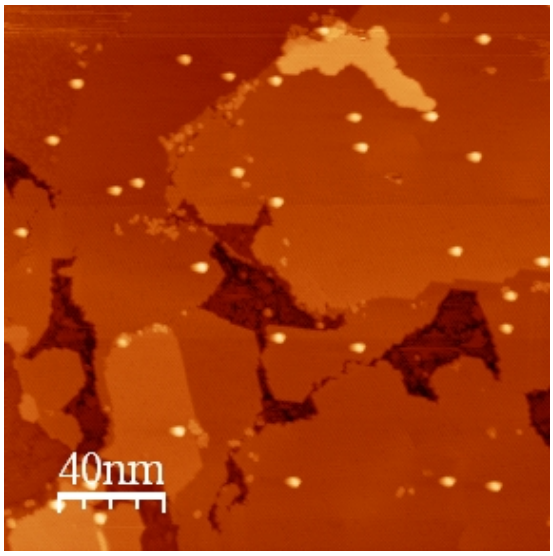

Figure 2.16: STM image of Ag_{86} clusters on 1.5 ML C_{60}/Au(111).

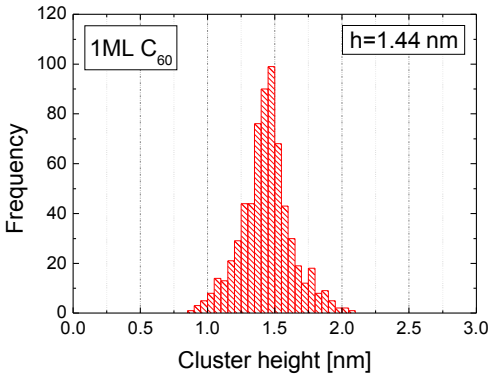

Figure 2.17: Height histogram of Ag_{86} clusters. Only the 1st ML could be evaluated.

The following two aspects have to be regarded before any further conclusions can be drawn:

1. The faulty positioning of deposition spots near to the sample's rim may have obscured the exact position of a particular spot. While not being likely, it is conceivable that the positions for Ag_{84} and Ag_{86} interchanged. With this correction in mind Ag_{84} would no longer show an intermediate increase in height.
2. The measured height is dependent on the limited resolution of the cluster machine. A mixture of the main and neighboring clusters is expected for a single deposition spot. Ag_{84}, for example, also encompasses Ag_{83} and Ag_{85}, possibly even Ag_{82} and Ag_{86}. A detailed analysis of this effect can be found in section 2.2 on page 80. If the size of Ag_{84} and Ag_{86} had been close to a height change, the mixing of several sizes with different heights could have resulted in a broadening and potential shift of one or both height distributions.

2.1.4 Stability of Ag_{55}-Ag_{138} on C_{60}/Au(111)

Ag clusters of different sizes on 1 and 2 ML C_{60} are highly stable at 77 *K*, as STM investigations showed. Even after several weeks of scanning, no change in distribution or height could be observed. While soft landing was conducted in every experiment so far, later on changes were provoked by increasing the sample's and thus cluster's temperature. This process (see section 1.5.4 on page 43) allows the clusters to gain additional energy so that they are able to rearrange the atoms, they consist of, in a way that is more energetically favorable. A successive scanning via STM after annealing reveals the height of rearranged clusters and thus enables the experimenter to deduce their altered shape.

In earlier experiments conducted by *S. Duffe* [123] a specific decay process in Ag_{309} clusters on 1 ML C_{60}/Au(111) was observed at room temperature while it did not occur on 2 ML C_{60}/Au(111) under otherwise identical conditions. Molecular dynamic simulations revealed that in the case of 1 ML C_{60} the formation of a dimer at the bottom of the silver cluster effectively reduces the energy barrier so that a transport of matter can occur. During the process one atom of the pair is close to the cluster while the other one approaches the substrate. In this configuration no atom has effectively left the cluster compound, yet a single atom is much closer to the gold surface than before. Consequently the energy barrier, which must be surpassed, is reduced to 1.05 *eV* in the case of Ag_{309}. At room temperature about 0.9 *eV* is available so that the barrier can be surpassed (see table 3.1 on page 118), and the cluster decays in time scales of hours.

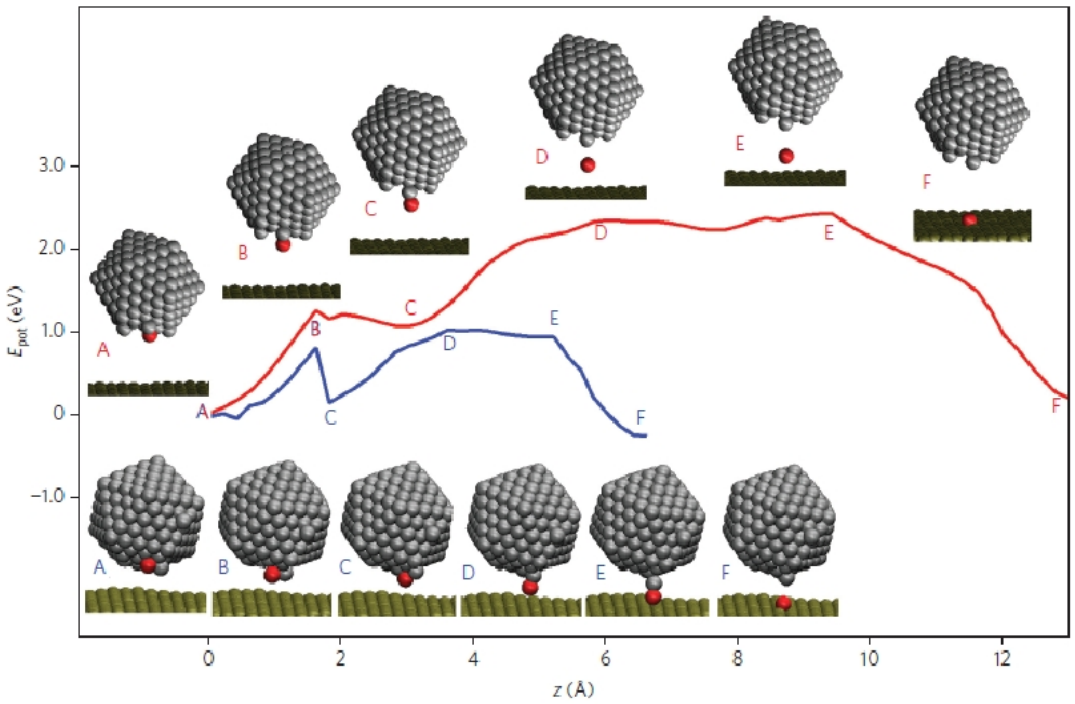

Figure 2.18: Decay of an Ag_{309} cluster on 1 ML C_{60}. The formation of a dimer and subsequent creation of a bridge between cluster and surface lowers the potential energy (blue curve; blue letters) sufficiently for a decay to take place. On two monolayers the gap is too large to overcome (red curve; red letters) [149].

On 2 ML C_{60} the energy barrier between Ag_{309} cluster and Au(111) substrate has a quantity of 2.4 *eV*. This significantly larger value prevents any decay in reasonable time scales ($t > 10^{20} a$) [149]. This calculation was confirmed experimentally for Ag_{309} clusters. A depiction of the decay process or lack thereof is shown in figure 2.18.

To investigate the stability of cluster with varying sizes, annealing experiments have been conducted for several cluster sizes smaller than or equal to Ag_{138}. Each sample was not only heated to room temperature but underwent several annealing steps for various amounts of

time so that possible intermediate states in cluster shape evolution could be observed. In the following sections the results are organized by experiment.

2.1.4.1 Annealing of Ag_{55} and Ag_{95} on 1 ML C_{60}/Au(111)

Ag_{55} and Ag_{95} (see chapter 2.1.1) were located on the same sample so that they underwent identical annealing conditions. The sample, normally cooled to 77 *K*, experienced the following three successive annealing steps: 1 *h* at 200 *K*, 1 *h* at 250 *K*, 20 *min* at RT. Annealing started at 200 *K* because no major effects to the clusters were expected at lower temperatures. With the sample approaching room temperature, the time was shortened from 1 *h* to 20 *min* because changes where expected to occur more rapidly.

The upper most histogram in figure 2.19 shows the cluster height distribution of Ag_{55} at 77 *K* measured with STM on C_{60}/Au(111). Below are several successive annealing steps. The height distribution changes visibly after annealing the sample for 1h at 200 *K*. In addition to the main peak at about 1.3 *nm* another cluster height of 1 *nm* emerges but until this point with less than half the frequency. Another annealing at 250 *K* leads to quite significant changes. It seems that now again only one peak at 1.3 *nm* is present. However, the histogram is broadened in comparison to the previous annealing step. Thus it is conceivable that the additional height at 1 *nm* and another one at 1.5 *nm* are present but barely detectable due to a low cluster count. It seems that additional heights disappeared and only the one with 1.3 *nm* remained. This observation is confirmed when investigating the last annealing step. After an additional 20 *min* at room temperature, most of the cluster material is decayed as the reduced overall frequency of the histogram suggests. However, one peak at 1.3 *nm* remains, which vindicates the continuation of the previously mentioned cluster height evolution. In conclusion Ag_{55} clusters can rearrange into a particularly stable configuration with an average height of 1.3 *nm* on a C_{60} surface. Other configurations with heights of 1 *nm* and 1.5 *nm* occur. However, with more energy for atomic rearrangement available, only the supposedly most stable configuration with a height of 1.3 *nm* remains. Other experiments suggest that a successive prolonged annealing at room temperature would have caused a decay of all remaining clusters [123].

At a first glance Ag_{95} seems to behave quite differently to Ag_{55} on C_{60}/Au(111). In figure 2.20 the respective histograms of Ag_{95} are shown. This cluster size experienced the exact same annealing steps as Ag_{55} because both were located at the same sample. The difference is, however, mostly a perceived one. After the first annealing step at 200 *K*, the histogram shows a shoulder at 1 *nm*. This can be interpreted as being the same configuration that caused the additional peak in the case of Ag_{55}. The only difference is the lower relative frequency of the additional peak for Ag_{95} clusters. The broadening of the histogram suggests that a peak at 1.3 *nm* is forming but merges with the main Ag_{95} peak (1.5 *nm*). Thus peaks at 1 *nm*, 1.3 *nm* and 1.5 *nm* are evolving for Ag_{95}. After annealing the sample for an additional 1 *h* at 250 *K*, the behaviors of Ag_{55} and Ag_{95} start deviating. The latter still shows the semi stable height of 1 *nm* but adopts several different configurations of multiple heights, non of which seem to be favorable to another. Even after 20 *min* at room temperature a similar accumulation of

unidentifiable heights emerge while 1.3 *nm* still seems to be preferred. Assumably Ag_{95} forms the same configurations as Ag_{55} but starts from a larger amount of atoms per clusters and thus takes longer to decay.

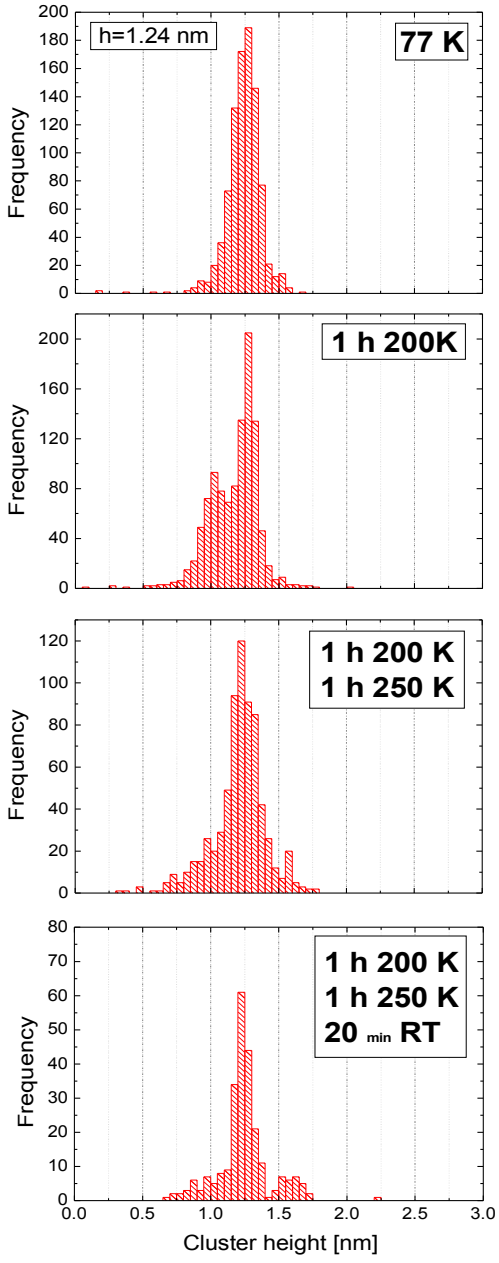

Figure 2.19: Height histograms of Ag_{55} on 1 ML C_{60}/Au(111) initially and after annealing.

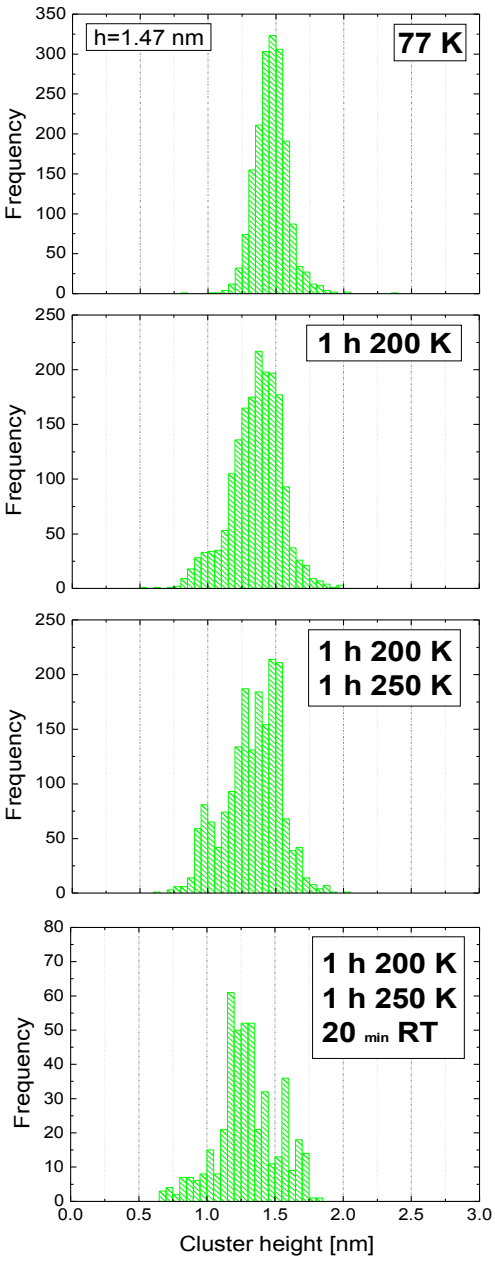

Figure 2.20: Height histograms of Ag_{95} on 1 ML C_{60}/Au(111) initially and after annealing.

2.1.4.2 Annealing of Ag88 and Ag138 on 1 *ML C60/Au(*111*)*

Both cluster sizes were located on the same sample so that they experienced the same annealing steps. In contrast to previous annealing experiments, this time the sample was only annealed at room temperature two times for 15 *min*.

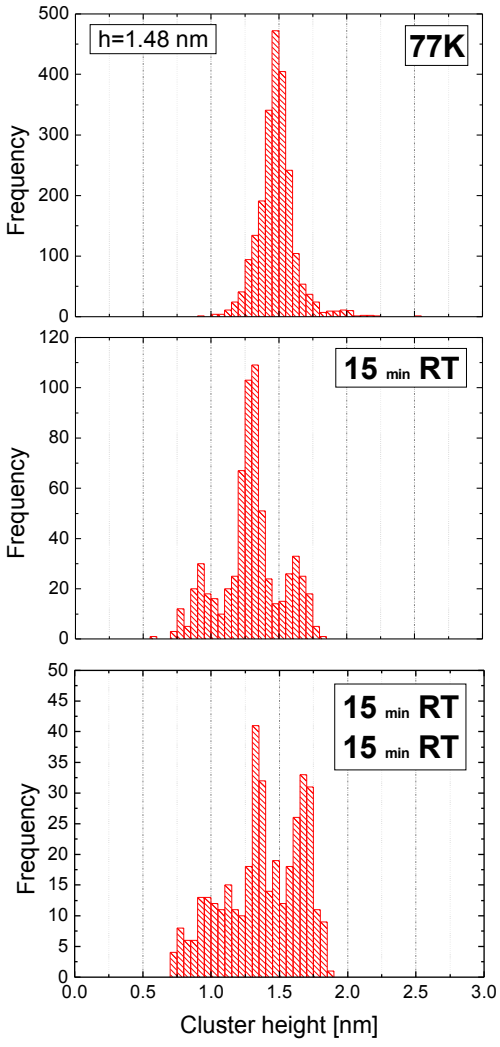

Figure 2.21: Height histograms of Ag_{88} on 1 ML C_{60}/Au(111) initially and after annealing.

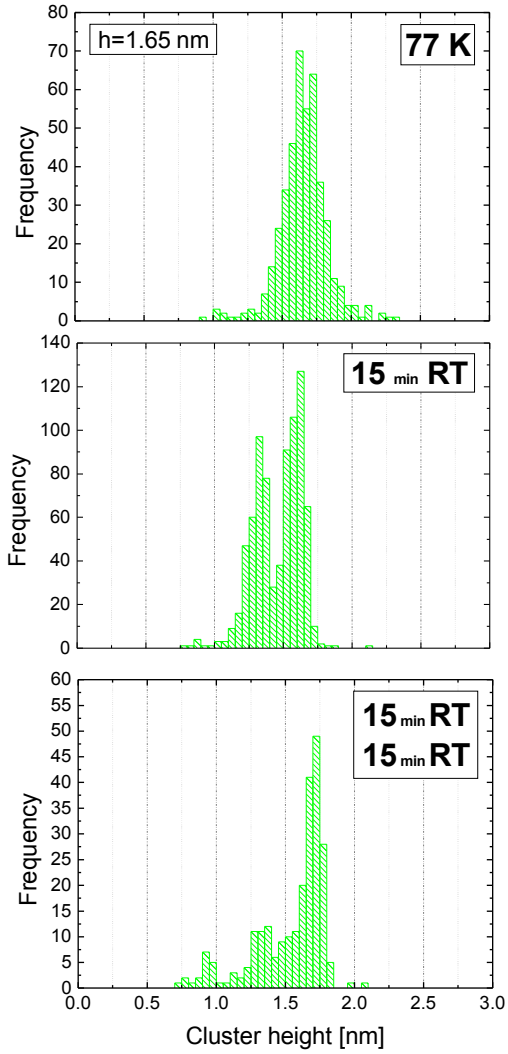

Figure 2.22: Height histograms of Ag_{138} on 1 ML C_{60}/Au(111) initially and after annealing.

In figure 2.21 the upper most histogram shows the unaltered height measurement of Ag_{88} clusters on 1 ML C_{60}/Au(111). Similarities to previous experiments are instantly visible after annealing at room temperature for 15 *min*. Three peaks are emerging at 0.9 *nm*, 1.3 *nm* and 1.6 *nm*. With slight variations they correspond to the three peaks of both Ag_{55} and Ag_{95} mentioned in chapter 2.1.4.1 on page 65. An additional annealing at room temperature for 15 *min* seems to cause a greater variation of heights. However, the lower overall amount of clusters counted compared to the previous annealing step hints rather to a statistical effects.

The upper most histogram in figure 2.22 shows the unaltered height measurement of Ag_{138} clusters on 1 ML C_{60}/Au(111). After annealing the sample for the first time at room temperature for 15 *min* an additional peak at 1.3 *nm* appears. In contrast to Ag_{55} and Ag_{88} the peak expected around 1 *nm* is completely missing. This changes, however, after annealing the sample again at room temperature for 15 *min*. Now all three peaks are detectable. It seems that clusters tend to form peaks first that are near their original height. The distribution of heights for the last annealing step of Ag_{138} (2×15 *min* RT) confirms this: The peak around 1.65 *nm* (original height) is largest, a peak around 1.3 *nm* has an intermediate cluster count while the peak at 1 *nm* is smallest.

2.1.4.3 Annealing of Ag_{82} on 1 *ML and* 2 *ML C_{60}/Au(*111*)*

The sample system, described in section 2.1.3 on page 61, encompasses Ag_{82}, Ag_{84} and Ag_{86} clusters. However, only Ag_{82} was further investigated due to the limited time available and the fact that only the Ag_{82} deposition area showed larger amounts of 2nd monolayer islands. This time the sample was annealed twice at room temperature for 15 *min* and 26 *min*, respectively. Only after the first annealing step, data was sufficient for the evaluation using a histogram. Figures 2.23 and 2.24 show the sample after the annealing steps. The cluster coverage density on the 2nd monolayer did not change noticeably while almost all clusters on the 1st layer disappeared as a comparison to figure 2.14 shows.

On one monolayer C_{60} Ag_{82} behaved in accordance to Ag_{88}. Again three peaks are observable in figure 2.25 with associated heights of 0.9 *nm*, 1.2*nm* and 1.5 *nm*. The green curves illustrate enveloping Gauss curves for the heights of the three occurring cluster configurations. The same has been done for clusters on the 2nd monolayer after annealing the sample for 15 *min*. The histogram in figure 2.26 shows in contrast to that of the 1st monolayer only two peaks. The lower one corresponds to the original height of about 1.3 *nm* while the other one displays with 1.7 *nm* a slightly larger height than on 1 ML C_{60}. While both peaks seem to be slightly shifted when comparing the 1st and 2nd monolayer, they can non the less be thought to represent the same cluster configuration. Minute differences in electronic behavior, changes in tip state or variations due to statistical effects can cause the observed shift.

As mentioned in the beginning of section 2.1.4 on page 63, cluster decay is expected on the 1st monolayer while no cluster material is expected to disappear on the 2nd monolayer. Obviously an additional process to decay takes places as the additional height peak on the 2nd monolayer suggests. *S. Duffe* theorized that a process called *Ostwald* ripening [155–157] may be responsible for the emergence of higher structures [123].

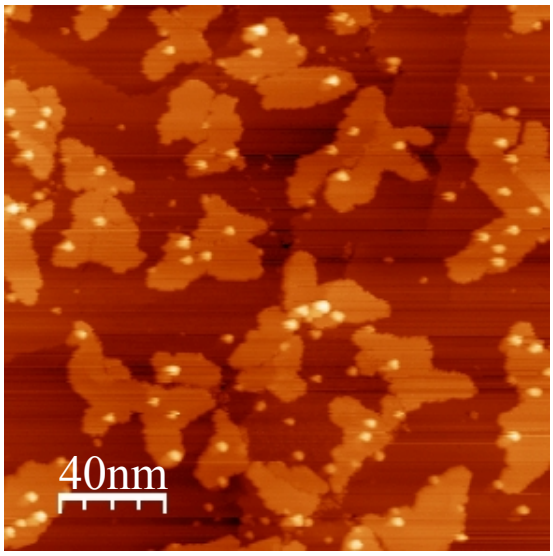

Figure 2.23: STM image of Ag_{82} on 1.5 ML C_{60}/Au(111) after annealing for **15** ***min*** at RT.

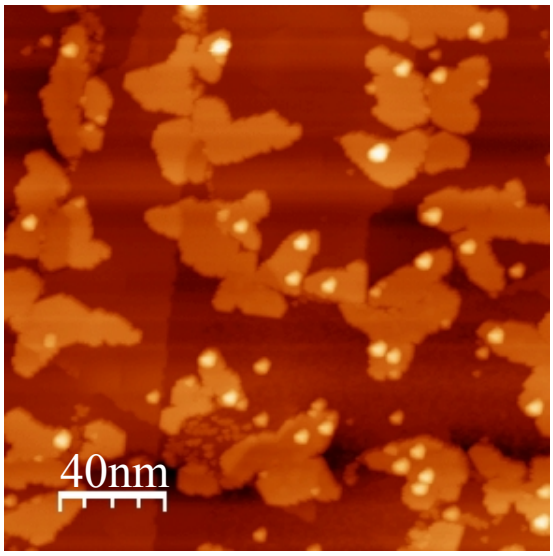

Figure 2.24: STM image of Ag_{82} on 1.5 ML C_{60}/Au(111) after annealing for **41** ***min*** at RT.

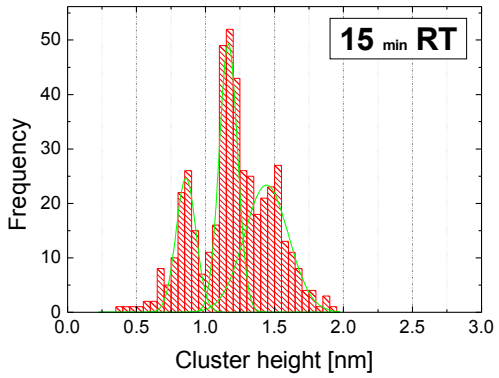

Figure 2.25: Height histogram of Ag_{82} on **1 ML** C_{60}/Au(111) after annealing for 15 *min* at RT.

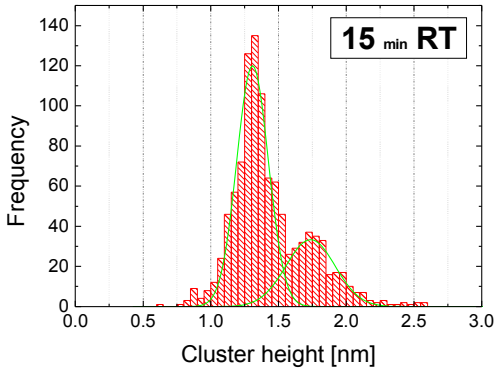

Figure **2.26:** Height histogram of Ag_{82} on **2 ML** C_{60}/Au(111) after annealing for 15 *min* at RT.

Ostwald ripening is responsible for the disappearance of smaller particles in favor of larger ones. At a given temperature single atoms can gain a varying amount of kinetic energy, the amount of which is governed by probability and the total thermal energy available in the system. Atoms in small particles are only weakly bound so that just a small amount of kinetic energy is needed to free the atom. The opposite is true for large particles. Atoms are easily incorporated but tend to stay fixated on the compound. Because a thermal microscopic environment is governed by statistical processes, incorporation and dissolution takes place in particles of all sizes. In a statistical average a shrinking of smaller and growing of larger particles is observed (see figure 2.27). However, this explanation does not fit the observed heights for clusters on the 2nd monolayer for the following reasons:

1. In the case of Ostwald ripening one or multiple heights significantly smaller than the original height should most likely be observed. For Ostwald ripening to take place, Ag_{82} clusters would have to loose atoms, which causes them to show a reduced height. Note that in figure 2.26 no heights much smaller than the original one are present.
2. The cluster coverage density did not change significantly after annealing on the 2nd monolayer C_{60}. However, a decrease is expected because in the case of Ostwald ripening a disappearance of smaller structures should occur.
3. The diffusion barrier for particles on C_{60} is quite large compared to other substrates. It is questionable if atoms gain enough energy to leave the cluster (typically 2-2.5 *eV*, see figure 2.18 and DFT calculations in [149]) and move unhindered over the surface.

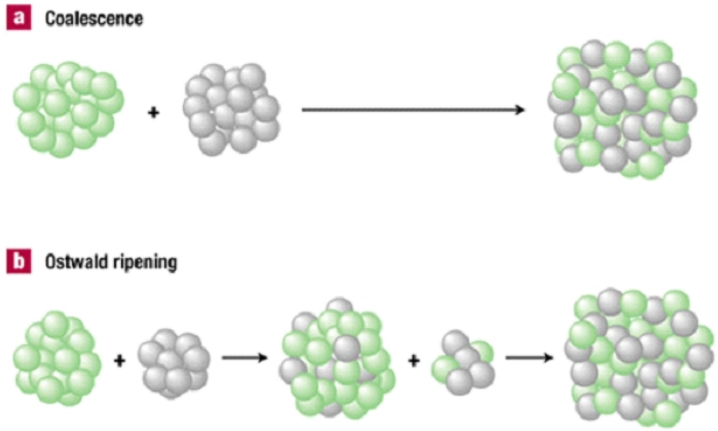

Figure 2.27: Illustrations of a typical coalescence process (a) and Ostwald ripening (b). In the case of coalescence two particles of similar size come in contact and form a new larger compound by fusing. In the case of Ostwald ripening smaller particles loose atoms over time, which are incorporated into larger ones until only the larger particle remains [158].

A rearrangement of atoms within the clusters seems to be a more likely cause for the appearance of an additional cluster size than Ostwald ripening. Less energy is needed to reposition the atoms of a cluster than removing them entirely [149]. This leads to the conclusion that at least mass selected Ag_{82} clusters have no energetically optimal shape when soft landed on a C_{60} surface. They seem to adopt an arrangement with a larger measured height when they are allowed to optimize their internal chemical bonds. Further experiments under different conditions, described in the next section, were conducted to gain a deeper inside in the processes at work.

2.1.5 Ag Evaporated onto C_{60}/Au(111)

In addition to mass selected clusters, silver was evaporated onto an Au(111) surface functionalized with several C_{60} monolayers. While the amount of mass selected clusters can be simply determined by counting their number, evaporated silver reaches the sample as single atoms, which have to coalesce before forming small islands. Thus their amount is estimated by frac-

tions of a single monolayer silver that would cover the surface. In all experiments 0.5 ML silver was evaporated onto the surface, which resulted in a great number of well separated, small silver islands.

This experiment aimed at comparing the behavior of islands self assembled directly on a C_{60} surface to clusters mass selected and deposited by soft landing. With a low temperature surface, mass selected clusters keep their size entirely while evaporated silver forms new, larger structures. To get a clear picture of the similarities and differences, the height of the consequently formed islands was investigated by STM, both at 77 *K* and after annealing the sample at several higher temperatures.

The evaporation procedure will not be explained here. A detailed description can be found in [159]. When the silver atoms reach the surface, they have a high movability due to their thermal energy. Thus they automatically form islands preferably on edges of C_{60} layers or defects on the surface. With a clean sample, however, most islands grow in a random pattern on the whole C_{60} area. Note that the sample temperature has a great influence on the ability of the forming islands to reach a state of equilibrium. In these experiments the temperature during evaporation was <50 *K* while the following measurements took place at 77 *K*. The repercussion of this choice will be examined in this section.

2.1.5.1 Preceding Experiment

The experiment described in this section was preceded by an earlier very similar experimental setup. The main differences lay in the amount of C_{60}, which was 1.3 ML in the preceding experiment, the length and temperature of the annealing steps and the overall statistics of the analyzed clusters. In [123] and [143] a detailed description of these experiments can be found. Note that the preparation procedure, which involves evaporation, scanning with STM and annealing, are almost identical to later experiments. Of special interest was the behavior of the evaporated material on the 2nd monolayer C_{60} because clusters as well as evaporated silver decayed on and formed silver islands below the first C_{60} layer.

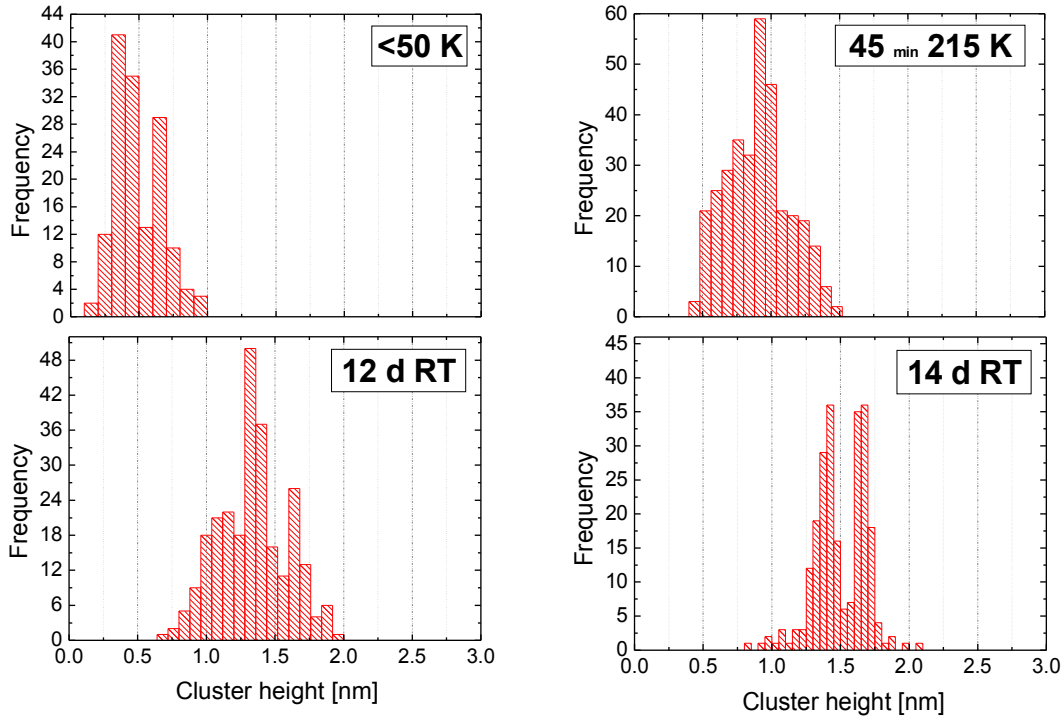

Figure 2.28: Histograms of 0.5 ML grown Ag clusters evaporated onto 1.3 ML C_{60}/Au(111) and measured on the 2nd ML C_{60}. The sample has been annealed in several steps. A continuous change of the cluster material to larger structures with a lesser amount of different heights is observable [123].

As the height measurements conducted with STM show, grown clusters can also be considered stable on the 2nd monolayer in contrast to the 1st. Even after 14 days at room temperature no material seems to have disappeared (see figure 2.28). Furthermore annealing the sample for 45 *min* at 215 *K* causes first rearrangements of the silver atoms. With a broadening of the histograms, the occurrence of multiple semi stable structures seems plausible. This is further emphasized by the following annealing step, which cause the emergence of two stable heights. The larger one at 1.7 *nm* dominates at first but reaches an equilibrium with the smaller height at 1.3 *nm* after 14 days at room temperature.

2.1.5.2 New Experiment

Due to the rapid decay of silver clusters on the 1st monolayer, the experimental setup was modified in order to get larger 2nd monolayer islands of C_{60}. Thus the amount of evaporated material was increased to 1.6 ML C_{60}. Note that an even larger amount could have compromised the experiment because uninterrupted layers prevent the experimenter from unequivocally distinguishing the 2nd from other layers. The following experiments were conducted with the involvement of *K. Mende* and some of the results can be found in his diploma work [160].

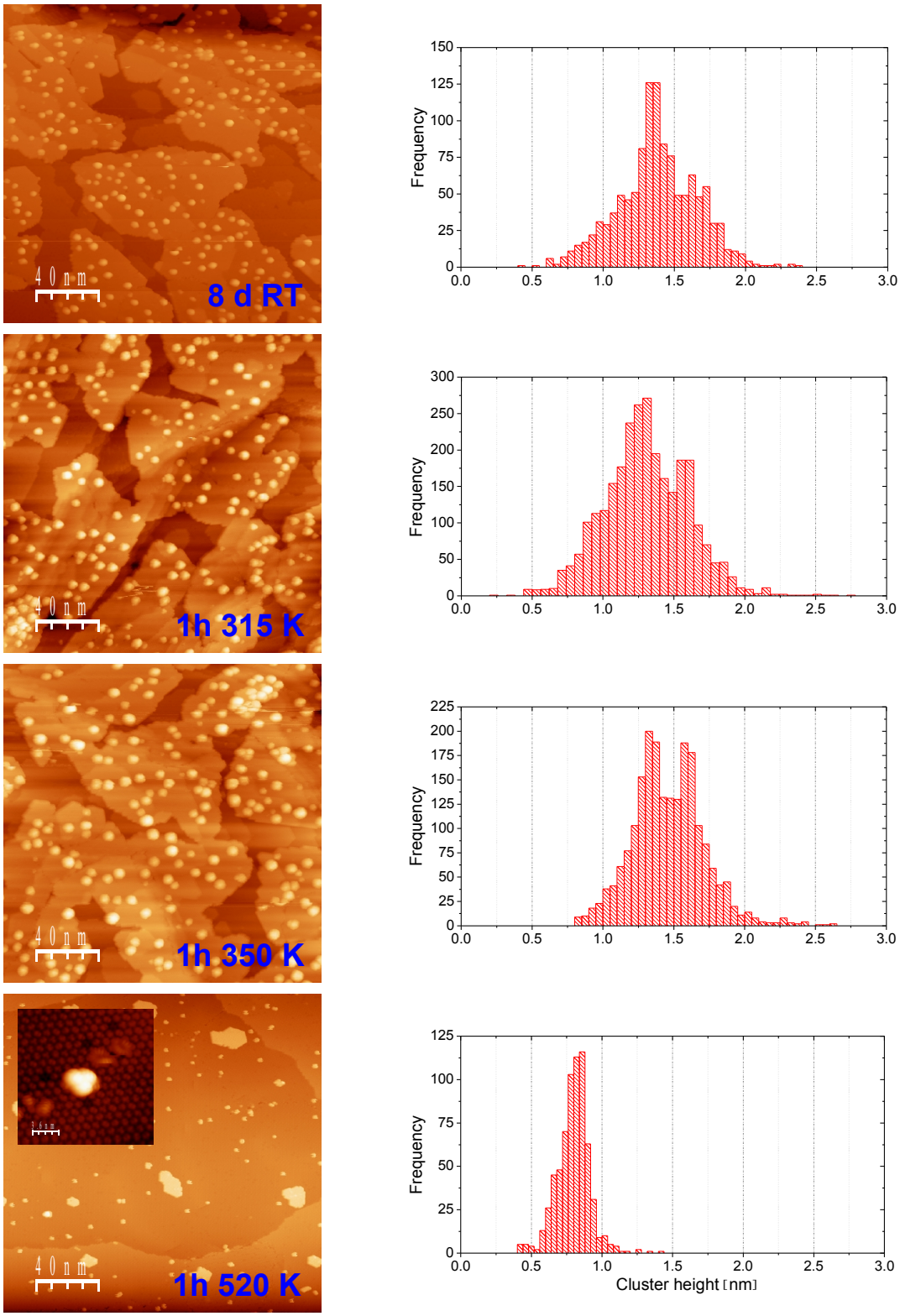

Figure 2.29: STM images of 0.5 ML *Ag*/1.6 ML *C_{60}/Au*(111) (left) associated with their respective histograms (right) for several annealing steps. For 1 *h* at 520 *K* the sample surface was significantly altered. A magnification (upper left corner) shows a structure probably consisting of C_{60} considering the average height. Up until annealing for 1 *h* at 350 *K* two heights of 1.3 *nm* and 1.6 *nm* emerge.

Initial measurements of silver islands directly after evaporation were compromised due to unfavorable tip states. Despite of that silver islands were shown to exist so that no further attempts to improve the measurement conditions followed. This has been done with the fact in mind that the preceding evaporation experiment already provided data for that special case. A further annealing for 8 days at room temperature followed in order to directly compare the results to the preceding experiment (see figure 2.29). In accordance to the preceding experiment two heights emerge. The main peak represents the first at 1.3 *nm*. The second height is indicated by a shoulder at 1.7 *nm* and less developed than expected. However, with 8 days this sample was annealed for a significantly shorter time than the comparison sample (14 days). Furthermore environmental conditions vary, considering differences in the exact composition of the C_{60} layers or silver evaporation temperature.

In contrast to the preceding experiment, the sample was also annealed above room temperature in order to detect possible differences in the behavior of silver structures. Thus the sample was annealed to 315 *K* for 1 *h*. Now the second height, previously only indicated by a shoulder, is represented by a clear peak in the height histogram at 1.6 *nm*. This hints to a further more complete rearrangement of the silver atoms on the C_{60} surface. Less desirable structures disappear in favor of only very few exceptionally stable arrangements with identical heights. After further annealing the sample at 350 *K* for 1 *h* both heights at 1.3 *nm* and 1.7 *nm* are represented by two peaks with similar frequency in the histogram. A further narrowing of the distributions is also observable. This result is similar to the 14 *d* annealing at room temperature. It is therefore conceivable that higher temperatures, at least up to 350 *K*, do not alter processes observed at room temperature but instead just accelerate them.

In a final annealing step the sample was heated to 520 *K* for 1 *h*. As seen in figure 2.29 a completely new arrangement appears. However, the height of the structures indicate that silver has completely disappeared from the surface or is at least not detectable. Instead small clusters as well as islands seem to consist of C_{60}. With a height of 0.8 *nm* they roughly fit the size of C_{60} fullerenes.

2.1.5.3 Silver Rearrangement Processes

The described experiments raise the question, which processes are responsible for the observed height evolution. As mentioned before, silver clusters mass selected and deposited onto a 2nd monolayer C_{60} surface are stable even at room temperature. Therefore a decay of the grown clusters through both of the two C_{60} layer is not probable.

Instead two main processes may govern the cluster size evolution for evaporated silver. Coalescence (see figure 2.27 on page 70) had to take place directly after evaporation. Single atoms on a C_{60} surface are energetically less favorable than larger compounds that can reduce their internal energy by forming covalent or even metallic bondings. The second process, Ostwald ripening, has been discussed before in section 2.1.4.3 on page 68 and was deemed unlikely to occur for mass selected clusters on C_{60} even at room temperature. Note that in the following discussion for evaporated Ag both Ostwald ripening and coalescence are considered due to an observed reduction in cluster coverage. This discrepancy in the behavior of mass selected and grown silver clusters will be discussed at the end of this section.

The height of a cluster is the only information regarding its shape that the STM measurement can normally deliver. Lateral information is not available for small structures because of the broadening of imaged objects due to the tip shape. However, several experiments hint to a non-spherical cluster shape. Investigations of mass selected clusters indicate that deformations are quite common. This is reflected by the observation that a sudden cluster height change occurs if the amount of atoms in the cluster is increased above a certain level (see section 2.2 on page 80). This can be explained best by a flattening or stretching of the cluster governed by the strength of the cluster-surface interaction. It has also been observed by *J.-G. Lee et al.* that clusters, grown by evaporating silver onto a graphite surface at 950 *K*, are not only flattened but retain a certain height-to-width ratio regardless of their size as figure 2.30 illustrates. This is the case while the particle undergoes a sublimation process that causes the cluster to completely disappear after 125 *sec* using high resolution electron microscopy as method of measurement [161].

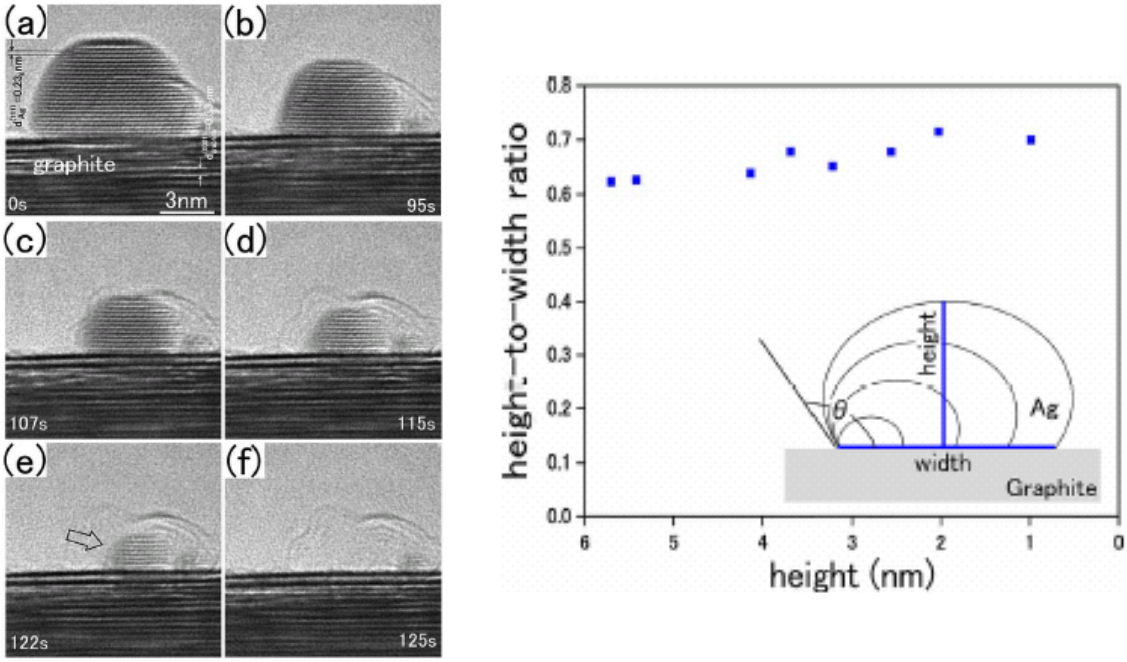

Figure 2.30: Visualization of the sublimation of a silver cluster on graphite using high resolution electron microscopy (left). Schematic depiction of a silver cluster in the process of sublimation (right). The height-to-with ratio stays fairly constant during that [161].

The clusters on a C_{60} surface are most likely flattened due to the interaction with the surface. It is expected that a cluster will adopt the shape of an ellipsoid because it delivers both a compact form for reduction of internal energy and a reduced height in order to move the atoms it exists of closer to the surface.

2.1.5.4 Cluster Shape Model

A cluster shape model for silver on a C_{60} surface has already been developed in the context of the preceding experiments [123]. An important assumption of this model was a

width-to-height ratio independence of temperature and cluster size. With this assumption a decrease of cluster heights is only possible if clusters are able to decay. While this is justified for some substrates and temperatures, experiments showed that clusters did not decay on 2nd monolayers of C_{60}/Au(111). Furthermore annealing the sample above room temperature did not alter the process but only accelerated it. Thus it is likely that a decay does not occur for temperatures up to 80°*C*. Note that annealing the sample at 520 *K* is not included in either this discussion nor the following evaluation because clusters and the C_{60} film were clearly altered to a point where unrelated processes dominated.

For a new cluster shape model, which delivers information on the width-to-height ratio of a cluster, the amount of cluster material is now thought to be constant while shapes deviate.

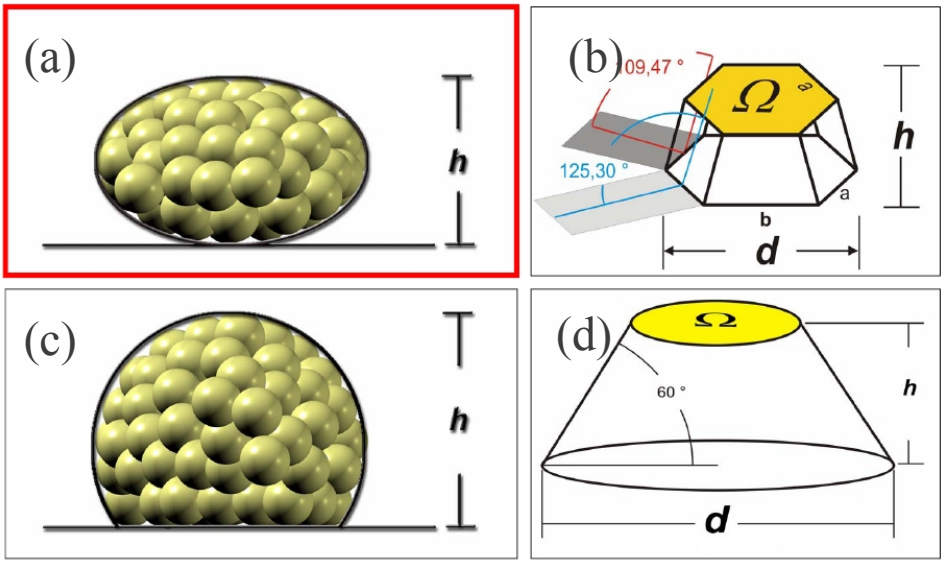

Figure 2.31: Depiction of 4 possible cluster shapes on a surface [62,159]. Both faceted shapes (b,d) are discarded because no facets were observed experimentally. The ellipsoid model (a) is used here.

Figure 2.31 presents a selection of four possible cluster shapes for clusters on substrates. Example (b) shows a faceted octahedron. This shape was observed for clusters grown on surface defects like nano pits [162]. Note that only clusters with more than around 1000 atoms display facets [159]. The missing of facets in STM images exclude this model for the following evaluation. Similarly a model using a cone as a basic shape (d) has comparable deficits, especially because faceted clusters must be assumed. In contrast to that both ellipsoid cluster models (a,c) fit the requirements for a moderately bound, not faceted cluster. For a given width-to-height ratio a truncated sphere (c) and an ellipsoid (a) lead to similar cluster volumes [62].

Considering the moderate cluster-surface interaction, the ellipsoid (figure 2.31, a) will be used for the following computation of a width-to-height ratio. It allows a minimization of internal energy due to its symmetrical shape and incorporates the cluster-surface interaction which leads to a flattening of the ellipsoid.

Only the height is directly accessible by STM measurements. As mentioned before, the width is not measurable and must be identified by different means. Under the assumption that the known total amount of silver stays constant during the entire experiment, the combined volume of all clusters can be computed from the given evaporation parameters. With the number of monolayers evaporated N_{ML}, the height of a monolayer h_{ML} and the total measured area of the sample A_{tot} covered with silver, the total Ag volume V can be computed by the following formula:

$$V = N_{ML} h_{ML} A_{tot} \tag{2.1}$$

With the given cluster model the volume V is identical to the accumulated volume of all i ellipsoids in the measured area. Note that silver reached the first monolayer but only the second was evaluated on a fraction of the total area covered with silver. Therefore the volume of the ellipsoid (red box) has to be increased according to the ratio of the 2nd monolayer and the total area A_{2nd}/A_{tot} in the following formula:

$$V = \sum_i \boxed{\frac{4}{3}\pi \frac{h_i}{2}\left(\frac{w_i}{2}\right)^2} \cdot \left(\frac{A_{2nd}}{A_{tot}}\right)^{-1} = \sum_i \left(\frac{A_{2nd}}{A_{tot}}\right)^{-1} \cdot \frac{\pi}{6} x^2 h_i^3 = \frac{A_{tot} \cdot \pi}{6 A_{2nd}} x^2 \sum_i h_i^3 \tag{2.2}$$

The height h_i of a cluster i is measured while the width w_i can be replaced with the width-to-height ratio x by using the equation $w_i = h_i x$ in the above formula. By replacing the volume with the parameters of equation 2.1, the following equation results for the width-to-height ratio x:

$$x = \sqrt{\frac{6 N_{ML} h_{ML} A_{2nd}}{\pi \sum_i h_i^3}} \tag{2.3}$$

With N_{ML}=1.6 ML and h_{ML}=0.236 *nm* [122], only the area A_{2nd} and the sum of all heights are as yet unknown. The former can be determined by using the software *WsXM* where the area of a certain height level in an STM image can be identified. Note that the total area A_{tot} has not to be known and that the sum in equation 2.3 encompasses all measured cluster heights. The width-to-height ratio x has been computed for both experiments and the different annealing steps.

As figure 2.32 illustrates, three fairly constant values for x have been measured. The data set of the first experiment displays a sudden shift in the ratio between 45 *min* at 215 *K* and 15 *min* at *RT* from about 2.5 to 3.5. So it is conceivable that at least at one point a significant change in the width-to-height ratio occurred. After annealing the sample at 215 *K* both final heights at 1.3 *nm* and 1.6 *nm* were not yet reached, as it is the case in all following measurements. This hints to a rearrangement process of the cluster atoms that can only occur in observable time scales if a sufficient amount of thermal energy is available. Thus after exposing the sample to room temperature, this process might have been completed so that no further change in width-to-height ratio took place even at higher temperatures.

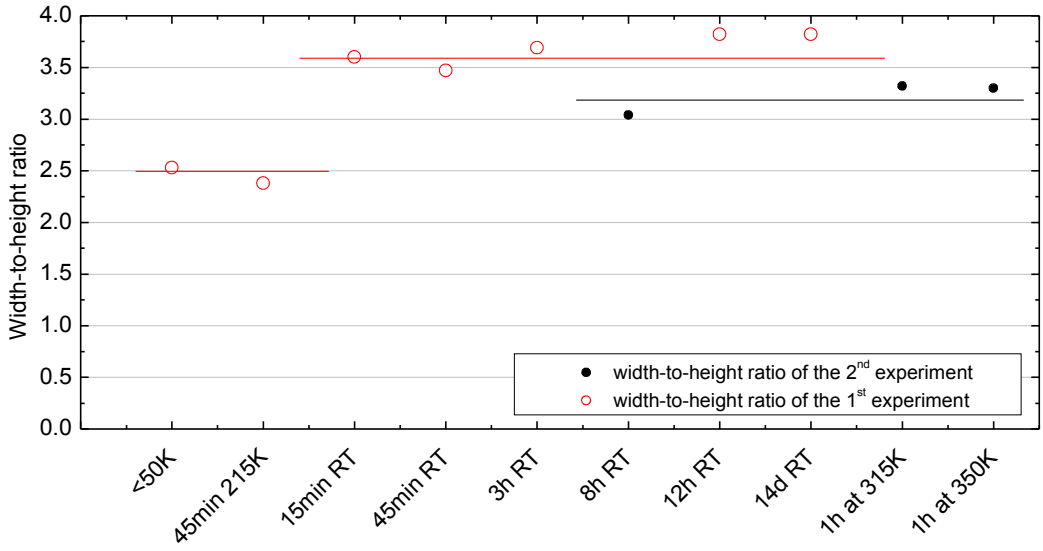

Figure 2.32: Width-to-height ratio for several annealing steps. The first experiment (red circles) reveals a sudden change in width-to-height ratio after annealing the sample at RT for 15 min. The second experiment shows that the altered ratio stays unchanged for temperatures above RT. The deviating width-to-height ratios of both experiments can be attributed to experiment related errors.

Note that the 2nd experiment was expected to produce identical results, at least for the ratio, after annealing the sample for 8 days at room temperature. However, the ratio is with about 3 significantly lower than the expected value of 3.5. The fact that there is no further significant shift in the width-to-height ratio hints to a systematic error. It is conceivable that the total amount of evaporated silver is afflicted with several uncertainties. Note that both evaporation time and temperature of the crucible have to be precisely controlled. A small deviation in those parameters could alter the results in the observed fashion. Furthermore the silver coverage cannot be thought to be uniform on the entire sample. Both measurements may have been conducted in the evaporation center so that an area close to the maximum coverage is measured, but said center can only be estimated. Another possible source of error is the quantification of the size of the 2nd monolayer on any of those samples. While the latter may produce slightly different results for varying layer geometries, it is unlikely to produce the deviation observed. Note that the height change within the first experiment is not affected by these errors.

It must be noted that there has been no distinction between the cluster types represented by two distinct height peaks in the respective histograms. It is possible that a change in the width-to-height ratio occurs and both cluster types are identical in their number of atoms.

With this in mind an estimation of the atoms a cluster consist of is possible. Because the volume V of a cluster and the specific height h are now known (using the computed ratio x in equation 2.3), only the volume V_u of a silver unit cell is needed. With a lattice constant of

a=0.409 *nm* for silver [122], the following formula allows the computation of the amounts of atoms N in a spherical cluster:

$$N = \frac{V}{V_u} = \frac{4}{3}\pi\left(\frac{h}{2}\right)^3 \cdot \frac{4}{a^3} \tag{2.4}$$

With equation 2.4 a spherical cluster with a height of 1.3 *nm* encompasses about 70 atoms. An equally high evaporated cluster consists of 750 atoms. A cluster with a height of 1.6 *nm* consists of 1400 atoms. For the latter two values a width-to-height ratio of x=3.3 was used.

2.1.6 Discussion

Both evaporation experiments, conducted on separated samples with varying amount of cluster material and C_{60} coverage, show that a flattening of the observed structures is most plausible. The average width-to-height ratio of x=3.3 is most likely caused by the C_{60} underlayment, which delivers a certain cluster-surface interaction that would favor an ellipsoid shape. Note that the flattening for evaporated silver on graphite, displayed in figure 2.30, is less distinct with a width-to-height ratio of x=1.4. The same ratio has been found for Ag_n cluster on HOPG measured with STM and TEM [163]. This is in accordance with the weaker cluster-surface interaction of graphite, which does not favor a significant deviation of the clusters from a spherical shape.

The emergence of two final heights (h=1.3 *nm*; h=1.6 *nm*) in both evaporation experiments hints to particularly stable atomic configurations. Both heights also appear in the annealing experiments using mass selected clusters. Using equation 2.4, a spherical cluster with a height of 1.3 *nm* would consist of just 70 atoms. Note that a soft landed mass selected silver clusters with 80 atoms also displays a height of 1.3 *nm* before annealing. This is in good accordance with a spherical cluster, which is very similar in shape because Ag_{80} resembles a partly formed icosahedron. Grown clusters consist of around 10^3 atoms on C_{60} at 77 *K*, as the cluster shape model suggest. Despite an enormous difference in size both grown and size selected clusters display the same heights after annealing.

Despite the mentioned similarities in both processes, a clear difference is apparent. In the case of size selected clusters processes like coalescence and Ostwald ripening are excluded while they play a major role in the evolution of grown clusters during annealing. This can have several reasons. For once grown clusters usually display a higher coverage in the experiments with the given evaporation rate, which most likely facilitates coalescence and Ostwald ripening. This is also emphasized by the fact that the rearrangement seems to be quite abruptly concluded at room temperature. Note that in this case the cluster coverage decreases significantly so that further coalescence might not be possible any more. Smaller clusters are also present, which might gain sufficient energy for the atoms to leave the compound and overcome the high diffusion barrier of C_{60}. Furthermore grown structures might be less stable than mass selected clusters and thus have a greater tendency to loose atoms. Another aspect that might have influence during the annealing involves C_{60} fullerenes. Because they rotate

without a lateral movement at room temperature, a dislocation of clusters due to this effect is at least conceivable.

It may well be that the number of layers the cluster consists of is the defining factor for its stability. The difference of both heights is quite similar to the height of a single atomic layer with h_{ML}=0.236 *nm*. So both cluster shapes may have a comparable stability but undividable atoms force the emergence of two heights. The preference of a certain number of layers and thus a specific height might hint to the existence and importance of so called *quantum well states* (QWS) [164–169]. Because electrons can move quasi freely in a metal, electronic waves can expand over the entire compound. The waves are reflected at the boundaries of the cluster, resulting in standing waves. In large compounds like macroscopic solid bodies this effect is negligible. If, however, the size of the object is in the order of the Fermi wave length λ_F, which is about 1 *nm*, quantum effect become important [170]. Note that small clusters of a few atoms might lack the needed metallic properties to allow delocalized electrons. For the cluster size in question, in the order of 100 atoms, no conclusive picture of the electronic structure exists as yet for clusters on surfaces. However, evaporated Pb grown in HOPG nano pits, having a size in the order of 1000 atoms, have been shown to display QWS effects. They appeared more frequent if the energy of QWS electron waves was distant from the Fermi level [171]. This is plausible because these QWS have an overall lower energetic state and thus display a greater stability [164,172]. This effect has been simulated by *C. M. Wei et al.* for thin Pb films [173]. Their findings cannot be simply adopted to silver but a similar effect was experimentally observed for it as well [174]. A layer dependent stability of clusters could be a first hint to the influence of QWS effects.

A layer related effect is further emphasized by the observation of a possible height change between the mass selected cluster sizes Ag_{80} (1.31-1.41 *nm*) and Ag_{88} (1.48 *nm*). A further analysis of the the cluster sizes in question will follow in the next section.

2.2 Height Evolution of Ag_{80-88} on 1 ML C_{60}/Au(111)

Earlier experiments lead to the conclusion that clusters normally do not move on the surface or loose atoms to the environment at sufficiently low temperatures while simultaneously being fixated on a C_{60} film. Thus decay processes, coalescence and Ostwald ripening could be excluded. Furthermore it was shown that the great majority of clusters stayed separated if the deposited amount did not surpass a certain quantity. Some experiments hinted to a reshaping of clusters that depends on the cluster size. This or as yet unknown electronic effects resulted in a sudden change in height in the STM measurement.

The following experiments aimed at investigating the relevant region between Ag_{80} and Ag_{88} more extensively in order to validate the existence of a sudden height change with the help of new measurement and evaluation methods.

2.2.1 First Results

In early experiments we observed that certain measured cluster heights did not behave according to calculations using a spherical cluster shape. Instead they tended to be of the same measured height until a supposed sudden change took place. It was clear that the measured height did not change dramatically for Ag_{55}, Ag_{68} and Ag_{80}. Ag_{88} and Ag_{95}, however, were observed to be higher according to STM data. So in the case of lower clusters a height of about 1.35 *nm* was measured whereas in the case of larger ones a height of about 1.47 *nm* was identified. At that point the results were not conclusive because a lot of intermediate cluster sizes were missing and measured heights of smaller clusters deviated noticeably. In addition to that each size was deposited using a different sample so that the environmental conditions could not thought to be identical.

To narrow down the relevant sizes, we decided to deposit Ag_{82}, Ag_{84} and Ag_{86} in one row. This time the new Movable Focus Lens (see section 1.5.2 on page 38) was used, which allowed to deposit clusters in a tighter spot. It was therefore facilitating the creation of multiple spots on a single sample. That way we could not only ensure that the same environmental conditions were enforced but also that the tip and its respective state stayed similar.

The sample was prepared the way mentioned in the beginning of section 1.5.5.1 on page 47 to calibrate and test out relevant parameter of the new Movable Focus Lens. However, it turned out that an entire half of the sample was free of clusters because the calibration had been inaccurate. So the experiment, which this section is about, used the remaining space for three additional deposition spots. Consequently the sample underwent much harsher conditions because it was moved around in the UHV chambers and was exposed to elevated pressures during both deposition procedures. It also stayed in STM for about 2 weeks during which it could have been contaminated by adsorbates. This might be a reason for difficulties discussed in this section later on.

Ag_{82}, Ag_{84} and Ag_{86} had been investigated two times up until this point. The first time, described in section 2.1.3 on page 61, no MFL was used. Furthermore an inconclusive behavior was observed where Ag_{84} was larger than both Ag_{82} and Ag_{86} which contradicts the notion of a sudden height change. However, as mentioned in the respective section, errors could not be excluded, which invalidates the results to some degree.

Now three clearly separated and well positioned spots were created using the MFL. Figure 2.33 shows the respective histograms and gives an overview of the state of investigation. It is noticeable that both Ag_{82} and Ag_{84} show low heights of 1.35 *nm* and 1.33 *nm* compared to the larger Ag_{86} that displays a height of 1.39 *nm*. This indicates that a sudden change in cluster height is indeed possible somewhere around Ag_{86}. However, Ag_{86} is only 0.4 *nm* larger than Ag_{82} while Ag_{84} is smaller than both Ag_{82} and Ag_{86}. These results hinted to the expected height change but were after all unsatisfying, especially compared to earlier experiments. For that reason a new and more elaborate experimental setup involving the MFL and 9 separated deposition spots was designed.

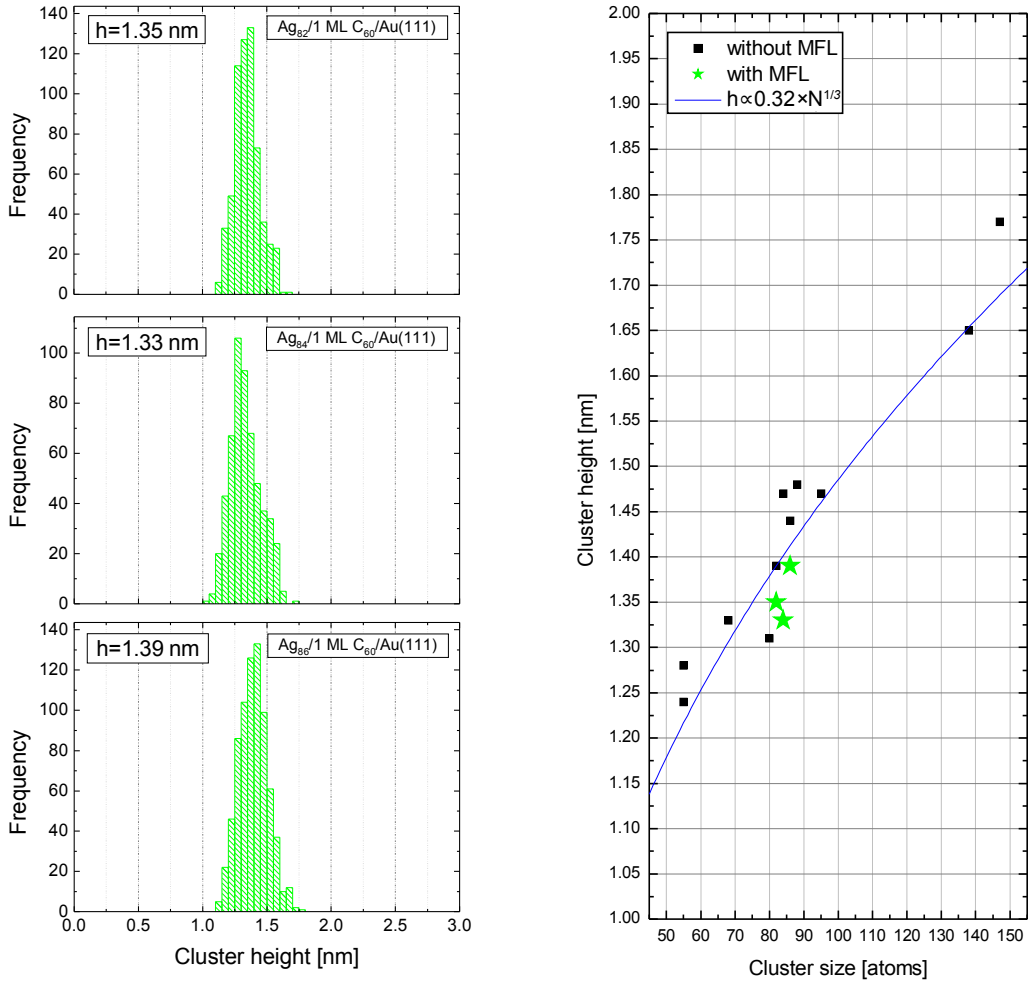

Figure 2.33: Height histograms of Ag_{82}, Ag_{84} and Ag_{86} measured with the Movable Focus Lens (left). Cluster sizes measured in multiple experiments (right). The blue curve displays theoretically predicted heights following the height of a spherical cluster. Especially around Ag_{85} measurements are inconclusive as the scattering of similar heights shows.

2.2.2 Adjusted Evaluation of Cluster Heights

Normally the measured height, extracted from STM measurements, varies despite stemming from a single cluster size. This is due to vibrations in the apparatus and different cluster orientations on the surface as symbolically indicated in figure 2.34.

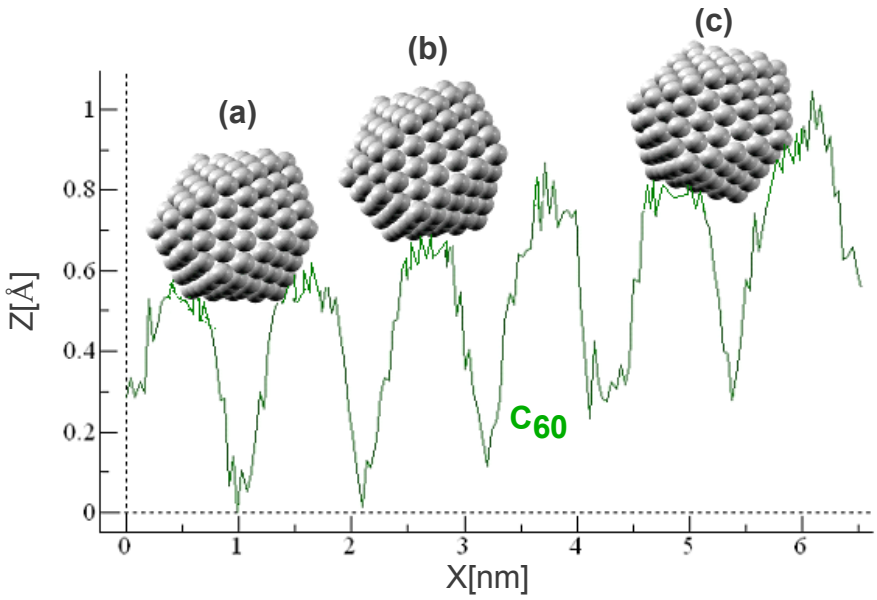

Figure 2.34: Clusters on a C_{60} surface are usually positioned in the spacings between C_{60} fullerenes (a,c) while displaying multiple orientations with varying subsequent measured heights. It might also be possible, but unlikely, that clusters are stable on top of a C_{60} molecule (b).

To solve this problem the data are normally presented in the form of a histogram which bundles similar heights. This method has the disadvantages that a bin size has to be selected which determines the amount of heights bundled into a single bar. This number is quite arbitrary and a visual inspection of the distribution is necessary to determine the correct settings. Finding the maximum of a certain peak is therefore difficult due to the limited bin size. It would be necessary to calculate an enveloping curve. This is, however, futile because the histograms normally do not follow any simple mathematical formula. Several methods can now be thought out to solve these problems.

To make full use of the quite detailed height information, the data must be bundled in a more continuous way. For that reason a Perl script was coded that is able to associate each height with a normal distribution or Gauss curve, respectively. This curve is determined by its position, height and width. The latter is normally described by the value σ, which is the standard deviation of a normal distribution:

$$f(x)=\frac{1}{\sigma\sqrt{2\pi}}\exp\left(-\frac{1}{2}\left(\frac{x-\mu}{\sigma}\right)^2\right) \qquad (2.5)$$

The value μ in equation 2.5 determines the location of the curve's maximum on the x-axis and thus its position. Consequently a particular experimental height determines the position of the curve while the width is a remaining free parameter. With the correct choice of σ, which is a value for the width, a histogram can be transformed into a continuous representation. The

curve, resulting from added up Gauss curves, roughly behaves as if it would envelope the respective histogram.

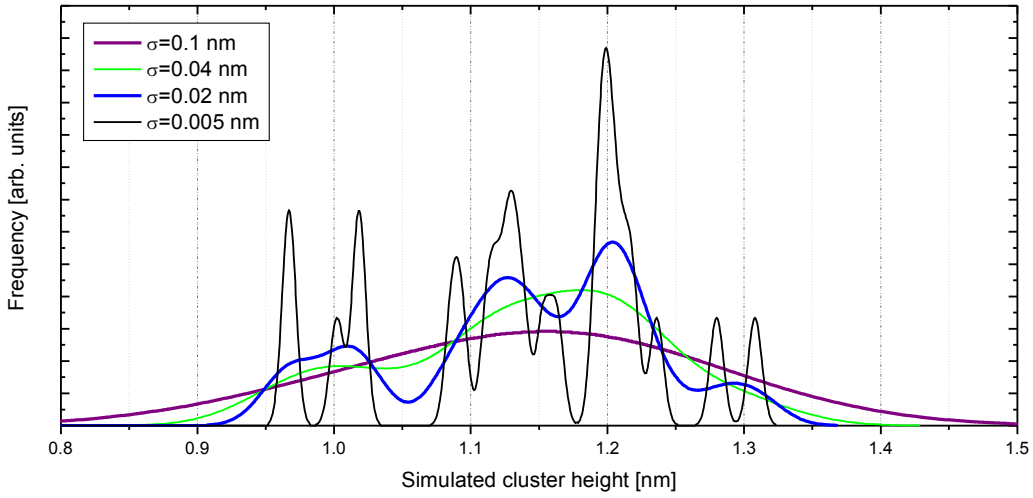

Figure 2.35: Displayed are multiple randomly chosen heights broadened by Gauss curves with varying σ. With increasing σ the curves start to merge.

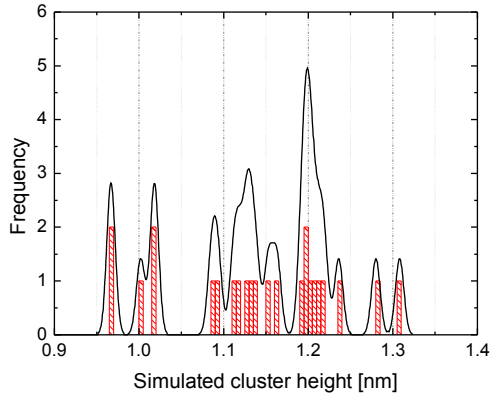

Figure 2.36: Comparison between a histogram with a bin size of 0.01 *nm* and respective heights replaced by continuous Gauss curves with σ=0.005 *nm*.

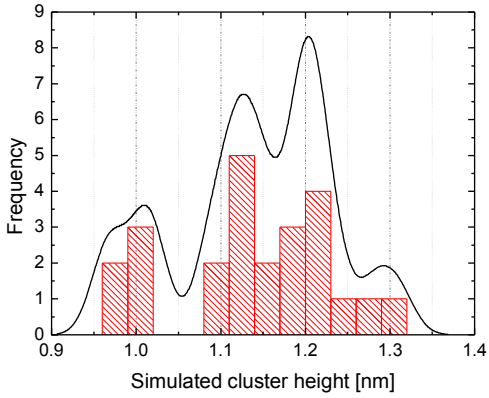

Figure 2.37: Comparison between the same histogram as in figure 2.36 with a bin size of 0.03 *nm* and heights replaced by Gauss curves with σ=0.02 *nm*.

Figures 2.35 to 2.37 clarify the concept. While figure 2.35 shows several curves that start to merge with increasing width, thus with a larger σ, figures 2.35 and 2.37 demonstrate the working principle. The bars of the histogram in figure 2.36 are already less precise in showing the position of the actual height than the normal distributions, which provide a more accurate picture. This particular example, however, defies the purpose of a histogram because the given heights are not bundled. This is done in figure 2.37 by selecting a larger bin size so that

several heights are represented by a single bar. Increasing the widths of the respective Gauss curves provides a similar method of displaying the data. However, substructures are shown more clearly. Note that the added curves might create the illusion of a large frequency while the amount of data is actually quite low. For that a histogram might provide a clearer picture.

The meaning of the resulting curves can be interpreted in the following way: Every measurement of a cluster has a limited accuracy. Thus each height is associated with an error so that only a certain probability of displaying the correct height exists. By replacing a single value by a normal distribution, this effect is taken into account. Thus a certain height is replaced by a larger number of heights and their occurrence is weighted by their probability of existing. Adding up multiple heights results in the weighted curves described above. If they are normalized, they represent the specific probability of a cluster with a certain height existing on the sample. However, the accuracy of this method heavily depends on the exact knowledge of the respective error associated with each height measurement. This value can only be estimated and is influenced by many unknown factors.

In the next sections this method will be called ***summed Gauss curves*** **(SGC)**. To reduce the possible bias of the experimenter toward a certain result, the standard deviation of the mentioned Gauss curve (σ) is varied over a large range. This causes the blurring of substructures to varying degrees. In a second step the maximum height of the curve is identified. A further increase of σ causes the deviation from the mean value to be less prominent.

2.2.3 Simulation of Ag_{80-88} on 1 ML C_{60}/Au(111)

The deposition of Ag_{80} to Ag_{88} atom by atom faces certain difficulties. As mentioned in section 1.5.1 on page 35, the cluster machine has a limited resolution. This means that in the case of e.g. Ag_{80} a mixture of Ag_{78} to Ag_{82} clusters would be expected. The ratio of mixed in clusters can be thought as behaving roughly Gaussian.

For simulation purposes a Perl script was coded that creates height histograms while simultaneously taking the limited resolution of the cluster machine into account. For that a modified Gauss curve for the ratio of mixed-in clusters is necessary:

$$f(x) = A \cdot \exp\left(-\frac{1}{2}\left(\frac{x-n}{n \cdot r}\right)^2\right) = A \cdot \exp\left(-\frac{1}{2r^2}\left(\frac{x}{n}-1\right)^2\right) \qquad (n, x) \in \mathbb{N} \qquad (2.6)$$

In equation 2.6 the standard deviation varies depending on the percentage resolution r and the cluster size n that the cluster machine is set to. With this equation the ratio of a neighboring cluster size x can be determined. Note that n and x can only adopt discrete values because cluster sizes change atom by atom. The prefactor A can be computed later by adding up the achieved values and defining the sum as 100 % (see table 2.1).

Before giving a concrete example, the resolution r has to be determined. Figure 2.38 demonstrates the usually used method. Visible is a part of the measured mass spectrum. The red line, which was calculated by adding up Gauss curves, shows a good accordance with ex-

perimental data (black crosses). The standard deviation of each computed Gauss curve depends on the respective cluster mass while the ratio *r* of standard deviation and cluster mass remains constant. From now on the size distributions will be called ***Cluster Size*** curves or distributions (CS-curve/ CS-distribution).

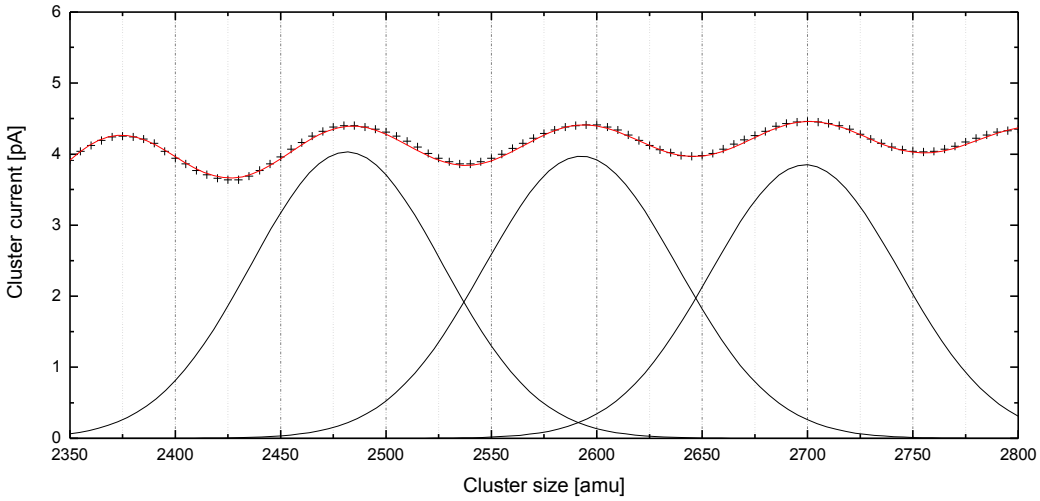

Figure 2.38: Cluster current measured for several cluster sizes (black crosses) during the adjustment of the cluster machine. The red line shows the summation of several Gauss curves, computed to fit the measurement; three of them are shown below. 2600 *amu* corresponds to a cluster size of about 24 atoms.

The evaluation showed that in this experiment a percentage resolution r=1.78 % existed. As a concrete example Ag_{86} is chosen as a representative cluster size. Equation 2.6 can now be used to calculate the ratio of several neighboring cluster sizes. The sum of all sizes constitutes the total amount of deposited material. Note that the frequency of cluster sizes in the beam tends to deviate. In the short interval between Ag_{80} and Ag_{88}, however, each cluster size is about equal in occurrence. With the given resolution, the following cluster size ratios for a deposition of Ag_{86} can be expected:

Cluster	Ag_{82}	Ag_{83}	Ag_{84}	Ag_{85}	**Ag_{86}**	Ag_{87}	Ag_{88}	Ag_{89}	Ag_{90}
Gauss value	0.033	0.147	0.426	0.807	1	0.807	0.426	0.147	0.033
Percentage	<1 %	4 %	11 %	21 %	26 **%**	21 %	11 %	4 %	<1 %

Table 2.1: **Simulated** distribution of deposited cluster sizes

The desired cluster size (in this case Ag_{86}) together with its two closest neighbors represent up to about 70% of the total amount of cluster material. This may be sufficient for a rough estimation of the relevant sizes during deposition but for a detailed investigation other sizes have to be regarded, too. An illustration of the Gauss curves with the respective cluster size ratios is given in figure 2.39.

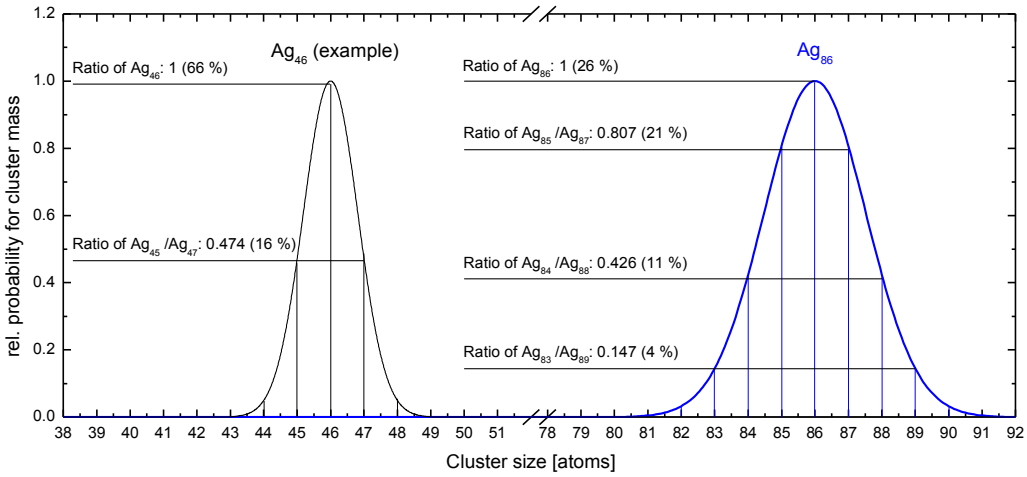

Figure 2.39: Two distributions describing the occurrence of mixed in cluster masses. For the distribution on the left the cluster machine is set to Ag_{46}, for the one on the right to Ag_{86}. The resolution is r=1.78 %.

The height change simulation uses Gauss distributions, which are modified according to the relevant resolution as demonstrated above. It incorporates the next twenty smaller and larger clusters. As shown in table 2.1, every cluster size not being part of the simulation should be well below any detection limit in the case of a real experiment.

In addition to that certain deviations in height are expected due to the limited accuracy of an STM measurement, which has to be taken into account in a simulation. At this point it should be noted that from now on there will be an additional kind of distribution, which does not relate to CS-curves in any way other than being part of the same simulation. It simulates inaccuracies during the STM measurement and while in reality being closer to a log normal distribution, it is also nearly Gaussian due to the ratio of the average cluster height and the standard deviation of the curve [175]. In the simulation *Box-Muller* transformation [176] is used to create random numbers weighted by a log normal curve. From now on this distribution will be called ***Cluster Height*** curve/distribution (CH-curve/ CH-distribution).

With the limited resolution and broadening of the cluster heights due to STM measurements taken into account, the simulation can be run. Now it is crucial to choose fitting parameters in order for the simulation to be as close as possible to the experiments. First of all the total number of simulated clusters of a single size must be set. In the case of a typical experiment this value can vary dramatically according to the number of individual STM images and the clusters present. In most cases a few hundred clusters for a single size can be found. Unfortunately this number is normally not large enough to get a smooth and clear normal distribution. To avoid the mentioned problem, 100,000 clusters were simulated for a single size. The resolution of the cluster machine was taken from the experiment's mass spectrum and determined by measuring the broadening of the peaks.

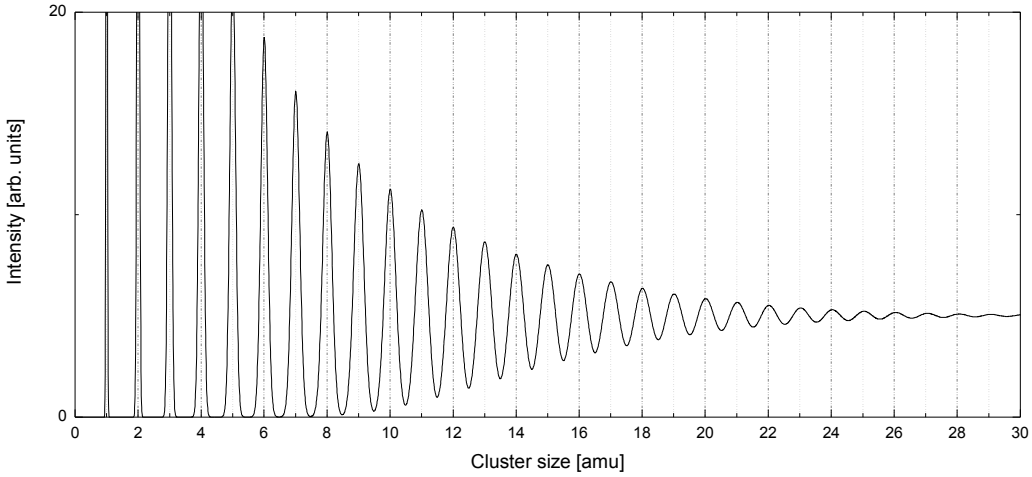

Figure 2.40: Simulation of a mass spectrum comparable to those measured using the cluster machine (see figure 1.28 on page 38). Each peak is generated by a normal distribution broadened by the given resolution (1.78 % of cluster mass). Consequently peaks start to merge until they are no more visible. Several further effects that influence the intensity are not considered.

Figure 2.40 illustrates that simulating an entire spectrum using a percentage resolution of 1.78% leads to a spectrum similar to that of figure 1.28 on page 38. The resolution is lost at around r_l=28 *atoms*. This phenomenon can also be used to determine the resolution. with the relation r_l=1*/(2r)* (r=0.0178 being the percentage resolution). By analyzing the measured spectrum of the height change experiment, the resolution of 1.78 % was determined. This value multiplied with the number of atoms in the respective cluster is the standard deviation of the CS-distribution whereas the maximum value A (see equation 2.6) can be derived from the total amount of deposited clusters (100,000).

The distribution of heights in STM measurements depends on errors due to vibrations and inaccuracies during scanning. The according standard deviation of the CH-distribution can vary tremendously because of strong variations in scanning conditions and sample quality. In this experiment the standard deviation of the CH-distribution was estimated to be 0.05 *nm* for all cluster sizes and measurements.

The position of the maximum of the CH-distribution is of great importance because it depends on the average cluster height of a measured size. To simplify matters, only two heights were chosen to model the effect of a sudden height change. The lower number was set to be 1.37 *nm* and the larger one to be 1.48 *nm*. They were determined in reverse by running a couple of simulations and comparing the results to the data from the measurement. After a good accordance was achieved, the heights were kept for further analyses.

The last and most important step is the specification of the the actual cluster size, which shifts in height. This proves to be of some difficulty because there are several candidates that behave in accordance to the data. In addition to that it is not yet clear if the height change even occurs after adding a single atom to a relevant cluster. It may well be that the effect is

best described by a smoother transition of heights. However, a sharp transition was modeled with Ag_{87} being the first cluster on a step of larger heights.

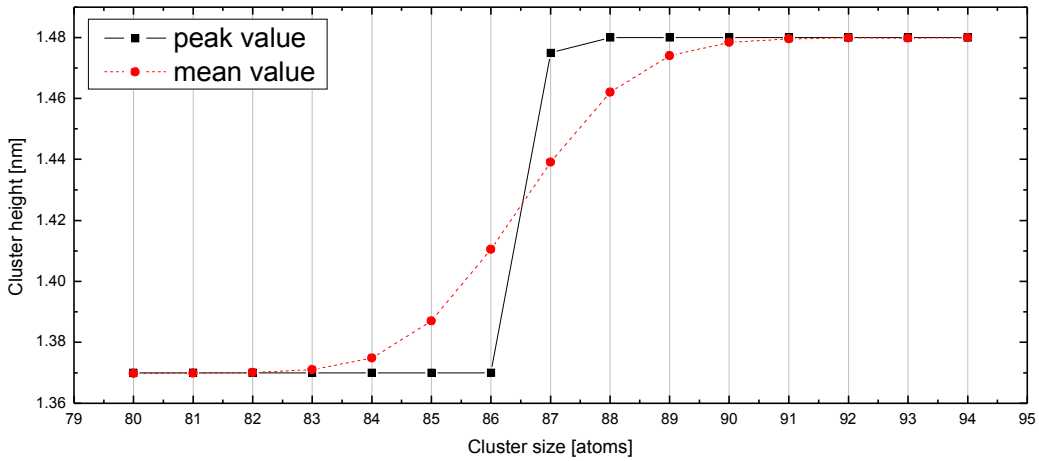

Figure 2.41: Simulated height distributions with a height change from 1.37 *nm* to 1.48 *nm* between Ag_{86} and Ag_{87}. The red dots show the average height of a simulated cluster size with a frequency of 100,000 *counts*. Black squares show the peak position of the respective distribution in a histogram with a bin size of 0.02 *nm*. While the mean heights of the histograms transition smoothly between the heights due to intermixing of cluster sizes, the peak value is less affected by this.

Figure 2.41 shows the result of the simulation. The black squares represent peaks in height histograms. The new SGC method was not used because the simulated histograms provide a sufficient frequency to avoid bin size related difficulties. The black line illustrates the transition, which takes place around Ag_{87}; a clear step is visible that indicates a shift in cluster height.

The red rhombuses show the average height of a distribution belonging to a certain cluster size. It is clearly visible that the red dashed line shows a much smoother transition than the black one. This is due to mixing of different cluster heights near the step. As seen in the distributions in figure 2.45 on page 93, the enveloping curve is not approximately Gaussian any more but has a shoulder either on the right or left side. These shoulders indicate the lower amount of another cluster height in the mix. In consequence the average height value is altered accordingly.

2.2.4 Measurement of Ag_{80-88} on 1 ML C_{60}/Au(111)

Ag_{80-88} cluster have been soft landed on 1 ML C_{60}/Au(111). The process of preparing Au(111) is described in more detail in section 1.5.5.1 on page 47. The subsequent evaporation of 1 monolayer C_{60} onto the surface is described in section 1.5.5.2 on page 48. To enable stable conditions for the clusters, the temperature was set to 77 *K* during deposition and measurement.

We used multiple deposition spots on a single sample, which were created with the Movable Focus Lens. For an STM measurement the usable space on the sample is limited by the area the STM tip is able to reach, which is 5×5 mm^2. Because each deposition spot has a diameter of about 1 *mm*, a distance of at least 1 *mm* between the spots is mandatory. To be save, 1.5 *mm* is usually chosen as a distance between two neighboring spots so that they do not overlap and a minimum of 0.5 *mm* space void of any clusters is between them. This is true for both directions so that a grid with 9 spots can be created, which occupies an area of 4×4 mm^2 while the relevant centers of the spots are expected to be found in an area of 3×3 mm^2. Thus there remains a margin of about 1 *mm* in each direction in order to compensate for a possible error in the positioning of the entire grid. Note that the relative positions of the spots are accurate to about 0.1 *mm* while their centroid depends on the relative position of sample, thus manipulator and ion optics. The exact coordinates shift depending on the temperature of the manipulator, which influences its length, and the positioning of the sample inside its holder. Both parameters were eventually identified quite accurately by using the information provided by preceding experiments.

In this experiment 9 spots were positioned in a 3*x*3 grid with a distance to each other of 2 *mm*. With a diameter of 1 *mm* the spots were clearly separated as measurements in between confirmed. Each deposition spot received a coverage of 10 *pAmin*. Thus it was expected that the cluster coverage density was identical for all spots. A deposition process included varying numbers of cluster sizes and spot positions. The deposition energy of each cluster size was set to 3 *eV*. Only one *manipulator bias* vs *cluster current* curve was acquired for all 9 cluster sizes. This proved to be sufficient as earlier tests confirmed.

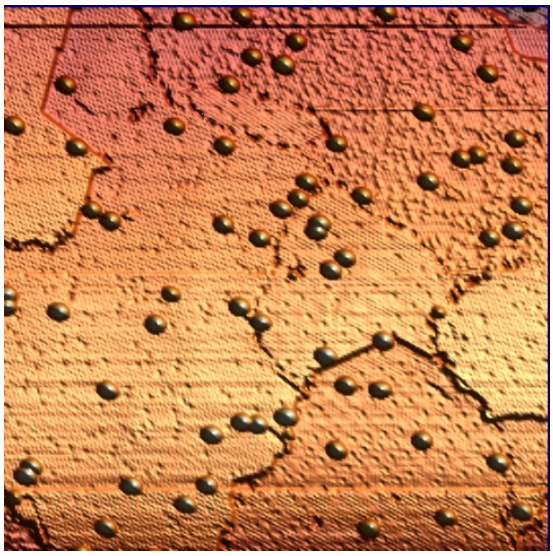

Figure 2.42: A 3D illustration of Ag_{80} cluster on 1 ML C_{60}/Au(111) not only shows the imaged shape of each cluster but also the structure of the C_{60} surface. The image size is 134×134 nm^2.

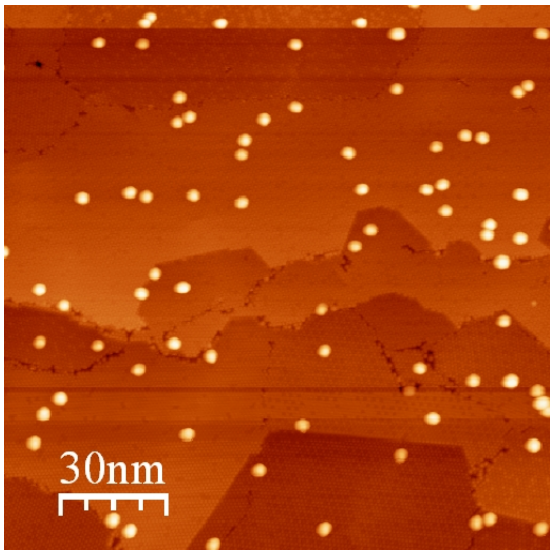

Figure **2.43:** Ag_{80} on 1ML C_{60}/Au(111). The STM images are without major disturbances and show close to no foreign material.

The scanning of the sample provided around 50 images in total. Normally this leads to around three weeks of scanning. This can be considered the limit when facing problems like unwanted adsorbates on the sample due to residual atoms and molecules in the vacuum in combination with low temperatures. Consequently the frequency of clusters is lower than in many previous experiments, which contained fewer deposition spots.

A major obstacle during measurement, especially if the accurate height information is of paramount importance, is the continuous shift in tip states. This phenomenon, most often caused by collecting cluster material and incorporating it into the tip, can strongly alter the height measurement. Experience shows that there can be major changes in tip state. The very first three images, which stem from measurements of Ag_{80}, show very stable conditions, no obvious cluster rearrangement occurred (see figures 2.42 and 2.43).

However, such a stable tip could not be kept for the whole experiment. Changing tip states produced varying shifts in height measurement. Fortunately the tip state induced height change proved to be much smaller than the crucial observed height step. Furthermore certain strategies were thought out to prevent compromised results. First of all STM images of a single deposition spot were not scanned in a row but in an alternating fashion. So we switched back and forth between several spots. In addition to that larger cluster sizes were measured just after measuring smaller ones and vice versa. Note that a height change was already expected around Ag_{86} so that this strategy was not based on pure guess work.

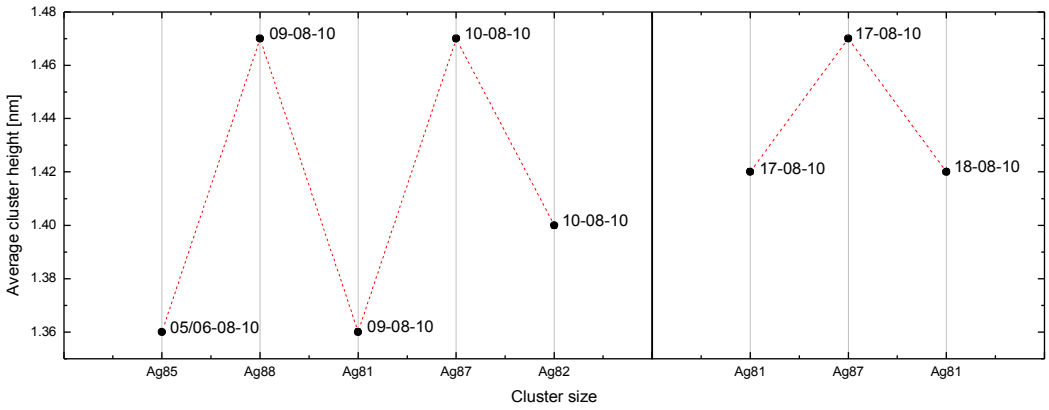

Figure 2.44: Cluster sizes in the order and date they were measured. Cluster sizes with expected larger and smaller heights have been measured in an alternating fashion. The zig-zag shape of the line illustrates that Ag_{87} and Ag_{88} display a larger height independent of tip state induced height changes. At the position of the vertical black line between Ag_{82} and Ag_{81} several measurements of smaller cluster heights took place, which are not displayed here.

Graph 2.44 demonstrates that the measured height change is most probably tip state independent. It shows several smaller cluster sizes between Ag_{80} and Ag_{85} in direct comparison to the larger Ag_{87} and Ag_{88} clusters. Note that the x-axis shows the order in which the measurement was conducted. The exact time, the images were scanned, is depicted beside the black dots. A random shift due to changes in tip state would produce these results only in a highly unlikely case.

We also made sure that the amount of measured clusters was large enough to marginalize the tip state influence by means of sufficient statistics. That way changes in tip state were much less likely to influence the real height change, which revealed itself after evaluating all available images.

In the following evaluation the height of each cluster size was investigated both using a histogram and the new SGC method described in section 2.2.2 on page 82. Theoretically the measured distributions should show a Gauss curve (CH-curve) in analogy to the simulation. This is not the case, mainly because the total amount of clusters for each histogram varies between 250 and 800. In this case statistical effects make it difficult to extract anything but the average height. There can however be hidden information in the height values. As shown in the simulations, the distribution does not have to be symmetrical because of a mixing of several cluster sizes. Furthermore coalesced clusters and adsorbates may produce multiple peaks, which do not carry the desired information.

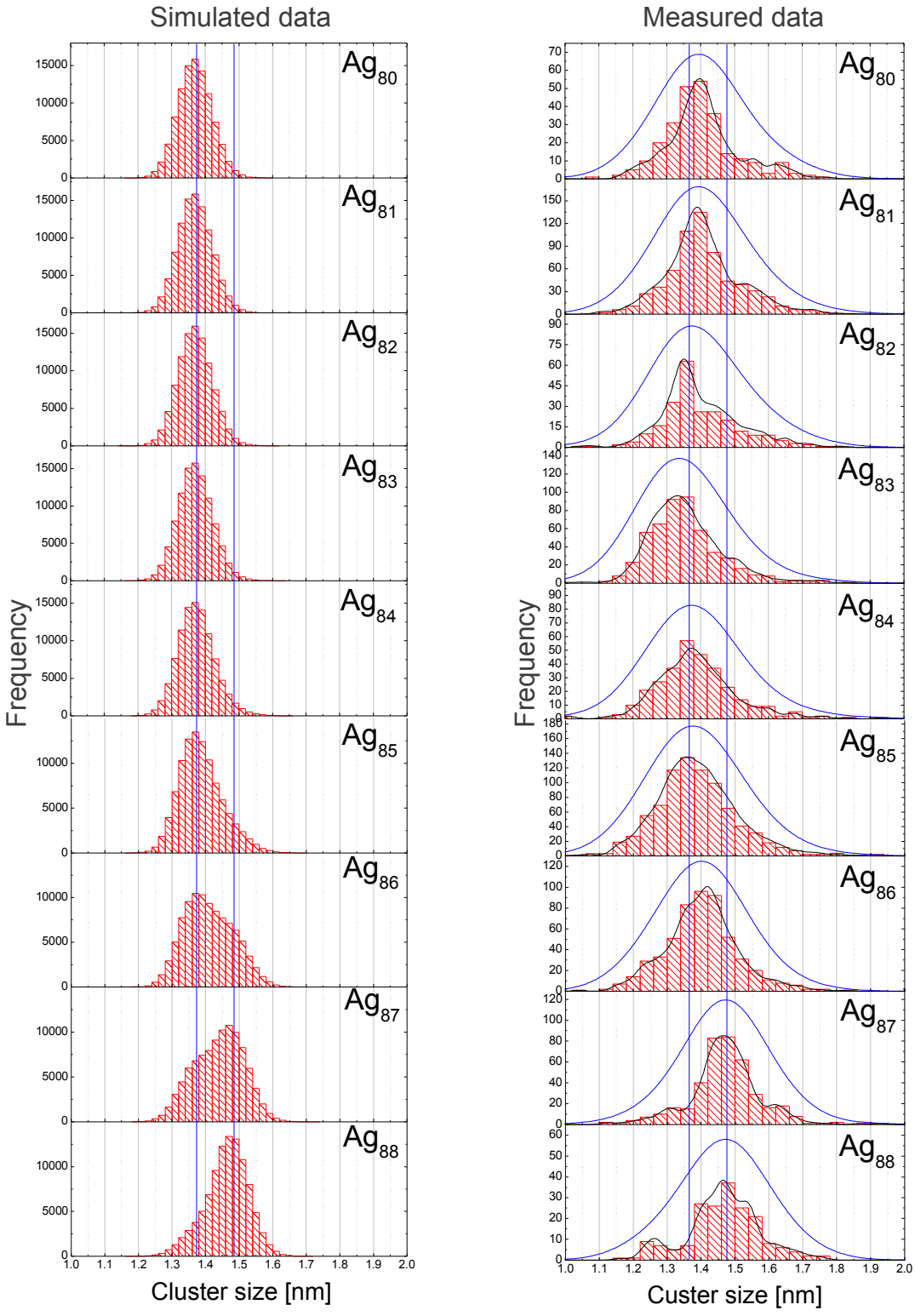

Figure 2.45: Simulated and measured cluster height distributions of Ag_{80}-Ag_{88}. Measured distributions are complemented by SGC curves with σ=0.02 *nm* (black line) and σ=0.1 *nm* (blue line).

Figure 2.45 shows the respective histograms of simulating and measuring Ag_{80}-Ag_{88}. The simulated histograms clearly show a very Gauss-like distribution for Ag_{80}-Ag_{84}. Then a shoulder is forming on the right, which is followed by a sudden shift of the maximum in the case of Ag_{87}. While the measurements are not as conclusive, a shift of the whole distribution to larger values is also visible. The new SGC method is used to conduct a more detailed analysis of the experimental data.

Average heights, as well as the maximum value found with SGC, are plotted in figures 2.46, 2.47 and 2.48. As mentioned before, the broadening of the simulated distributions depends on the value σ. A wide range of values for σ has been used to compute the maxima of several summed Gauss curves. Figure 2.46 shows the average height for several measured cluster sizes. It is quite noticeable that the mean value shows a height change for Ag_{87}. However, certain substructures in the height distributions and the small magnitude of the shift complicate matters. The maxima of the distributions, computed with SGC with $\sigma<0.05$ *nm* (upper left box), evolve partly in accordance to the mean curve. The maxima for Ag_{80}-Ag_{85} are invariably below the mean curve. Larger cluster sizes deliver no clear picture. For $\sigma>0.05$ *nm* SGC maxima transition more smoothly towards the mean value. In addition to that most maxima are below the mean curve for Ag_{80}-Ag_{85} and above for Ag_{87} and Ag_{88}.

For a further evaluation, a fitting σ must be chosen. Thus several values for σ have been computed and the mean value was subtracted in figure 2.47. It is noticeable that the maxima approach the mean value for larger σ as expected. However, lower σ display a more chaotic behavior. This is not surprising because with a low σ substructures of a respective histogram become more prominent. This can lead to multiple local maxima that only reflect unwanted statistical effects. At some point though substructures are blurred and resolution related effects take over. With a very large value for σ, even those effects are blurred so that effectively mean values emerge. Figure 2.47 allows a quantification of those effects. With $\sigma=0.1$ *nm* a certain threshold seems to be surpassed. Chaotic effects disappear and the maxima approach their respective mean values. Thus at this point the leaning of the measured data towards a certain direction is modeled best while simultaneously avoiding certain errors.

In figure 2.48 $\sigma=0.1$ *nm* has been chosen for the SGC maxima. The black round dots represent the maxima of the height distributions of several cluster sizes whereas the red rhombus shaped dots represent the average value. The lines show the evolutions of those heights. There are obviously similarities as well as differences to the simulated curves in figure 2.41 on page 89. First of all a sudden change in height is clearly visible around Ag_{86}. This is the case for the SGC maximum as well as the mean value. Interestingly there is also a sharp dip for Ag_{83}. The reason for that is not yet clear. It may be due to the changes in tip state mentioned before but it could also stem from a hypothetical physical effect. Because the deviation may only exist due to an unknown experimental error, the existence of Ag_{83} is only implied by a dashed line in figure 2.48.

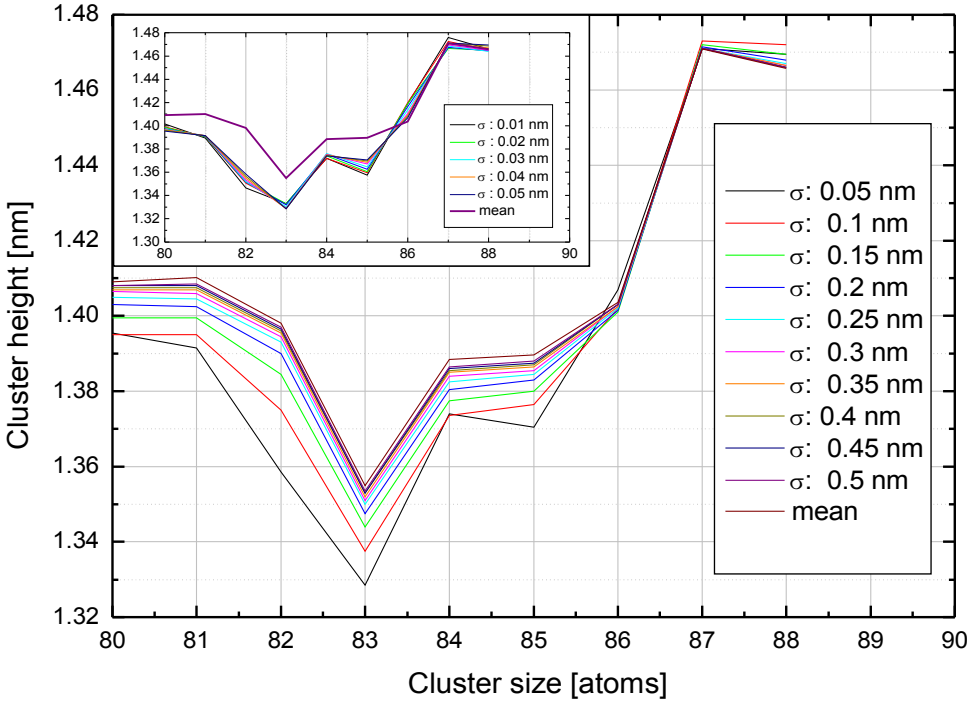

Figure 2.46: Measured cluster height given for Ag_{80-88} clusters. The new SGC method has been used to compute distributions with varying σ. For σ between 0.05 *nm* and 0.5 *nm*, curves are mostly below the respective mean value for Ag_{80-86} clusters. The curves are above for Ag_{87-88} clusters. In the upper left similar graphs with lower σ are shown. The behavior of the curves is less clear in this case.

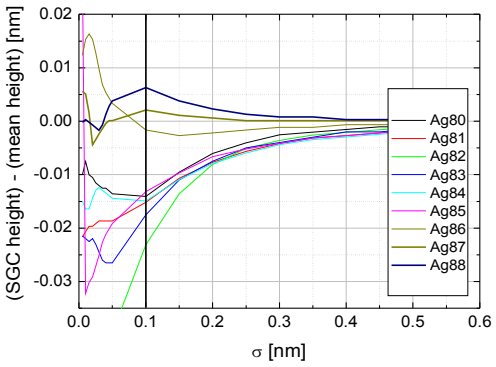

Figure 2.47: Difference between SGC heights and mean heights shown for several σ. For σ<0.1 no clear evolution is visible because of statistical effects that randomly shift the SGC maximum. For σ>0.1 SGC maxima approach the mean value monotonously. Furthermore Ag_{80-85} approach from below and Ag_{87-88} from above, while Ag_{86} is unclear.

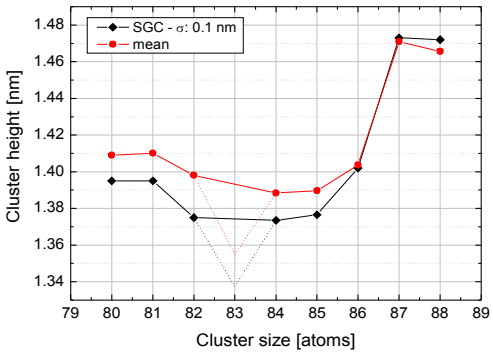

Figure 2.48: Measured height distributions of Ag_{80-88} on 1 ML C_{60}/Au(111). The mean height of the graphs is shown as red dots and transitions to larger heights between Ag_{85} and Ag_{87}. The SGC maxima, shown as black rhombuses, shift from being below to being above the SGC curve. A sharp dip of the average as well as SGC height is visible for Ag_{83}.

Aside from the mentioned problems, the similarities between simulated and experimental data is clearly visible. Thus it is highly conceivable that a sudden height change indeed takes place for Ag_{87}. This experimental result leads to further questions. First, there seems to be no obvious reason that this particular size should show such a peculiar behavior. Second, the magnitude cannot be explained easily, either. The following section will deal with these questions in more detail.

2.2.5 Discussion

There have been many observations of clusters in recent years that indicate a shape shift at a certain point if the number of atoms is reduced or increased only slightly. However, this information has either been gathered from clusters in free beam or it stems from a purely theoretical approach. *F. Furche et al.* [177] for example observed a transition from a two dimensional to a three dimensional shape when the size of a gold clusters reaches about 12 atoms. Free beam experiments found similar results for gold [178]. Such a sudden shift in shape could translate to a height change on a surface. Our experiments, however, were unique in respect to a few key aspects:

1. The clusters consisted of silver instead of gold.
2. The clusters were soft landed on a C_{60}/Au(111) substrate. The presence of a surface was a key difference to all free beam experiments.
3. The clusters were quite big in size compared to previous experiments, ranging from Ag_{80} to Ag_{88}.

The experiments revealed that a sudden increase in cluster height occurs for Ag_{87} clusters. Clusters with slightly less atoms display a height of roughly 1.39 *nm*, while Ag_{87} and larger clusters have a height of about 1.47 *nm* on the C_{60} film. Thus a height change of about 0.08 *nm* is detectable. Before discussing the magnitude of this effect, the cluster size at the position of the height change will be analyzed. The size hints to a geometric effect. With 87 atoms an arrangement is possible where each shell atom has the same distance to a core atom. The structure would encompass a total of 6 shells [179]. As shown in figure 1.3 on page 6, surface independent Xe_{87} shows an extraordinary stability possibly due to this geometric effect. The same argument might also apply to silver. It is conceivable that clusters smaller than Ag_{87} are prolate due to the interaction with the C_{60} surface. If, however, Ag_{87} has a greater stability than its neighbors, a spherical shape could be favorable to an oblated one. This would alter the bond lengths between atoms and thus allow a height change smaller than a single monolayer.

As described in section 1.1.1.1 on page 4, some metal clusters, among them silver, are expected to form partly of fully formed icosahedra. With 87 atoms the cluster size in question is not close to both neighboring geometrically magic cluster sizes, Ag_{55} and Ag_{147}. Both differ by just a single outer layer, and intermediate sizes have partly formed outer shells.

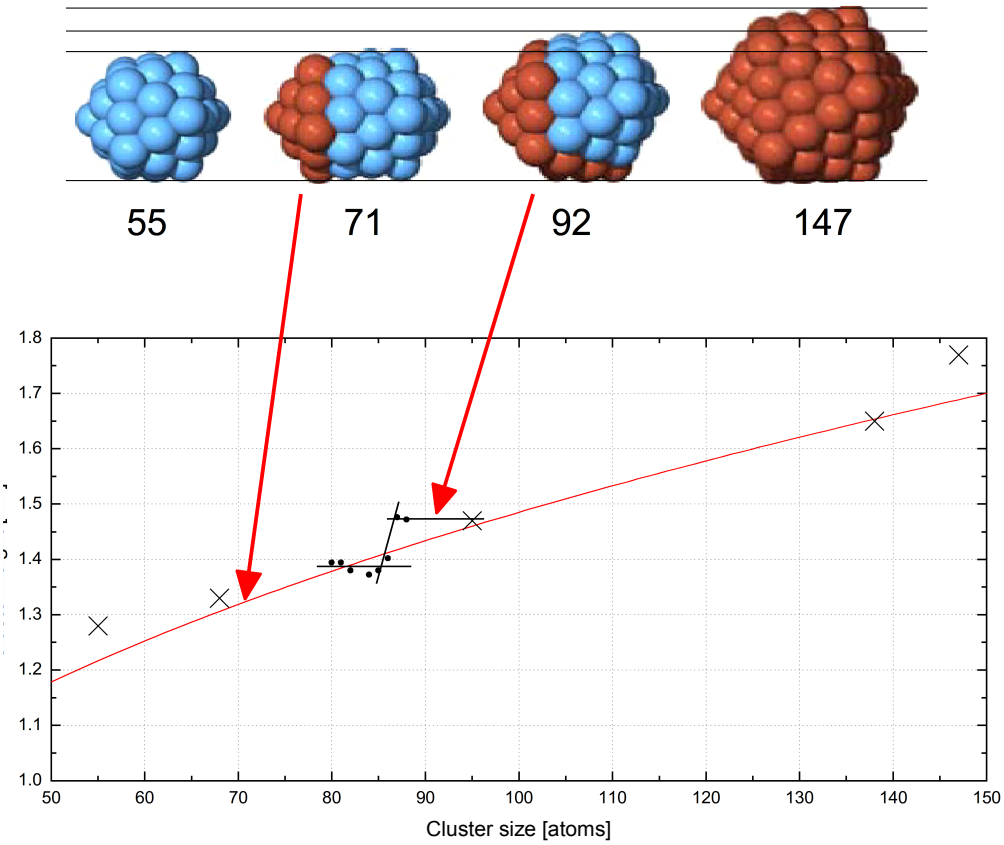

Figure 2.49: Possible explanation for the observed height change measured in STM between Ag_{86} and Ag_{87}. The graph shows multiple measured cluster sizes as black dots as well as the theoretical heights of spherical clusters as a red curve. Measurements prior to this experiments are marked as crosses. The height transition is emphasized by short black lines. Above are theoretical models of four magical cluster sizes [180] of which two, Na_{71} and Na_{92}, are of special relevance in this context. Their respective position in the graph is marked with red arrows.

Figure 2.49 shows free Na_{55} and Na_{147} clusters with fully formed shells [180]. Intermediate sizes like Na_{71} consist of a Na_{55} cluster with an additional cap at one side. This is true for free clusters but if a surface is added additional effects occur. Then this arrangement encloses the possibility of basically showing the same height as Ag_{55}. This is not the case if the amount of atoms is increased further. For Na_{92} an additional cap is formed, which makes it impossible for the cluster to hide its size from an STM measurement by means of orientation. If silver behaves analogous to sodium, the mentioned arrangement of atoms could explain the observed height change between Ag_{80} and Ag_{88} at least partly.

The experiment shows no continuous transition but a sudden one. The data indicates that only a few cluster sizes are involved in the actual height change. Obviously a massive atomic rearrangement occurs around Ag_{87}. With 0.08 *nm* height change, the effect is about a factor 3 smaller than the size of single atoms. There are, however, different explanations to account for this discrepancy. It is assumed that clusters can be stable in different orientations on C_{60}, which may lead to deviating measured heights. This phenomenon is only countered by a large enough number of scanned clusters, which would then average out these effects. If the height

change only takes effect in one of the possible orientations, the difference would seem smaller due to a mixing of the heights. However, this would result in the broadening of the distributions, which was not observed. More likely is a tilting of the cluster relative to the surface. This way the height change effect would be effectively reduced.

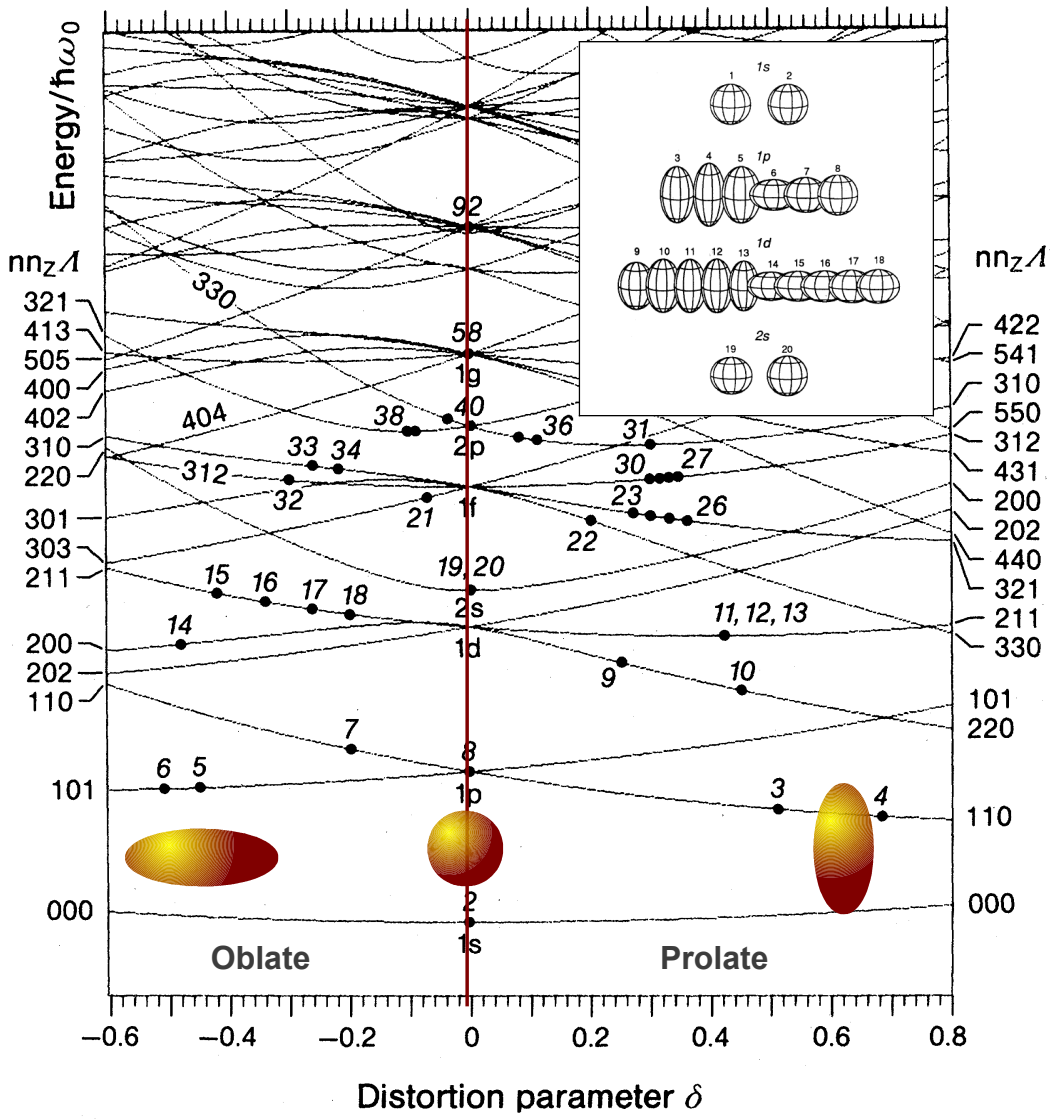

Figure 2.50: Nilsson diagram of the cluster energy as a function of its distortion parameter δ. With $\delta<0$ clusters are oblate, with $\delta>0$ they are prolate (after [181]). In the upper right is a depiction of several oblated and prolated clusters following the Nilsson model [26].

Changes in shapes and thus deviating measured heights can also be explained by electronic effects. The *Jahn-Teller* theorem [182] suggests that spherical shapes for free clusters are only favorable if closed electronic shells are possible (see section 1.1.1.2 on page 6). Figure 2.50 illustrates this effect. The electronically magic cluster size Ag_{92} [25] could consequently

influence the resulting height. It is conceivable that the cluster tends to change from an oblate to a spherical shape somewhere between Ag_{71} and Ag_{92} due to electronic effects.

In addition to that electronic effects can have an influence on the tunneling conditions. With a changing density of states, the probability of tunneling electrons is altered. Thus the tunneling current changes, which causes the tip to approach to or retract from the cluster. Consequently the height measurement is altered without there being any geometric change.

Finally unexpected deviations in the measured cluster heights must be discussed. In particular the significantly reduced height around Ag_{83} is peculiar. There could be indeed a single smaller cluster size present surrounded by larger ones. This is, however, unlikely for the following reason: If a single size would indeed display a reduced height, the limited resolution of the cluster machine would force an intermixing of that particular size. Because the neighbors are indiscriminately larger, the mean curve should not display the same prominent dip, which it does. Additionally the difference between SGC and mean curve does not change significantly for sizes below Ag_{86} as visible in figure 2.47. Thus an error of some kind is the more likely explanation.

Another aspect of some interest might be the RMS (root mean square) value of the distribution. It provides information on the broadening of the curve. A mix of cluster sizes with different associated average heights would increase the RMS value. This exact phenomenon could be observed in the simulation.

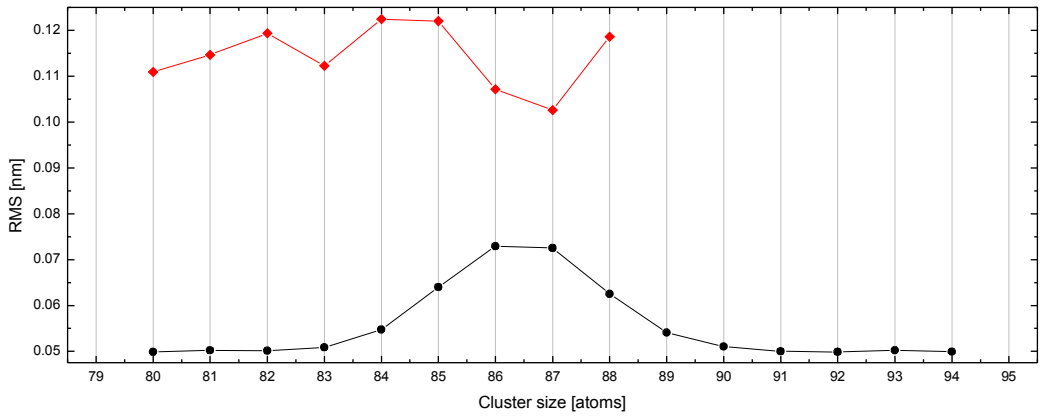

Figure 2.51: Evolution of the RMS value of simulated (black dots) and measured (red rhombuses) cluster sizes with a height change from 1.37 *nm* to 1.48 *nm* between Ag_{86} and Ag_{87}. For the simulated data the cluster frequency for each cluster size was 100,000 *counts*. The broadening of the curves due to intermixed cluster sizes is clearly visible, especially near the transition point at Ag_{86}/Ag_{87}. The measured data, however, shows an inconclusive evolution.

Graph 2.51 shows the simulated RMS value as black dots connected with a black line. The respective histograms are shown in figure 2.45. Around Ag_{86} and Ag_{87} a significant increase is visible. The experimental data, depicted as red rhombuses, however, shows an inconclusive

picture. First, all height distributions are broadened compared to the simulation. This is not surprising because external errors are excluded in the simulation. Second, the evolution of the experimental curve follows no clear pattern. As mentioned before, multiple changes in tip state had been detected. With sufficient statistics, constantly changing measured heights can be averaged out so that the effect is diminished with increasing cluster count. The RMS value on the other hand is heavily affected by this. Thus this particular evolution is likely to be error related.

2.3 STS of Ag_{55} on 1 ML C_{60}/Au(111)

In our case the standard method of investigating a sample system like Ag_n/C_{60}/Au(111), which can be considered moderate in terms of cluster-surface interaction, is usually STM. However, this device also allows the use of STS (Scanning Tunneling Spectroscopy) as a method of gathering information on the cluster's electronic structure. A description of the sample system can be found in section 1.5.5.1 on page 47 and section 1.5.5.2 on page 48 while the evaluation method is described in section 1.5.6.3 on page 51.

Ag_n clusters were deposited under soft landing conditions (see section 1.5.3 on page 42) on an Au(111) surface functionalized with a single layered C_{60} film and an average kinetic energy per cluster of 3 *eV*. A special focus lay on small clusters, in this case Ag_{55}, Ag_{88} and Ag_{138}, in order to expand spectroscopy data already gathered for Ag_{309} and Ag_{923}. STS was performed on single clusters while simultaneously taking C_{60} spectra as reference. In contrast to most of the other experiments, the sample was cooled to 5 *K*, which was achieved by filling the cryostat of the analysis chamber with liquid helium. This was done in order to reduce thermal drift, piezo non-linearity and creep [183], which is always mandatory in the case of an STS measurement.

2.3.1 Experimental Results

Prior experiments were conducted by *S. Duffe* [123], while the later results can also be found in the diploma work of *N. Miroslawski* [154]. During the course of the experiment about 150 clusters have been investigated using STS with about 20 spectra each. Every cluster measurement was preceded and followed by around 10 C_{60} spectra. The exact number varied and depended on the cluster as well as the substrate quality in the specific area. Note that it was very important to measure spectra close to the center of the cluster. The fact that only the outer most atoms of the tunneling tip contribute to the measured current enables such a precision. However, a number of effects complicate the measurement and hinder reproducibility. Even at 5 *K* drift is not completely eliminated so that stopping the scanning in order to perform the measurements, results in slight mismatches between the real surface and shown STM image. Thus, the center of a cluster may not have been identified correctly. In standard STM images (from 100×100 *nm* to 200×200 *nm*) this effect is only slightly noticeable, which is not the case if it is scaled down to about 5×5 *nm*.

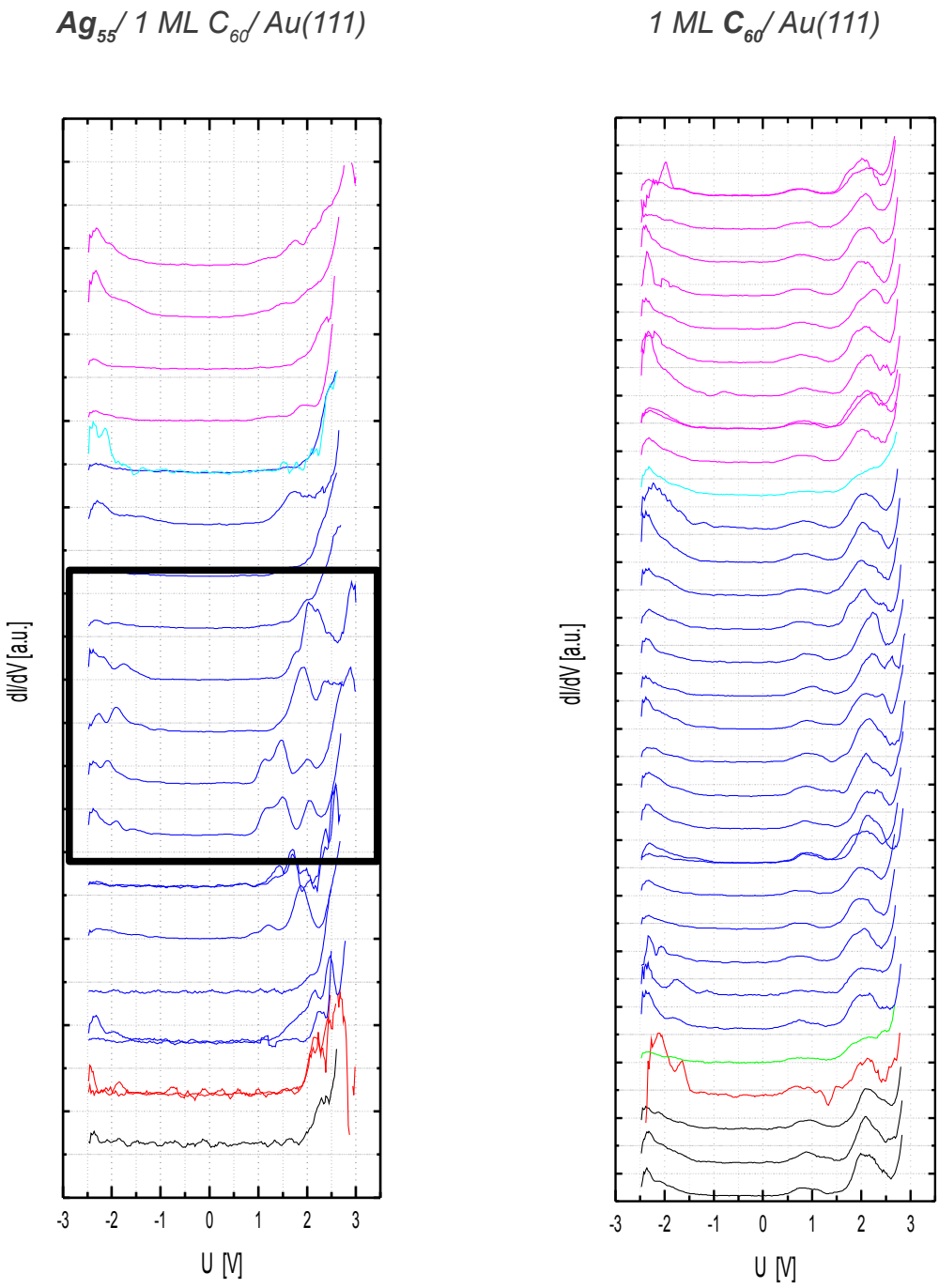

Figure 2.52: STS spectra of individual, different Ag_{55} clusters (left) together with C_{60} spectra measured before and after. Ag_{55} clusters that are depicted in the same color were measured with the same tip state, as the respective C_{60} spectra suggest. The Ag_{55} spectra in the black box were extracted as useful results with the analysis method described in the text and were used for further evaluations.

The tip's shape has an even greater influence on the appearance of the imaged cluster, which has been discussed earlier regarding the measured lateral size of a cluster compared to the real one. Additionally clusters can be destroyed, reshaped or collected by the tip. However, all these effects can be either detected in the STM image or STS spectra. Thus an extraction of the useful results is mandatory, which requires a careful and critical analysis of the data. Eventually the spectra were sorted, averaged and plotted in a waterfall diagram together with their respective C_{60} spectra for comparison.

Note that figure 2.52 only represents a fraction of the measured data. Both Ag_{88} and Ag_{138} did not deliver useful spectra and were thus discarded (data shown in appendix on page 156). For each Ag_{55} spectrum there is a preceding and succeeding C_{60} spectrum, which has been used as a reference. In both figures the color coding has been used to bundle spectra measured with an identical tip state. The latter has been identified by monitoring the C_{60} spectra. The disappearance of certain peaks or the shift of the entire spectrum in one direction indicates a change in tip state. Note that for each presented spectrum several sub-spectra have been averaged. If a single sub-spectrum deviated noticeably from the rest it was discarded. However, if this was the case for several sub-spectra, they were bundled and plotted together with the remaining spectra, which showed a higher frequency. While this was not often the case, the appearance of such a phenomenon shows that even during a measurement cluster spectra can change so that a very careful evaluation is mandatory.

As the blue spectra in figure 2.52 indicate, several clusters have been analyzed with a very similar tip state. Note that the cluster spectra non the less deviate. This may be due to the different orientations of individual clusters on the substrate. Furthermore, as mentioned before, the center of a cluster was not necessarily found in each case. However, the 4 spectra inside the black rectangle display a very similar peak structure. Noticeable are two peaks slightly above $+2\ eV$ and slightly below $-2\ eV$ in all of the mentioned spectra. There is also another superimposed peak in two of the spectra around $1.5\ eV$. Two peaks with similar distance from the Fermi level, one above and one below, have been observed before in the case of Ag_{923} and Ag_{309} and lead to the conclusion of an energy gap emergent from the orbitals or band structure of the metal. The Ag_{55} spectra, which were measured in this experiment, fit the previous observations. The spectra for Ag_{55}, Ag_{309} and Ag_{923} are shown in figures 2.53 to 2.55. The measurement process, as described above, is depicted in figure 2.56.

The energetic distance between the peaks in figures 2.53 to 2.55 increases with a reduced cluster size. The peak at the negative energy axis might be interpreted as LUMO-orbital (*lowest unoccupied molecule orbital*) and the peak at the positive energy axis as HOMO-orbital (*highest occupied molecule orbital*). While this is a useful first approximation, the interpretation of the STS spectra is most probably not that simple as will be discussed in more detail in the next section.

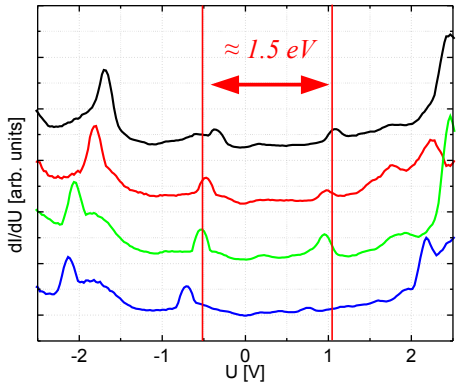

Figure 2.53: STS spectra of Ag_{923}/1 ML C_{60}/ HOPG [123].

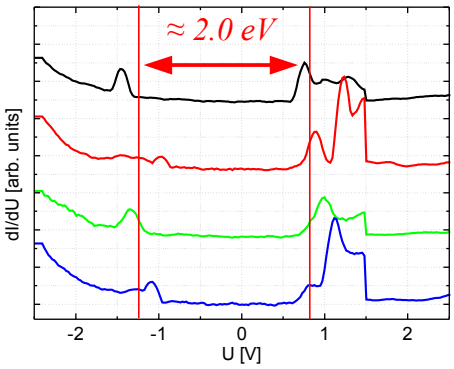

Figure 2.54: STS spectra of Ag_{309}/ 2 ML C_{60}/ HOPG [123].

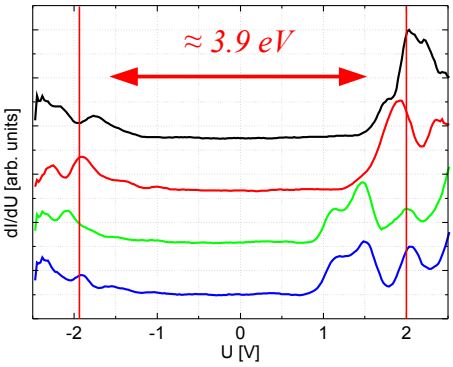

Figure 2.55: STS spectra of Ag_{55}/ 1 ML C_{60}/ Au(111).

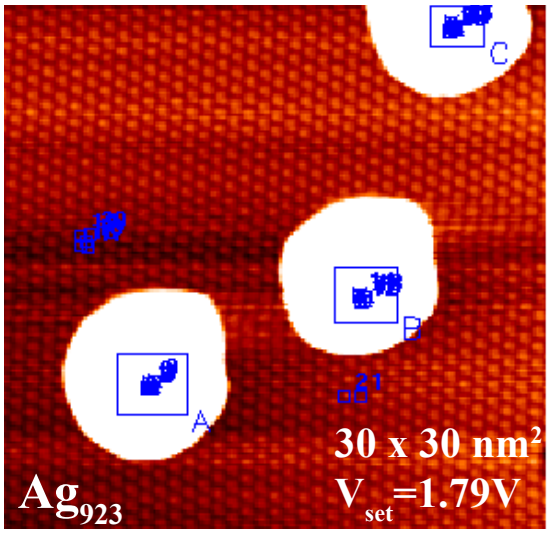

Figure 2.56: Example image of an STS measurement. Ag_{923} clusters are visible on a C_{60} surface. Positions of the measured spectra are marked blue.

2.3.2 Discussion

The electronic structure of small metal clusters can be described by discrete orbitals. At a certain size the orbitals must be replaced by continuous bands. Adding a single atom has tremendous influence on small clusters, but the effect becomes less extreme as soon as the compound gets bigger. So it is conceivable that between Ag_{55} and Ag_{923} the changes in electronic structures are quite noticeable.

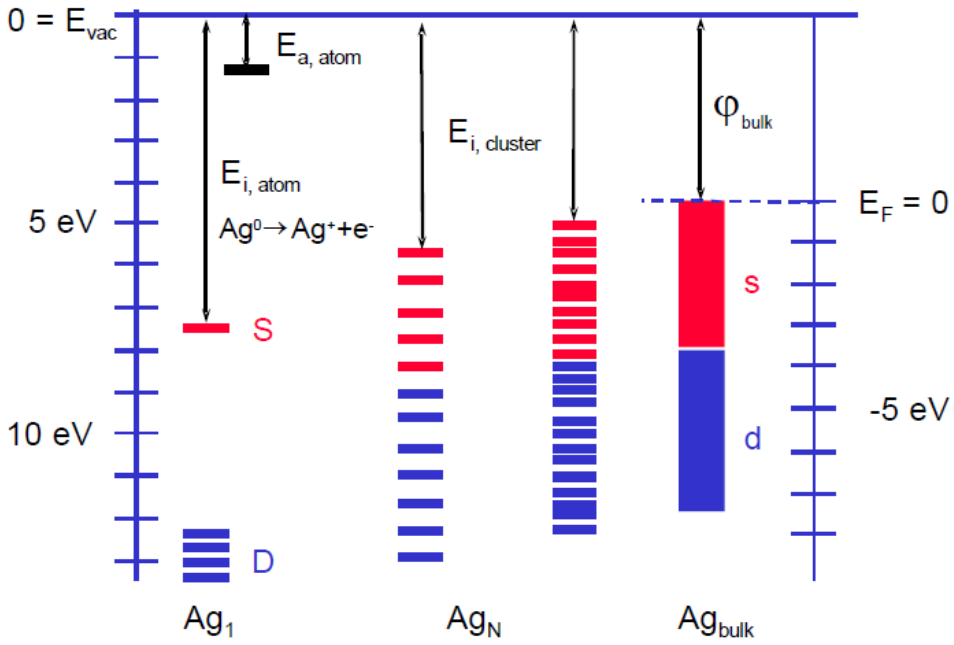

Figure 2.57: A single Ag atom (left) usually has one electron in the s-band (red) and 4 pairs in the d-band (blue). With an increasing number of atoms new orbitals are added while the energy gaps are reduced (middle). With enough atoms the orbitals become so close that they form a continuous band structure (right).

Figure 2.57 illustrates the transition of an atom with discrete orbitals to a metal with band structure. Single orbitals increase their proximity to each other until the gaps are closed. The interpretation of the peak structure in figures 2.53 to 2.55 as an energy gap that increases with decreasing cluster size is thus justified. Further conclusions from the given data are, however, problematic. Of importance is the fact that the earlier experiments used HOPG as an underlayment for the C_{60} film while Au(111) was used in the recent experiment. It is not clear how this affects the measured electronic structure in detail. Furthermore the experiments are normally strongly influenced by the measuring probe, which is the tunneling tip in this case. As mentioned in several other chapters, the tip has an unknown individual shape, which greatly influences its local density of states. This affects of course the tunneling probability of an electron, which in turn alters the electrical current and thus the measured spectrum. Just like the tip, the cluster has a spatially deviating density of states. With the exact position of the tip as well as the number of outer most atoms involved in the tunneling process unknown, a precise positioning cannot be guarantied. In consequence it can only be assumed that a slightly altered density of states close to the top of the cluster has been measured.

Theoretical models by *De Menech et al.* [184] indicate that interpreting the gathered spectra as distributions of densities of states is only partly justified. It seems that some states do not contribute to the conductance so that STS spectra show a reduced number of peaks. This effect of hidden states also strongly depends on the relative position of tip and cluster.

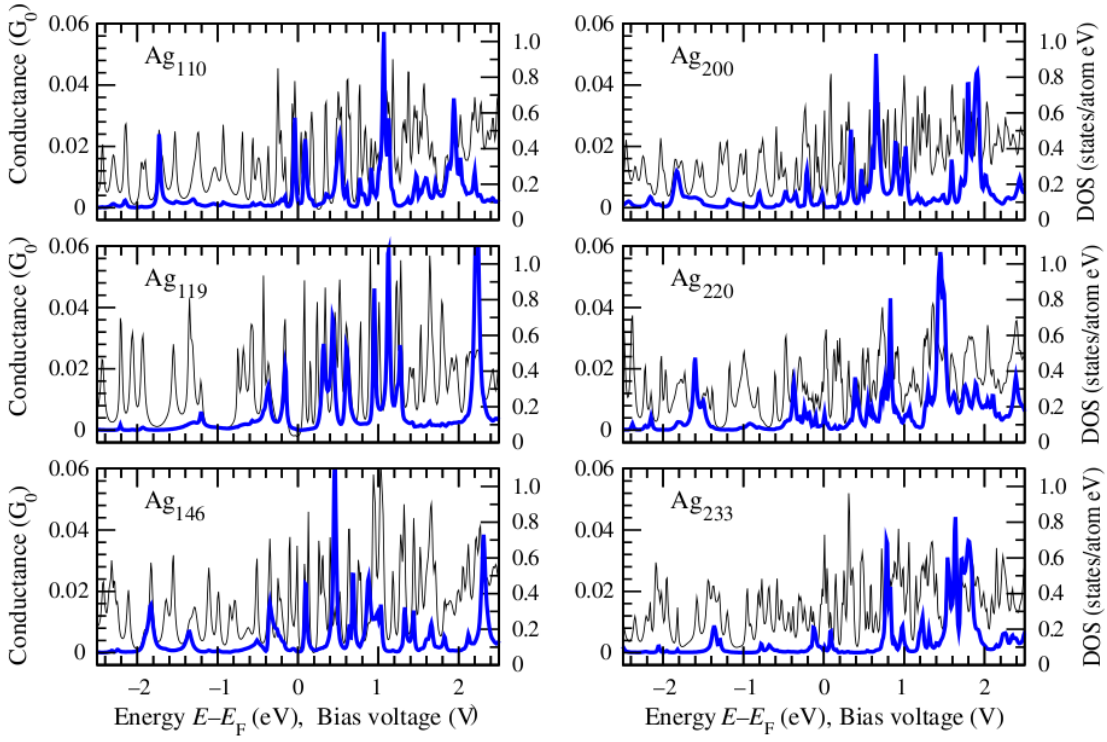

Figure 2.58: Simulated STS conductance of silver clusters of different sizes on a graphite surface (thick blue lines, left axis). Thin black lines (right axis) show the according simulation of the density of states. $G_0=2e^2/h$ is the quantum unit of conductance. In STS many peaks are missing while most remaining are reduced and only few are increased [184].

As illustrated in figure 2.58 clusters with varying sizes show a highly structured density of states. While STS is able to reproduce some of the peaks, most are missing completely with a reduction of the majority of the remaining ones. In some cases peaks can also be increased, but this is a rare exception. Note that calculations were also conducted using a flat electrode instead of a sharp STM tip. The results were noticeably closer to the simulated density of states. However, creating such a probe would be highly problematic in an experimental sense.

Depending on the distance between cluster and surface, a complicated shifting of individual peaks has also been observed. Note that the experiments described in this chapter use a C_{60} surface with an Au(111) underlayment. It is possible that the latter still interacts with a cluster while different orientations of clusters on C_{60} alter the distance to the Au(111) underlayment.

These obstacles illustrate that an improvement of the experimental setup is mandatory. Increasing the quality of tip and STM precision would be an obvious task. Another approach that addresses the problem of tip positioning while simultaneously providing additional data, would be the complete mapping of a cluster. In combination with simulations, this might enable the quantitative identification of and consequent correction for many of the mentioned errors.

3 Experimental Results for Strong Cluster-Surface Interaction

Strong cluster-surface interaction was investigated on three basic sample systems. In each case mass selected silver clusters were deposited on free Au(111).

The first sample was also functionalized with C_{60} giving an insight in the behavior of clusters on both an Au(111) and C_{60} surface. Several cluster sizes were deposited in a first attempt to test the usability of the new Movable Focus Lens. In the rim regions of the sample free Au(111) areas existed, and there Ag_{86} produced exploitable results for the investigation of silver on Au(111). Thus the average cluster height was measured before annealing the sample to 200 *K*, which resulted in the total decay of the clusters. In order to investigate intermediate annealing steps, three additional cluster sizes were deposited on free areas of the same sample, which resulted in the second sample system. In a third step a completely new Au(111) sample was prepared without a C_{60} film. 9 varying cluster sizes were deposited with different impact energies.

3.1 Ag_{86} on 1 ML C_{60} and Au(111)

First experiments focusing on Ag_{86} on C_{60}/Au(111) showed areas of free Au(111) at the rim regions of the sample. Despite this being a side effect of lower C_{60} coverage at the rim of the deposition spot, it gave a first insight in the behavior of silver clusters on a metal surface at 77 *K*.

Free Au(111) was first found on the sample system described in section 2.1.3 on page 61. Ag_{82}, Ag_{84}, Ag_{86} and Ag_{110} where measurable but the biggest ratio of free Au(111) compared to C_{60} was found in the case of Ag_{86}. Thus the following investigations will focus on this particular cluster size. The average energy per atom during impact was 3 *eV*, while the sample's temperature was kept at 77 *K* during and after deposition.

The first question concerning silver clusters on an Au(111) surface focused on their stability. At this point it was not clear if the clusters had decayed, scattered or coalesced in any way. It was known that clusters would keep shape and position when deposited onto C_{60}/Au(111) under the conditions mentioned above. Thus a comparison of cluster densities between clusters on C_{60}/Au(111) and bare Au(111) could deliver first information on the stability of silver clusters on an Au(111) surface at 77 *K*.

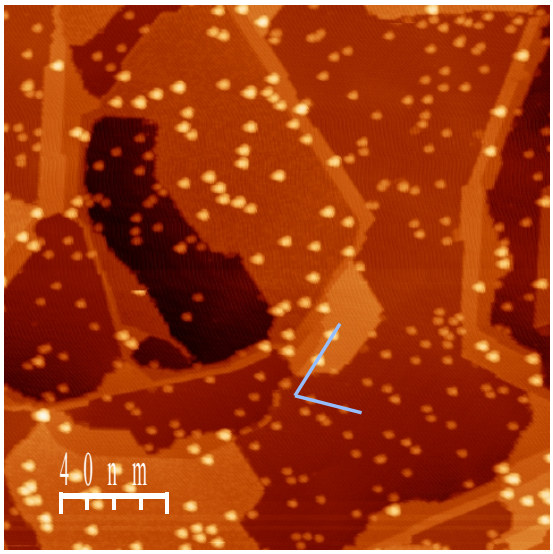

Figure 3.1: STM image of Ag_{86} on C_{60}/Au(111) and on bare Au(111) .

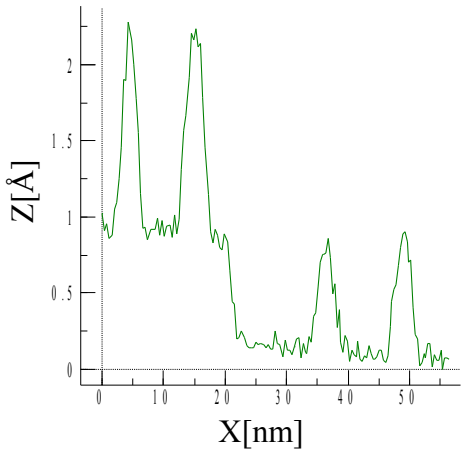

Figure 3.2: Line profile marked in figure 3.1. Deviating cluster heights are visible for different layers.

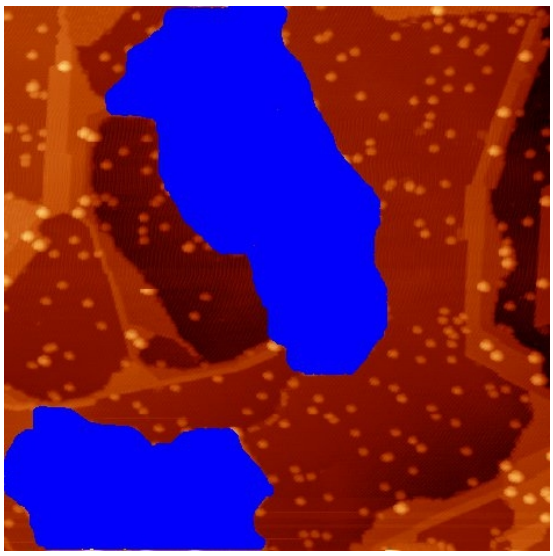

Figure 3.3: Cohesive areas of C_{60}/Au(111) marked in blue.

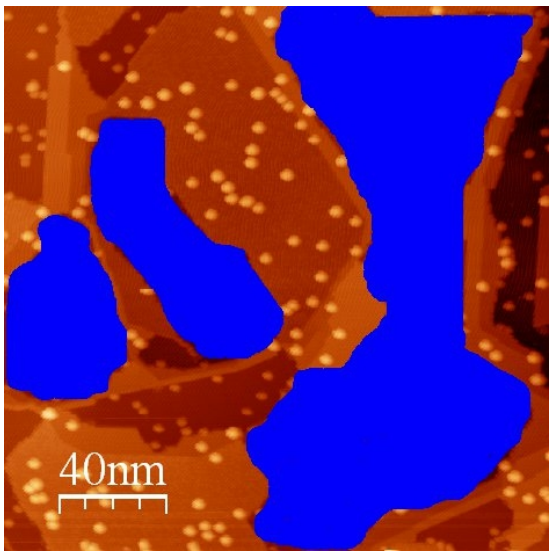

Figure 3.4: Cohesive areas of free Au(111) marked in blue.

Figure 3.1 shows an STM image of both Ag_{86} on C_{60}/Au(111) and Ag_{86} on bare Au(111). The line profile in figure 3.2 illustrates that indeed different cluster heights could be observed depending on the specific layer. In order to estimate the ratio of covered and free Au(111), the respective areas have been marked blue and the total pixel content was counted using *gimp 2.6* [185,186]. With the total pixel content of the whole image known, the respective ratios could be computed. This was done by *N. Miroslawski* and more details concerning this topic can be found in [154]. Figure 3.3 shows cohesive C_{60} areas marked blue while figure 3.4 does the same for bare Au(111). Figures 3.1, 3.3 and 3.4 show the same basic image. A counting of the clusters on each of the areas revealed the following numbers:

Ag_{86} on Au(111): $79.1/(100\times100\ nm^2) \pm 10\ \%$
Ag_{86} on C_{60}/Au(111): $75.1/(100\times100\ nm^2) \pm 11\ \%$

Both values are similar with respect to the given error. This shows that the number of clusters on bare Au(111) was not altered by the deposition process or later effects. Thus a scattering, coalescence or decay of the clusters can be excluded.

However, the height difference between clusters on both substrates hints to a reshaping of Ag_{86} on bare Au(111) during or after deposition. The strong interaction between both metals would suggest the formation of clusters of only a few monolayers height. Strictly speaking the emerging structures would be better described as islands than as clusters. This distinction is, however, avoided at this point in order to show their relation to mass selected clusters.

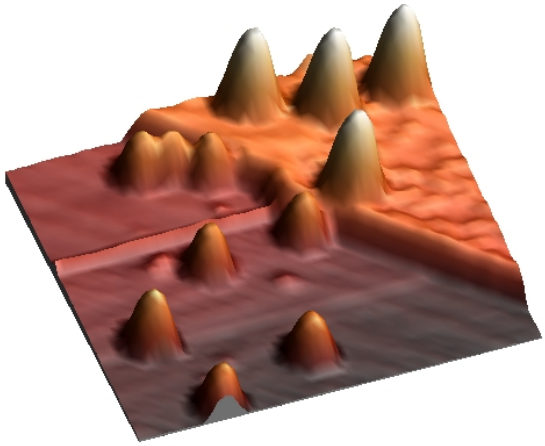

Figure 3.5: 3D illustration of Ag_{86} clusters on both 1 ML C_{60} and bare Au(111). Structures on Au(111) are distinctly smaller.

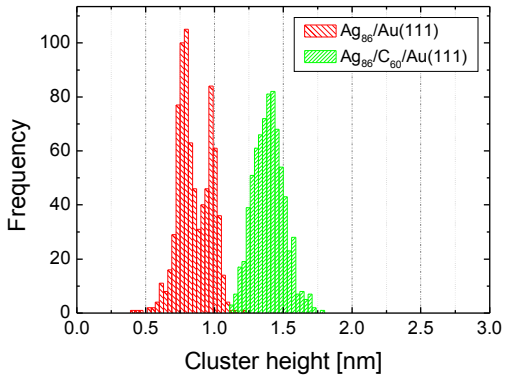

Figure 3.6: Histogram of Ag_{86} cluster heights on bare Au(111) (dashed red) and 1 ML C_{60}/Au(111) (densely dashed green).

In the 3D depiction of figure 3.5 the different substrates are clearly distinguishable. The C_{60} layer on the top right is about 1 *nm* elevated and displays a rougher surface than the bare Au(111) area, which covers the rest of the shown region. The height of both structures is also very different. While clusters on C_{60} are unaltered and thus have an average height of 1.39 *nm*, the structures on Au(111) display two heights of 0.8 *nm* and 1 *nm*. Obviously under the given circumstances at least two stable structures emerge. Because a reshaping always needs energy, it must have happened either by deposition or storage at 77 *K* afterward. At this point the data was, however, insufficient to draw further conclusions.

It is noteworthy that the STM images show no apparent broadening of the clusters on Au(111), despite them being lower with the same amount of atoms. In addition to that both the shape of clusters with and without a C_{60} underlayment cannot be visually distinguished.

This can be explained by the influence of the STM tip. As mentioned in section 1.2.3.1 on page 16, the appearance of the imaged structure strongly depends on the tip's shape.

3.1.1 Annealing Experiments

Cluster atoms always have the tendency to reach the energetically most favorable state, which is also most stable. However, this state is often not reached under certain conditions because thresholds like energy barriers prevent a further rearrangement of atoms. Thus the shape that emerges mainly depends on the initial usable energy at hand. The sample's temperature was kept at 77 *K* so that the equivalent thermal energy had a comparably low and constant value. This aspect will be discussed in more detail at a later point.

Because temperature must be understood as a statistical process, even at very low temperatures, tremendous changes can occur given the proper time frame. Most processes, however, become increasingly unlikely when 0 *K* is approached. But as later analyses will show, even at 77 *K* alterations to silver clusters on bare Au(111) happen. A more extreme reshaping of the clusters is observed when the thermal energy is increased. This annealing has been done by exposing the sample to 130 *K*, 160 *K*, 170 *K* and 200 *K* for 1 *h* in each case. At this point the needed temperatures and time for anything of interest to happen was only estimated.

After annealing the sample for 1 *h* at 130 *K* no visible changes to either the clusters on C_{60}/Au(111) or the clusters on bare Au(111) could be observed in the STM images. However, the height distribution of clusters on Au(111) changed noticeably.

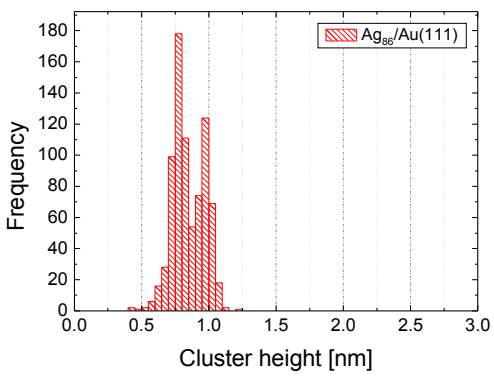

Figure 3.7: Height distribution of Ag_{86}/Au(111) at 77 *K*.

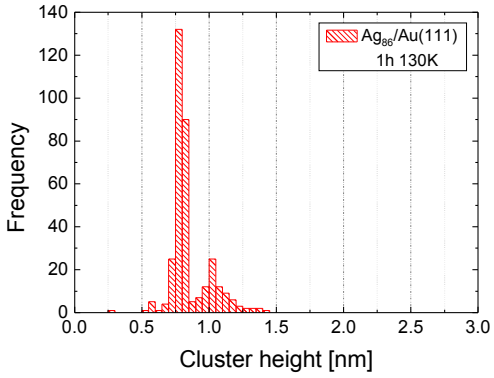

Figure **3.8:** Height distribution of Ag_{86}/Au(111) after annealing the sample 1 *h* at 130 *K*.

While both peaks in figure 3.7 differ only slightly in height, the second peak in figure 3.8 associated with larger cluster heights is noticeably smaller. In addition to that the distribution of figure 3.8 seems narrower, which hints to a rearrangement of intermediate structures to a single shape with a height of 0.8 *nm*. The same can be said for clusters associated with the second height peak. During annealing the additional energy enabled them to reshape into a structure with the lower measured height of 0.8 *nm*. Thus clusters tend to reduce their height

during annealing, which means that in consequence they are broadening if no atoms are lost. This is a first experimental hint to a flattening of the clusters.

After additional annealing at 160 *K* for 1 *h* visible changes in the STM images occurred. Now the forming islands seemed to be broadened enough to be imaged by the STM tip, which was itself too broad for a detailed depiction in previous measurements.

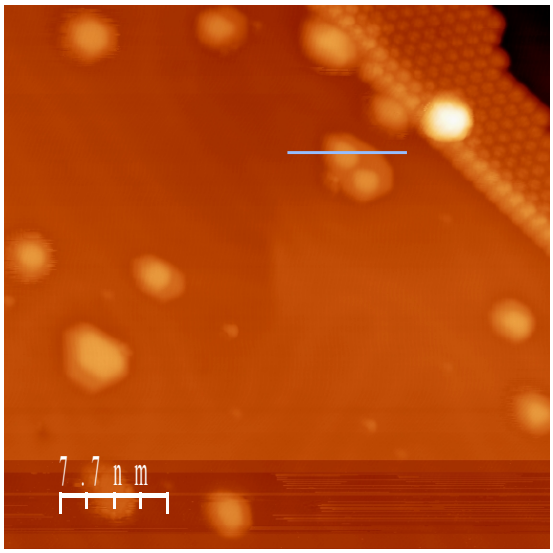

Figure 3.9: STM image of Ag_{86} on Au(111) after annealing 1h at 130K and 1h at 160K.

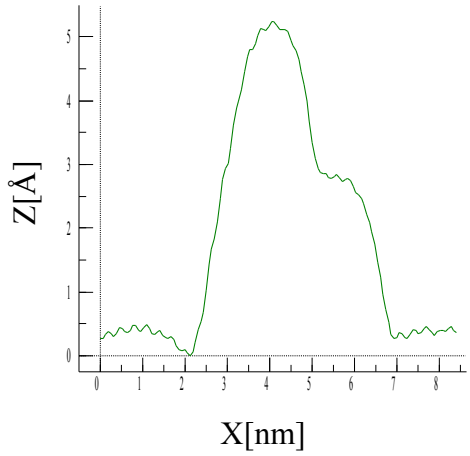

Figure 3.10: Line profile marked in figure 3.9. The line profile shows a partly flattened Ag_{86} cluster.

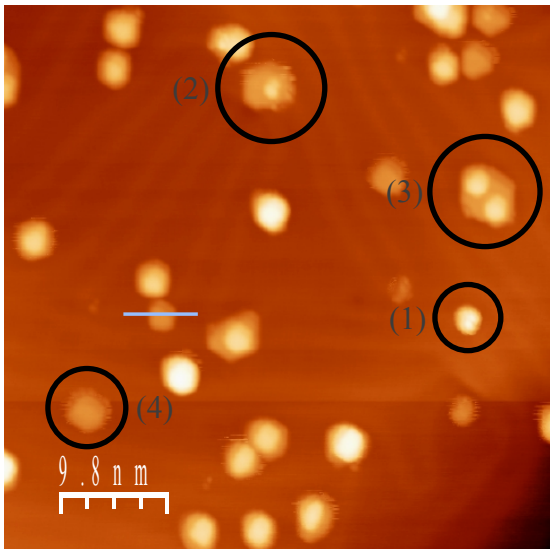

Figure 3.11: STM image of Ag_{86} on Au(111) after annealing 1 *h* at 130 *K* and 1 *h* at 160 *K*. Herringbone reconstruction is visible as thin brighter lines.

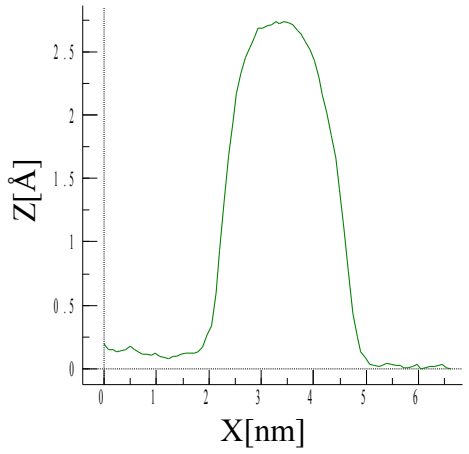

Figure 3.12: Line profile marked in figure 3.11: A fully flattened cluster with the height of a single silver monolayer.

Figures 3.9 and 3.11 show STM images after annealing them for 1 *h* at 130 *K* and 160 *K*. Note that in the STM image of figure 3.9 the edge of a C_{60} layer is visible in the upper right part. Four types of clusters transitioning into flattened structures can be seen (see number in figure 3.11):

1. Clusters are seemingly unaltered and resembled the ones in previous measurements. With several monolayers in height and an overall cone-like shape imaged by STM, the lateral structure is still hidden from the observer.
2. The next type of clusters has not flattened completely but to an extent where additional monolayers of silver remain on top of the whole structure. They can be described as having a bottom most Ag layer that is much broader than the remaining layers on top of that.
3. In other cases two or more clusters close to each other merge so that their bottom most layers became one. However, the remaining top layers stay separated and create the structure marked with a line profile in figure 3.9.
4. A final type of cluster can be observed that forms 1 ML structures on Au(111). As marked by the line profile in figure 3.11 and shown in figure 3.12, it has a height of roughly 0.26 *nm*, which resembles a single silver monolayer (0.236 *nm*).

As indicated by the observation above, visible rearrangements occurred when the sample was exposed to 160 *K* for 1 *h*. The respective energy content can help to determine the threshold of the energy barrier that prevents reshaping of the cluster at lower temperatures. This will be done at a later point.

In a successive step the sample was annealed an additional 1 *h* at 170 *K*. The behavior of the clusters followed the previously observed trend: They flattened further and less substructures could be seen. In addition to that certain 1 ML islands experienced a visibly greater broadening than previously observed. However, detailed analyses showed that most of the clusters that are reduced to 1 ML behave in accordance to the number of atoms they consist of.

Because the width of a structure measured with STM normally cannot be used for a detailed analysis due to the broadening of the the tip, the desired information is usually lost. However, the area of any flat region can be regarded as being correctly imaged. Thus as soon as a facet forms, the lateral information of the respective island can be extracted. Furthermore a theoretical approach for getting the expected size of an island can be used. Both methods will be entertained in the following paragraphs and the results compared afterwards.

Theoretically a single silver monolayer will arrange its atoms in an hexagonal close packed lattice. Thus the island area, consisting of 86 silver atoms, will be as large as multiples of a single unit cell.

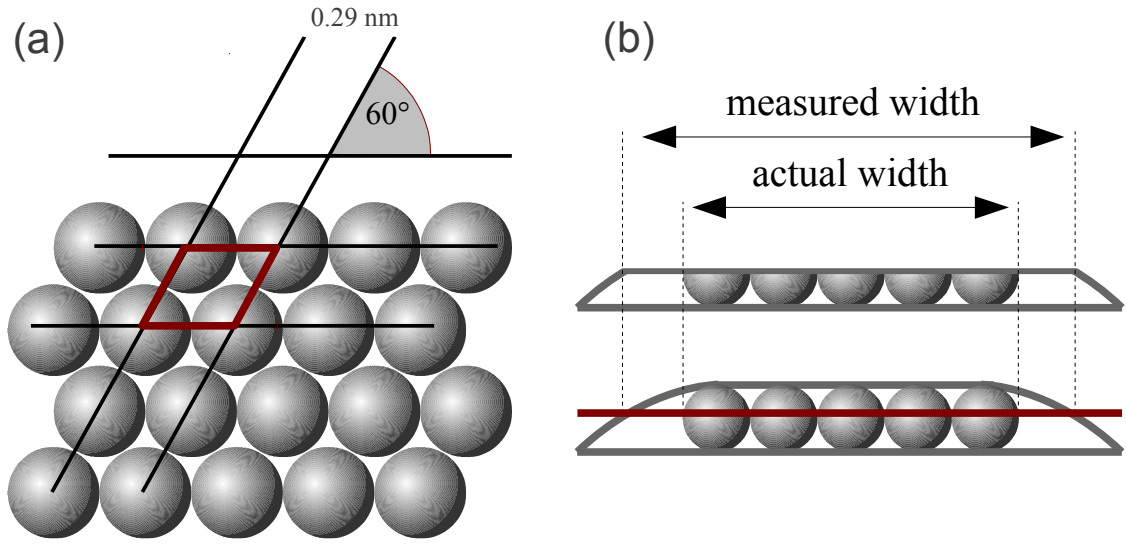

Figure 3.13: Schematic depiction of a silver monolayer (a). The total covered area is equal to the summed area of all unit cells. One unit cell is depicted as a red parallelogram. Deviation of measured width from actual width of the measured area due to the broadening of structures in the STM measurement process (b). For evaluation the surface is digitally cut in half as the red line indicates.

As shown in figure 3.13, the needed unit cell is 2-dimensional and has a trapezoid shape. With a covalent radius of 145 *pm* [122] the length of all sides of the parallelogram is 0.29 *nm*. Thus the area can be computed the following way if the number of 86 unit cells is taken into account:

$$A = 86 \cdot (0.29\,nm)^2 \cdot \sin(60^o) \approx 6.26\,nm^2 \qquad (3.1)$$

Experimental information could be extracted from the images at hand with the help of the *Cluster Evaluation Software* (CES) mentioned in section 1.4.3 on page 34. The software was able to find coherent areas on the sample and to associate them with the respective area in nm^2. The mentioned islands qualify as such. The rough position of any structure has to be given in advance by simply clicking on the object of interest. Analogous to cluster height evaluations a histogram can be created, which contains the desired island areas. So it was not only possible to identify the island area but also the overall size distribution.

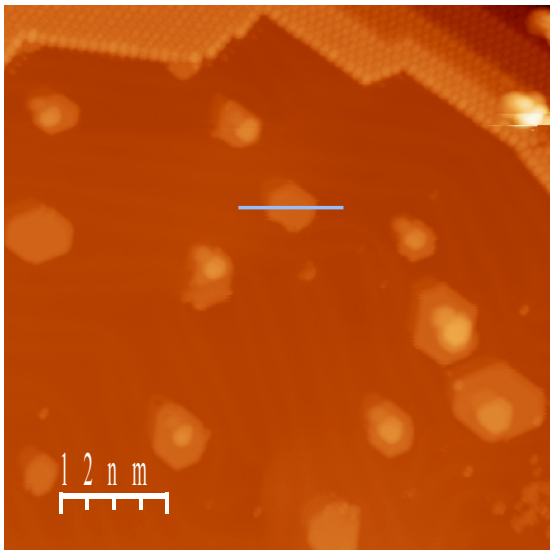

Figure 3.14: STM image of Ag_{86} on Au(111) after annealing at 130 *K*, 160 *K* and 170 *K* for 1 *h*, respectively.

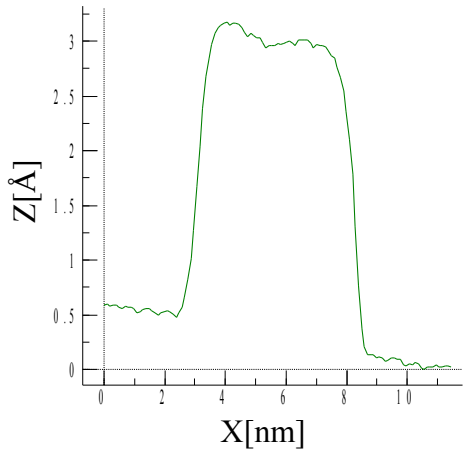

Figure 3.15: Line profile marked in figure 3.14. The line profile shows one or several coalesced and fully flattened Ag_{86} cluster.

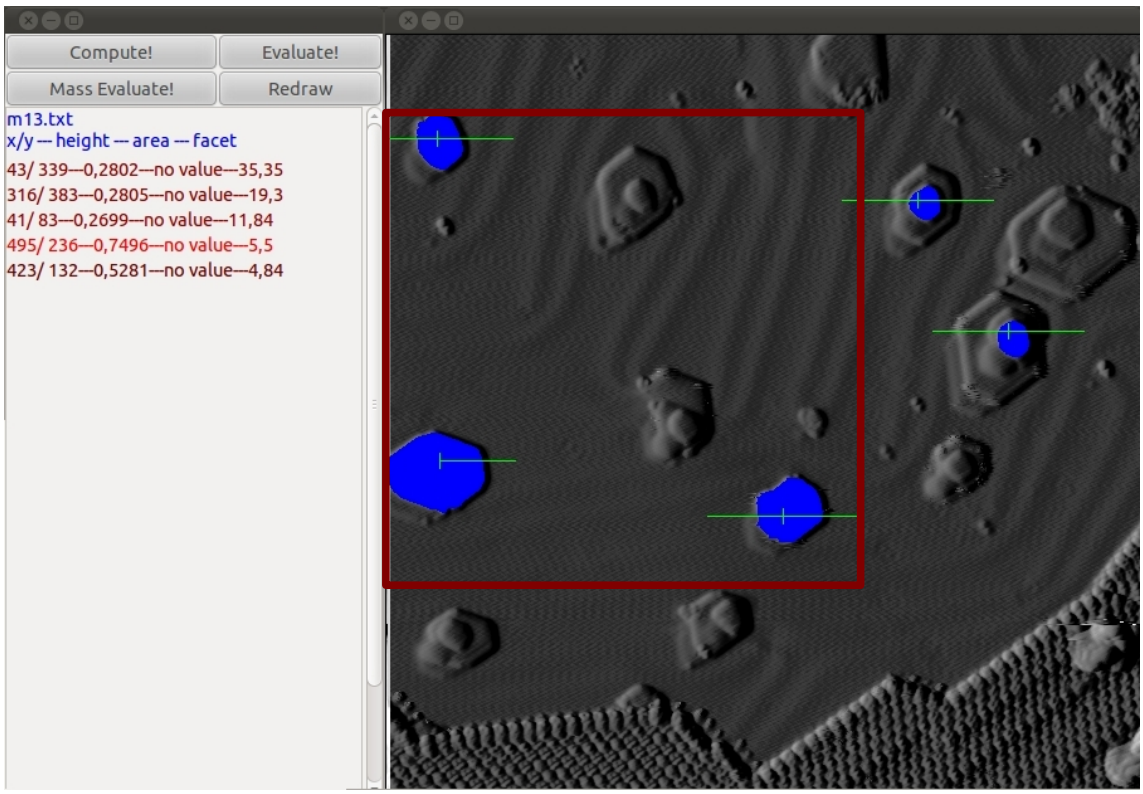

Figure 3.16: Example of an CES image used for evaluation. The height information is presented as a derivation along the scanning lines (left to right) of the original data and depicted in gray scale. Identified facet areas are marked in blue color. The larger three areas represent 1 ML islands used for evaluation, the smaller two that are outside the red box are examples of a possible evaluation of 2^{nd} ML clusters. The left window shows certain values of the identified clusters.

Several islands that formed out of former Ag_{86} clusters were evaluated. As shown in figure 3.16 not only 1 ML islands can be found but also larger structures. However, for the following evaluations only the 1 ML islands are used. To estimate the area of a particular facet, all pixels that are connected to each other and are higher than half the absolute height of the island are counted. Figuratively speaking the islands are cut in half horizontally; the resulting surface is then used to calculate the facet size. This was done because every island is not perfectly level so that adjustments like that are necessary. Of course this method may have produced errors, especially when the rim area of the islands is large compared to the rest of the facet. However, the resulting values can be considered sufficient to clarify if clusters coalesced or lost material during the annealing process.

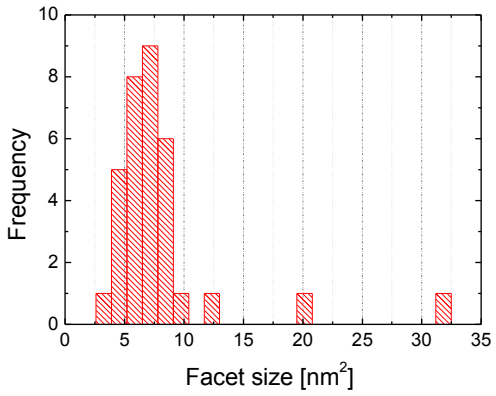

Figure 3.17: Size distribution of facets of 1 ML silver islands taken from after annealing Ag_{86} clusters on Au(111) at 160 *K* and 170 *K*.

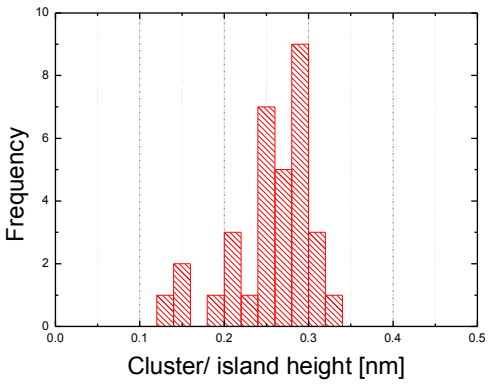

Figure 3.18: Height distribution of the same clusters/ islands shown in figure 3.17.

Figure 3.17 shows a histogram of the measured facet sizes. Most of them amass around 7 nm^2. Due to the limited frequency available, it is useful to exclude the facet sizes 20 nm^2 and 32 nm^2 that were obviously unusually large. For the rest, a mean value of 6.79± 0.32 nm^2 is identified. A direct comparison with the theoretically acquired value of 6.26 nm^2 shows that the measured one is larger than expected. However, given the nature of the measurement a perfect match cannot be expected. Note that the method of evaluation tends to produce larger areas than realistically exists as figure 3.13 (b) demonstrates. Due to the broadening of the tunneling tip, the islands are not sharply separated from the underlying surface. While it is theoretically possible to identify the beginning of the slope at the rim produced by the measurement process, it is compromised by practical issues as already described above. However, it is possible to estimate the error produced by that method with the following approach: The slope of the imaged island at the rim regions produced by the tip is replaced by a straight line with an estimated angle α=70° relative to the surface. Furthermore the island is estimated to be perfectly circular, which would result in a radius of 1.41 *nm*. For the following analysis A_{diff} is the difference between the total measured area A_{tot} and the computed theoretical area A_{theo}. The value *r* represents the radius of a perfectly circular cluster with 86 atoms while *d* is

the additional diameter of the added rim area. With half of the slope added to the radius, the area difference produced by the measurement method amounts to:

$$A_{diff} = \pi (r+d)^2 - A_{theo} = \pi \left(1.41\,nm + \frac{0.236\,nm}{2\tan\alpha} \right)^2 - 6.26\,nm^2 = 0.37\,nm^2 \qquad (3.2)$$

In this simple analysis the area is measured 0.37 nm^2 too large. While this value might serve as an approximation to demonstrate the orders of magnitude of the expected error, it is by no means accurate. A circular circumference, for example, reduces the rim area of a realistically shaped island. The slope at the rim produced by the imaging process might also differ significantly.

Figure 3.18 shows the combined height distribution of 1 ML Ag_{86} islands after annealing them at 160 *K* and at 170 *K*, respectively. Both histograms from figure 3.17 and 3.18 were created using the same set of selected 1 ML clusters. They have an average height of 0.26 *nm,* which is reasonably close to the theoretically predicted height of 0.236 *nm* for a single Ag monolayer.

The height distributions of all occurring islands gives an overview of the morphological evolution of the silver particles. While some of them formed 1 ML islands, most of them retained larger heights due to additional layers. There is also a possible difference between the two relevant annealing steps, 1 *h* at 160 *K* and an additional 1 *h* at 170 *K*.

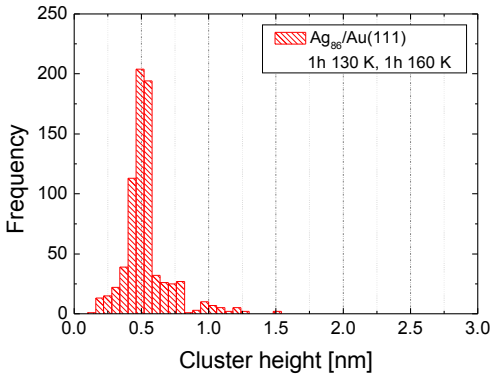

Figure 3.19: Height distribution of Ag_{86} clusters on Au(111) annealed 1 *h* at 130 *K* and 160 *K*.

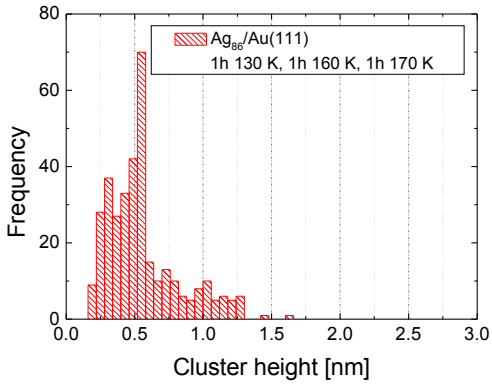

Figure 3.20: Height distribution of Ag_{86} clusters on Au(111) annealed 1 *h* at 130 *K*, 160 *K* and 170 K.

The histograms of figure 3.19 and figure 3.20 are not directly comparable. The amount of clusters counted in both cases is very different as the frequencies indicate. However, especially additional heights at around 0.25 *nm* are much more prominent in figure 3.20 than in figure 3.19. This leads to the conclusion that after annealing at 160 *K* most remaining struc-

tures have a height of about 0.5 *nm* or 2 ML silver. After an additional annealing at 170 *K* more clusters lost their top layer and formed single layered islands.

Note that the following annealing experiment took place before annealing clusters on a second sample system at 130 *K*, 160 *K* and 170 *K*. It is presented here for logical reasons, not because of the chronological order. In this step the sample was annealed at 200 *K* for 1 *h*. This resulted in a total structural change within the clusters. While after deposition at 77 K multilayered islands were visible (see figure 3.5 on page 108), only small remnants can be identified on the Au(111) surface after 1 h at 200 K.

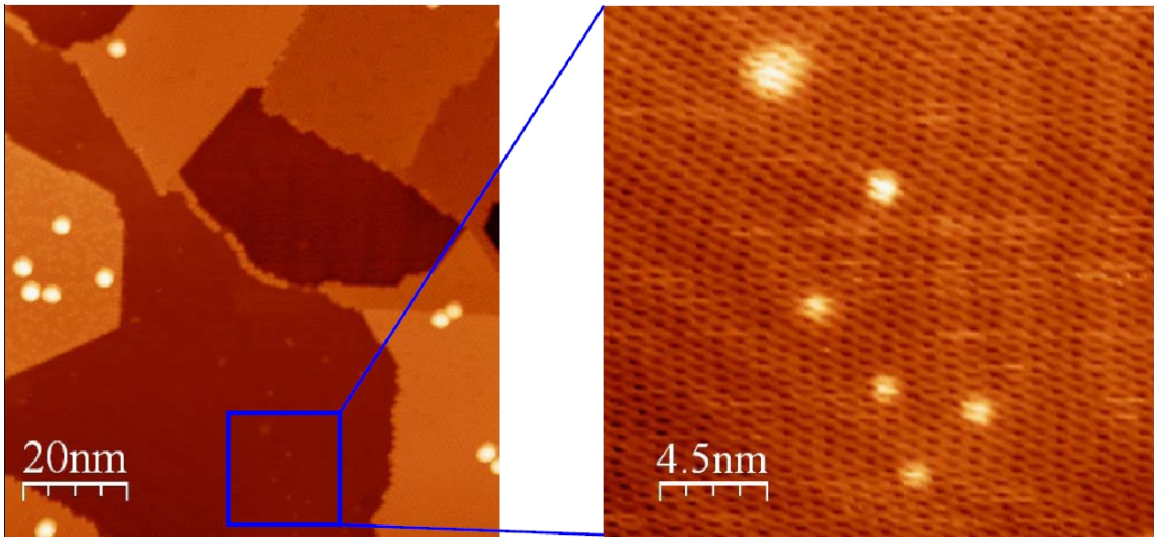

Figure 3.21: STM image of Ag_{86} clusters after annealing them at 200 *K* for 1 *h*. On the left an overview with additional C_{60} areas is visible that still contain clusters. However, the selected area shows an Au(111) surface, which is magnified and shown on the right. Only structures lower than a single silver monolayer are visible.

It is probable that most of the cluster atoms were detached from the compound and moved over the surface until reaching Au step edges. A comparison of several energy barriers, which have to be surpassed, can be found in section 3.2.6 on page 128. However, figure 3.21 demonstrates that remnants of clusters are still detectable. This can be explained by the formation of an $Ag_{(1-x)}Au_x$-alloy. In [70] 3 ML silver were evaporated onto an Au(111) surface at room temperature. With a successive annealing at 490 *K* both metals start to mix. After annealing the sample at 590 *K* Au atoms dominate at the surface with less than 5 % silver in the top layer.

The formation of an alloy starts at 450 *K* as shown in figure 3.23, which is much higher than in the experiments presented in this chapter. Here, the process seems to be concluded already at 200 *K*. However, this discrepancy can be explained by the deviating amount of silver that is wetting the surface. The metal always tends to form coherent monolayer in order to reduce its internal energy due to the formation of metal bonds. Islands formed from single Ag_{86} clusters are expected to be much less stable than coherent Ag layers, which have orders of magnitudes more atoms. The reduction of internal energy by the formation of a flat alloy surface becomes less significant with each added cluster atom. Thus a temperature of 200 *K*

in time scales of 1 *h* may well be sufficient to dissolve small silver islands but does not affect coherent silver layers.

Note that the formation of an alloy is not concluded in the annealing experiments of this chapter at 200 *K*. As figure 3.21 shows the cluster remnants are still visible while in [70] a total dissolution of the silver in the gold underlayment takes place. It is conceivable that figure 3.22 only represents a progressed but non the less intermediate state.

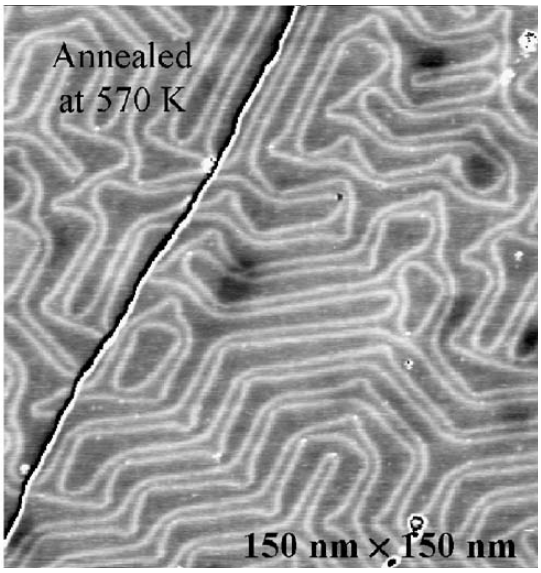

Figure 3.22: STM image of 3 ML silver on Au(111) after annealing the sample at 570 K, which resulted in an Au/Ag alloy [70].

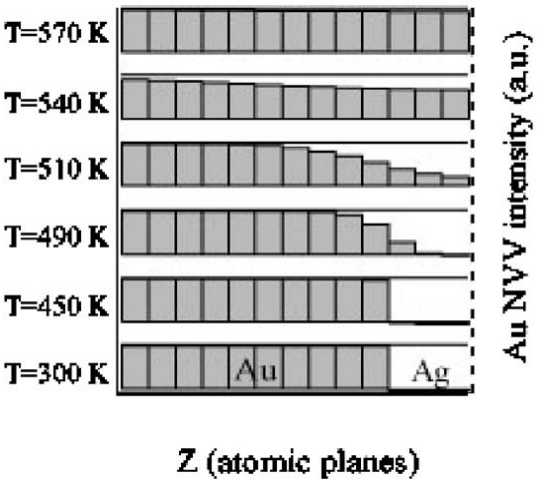

Figure 3.23: Demonstration of the alloy formation process. The ratios of Au to Ag are shown for each layer. At 300 K both metals are clearly separated, while they start to merge at higher temperatures [70].

3.1.2 Energy Discussion

For later evaluations it is useful to estimate the energies involved in the formation of the observed structures. Energy to rearrange atoms or break bonds comes only from three sources:

1. Kinetic energy from the impact.
2. Binding energy released during the initial contact between cluster and surface.
3. Thermal energy available during storage and annealing.

Both kinetic and binding energy are responsible for the deformation of the previously compact cluster, which results in the measured reduced height of the structures. The direct comparison between cluster on C_{60} and bare Au(111) clearly shows these effects. Due to the fact that the clusters have been measured for an extended period of time at 77 *K*, it is reasonable to assume that rearrangements taking place at 77 *K* were already concluded when the measurement started. Any further changes in the cluster shape must be attributed to the additional thermal energy provided by the annealing processes. Note that the emergence of temperature

is due to statistical processes. With this in mind the Arrhenius equation [187] is used in order to estimate the energy necessary to cause a deformation of the cluster. It allows to calculate the rate of events taking place in a system that is exposed to a certain temperature T for an energy E_a per atom, which is needed to surpass certain energy barriers. Thus it can be used to estimate the minimal requirements for a cluster to change its shape.

$$k = 1/t' \cdot e^{-\frac{E_a}{k_b T}} \qquad \Rightarrow \qquad E_a = -\ln(k\,t') \cdot k_b T \tag{3.3}$$

In equation 3.3 k is the rate constant, $1/t'$ the prefactor, T the temperature in kelvin, E_a the activation energy and k_b=8.617 eVK^{-1} the *Boltzmann* constant [61]. The value k can be set to be 1/*hour*, because this is estimated to be the minimum rate of events needed for a noticeable change in cluster shape within the duration of the annealing experiment. With the Debye temperature Θ_D=225 K of silver [122], the frequency at which atoms vibrate or move and thereby the time interval between two interactions, can be estimated. This leads to time intervals of $t'=h/(k_B\Theta_D)$=2.1×10^{-13}*sec* [149]. Using these values an estimation of the activation energy E_a is possible.

Temperature T [K]	77	130	160	170	200	300 (RT)
Activation energy E_a [eV]	0.23	0.39	0.48	0.51	0.60	0.91

Table 3.1: Estimation of the activation energy for a rate constant of 1 h^{-1} at several temperatures.

As expected the allowed energy barriers increase with increasing temperatures as demonstrated in table 3.1. Note that a room temperature (RT) measurement was not conducted in this experiment. However, this is a frequent annealing temperature in many other experiments so that it is included. In this special case the activation energy comes close to 1 eV, which is of special interest for the stability of Ag clusters on C_{60}/Au(111) as discussed in section 2.1.4 and especially demonstrated in figure 2.18 on page 64. With 0.23 eV activation energy, 77 K marks the other end of the spectrum. In most experiments the temperature was not lowered further.

3.2 Ag_{55}-Ag_{147} on Au(111)

The experimental results revealed an interesting opportunity to investigate the given sample system further. Depositing several clusters sizes on bare Au(111) could be easily accomplished while the relatively simple metal-metal system enabled a theoretical approach by molecular dynamic simulations. In addition to that the deposition could not only be conducted with different cluster sizes but also different impact energies. Thus a reshaping of clusters could be observed depending on the cluster size and energy.

The following experiments were closely linked in design and investigation to the theoretical approach used in molecular dynamic simulations (MD) and density functional theory (DFT). An overview of both methods can be found in section 1.2.3.4 on page 20.

3.2.1 Sample System

While earlier experiments allowed a first insight in the behavior of silver clusters on bare Au(111), many questions remained concerning their concrete evolution on the surface after deposition. To get further information on the cluster evolution, it was necessary to vary the size of the clusters as well as their impact energy. Both factors were thought to influence the arrangement of the clusters. To provide multiple deposition spots with individual size and energy parameters, the recently introduces Movable Focus Lens was used. With this device multiple spots can be brought onto the sample, which are clearly separated and precisely positioned.

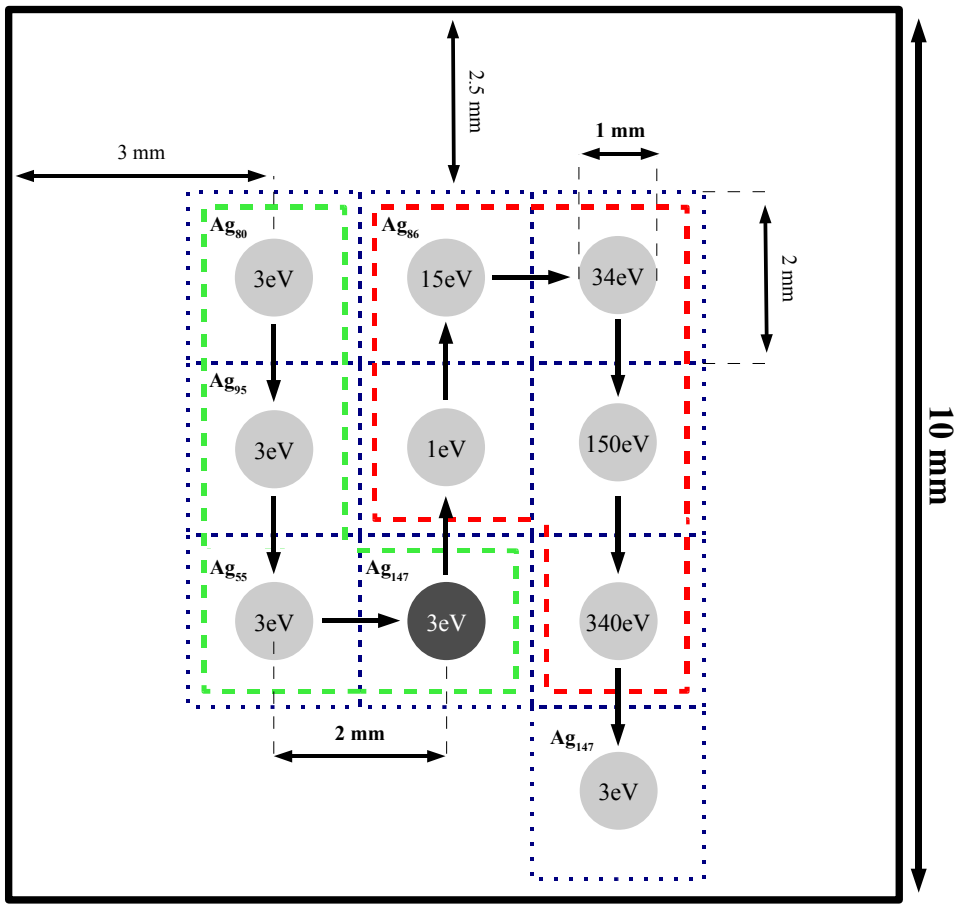

Figure 3.24: Deposition pattern used for the experiment; the cluster size is given in the upper left corner of certain boxes while the spots, encompassed with a red dashed line on the right, represent Ag_{86} clusters; The deposition energy is shown inside of each box; The first Ag_{147} deposition was accidentally mixed with Ag_{55} clusters so that it was deposited again (lower right corner); black arrows between spots show the order of deposition.

The Au(111) sample was prepared following the steps described in section 1.5.5.1 on page 47. Mass selected clusters were produced and brought onto the sample as described in section 1.5.3 on page 42 with an additional focusing and positioning using the Movable Focus Lens. The precision of isolating a cluster mass was 1.7 % of the cluster size. The temperature of the sample was kept constant at 77 *K* during deposition and measurement.

A deposition pattern similar to that described in section 2.2.4 on page 90 was used. A depiction of the concrete pattern is shown in figure 3.24. Note that several cluster sizes and energies are also shown, which will be described in detail in the next section. In this particular example the pattern is not quadratic but has an additional spot on the lower right side. This has been done in several cases if errors occurred during the deposition and a step had to be repeated.

3.2.2 Experimental Procedure

A total of 9 cluster spots with a unique combination of cluster size and deposition energy were brought onto the sample. The total number of clusters per spot amounted to 9 *pAmin*. Cluster sizes and energies are presented in figure 3.24. Table 3.2 gives an overview of the used parameters. Note that preceding experiments are also included, they are marked with the experiment number 1 and 2. Experiment 3 is the one described in this section. Only experiments are shown that produced usable data.

Cluster size [m_{Ag}]	Impact energy [eV]	Temperatures [K]	Experiment number
82±1	3	77, 200	1
84±1	3	77	1
86±1	3	77, 130, 160, 170	1, 2
55±1, 80±1	3	77	3
86±1	1, 3, 15, 34, 150, 340	77	3
95±2, 147±2	3	77	3

Table 3.2: Relevant deposition parameters. The cluster size is set by the mass selector and given as multiples of silver masses (m_{Ag}) together with the expected error. The impact energy depends on the bias applied to the manipulator. Temperatures, which a sample was exposed to, are either due to storage or annealing. Coherent experiments have the same experiment number.

In contrast to preceding experiments the sample was not annealed in this case due to time constraints and the fact that an extensive data set, especially for Ag_{86}, was already available. The setting of the deposition energies follows the procedure described in section 1.5.3 on page 42. As mentioned in the respective chapter, the kinetic energy distribution of a bunch of clusters resembles roughly a Gauss curve. This is shown in figure 3.25 for this concrete experiment. By applying a high bias, i.e. -37 *V*, to the manipulator the entirety of the clusters will reach the sample and thus shift the maximum of the distribution, which is in this case at -3 *V*, accordingly. The difference, which is 34 *eV*, determines in consequence the average kinetic energy. In contrast to that a much lower kinetic energy complicates matters. Only a fraction of clusters will reach the sample, marked in figure 3.25 by a dashed area for 1 *eV*. The centroid of this area is located at 0 *V*. With -1 *V* bias applied to the manipulator a kinetic energy of 1 *eV* results.

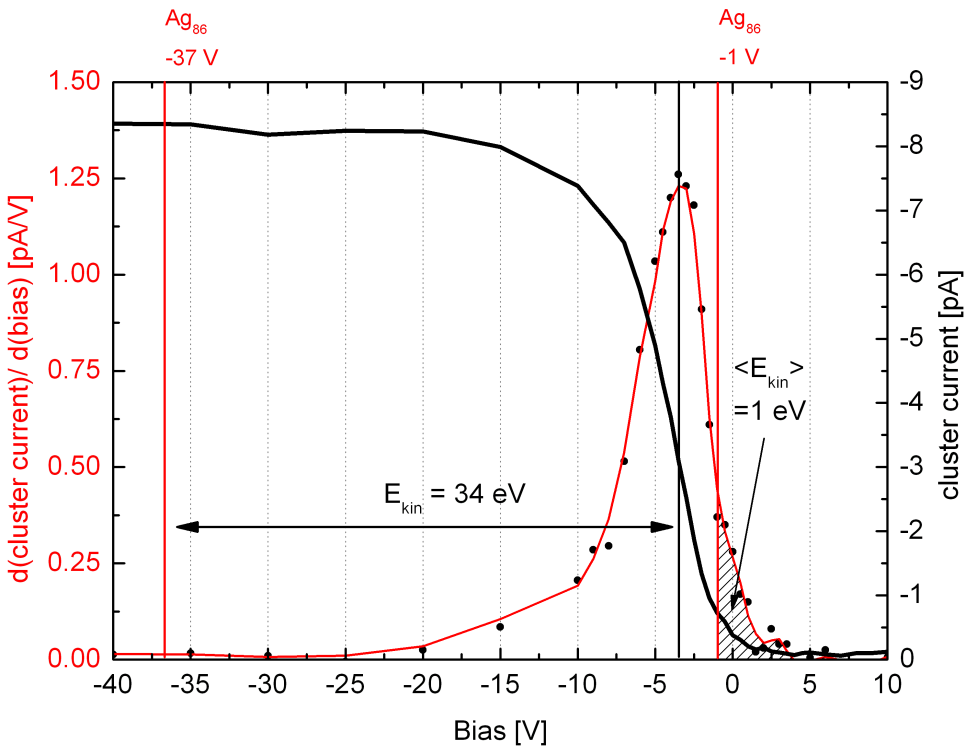

Figure 3.25: Cluster current (bold black line) and derived current (thin red line) measured for different biases. The derived line has been smoothed; it resembles a Gauss distribution. Black dots are measured and derived currents. With a certain bias applied, i.e. -37 *V*, all clusters can reach the sample with an energy of 34 *eV* (difference to the average energy of 3 *eV*). With 1 *V* applied only a fraction reaches the sample. The respective cluster energy is estimated by the centroid of the dashed area.

The variation of the kinetic energy and thus impact energy of the clusters has only been varied for Ag_{86}. The rest remained at the usually chosen 3 *eV* per cluster used for soft landing. This has been done because measuring Ag_{86} produced the best results in terms of annealing steps and STM image quality as well as cluster frequency in preceding experiments.

With this the lowest impact energy per atom was produced in the case of Ag_{86} at 1 *eV*, which results in 0.01 *eV* per atom. For Ag_{86} at 340 *eV* the largest kinetic energy per atom was produced. It amounted to 4 *eV* per atom. Thus a wide range not only of cluster sizes but also impact energies could be investigated.

In the experiments each deposition spot was independently identified with the STM by positioning the tip in a certain pattern on the sample. Each image showed varying concentrations of clusters. If a larger amount of clusters was found, the deposition center was thought to be nearby so that the respective area was searched in a denser pattern. Each spot was surrounded by an area void of any clusters so that a clear separation of cluster sizes and energies was ensured. In addition to that the spots were found to be positioned in the expected pattern illustrated in figure 3.24. The first deposition of Ag_{147} is marked with a dark gray color. It has been compromised by accidentally depositing Ag_{55} on the same spot for 20 *sec*, which amounted to an additional 1.7 *pAmin* Ag_{55} cluster in addition to the desired Ag_{147} clusters. Because it was

not clear how severe the effect of this error would be, an additional second spot was created. Note that this spot, which is shown in the lower right of the schematic depiction of the sample, could not be reached with the STM tip in its standard position. However, if the sample is pulled out of its holder a few *mm*, the rim area becomes accessible for measurement.

3.2.3 MD and DFT Simulations

Molecular Dynamic Simulations were conducted by *T. Järvi*. A system consisting of silver clusters equilibrated at 120 *K* coming in contact with a 77 *K* Au(111) surface was modeled. Note that 120 *K* is an estimation for the temperature at which the clusters form in the cluster machine. The initial shape of the clusters was modeled after structures from [188]. The impact energies have been varied to mirror the experimental setup. The larger the chosen energies are, the larger the area relevant for the simulation has to be. Thus the lateral surface size was set to be either 4.5×4.5 nm^2 with a depth of 2 *nm* for low energies or 10×10 nm^2 with a depth of 10 *nm* for high energies. In the lateral direction periodic boundary conditions were employed. At the bottom two layers were held fixed. For temperature control the *Berendsen* thermostat [189] with a time constant of 100 *fs* was used. Thermal contact was enabled by providing a lattice constant in the lateral direction and two additional layers for the bottom.

The clusters were randomly rotated and given an impact velocity. The simulation used Finnis-Sinclair potentials [190,191] for inter atomic interactions. The simulation preceded until no further evolution took place. In addition to that density functional theory (DFT) was used to model the evolution of a single cluster in greater detail. In order to model the flattening of a single cluster, nudged elastic band [192–194] (NEB) calculations were used [195].

3.2.4 Results from Experiments and MD Simulations

With each deposition spot measured, sufficient cluster height statistics in the form of histograms could be created. Other information on the cluster structure were due to the constraints of the STM measurements not accessible. Simulated data on the same cluster sizes with their respective energies were provided so that a direct comparison was possible.

Note that the experiments show a deviating frequency in cluster count, which is due to slight deviations in cluster coverage density at the identified spots and due to STM image quality. The frequency in the histograms stemming from simulated data is extremely low in comparison. This is due to the fact that each individual impact must be computed separately so that the computing time rises linearly with cluster frequency. This is, however, compensated by the lack of any error, which usually deteriorates the measurement.

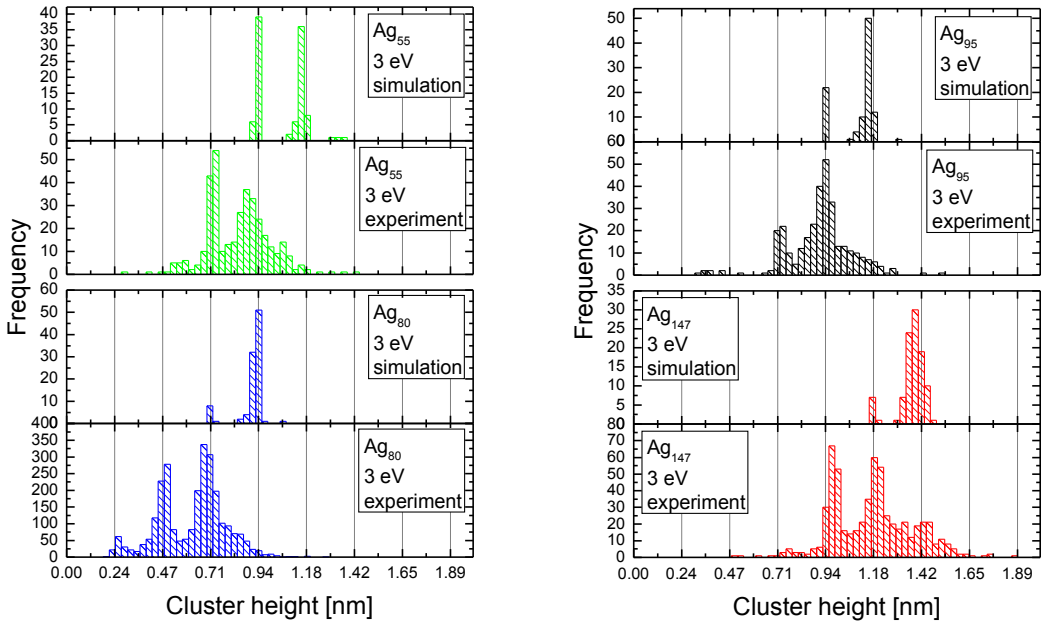

Figure 3.26: Comparison of experimental and simulated height histograms for different silver cluster sizes. In each case two most prominent peaks are visible. However, experimental histograms compared to the simulation are shifted invariably 1 ML to lower heights. Despite of that most peak ratios of experiment and simulation match. The experimental histogram of Ag_{147} and to a lesser degree other sizes show a shoulder that coincides with a peak in the respective histogram of the simulation.

As shown in figure 3.26, clusters deposited at 3 *eV* have two heights that appear with increased probability. For some cluster sizes a third peak may be present but that is highly questionable due to the low amount of counts it is composed of. This will be discussed at a later point in more detail. The ratio of the two heights with the larger associated frequencies is different for each deposition. Statistics play again an important role in the interpretation of those deviations. There is also an obvious difference in average height in the experimentally gained histograms. This can, however, be easily attributed to the difference in initial cluster size.

The simulated data, always shown together with the respective measured heights, shows both similarities and differences. The emergence of two peaks is also visible as well as a rough match in peak ratios in some cases. The main difference though lies in a an obvious shift to larger heights. By compensating for that, a good match of experimental and simulated data can obviously be achieved.

As simulations show the measured heights most likely resemble single silver monolayers. Thus the numbers at the x-axis in figure 3.26 are multiples of 0.236 *nm*, which are the heights expected if several layers of silver are stacked. Note that the fcc stacking order has to be taken into account, which results in a reduced height compared to the actual diameter of 0.29 *nm* of a silver atom. Obviously the simulated data fits very well, which is no surprise considering that it used these parameters to begin with.

While there is also a good match for the experimentally gathered heights of figure 3.26 with single silver monolayers, a preceding step enabling this has to be mentioned. For these histograms each heights have been shifted 0.06 *nm* to lower values. This has been done in order to correct for substrate related electronic effects, which are well known to cause deviations in height measurement [196]. To correct for this, a theoretically predicted height using multiples of single silver monolayers has been plotted against the measured heights associated with several measured peaks.

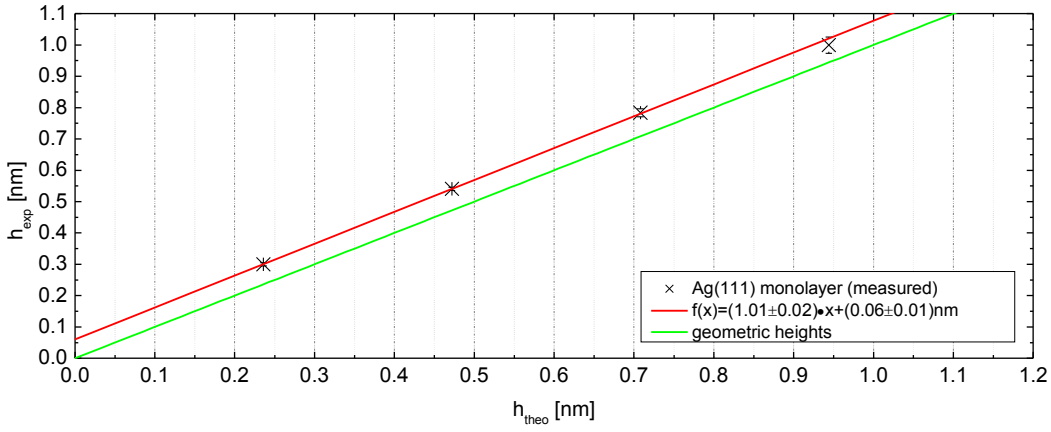

Figure 3.27: Expected cluster height plotted against measured cluster height. The fit (red line) shows that the layer distance evolves in steps of single monolayers. However, an offset of 0.06 *nm* must be taken into account. The error bars, being small compared to other values, show the scattering of individual heights.

Figure 3.27 illustrates that the measured heights are equal in distance, which in itself hints to single layers. In addition to that the distance is almost identical to 0.236 *nm*, thus the height of a single silver monolayer. Consequently the mentioned shift of 0.06 *nm* to lower values is revealed. With these corrections in mind, the mentioned shift between experimental and simulated data is identified to amount to exactly 1 monolayer.

Ag_{86} clusters deposited at varying energies have also been plotted together with simulated data in the same way. The mentioned height correction, thus the 0.06 *nm* shift of all experimental data, has also been done for the histograms in figure 3.28.

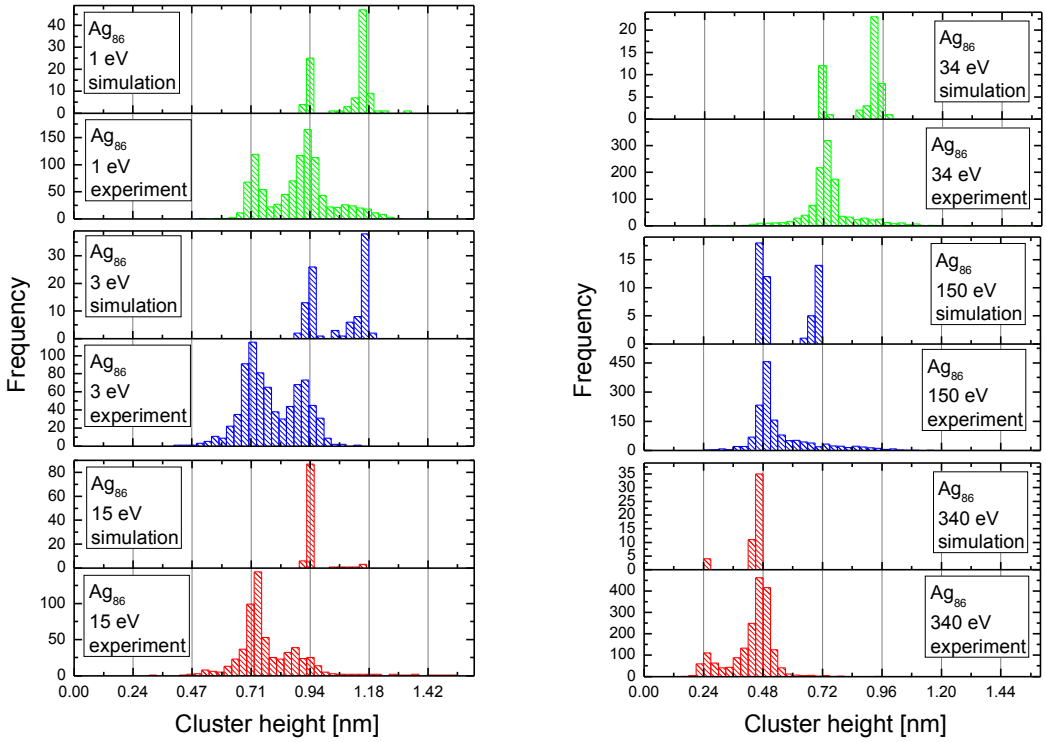

Figure 3.28: Comparison of experimental and simulated height histograms for Ag_{86} clusters deposited with different kinetic energies. Similar to figure 3.26 some experimental heights are shifted 1 ML to lower values with partly matching peak ratios (left). However, deposition energies between 34 *eV* and 340 *eV* (right) show some to no shift. For 34 *eV* and 150 *eV* one cluster type, represented by the *larger* peak, is missing, which means that it is most likely shifted 1 ML to lower values. For 340 *eV* deposition energy no shift occurs.

For low energies the same pattern as for different cluster sizes at 3 *eV* deposition energy emerges: The same amount of peaks with a shift of 1 ML between theory and experiment is obvious. However, for higher energies starting at 34 *eV*, the peaks begin to match. This change in appearance does not happen suddenly but in a certain pattern. Ag_{86} at 15 *eV* shows still two peaks in the experimental data with very uneven frequencies. The same is true for the simulated data, except that the peak associated with larger heights is only slightly detectable. A shift in height of a single monolayer is thus still present. This changes though at a deposition energy of 34 *eV*. The experiment produces a histogram with only one height peak while the simulation shows two peaks. The same is true for 150 *eV*. Finally at 340 *eV* there is an almost perfect match between simulation and experiment. No shift in height occurs.

The experimental compared to the simulated results reveal a certain pattern. For low deposition energies the measured clusters are shifted for as yet unknown reasons 1 ML to lower values. With the assumption that the simulation correctly represents the state of the cluster directly after deposition, a reshaping of the cluster on longer time scales has to occur if no atoms are lost or gained in the meantime. Because the simulation does not only provide height

information on the cluster but also exact internal atomic arrangements, the entire structure can be analyzed. The experiments reveal that a flattening of the clusters occurs for high deposition energies when at the same time experiment and simulation match. Thus an investigation of the layer structure on a theoretical level seems reasonable.

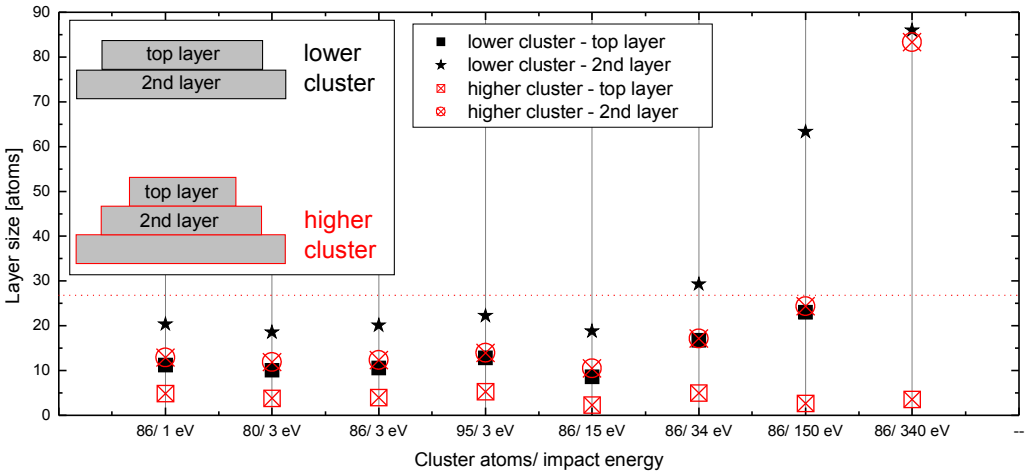

Figure 3.29: Layer sizes for cluster size and impact energy provided by MD simulations. The top most layer, named *top layer*, and the 2nd layer from the top, named *2nd layer*, are presented for both existing cluster heights (*higher* and *lower cluster*). The red dashed line marks a threshold of 27 *atoms*, which divides layer sizes in two groups. 2nd layers below that value loose their top layers in the experiment but not in the simulation. 2nd layers above the threshold keep their top layer in both experiment and simulation.

Figure 3.29 provides an overview of the relevant layer structure of the several investigated cluster sizes at different energies. Note that only the top most layer and the second layer from the top, in the following just referred to as 2nd layer, are regarded for each occurring cluster height. Because each histogram shows two most prominent peaks, a total of four layer sizes is given for each cluster size and deposition energy. Not all cluster sizes are included in this particular graph despite behaving accordingly.

The top layer of the higher clusters is always fairly constant in size and consists of roughly 5 atoms or less. It is conceivable that statistical effects have a great influence on the observed deviation. There is thus no energy dependent effect on this particular layer. The 2nd layer of the higher clusters and the top layer of the lower clusters behave nearly identically. Note that there would be no structural difference between those layers if the previously mentioned top layer, consisting of only about 5 atoms, would not exist. This and the fact that this small top layer is impact energy independent and is solely responsible for the emergence of a larger cluster height, allows to disregard the higher clusters completely for the following considerations.

In figure 3.29 the layer sizes of the lower clusters are marked with filled, black stars and boxes. The top layers are fairly constant in size while consisting of around 10 atoms. This means that they have on average a diameter of 3.6 atoms. For an impact energy of 150 *eV* it

gets slightly larger and encompasses about 20 atoms, which corresponds to a diameter of about 5 atoms. This is not significantly larger but non the less noteworthy. For 340 *eV* impact energy the lower cluster is identical to a single silver monolayer. Thus the 2nd layer would be the substrate. Because the latter cannot be considered part of the cluster, it has been left out in the graph. The 2nd layers of the lower clusters show the most interesting behavior. The size stays fairly constant with around 20 atoms until an impact energy of 34 *eV* is reached. The layers start to broaden so that their sizes increase.

With a threshold of 27 atoms layer size, a distinction can be made that is reflected in the histograms. It is marked in figure 3.29 with a dashed red line. Note that the value of this threshold is arbitrarily chosen to make the following distinction. It has no known relevance beside that. If the 2nd layer size of the lower clusters surpasses this value, the same clusters experience no decay after deposition. In contrast to that a decay is consequently observed for all energies up to 15 *eV*. For 34 *eV* and 150 *eV* a decay takes place for the higher clusters, not for the lower ones. As a consequence the higher clusters loose their top layer and both cluster types become identical. This is reflected by a single peak in the histograms. Figuratively speaking both peaks in the simulation histograms merge. The 340 *eV* deposition is a special case but both the 2nd layers of lower and higher clusters are above the mentioned threshold, which is reflected in the histograms by a lack of any height change.

In conclusion there is a strong correlation of the stability of a cluster and the size of any second layer from the top. This means that the size of the underlayment for a small top layer is decisive. If it is large, it stabilizes the top layer.

3.2.5 Results from DFT Simulations

Results from experiments and MD simulations do not match for lower deposition energies. Consequently MD simulations are not sufficient to model the behavior of silver clusters soft landed on Au(111). The following investigations revolve around Ag_{86} clusters. They were landed on the surface with 1 *eV* kinetic energy and annealed to 325-425 *K*. At these temperatures flattening was observable in MD simulations. The top layer disappeared after 3-200 *ns*. With equation 3.3 on page 118 this leads to an activation energy of about 0.4 *eV*. For nudged elastic band (NEB) a process was assumed in which the top layer of the cluster, consisting of 3 atoms, looses 1 atom over a decay pathway to the environment. This again resulted in an activation energy of 0.4 *eV*, confirming the results of the MD simulation.

At 77 *K* an activation energy of about 0.25 *eV* is possible for a decay with an annealing time of 1 *h*. This is much too low to explain any decay at this temperature. Thus NEB within density functional theory (DFT) was used by *T. Järvi* for a detailed analysis of a single Ag_{86} cluster. In a first run it was calculated without a surface, the results being in good agreement with MD simulations. Then the Au(111) surface was taken into account, which resulted in a reduced overall energy barrier of only about 0.2 *eV*. The simulated decay process, for MD, DFT without surface and DFT with surface are shown in figure 3.30. Atoms at the rim of the cluster form a chain to the surface alongside an edge. This allows an atom to reach the surface without being separated from the others.

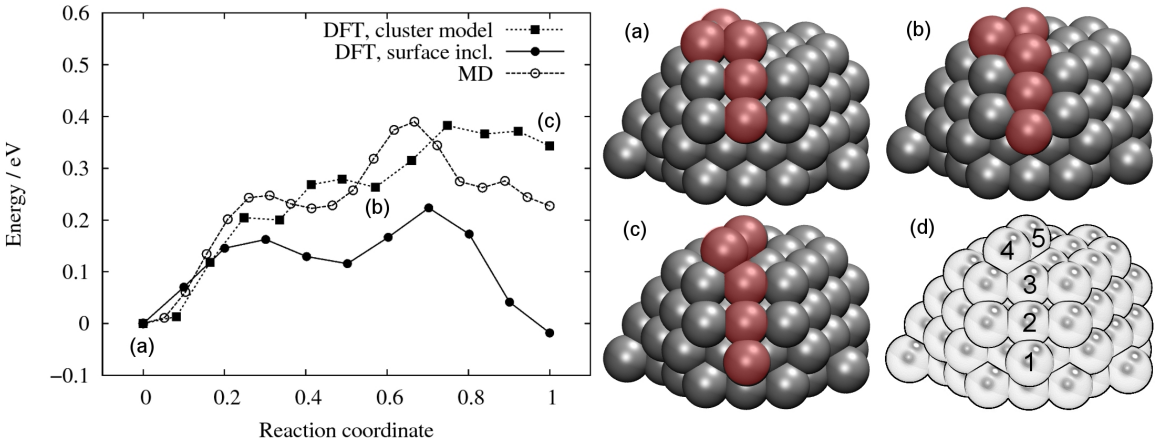

Figure 3.30: Cluster evolution calculated using MD and DFT (left). MD and DFT without surface are in good agreement while an additional surface in DFT reduces the energy barrier to about 0.2 *eV*. The decay process is depicted on the left. A chain (red) of atoms forms at the edge of a clusters allowing for a reduction of the energy barrier (right).

3.2.6 Discussion

Several conclusions can be drawn from the annealing experiments conducted for Ag_{86} clusters on Au(111) after annealing them at 160 *K* and 170 *K* (a previous annealing step at 130 *K* did not show any faceted clusters). In a first note the size and number of layers could be determined sufficiently well using the Cluster Evaluation Software (CES, see section 1.4.3 on page 34). The last step before decay involved the formation of single layered structures. The area of these could be determined and thus a comparison to theoretical computations could be made. This showed that in most cases the island size corresponds to the number of atoms in a single cluster. Thus no material was lost or gained so that only rearrangements of silver atoms occurred during annealing. Furthermore this should also have been the case for all previous arrangements of multiple layers because the number of atoms they consisted of was 86 during deposition and before decay. It was observed that a few partly flattened islands encompassed two or more separate top layers on a single bottom layer at 160 *K*. This leads to the conclusion that coalescence occurred in some cases. The increased size of some single layered islands after annealing the sample at 170 *K* hints in the same direction. In fact their size was so large, that they should have formed out of up to 5 previously separated clusters. This can be the case if the particles are very close to each other after deposition.

MD simulations show that the initial shape of a cluster is lost, independent of its previous kinetic energy. Due to the strong metal-metal interaction of silver and gold, the released binding energy is sufficient to cause a complete rearrangement of the atoms. At 77 *K* the surface dynamics can be described by a comparably fast terrace diffusion. This can be attributed to migration and Ehrlich-Schwoebel barriers, both being about 0.1 *eV* [156,197]. This results in a multi layered structure, the height of which being dependent on the initial size and speed of the previously free cluster. Roughly speaking the larger the size and the lower the kinetic energy, the larger the resulting structure will be. This is true for both experiment and simulation.

Annealing experiments demonstrated a partial decay or significant rearrangement of the clusters between 138-168 *K* if the temperature is corrected for deficiencies in measurement described in section 1.5.4.1 on page 44 (measured: 130/160 *K*). This can be translated into an activation energy between 0.41-0.51 *eV*. MD simulations predicted a barrier of about 0.4 *eV* for a decay of the top layer, thus confirming the experiment. Furthermore *Morgenstern et. al.* observed a fast Ag(111) island decay with downward diffusion over a step edge, which lead to similar results [157]. The detachment barrier of the atoms is estimated to be about 0.7 *eV* [156]. Experimentally an annealing temperature of 208 *K* (measured: 200 *K*) lead to a total decay of the clusters. Exposing the latter to this temperature for 1 *h* results in an activation energy of about 0.63 *eV*, which is reasonably close to the previously mentioned detachment barrier.

A deviation of experiment and MD simulation was shown to exist for low impact energies. The experiment lacked the top layer, which is included in the simulation. For high energies, no discrepancy was observed. It seems obvious that the additional energy influx of high energy clusters is responsible for the disappearance of the top layer. However, a closer investigation of the simulated cluster shape suggests that the size of each second layer (from the top) of a cluster determines if a top layer is included in the simulation or not. Only small second layers allow a decay of their top layers, which the experiment includes in contrast to the simulation. Consequently layer sizes play a major role in the energy discussion.

DFT simulations including the Au(111) surface revealed the following mechanism: Small layers provide sharp edges, which larger layers lack due to their bigger radius and thus smaller curvature. These edges allow atoms to form a chain, reaching to the surface. This results in a reduction of the barrier to only about 0.2 *eV*. At 77 *K* a barrier of 0.23 *eV* can be surpassed in a time scale of 1 *h*, thus allowing certain top layers to decay. With this effect included experiment and simulation are in perfect agreement [195].

4 Experimental Results for Weak Cluster-Surface Interaction

As mentioned in section 1.1.2 on page 9, UPS is a method that can be used for free clusters and weak cluster-surface interactions. A weak interaction is ensured by the right choice of the surface material in our particular experimental setup. As mentioned in section 1.3.2.2 on page 25, HOPG has many advantageous properties for this kind of experiment and is therefore used as an underlayment in all cases. A description of its preparation can be found in section 1.5.5.1on page 47.

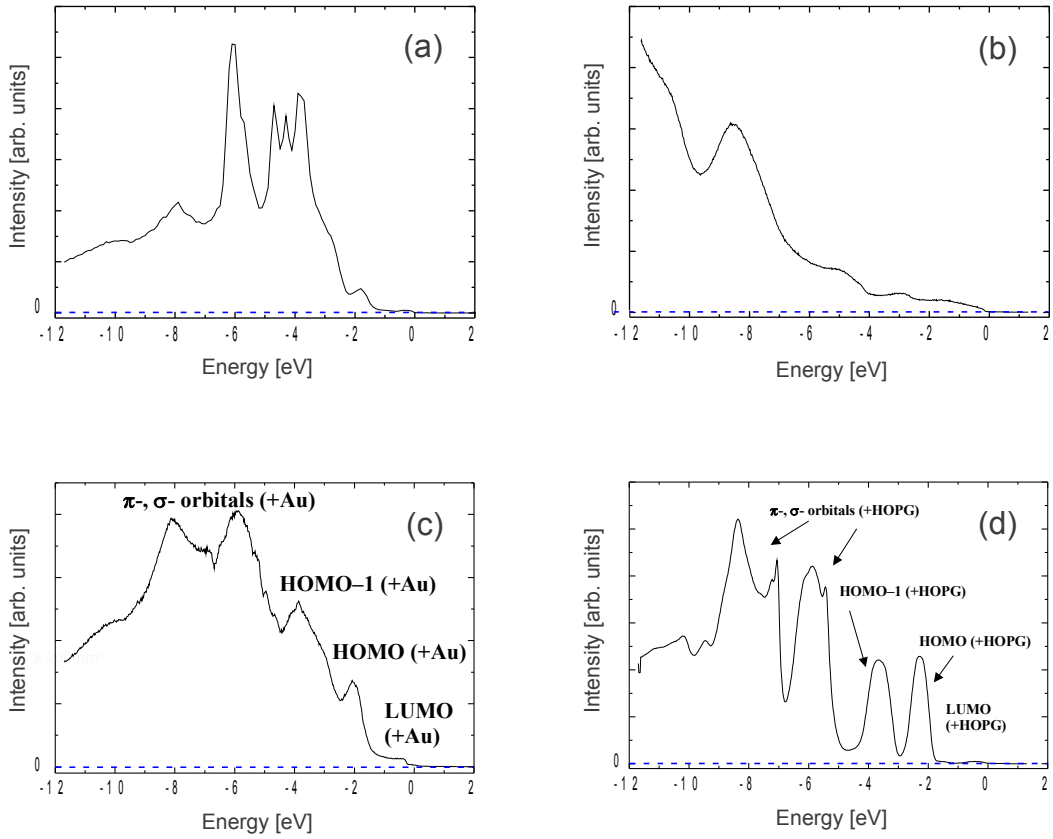

Figure 4.1: UPS spectra of the following surface substrates: Au(111) (a), HOPG (b), C_{60}/Au(111) (c) and C_{60}/HOPG (d) [123].

Figure 4.1 shows a selection of several possible surface materials. The d-band structure of noble metals can be shown e.g. by the UPS spectrum of an Au(111) surface depicted in figure 4.1 (a). In the region of -4 *eV* below the Fermi level is a very prominent array of peaks, which stems from a high density of states. Metal clusters may behave in many ways differently to bulk material but the overall d-band structure is similar. Thus surface materials must consequently lack structures in the energy range of interest in order not to mask cluster spectra. Figure 4.1 (c,d) shows Au(111) and HOPG functionalized with C_{60}. Both have a high density

of states in the energy range of interest so that they are not useful for the UPS experiments in question. A direct comparison between figure 4.1 (b) and (a,c,d) (for bulk Ag see figures 4.6 and 4.7) shows that the d-band of HOPG lacks a prominent electronic structure in the energy range of interest.

The measured spectrum does not solely depend on the used material but also on the chosen photon energy. While the overall structure of the spectrum remains unchanged, the photon energy determines how deep below the Fermi level the detector can reach. In our case a helium gas discharge lamp delivered photons with an energy of 21.2 *eV* in each experiment. This was sufficient to detect prominent HOPG structures in addition to investigating the d-band structure of Ag clusters of different sizes.

The mean free path of the emitted electrons [198] is in the order of the cluster diameter of a silver cluster with less than 1000 atoms. Thus most of the electrons emitted within a cluster reach the surface unaffected. In addition to that the total silver coverage is in all cases <<1 ML so that electrons emitted by HOPG and influenced by a cluster are the absolute minority.

4.1 UPS of Ag_{55}-Ag_{923} on HOPG

Usually each experiment starts with the deposition of mass selected clusters on bare HOPG. Either a single spot with about 3 *mm* diameter is created or the new Movable Focus Lens is used to produce multiple spots with about 1 *mm* diameter in a certain pattern. Because the detector is tilted relative to the manipulator's main axis, the sample must be arranged in a slight angle in order to measure normal emission. Because the manipulator can only be moved alongside its main axes, a repositioning in the x-axis always causes the sample to shift out of focus as depicted in figure 4.2.

However, by readjusting the y-axis the spot of interest can be brought back into focus. The optimal condition can be found by maximizing the amount of electrons registered by the electron analyzer. While this procedure is standard for all experiments, it caused problems if the intensity should be kept constant or the number of readjustments is to be reduced. Due to the given geometry of the setup this problem does not occur in the case of a repositioning in the z-direction.

Using a tantalum wire with a diameter of 0.2 *mm* on an HOPG surface, the size of the area detected by UPS can be identified. The manipulator together with the sample was moved alongside the z-coordinate so that the UPS focus transitioned over the wire. A set of UPS spectra were taken at different positions. Because HOPG lacks any prominent structure in that region, tantalum was the only relevant contributor for a strong signal. With the wire moving into the UPS focus, more d-band electrons reached the detector. For evaluation the intensity between 6.2-7.7 *eV* below the Fermi level was integrated for each spectrum at a certain position, resulting in the graph shown in figure 4.3. The peak at about 175 *mm* marks the position where the wire is exactly in the center of the UPS focus while the ground level marks the positions where the wire is outside. The full width at half maximum of the resulting curve shows

a diameter of 1.21 *mm* for the UPS focus. Note that the metallic rim of the sample caused a significant increase in intensity as soon as the UPS focus came in reach.

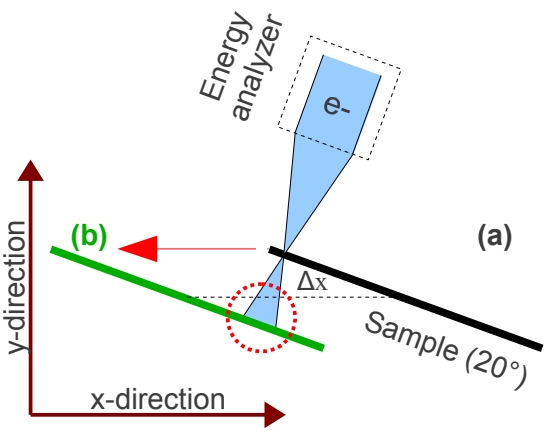

Figure 4.2: Schematic depiction of the defocusing of UPS electrons. In this example the sample is tilted 20° relative to the manipulator main axis. In (a) the distance between sample and analyzer is optimal. However, this causes sample position (b) to be out of focus (red circle).

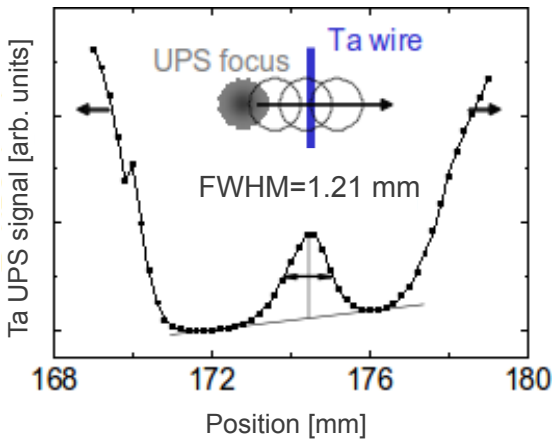

Figure 4.3: Integrated d-band intensity of a tantalum wire measured at varying z-positions. The energy range for integration ranged from 6.2-7.7 eV below the Fermi level. In the upper part a schematic depiction of wire, UPS focus and spot position over time is shown.

The Movable Focus Lens produces a spot diameter of about 1 *mm* so that most certainly no cluster material is expected to be outside the measured area. Simultaneously the focus is only insignificantly larger than the expected spot so that only little intensity is expected to be lost.

4.1.1 Preceding Experiments

Earlier UPS experiments also took place without the Movable Focus Lens so only one cluster size could be investigated in the course of an experiment. There have been, however, several experiments of that kind so that Ag_{55}, Ag_{309} and Ag_{923} were investigated. The latter two were part of *Stefanie Duffe's* work [123]. Without the Movable Focus Lens the deposition spot had a diameter of about 3 *mm*. This enabled the investigation of multiple areas within the spot because the UPS focus has a size of just 1.21 *mm* as demonstrated before. Note that the cluster coverage density decreases from the spot's center to its rim. Thus the amount of deposited material at a specific measured area transitioned smoothly from a maximum to none at all. Furthermore the total amount of clusters was chosen large enough to ensure coalescence in the deposition center.

The angle at which the emitted electrons reached the detector was set to normal emission. Unfortunately there was a defect in the UPS electronics, which resulted in a random shift of the detected energy by ±0.2 *eV*. This incident compromised any quantitative analysis of the data. The qualitative measurement was, however, unaffected by this.

4.1.1.1 UPS of Ag_{55} on HOPG

From this point onwards the exact experimental steps for Ag_{55} and Ag_{923} deviated. While Ag_{923} is described in detail in [123], the experiment for Ag_{55} had the most sophisticated setup. To reduce the cluster mobility during impact, the kinetic energy of the clusters was set to only 0.05 *eV* per atom, so soft landing condition were ensured. During deposition and measurement the temperature was kept constant at 50 *K*, which is significantly less than the 140 *K* for Ag_{309} and Ag_{923}. A lower temperature should have reduce coalescence of clusters by reducing their mobility after impact.

Preceding experiments allowed an estimation of the needed cluster material to cause coalescence in the deposition center. Due to the limited size of the spot, rim regions with a lower particle density remained for nearly every sensible amount of clusters. However, time proved to be the problematic factor. The total amount of deposited cluster material depends on the one hand on the cluster current, which must be maximized. On the other hand it can be increased by running the deposition process for an extended period of time. This is, however, limited by the target's lifetime and an increasing likelihood of occurring errors. It was estimated that a deposition process should not take more than 2 hours. With a total deposition time of 50 *min* and a cluster current of 11-12 *pA*, about 600 *pAmin* were deposited. The respective UPS spectra are shown in figure 4.4.

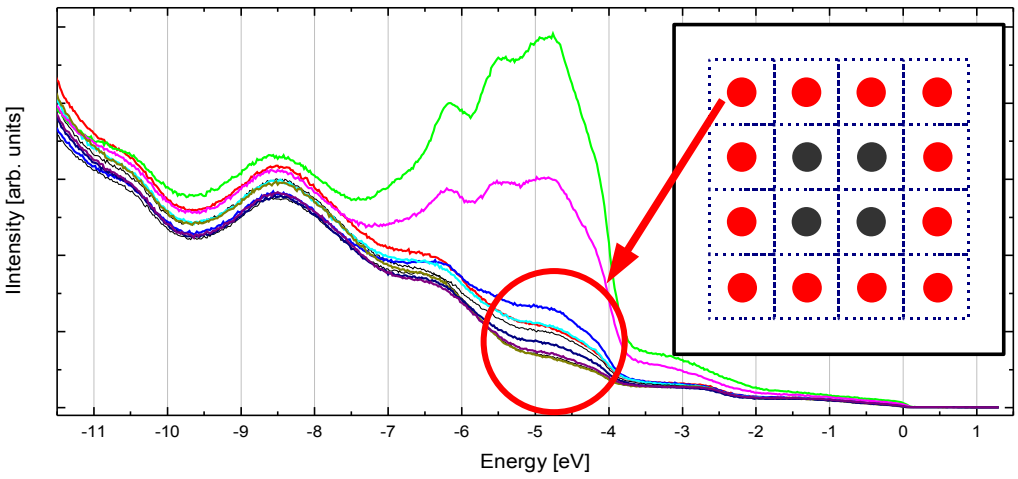

Figure 4.4: UPS spectra of Ag_{55} clusters on HOPG with a total coverage of 600 *pAmin* and a spot diameter of 3 *mm*. Spectra were taken from multiple positions within the deposition spot. While the center showed a d-band structure comparable to bulk silver, spectra at the rim area resembled those of single clusters. The black box in the upper right illustrates the sample with dots being measured areas. Rim areas can be associated with deviating d-band structure within the red circle.

To gain a useful variety of data without accidentally measuring a position twice, the surface was scanned by following a grid pattern in steps of 1 *mm*. In addition to that the spot could be mapped by gathering data from regions with densities varying from the maximum in the deposition center to no clusters at the rim. A subtraction of bare HOPG allowed to extract

the desired d-band information of Ag_{55} clusters as described in section 1.5.6.4 on page 52. A side effect of the low temperature was, however, the adsorption of foreign material onto the sample, which resulted in additional peaks that overlapped with the actual band structure. This was noticed during the course of the experiment so that additional HOPG spectra were taken from cluster free region of the sample. Because they showed the same additional structure information of the foreign material, they have been used to reveal the cluster's d-band structure by subtracting them from cluster spectra gathered shortly before or after (see figure 4.5).

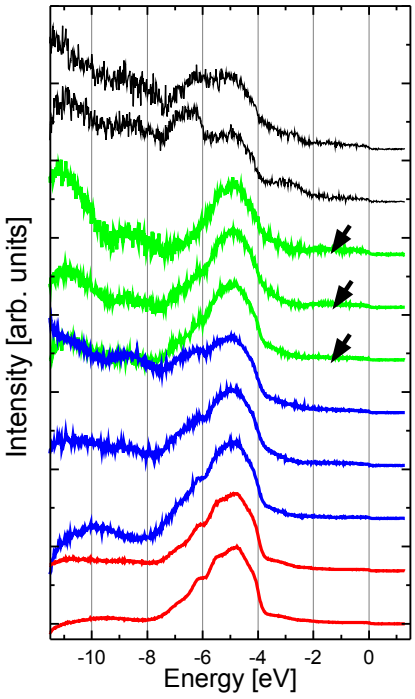

Figure 4.5: UPS spectra of Ag_{55} on HOPG after subtraction of the underlying HOPG and normalization. While the red curves (bottom) resemble bulk silver, and the black curves are strongly affected by disturbances, the green curves marked with arrows can be associated with single cluster spectra [199].

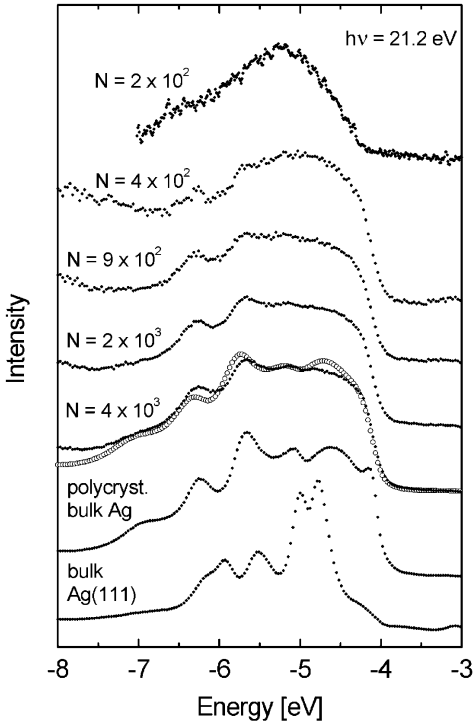

Figure 4.6: Multiple d-band spectra of silver evaporated on HOPG and measured with UPS. With a lesser amount of silver (top), assumably clusters are formed, which is reflected in the simplicity of the spectrum. With more material (bottom) bulk silver emerges. The open white dots correspond to a polycrystalline bulk silver spectrum that was altered by the dynamic final state effect (see section 4.1.4) [200].

Very noticeable in figure 4.5 is the deviating signal to noise ratio of different spectra. This is due to the variation in cluster quantity at specific positions, which increases from top to bottom. The spectra have been normalized. The noise thus affects lower amounts of deposited clusters more. Clusters with lower coverage show less structure in the d-band than the the ones with larger coverage. This may be attributed to coalescence, which is thought to occur in

the deposition center. Despite being mass selected clusters, the deposited material can be compared to evaporated Ag as long as the respective islands match roughly in size.

A corresponding analysis has been conducted by *H. Hövel* [200], who has investigated evaporated Ag on HOPG grown in nano pits using UPS. A transition from bulk Ag to small island spectra was observed. This is shown in figure 4.6. The forming clusters vary in size depending on the amount of evaporated material. For each spectrum a number is given that clarifies the estimated quantity of atoms the grown cluster consists of. The bottommost spectra in figure 4.5 show coalesced clusters because their closest resemblance is to the polycrystalline bulk Ag curve in figure 4.6. Ag(111) is also shown in figure 4.6 for comparison. The shape of the topmost spectra in figure 4.5 cannot be identified clearly enough in order to analyze them quantitatively. The three curves below that, however, which are marked with arrows, can be compared to about 2×10^2 atoms evaporated silver in figure 4.6. This may be 4 times as much atoms as Ag_{55} contains but it is roughly the same order of magnitude. Thus no or only little coalescence can have happened to the deposited clusters in the corresponding area.

4.1.2 Refined Evaluation Methods

Important aspect of all following experiments are the evaluation methods used. To understand the underlying idea, a closer look at figure 4.6 is useful. As mentioned before, the spectrum of a not too small metal cluster should be similar to the spectrum of polycrystalline bulk Ag.

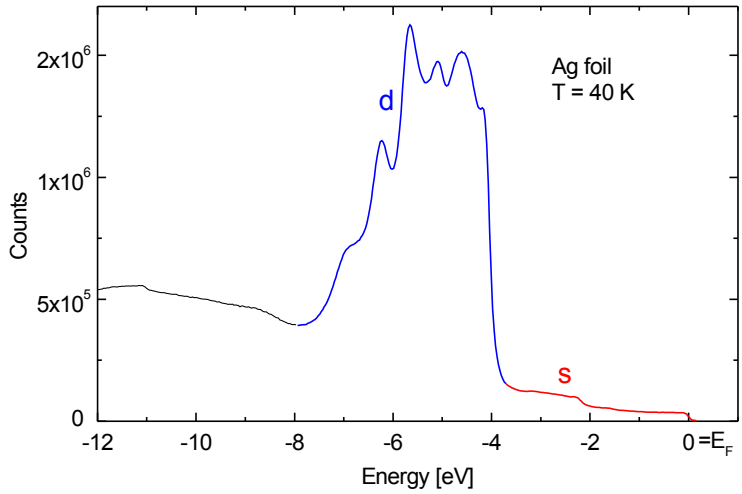

Figure 4.7: UPS spectrum of a silver foil measured at 40 *K*. With respect to the energy relative to the Fermi level the resulting spectrum can be interpreted as a d-band part (blue) and an s-band part (red). Lower orbitals are depicted gray.

Figure 4.7 shows the UPS spectrum of an Ag foil. It can be separated into three regions. The first ranging from 0 *eV* to about -4 *eV* represents the s-band of the metal with a low intensity in the spectrum. This is caused by a low density of states stemming from one electron per atom normally located in the s-band with parabolic dispersion. The flat d-band with little dispersion on the other hand shows very prominent structures. It starts at about -4 *eV* ranging

to about -8 *eV*. Bands at lower energies produce a smooth but moderately intense spectrum. This is also expected to be the case in any of the investigated cluster spectra.

Due to deviations in intensity, HOPG and HOPG+cluster spectra have to be normalized using a certain reference point. For preliminary checks the very prominent HOPG peak depicted in figure 4.1 (b) at about -8 *eV* is used. This neglects that a cluster spectrum at energies below the d-band region has significant density of states similar to the bulk. However, especially for small clusters the energy range below -8 *eV* is still important and cannot be simply disregarded.

It was decided to modify the subtraction process in some cases so that the resulting cluster spectrum roughly resembles some features of the spectrum of bulk silver. Thus a program called *var-alpha* was coded by *D. Engemann* during the course of the respective experiments. The normalization factor α of a particular HOPG spectrum is varied before subtraction. There are two modes of operation to find a fitting α. In the first mode the program integrates a part of the spectrum in the below d-band region and compares the result to an integral over the d-band. Only spectra with a ratio resembling that of bulk silver are selected. In the second mode only below d-band values are regarded. Here, the summed, squared deviation from a mean value is minimized. This results in a region with only little peaks or indentations. For later evaluations the second mode is used. A depiction of both processes is shown in figure 4.8.

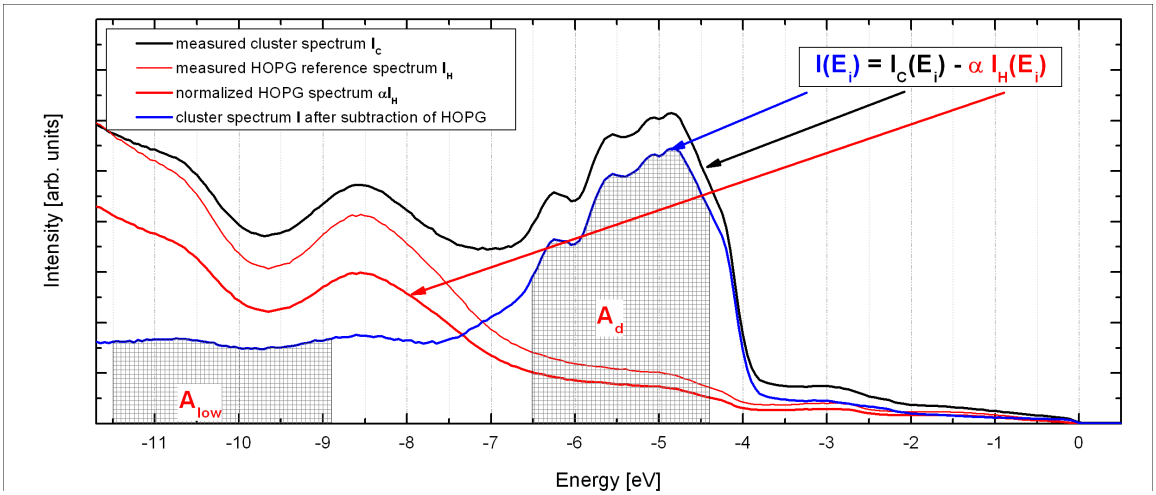

Figure 4.8: UPS spectra of HOPG+Ag_{561}/60 *pAmin* and HOPG. Method 1: The normalized HOPG spectrum is subtracted from the cluster spectrum. After that the integral over the d-band range A_d is divided by an integral over a lower energy range A_{low}. The ratio A_{low}/A_d is constant for a particular material and is set to resemble a particular bulk material. Method 2: The summed, squared deviation from a mean value of the below d-band region is minimized.

Later experiments measured the HOPG sample at positions chosen for a cluster spot before the deposition took place. This method proved to produce less errors during subtraction.

4.1.3 Experiments with Movable Focus Lens

The following experiments, in which the Movable Focus Lens was used, will focus on the investigation of two basic types of clusters. Smaller ones that do not surpass 100 atoms and larger ones that do. Small clusters are expected to produce more interesting results due to their supposedly less developed d-band structures. Larger clusters, however, are easier to measure because they consist of more atoms and can therefore emit more electrons for the UPS measurement, which results in a stronger signal.

4.1.3.1 Experimental Setup

The new Movable Focus Lens enabled the deposition of the same amount cluster material onto a much smaller area than before. As a consequence multiple depositions were conducted on a single sample. The distance between the spots was set to at least 2.5 *mm* in order to ensure a clear separation of cluster sizes. Note that the area, which is detected by the UPS apparatus, has an average diameter of about 1.21 *mm*. This is significantly less than the chosen distance between deposition spots. An overlapping of two or more spots would make it impossible to assign an UPS spectrum to a specific cluster size. To make optimal use of the given sample without endangering the integrity of single spots, the following deposition pattern was chosen:

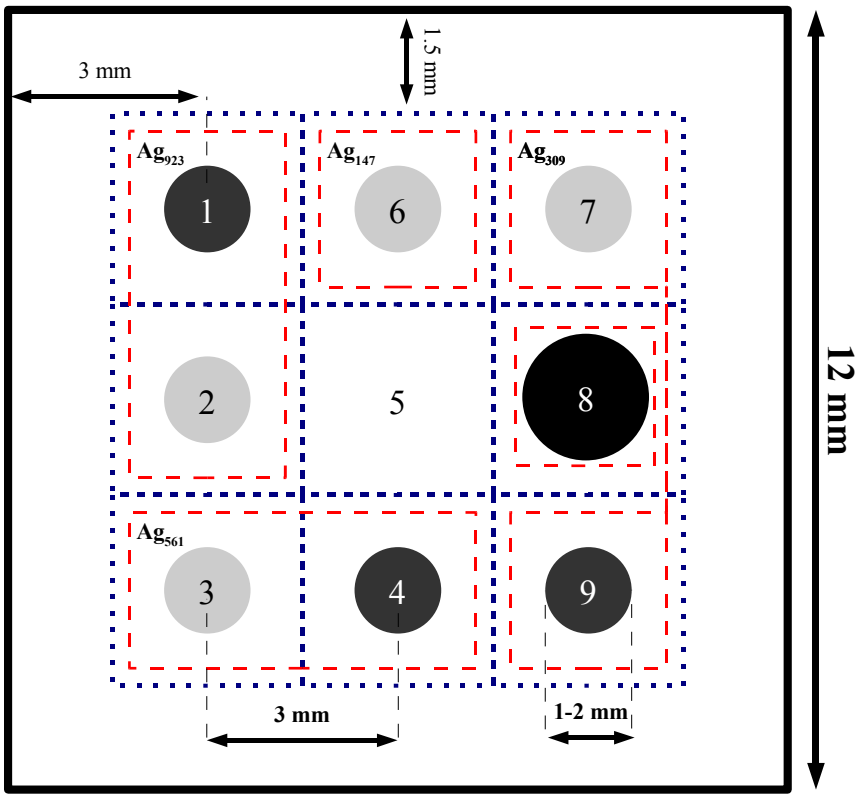

Figure 4.9: Example of a deposition pattern; numbers (1-9) indicate the order of deposition; a cluster amount of 20 *pAmin* is depicted dark gray while an amount of 10 *pAmin* is light gray; deposition spot 8 was overexposed with 63 *pAmin* and spot 5 was left empty.

As can be seen in figure 4.9, the center spot was left out. This was done for two reasons. First, it ensured that an HOPG reference area was present, which had approximately the same distance to each deposition spot. Second, it seemed easier to identify the spots relative to each other when characteristic points of reference were present. If 9 spots had been present it would have been quite difficult to distinguish several spots successfully when most of them are surrounded by other spots. There was no way to see the deposition spot visually nor did an UPS signal necessarily deliver a clear d-band structure because the underlying HOPG signal had still to be subtracted. Additionally without a lengthy evaluation the measurement contains only little information about the measured cluster size. So it was useful to create one spot that was easily detectable and easily distinguishable from others. If one coordinate was known, others could be extrapolated from that. So in addition to the blank center another spot was chosen to consist of a much greater amount of deposited material. This ensured a good detectability concerning the UPS measurement.

The depicted example was set up to contain 4 individual cluster sizes (Ag_{147}, Ag_{309}, Ag_{561} and Ag_{923}). The red boxes illustrate, which spots contained clusters of the same size. In most cases they were deposited in direct succession. This way the cluster size had to be changed less often. The dark gray color marks spots with a total cluster amount of 20 *pAmin* and the light gray ones those with a total amount of 10 *pAmin*. Numbers from 1 to 9 illustrate the order of deposition. Position 5 was left out while the spot of position 8 is depicted slightly bigger. This marks the much greater deposited amount of 63 *pAmin*. Note that position 7 and 9 encompassed the same cluster size without being in close proximity to each other. The following experiments used similar deposition patterns, however not identical ones.

4.1.3.2 Small Clusters: Ag_{55}-Ag_{147} on HOPG

Here, a grid of 3×3 spots with a distance to each other of 3 *mm* was chosen. Cluster quantities of 2 *pAmin*, 4 *pAmin* and 8 *pAmin* were chosen for deposition under soft landing conditions, with sizes ranging from Ag_{55} to Ag_{923}. As it turned out only larger clusters deposited with 8 *pAmin* could be identified and measured. While Ag_{923}/ 8 *pAmin* had the strongest signal, it was located too close to the rim of the sample so that the respective spectra where therefore compromised by an uneven HOPG underlayment. In consequence only Ag_{71}, Ag_{92} and Ag_{147} clusters, each deposited with an amount of 8 *pAmin*, could be evaluated. In addition to that the UPS measurement started with a sample temperature of 50 *K*. Preceding experiments suggested that coalescence of clusters would not take place under these conditions. However, foreign material adsorbed on the sample so that the resulting usable data was very limited. The temperature of the sample was therefore increased at a later point. Unwanted material desorbed at 125 *K*, which in consequence allowed measurements with useful results. Note that the data might have been influenced by the desorption process.

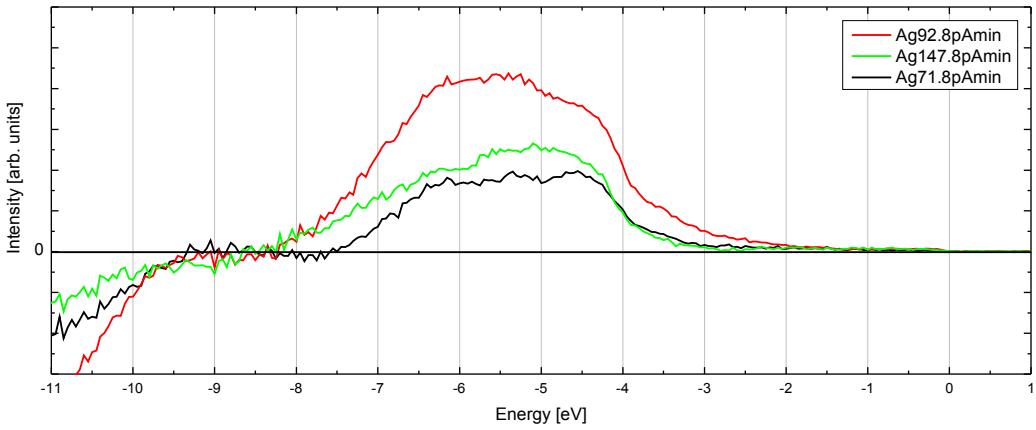

Figure 4.10: UPS spectra of Ag_{71}, Ag_{92} and Ag_{147} after subtraction of HOPG (normalizing on the -8 *eV* HOPG peak) and Fermi level set to zero.

The subtraction of the HOPG signal for the cluster spectra in figure 4.10 was performed by normalizing to the -8 *eV* HOPG peak. This forces the signal to zero at this energy (compare to the energies >0 eV above the Fermi level) but produces artifacts e.g. at energies <9 *eV*.

The experiment was later repeated with minor deviations. For once the amount of deposited material was increased in order to get a stronger signal. Each spot was deposited with 15 *pAmin* and 30 *pAmin*, respectively. Thus the lowest coverage of this sample was about double the maximum coverage of the preceding one. In addition to that an overexposed spot similar to that depicted in figure 4.9 was used for the first time. It consisted of Ag_{55} clusters with a coverage of 129 *pAmin*. Moreover the temperature was set to 125 *K* from the start in order to prevent adsorption of unwanted foreign material.

Note that at this point it was not yet clear, which cluster coverage density must be surpassed for coalescence to take place. Thus a direct comparison of these results with those of the preceding experiment is necessary.

Figure 4.11 shows several spectra of Ag_{55}-Ag_{147} clusters after subtraction of the underlying HOPG signal. Note that the newly developed var-alpha method has been used for subtraction. This is clearly visible for energies below -8 *eV* where a virtually structureless zone remains just like in figure 4.7.

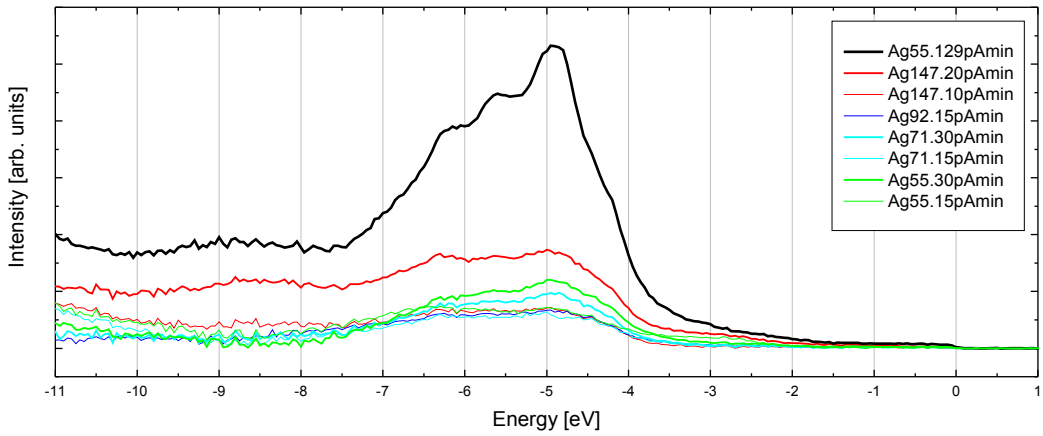

Figure 4.11: Several UPS spectra of Ag_{55}-Ag_{147} clusters with varying occupancies after subtracting the underlying HOPG signal. The subtraction has been conducted using the new **var-alpha** method, which aims at preserving the shape of a silver bulk spectrum.

As mentioned before, the intensity of each spectrum depends on two factors under the assumption that the entire deposition spot contributes to the observed intensity. First, the amount of deposited clusters is important. Second, the size of a cluster has an influence. Roughly the total amount of silver atoms in the area in question determines the measured intensity. Note that the effect is linear here because the elastic scattering length of an electron is in the order of the diameter of a cluster so that double the amount of atoms causes double the intensity. In consequence it is possible to normalize each spectrum to display the same relative intensity.

Figure 4.12 shows UPS spectra of Ag_{55}-Ag_{147} clusters. All of them have been evaluated using the new var-alpha method. In addition to that the curve data has been divided by the ion current, deposition time and cluster size, which is proportional to the total amount of atoms inside the respective deposition spot. Clusters with an overall lesser amount of atoms and lower coverage tend to show spectra with less visible structures.

The spectra of figure 4.12 are of two types. The first emerges for coverages >20 *pAmin*. They have similarity to clusters associated with bulk Ag(111) shown in figure 4.6. This is especially visible for Ag_{55}/129 *pAmin*: The peak at -5 *eV* is much more intense than the one at -6.5 eV. This is also confirmed by the experiments conducted prior without Movable Focus Lens (see section 4.1.1.1 on page 133). Comparable structures have formed for Ag_{55}/30 *pAmin* and Ag_{71}/30 *pAmin*.

The depositions with a coverage ≤20 *pAmin* produced different cluster spectra. Now both peaks at -5 *eV* and -6.5 eV have about the same intensity. They show more features of Ag polycrystalline than Ag(111).

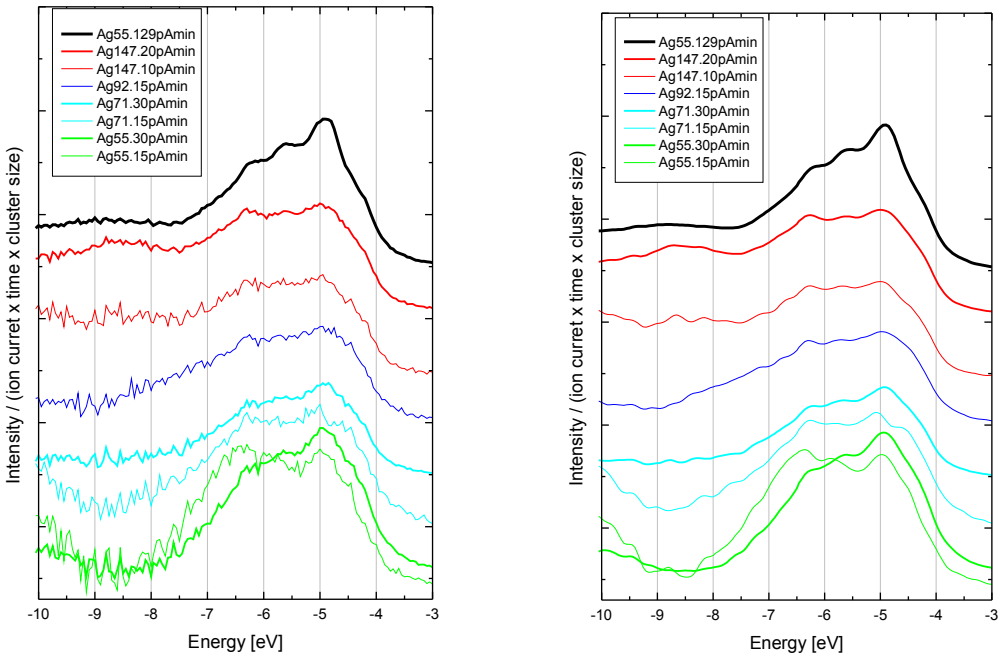

Figure 4.12: UPS spectra of Ag_{55}-Ag_{147} clusters after subtraction of bare HOPG (left). Normalized using the new **var-alpha** method and by dividing by the number of atoms in the measured deposition spot. Clusters of identical size are depicted in the same color. The same graphs after smoothing are depicted on the right.

Note that the mentioned effect is not caused by differences in the intensity of the spectra. In figure 4.11 Ag_{147}/20 *pAmin* has a strong signal, but figure 4.12 shows that the spectrum resembles those of smaller clusters with lower coverage and thus very low spectrum intensity. Simultaneously Ag_{55}/30 *pAmin* has a weaker overall signal but displays a spectrum closer to Ag(111).

4.1.3.3 Large Clusters: Ag_{147}-Ag_{923} on HOPG

Several cluster sizes between Ag_{147} and Ag_{923} were deposited to complement the results for smaller clusters. An overexposed deposition spot of Ag_{561} was used as a point of reference. The respective layout is shown in figure 4.9. It was suspected that coalescence might already have taken place for the overexposed spot. For smaller spots it was uncertain whether coalescence would occur.

10 *pAmin* and 20 *pAmin* had been deposited under soft landing conditions for each cluster size, except for Ag_{147}, which was only deposited with 10 *pAmin*. It was hoped that one of those two variations would avoid coalescence on the one hand but allow a sufficient detectability on the other.

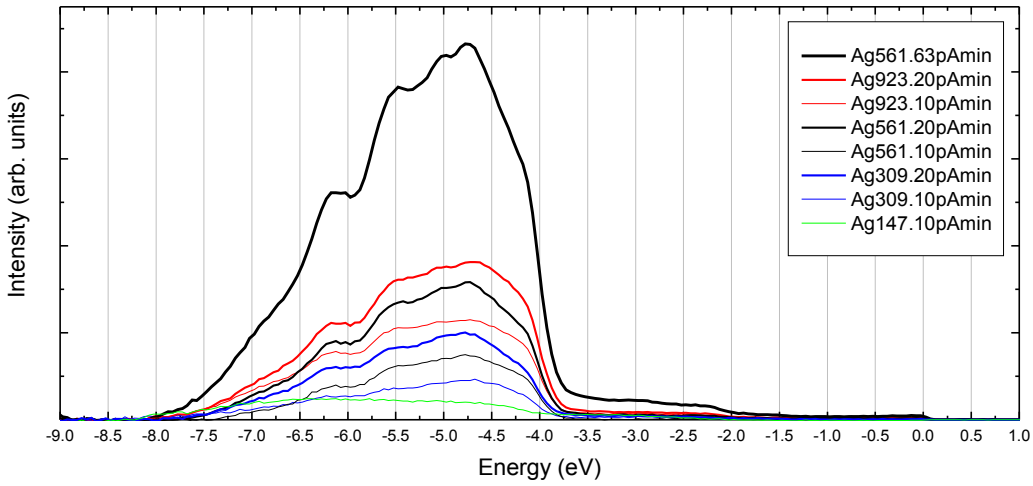

Figure 4.13: Several UPS spectra of Ag_{147}-Ag_{923} clusters with varying coverages on HOPG after subtraction of the underlying bare HOPG signal.

Figure 4.13 shows spectra of Ag_{147}-Ag_{923} clusters after subtraction of the bare HOPG signal by adjusting to the -8 *eV* peak of HOPG. Because it was not possible to use an HOPG spectrum from the same position as the deposition spot, HOPG spectra from different positions on the sample were taken and averaged. Furthermore, it turned out that HOPG close to the actual spot showed the same amount of deviations as those from any other position.

Without normalization, it is already visible that the spectrum of Ag_{561}/63 *pAmin* is closer to Ag(111) than to polycrystalline silver (see figure 4.6). This coincides with the earlier measurements of large coverages.

For a further evaluation the curves have been normalized in figure 4.14 using the total amount of atoms in the measured area (see section 4.1.3.2). The spectra show a similar shoulder as Ag_{561}/63 *pAmin* at around -6 *eV*, but both depositions of Ag_{923} differ slightly in their structure at around -4.5 *eV*. They have a flank at this energy that is more rounded compared to other cluster sizes. In contrast to small clusters, all spectra in figure 4.14 have a closer resemblance to bulk Ag(111) than polycrystalline silver even though all coverages are ≤20 *pAmin*. Ag_{147}, only deposited with 10 *pAmin*, has too little count rate for an evaluation.

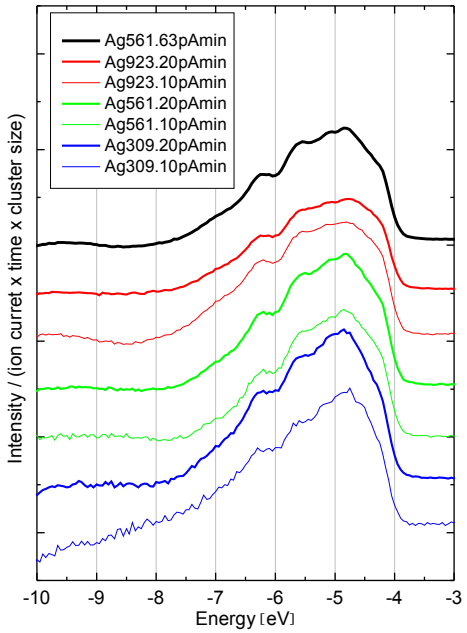

Figure 4.14: UPS spectra of Ag_{309}-Ag_{923} clusters after subtraction of bare HOPG. Normalized by adjusting to the -8 *eV* peak of HOPG and dividing by the amount of atoms in the measured area. Spectra of the same color represent identical cluster sizes. Ag_{923} deviates slightly from other spectra by displaying a more rounded flank at around -4.5 *eV*.

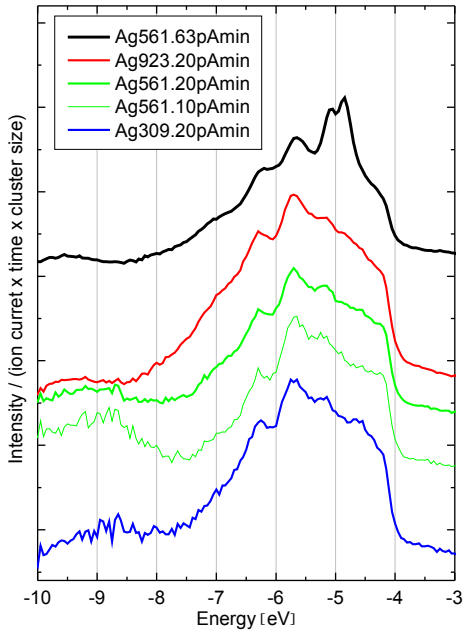

Figure 4.15: UPS spectra of Ag_{309}-Ag_{923} clusters after annealing the sample at RT. However, the respective measurements took place at 125 *K*. Ag_{561}/63 *pAmin* resembles bulk Ag(111). Deposition spots with lower occupancy resemble polycrystalline bulk silver (see figure 4.6).

The sample containing all cluster sizes from Ag_{147}-Ag_{923} had been annealed at RT for 10 *min*, which ensured thermal equilibrium. At this temperature coalescence is suspected for all cluster sizes. The respective results can be seen in figure 4.15. Note that some sizes and coverages are not shown at this point because they deliver the same basic effects without displaying spectra of the same quality. Ag_{561}/63 *pAmin* behaves differently to any other deposition. The resulting spectrum strongly resembles bulk Ag(111) after annealing while the other spectra resemble polycrystalline bulk silver (see figure 4.6). Any explanation would logically attribute the observed behavior to the way clusters of different coverages coalesce. A more thorough discussion together with the investigation of further effects follows in the next section.

4.1.4 Discussion

Three main factors play a major role in the UPS experiments of this section. First, the sample temperature is relevant. Second, the cluster coverage is of importance because it determines not only the subsequent signal intensity but also the interaction of clusters with each other. Third, the size of individual clusters is important. As a general trend larger clusters express a

greater stability due to an overall lowered internal energy per atom. Furthermore large clusters have a reduced movability due to their greater mass, which requires a greater influx of kinetic energy to reposition the particle. Thus the consequent likelihood of coalescing clusters depends on the cluster coverage, the given temperature and the cluster size. Other effects like changes in orientation or deformation most likely also mainly depend on those factors. However, in these cases the surface structure of the sample and maybe even the concrete shape of the clusters could be crucial. The following observations were made in the experiments of this section:

1. The fact that deposition spots, created with the Movable Focus Lens, encompass the entirety of deposited size selected clusters, allows the direct computation of the number of silver atoms, which contributes to the resulting UPS signal.
2. Spectra of Ag_{55} clusters with sufficiently low coverage are shown to resemble silver clusters of similar size grown on HOPG nano pits. With their broad shape, these spectra are closer to Ag polycrystalline (see figure 4.6).
3. The spectra of Ag_{55}-Ag_{147} clusters are of two types. Which one a specific deposition spot shows, depends on the cluster coverage. For coverages $\leq$20 *pAmin* the spectrum is broadened so that a certain resemblance to polycrystalline silver is present. Spots with higher coverage show slightly different spectra, which may be closer to bulk Ag(111).
4. The spectra of Ag_{309}-Ag_{923} clusters show features of bulk Ag(111) at 125 *K*. This is true for all coverages.
5. Ag_{923} with both 10 *pAmin* and 20 *pAmin* coverage displays a slightly different spectrum than any other cluster size/ coverage combination at 125 *K*. It has a more rounded flank at about -4.5 *eV* below Fermi level. Note that Ag_{923} is the largest deposited cluster size of all experiments. It is also a geometrically magic cluster size.
6. After annealing Ag_{309}-Ag_{923} at room temperature, all spectra except Ag_{561}/63 *pAmin* resemble polycrystalline silver. The latter resembles bulk Ag(111).

A graphical display of all experiments is shown in figure 4.16. Partial coalescence, which can force clusters in an even orientation and thus an Ag(111)-like structure, might occur for small clusters and high coverages at 125 *K*. For low coverages clusters are scattered over the surface without uniform orientation. This result in a structure showing features of polycrystalline silver. The importance of cluster size and coverage for coalescence or a reorganization process seems obvious. In the case of small clusters, below or equal to Ag_{147}, the total coverage has a greater influence than the cluster size.

Larger clusters are unlikely to be displaced at 125 *K* but show a tendency towards an Ag(111) structure non the less, even for low coverages. This could be explained by the shapes of larger clusters. In a simplified model they can orient their bottom facets parallel to the surface coherently. Some of the clusters might than have an opposing top facet that is also parallel to the surface (note that the clusters usually have the shapes of fully or partly formed icosahedra). The (111) structure of such facets can cause the emergence of an UPS spectrum that is closer to Ag(111) than to polycrystalline silver.

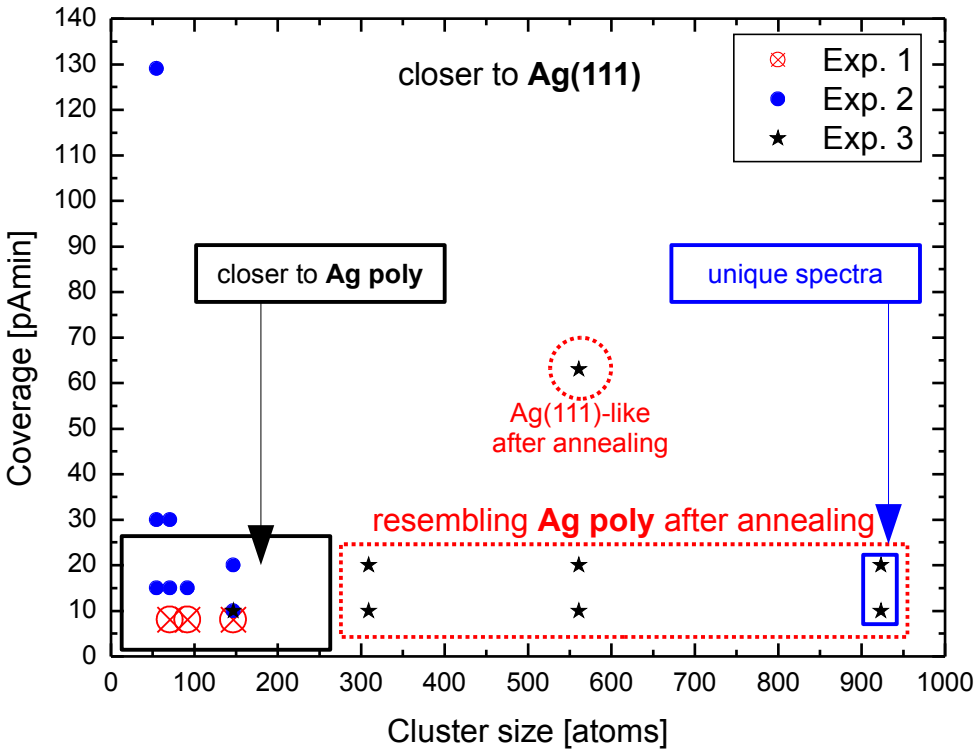

Figure 4.16: UPS experiments sorted by coverage and cluster size. "Exp. 1-3" in the upper right box are the experiments in the same order as in this section. The black box (continuous line) separates schematically UPS spectra being closer to polycrystalline silver. The dotted, red box separates polycrystalline from Ag(111) spectra after annealing. Ag_{561}/63 *pAmin* (dashed red circle) resembles Ag(111) **after annealing**. The blue box marks unique polycrystalline spectra. Other spectra, including Ag_{309}-Ag_{923} **before annealing**, are closer to Ag(111).

Note that the mentioned effects are not expected to be the only factors for the emergence of certain UPS spectra. Coalescence or the facet orientation of clusters are probably mixed with other effects emergent from the cluster size, the cluster orientation or the cluster-surface interaction. The visible difference of cluster spectra to either bulk Ag(111) or bulk Ag polycrystalline spectra can be attributed to this.

During annealing the sample that contains Ag_{309}-Ag_{923} at room temperature, the clusters moved over the surface. The clear Ag(111) bulk spectrum of Ag_{561}/63 *pAmin* after annealing suggests that the clusters formed large coherent islands, possibly aligned in the same direction due to the underlying surface orientation. For lower coverages, however, polycrystalline silver results, which seems contradictory to their previous (111) orientation. The clusters are obviously less ordered after annealing than before. At this point the surface structure might help to solve this contradiction. HOPG often shows ridges, step edges and defects on the surface.

Directly after deposition, a soft landed cluster does not have enough kinetic energy to move away from its impact position at sufficiently low sample temperatures. Only in very few cases does a cluster land on a defect or step edge. During annealing, however, the cluster can move quasi freely so that it is finally stuck at the open carbon bondings of the mentioned surface structures. The cluster might then align randomly, deform or even melt.

Ag_{923} seems to be a special case among all investigated cluster sizes. Deviations in the spectrum could be the result of a dynamic final state effect [201]. It is caused by the positive charge that a cluster carries if one of its electrons is removed by the UPS measurement process. The resulting potential W decelerates the emitted electron so that its kinetic energy is reduced, which is in consequence reflected by a Fermi level shift ΔE. Without a surface, W is maximal and the following equation applies (with R being the cluster radius):

$$\Delta E = W_{max} \propto \frac{1}{R} \tag{4.1}$$

Because both substrate and cluster are not in perfect contact, the equalization of the positive charge requires a typical time τ. The latter is heavily influenced by the magnitude of the cluster-surface interaction. With a small τ the alteration to the spectrum becomes more complicated. Instead of just being shifted, it is now slightly warped.

The open white dots in figure 4.6 show polycrystalline bulk silver with the computed dynamic final state effect taken into account. Comparing the result to polycrystalline silver shows that substructures are blurred and that peaks are slightly distorted. Especially the flank at -4.5 *eV* is less steep for bulk Ag. With these changes the spectrum fits well to the data for Ag clusters with about 4×10^3 atoms at HOPG nanopits [200]. The magnitude of the dynamic final state effect is larger for smaller cluster radii R as equation 4.1 shows. However, the more likely cause for deviations in both Ag_{923} depositions is a different cluster-surface interaction in comparison to other sizes and thus an altered τ.

5 Summary

All experiments involved either mass selected or grown silver clusters. Their behavior is mostly defined by the surface they were deposited onto. The following list shows the sample systems together with their associated strength of interaction:

1. Mass selected and grown clusters on 1 ML or 2 ML C_{60}/Au(111) – **moderate** cluster-surface interaction; investigated with STM and STS.
2. Mass selected clusters on Au(111) – **strong** cluster-surface interaction; investigated with STM.
3. Mass selected clusters on HOPG – **weak** cluster-surface interaction; investigated with UPS.

Soft landing conditions were employed for mass selected clusters in most cases. Height measurements of the resulting structures showed that the clusters were unaltered by this process with the exception of strong cluster-surface interaction. In most experiments thermal energy was injected into the system by annealing. An overview of these experiments follows in the next sections.

5.1 Experiments for Moderate Cluster-Surface Interaction

Annealing experiments involving clusters on C_{60}/Au(111) showed that two factors determine the consequent rearrangement process (see section 2.1 on page 54). First, the layer thickness is important. C_{60} essentially serves as a buffer between the cluster and the Au(111) underlayment. With increasing gap the interaction is further reduced and the cluster thus stabilized. Consequently Ag_{309} clusters decay on 1 ML C_{60} even at room temperature as previously shown and confirmed in the experiments discussed here. Additional layers do not allow a decay so that only rearrangements of the cluster atoms can take place. These have been investigated on the second monolayer. Annealing Ag_{82} (height at 77 K: 1.4 *nm*) up to room temperature revealed the emergence of two cluster heights at 1.3 *nm* and 1.6 *nm*, respectively. The same heights appeared on 1 ML under identical conditions in addition to the decay process. Evaporated silver also showed heights of 1.3 *nm* and 1.6 *nm* on the second monolayer C_{60} under comparable conditions. Thus it was concluded that these heights correspond to a configuration of silver atoms that is especially stable on C_{60}. The emergence of these heights is ascribed to a change in width-to-height ratio of the clusters in both cases. However, it was concluded that grown clusters in contrast to mass selected ones underwent Ostwald ripening in addition to that so that the emerging structures encompass about 10 times more atoms than their mass selected counterparts. It was theorized that not the number of atoms is responsible for a deformation of the clusters but the number of layers.

A possible explanation can be found in the formation of quantum well states within the cluster. These can influence the stability of a cluster by lowering the energy of the entire system. However, a quantitative analysis and thus confirmation requires computer simulations, which might be a future endeavor.

The **height evolution of Ag_{80-88}** on 1 ML C_{60}/Au(111) at 77 *K* has been analyzed by steps of single atoms (see section 2.2 on page 80). A sudden increase in height of about 0.1 *nm* for Ag_{87} was identified (from about 1.4 *nm* to 1.5 *nm*). Earlier experiments hinted to only slight changes in height for clusters a few tens of atoms larger or smaller than Ag_{87}.

The experimental results are in accordance with some earlier findings involving clusters in free beam. As mentioned in the respective chapters, tremendous changes in shape can be enforced by adding a single atom. Most prominent examples involve transitions from 2D to 3D shapes. A possible explanation for larger clusters, like these, involves geometric effects. Ag_{87} could consist of an unusual stable structure composed of 6 fully filled shells. Each atom in a given shell has the same distance to one core atom. Normally cluster-surface interaction causes a cluster to adopt an oblated shape. This might change for intermediate stable structures, which prefer a more spherical arrangement.

Ag_{87} is quite close to the electronically magic Ag_{92}. As mentioned in the respective section, these sizes tend to become spherical if they are independent of a surface. If smaller clusters express an oblated shape, it could explain the observed height change. Ag_{87} is the first cluster in a height step, and it has 5 atoms less than Ag_{92}. This might be due to the interaction with the C_{60}/Au(111) surface.

Not only geometric cluster properties may be important but also electronic ones. The latter can directly influence the height measurement. Note that the tunneling current of an STM measurement is kept constant by adjusting the distance between cluster and tip. If the density of states of a cluster changes, the height measurement is altered accordingly. Another explanation involves the orientation of clusters on C_{60}. It is possible that adding atoms to a cluster forces it in different orientations and thus causes an increased measured height.

Most recent experiments using copper as a cluster material on an otherwise identical sample system hinted to a comparable height change around Cu_{87}. Further evaluations are still necessary to confirm those results.

STS experiments were conducted for Ag_n clusters on 1 ML C_{60}/Au(111) (see section 2.3 on page 100). For that reference spectra of C_{60} were used in order to identify intermediate changes in tip state. Major difficulties prevented an evaluation of most spectra so that only Ag_{55} provided usable data. Together with earlier experiments, a cluster-size dependent gap between peaks around the Fermi level could be observed. An interpretation of those peaks as electronic states representing HOMO and LUMO orbitals is probably misleading. This is because numerous electronic effects induced by the tip and cluster geometry must be considered. The results are further complicated by the fact that earlier experiments used HOPG as an underlayment below the C_{60} film instead of Au(111). The repercussions for the distribution of electrons within a cluster are difficult to determine. However, the peak distance decreases with increasing cluster size, which at least hints to a gradual transition of the cluster to bulk properties. This effect, which can be interpreted as an increase in electronic states together with reduction of energetic band gap distances, is expected independent of the specific composition of the cluster.

5.2 Experiments for Strong Cluster-Surface Interaction

Measurements were conducted involving **Ag_{82}-Ag_{86} clusters on C_{60}/Au(111) and Au(111)** at 77 *K* and after annealing (see section 3.1 on page 106). First experiments provided C_{60} films on Au(111) with free regions of bare Au(111). This enabled a direct comparison of clusters on both substrates. These experiments demonstrated that clusters of this size do not decay on either of the substrates at 77 *K*. However, it was quickly realized that the strong cluster-interaction between cluster and Au(111) together with the thermal energy available caused a severe deformation process. Two heights for one and the same cluster deposition parameter, emergent from the statistical nature of the impact process, were observed. An additional influx of thermal energy by annealing caused a further flattening of the structures, allowing them to eventually wet the surface and thus reach an even more energetically favorable state by increasing the contact area between both metals. By analyzing the resulting structures, a relation between cluster shape and temperature could be identified.

Following these findings a new experimental setup was designed. This time multiple deposition spots were created on the same sample using the new Movable Focus Lens. **Cluster sizes between Ag_{55} and Ag_{147}** were deposited **on Au(111)** with varying impact energies and their heights and structures were analyzed via STM (see section 3.2 on page 118). Simulations of the process provided by *T. Järvi* and *M. Moseler* allowed a direct comparison of the results. Annealing experiment showed a good correlation with the calculated energy barriers provided by MD simulations. The detailed height structure of our experiments compared to MD simulations revealed an almost perfect correlation except for an unexpected difference in height by one monolayer for some cluster size/ deposition energy combinations. This shift, always towards lower heights compared to the simulation, was interpreted as an additional decay process. An analysis of the concrete atomic composition of the cluster, provided by MD simulations, revealed a layer size dependence of this effect. A decay of the top most layer only took place if the underlying layer was smaller than a certain threshold. Additional DFT calculations showed a further reduction of the energy barrier if atoms were able to decay alongside sharp edges only present at small layers. The barrier was reduced sufficiently for a decay of the topmost layer to take place at 77 *K,* and thus it was causing a height decrease by 1 ML. With these corrections experimental and data from simulation show an almost perfect match.

5.3 Experiments for Weak Cluster-Surface Interaction

A wide variety of **UPS** experiments involving Ag_{55}-Ag_{923} cluster on HOPG were conducted (see section 4.1 on page 131). Latest experiments using copper as a cluster material are not included here because they have been too recent.

Preceding UPS experiments investigated Ag_{55} clusters on HOPG at 50 *K* and analyzed multiple cluster coverages that were difficult to quantify. Spectra of Ag_{55} on HOPG showed a certain resemblance to the spectra of clusters grown on HOPG nano pits. The investigation of several small sizes from Ag_{55} to Ag_{147} followed at 125 *K*, from now on with well defined cluster coverages. Finally larger clusters between Ag_{147} and Ag_{923} were investigated at 125 *K*.

The same sample was annealed in several steps and was again investigated at 125 *K*, which provided information on coalescence processes.

Low coverages ≤20 *pAmin* and clusters smaller or equal to Ag_{147} produced a broad UPS spectrum with two peaks equally prominent at -5 *eV* and -6.5 *eV* below the Fermi level. Thus they appeared to be much closer to polycrystalline silver than Ag(111). This phenomenon was attributed to the small size of the clusters and their random orientation on the surface. However, small clusters showed different spectra for coverages >20 *pAmin*. Now the peak in the spectrum at -5 *eV* was more prominent than the one at -6.5 *eV* so that the spectra were closer to Ag(111) than polycrystalline silver. A possible explanation was found to be partial coalescence occurring for small cluster sizes and large coverages because of the close proximity of individual clusters.

Cluster sizes, ranging from Ag_{309} to Ag_{923}, have been found to show spectra closer to Ag(111) than polycrystalline silver independent of coverage. Because larger clusters are less likely to coalesce than smaller ones, another explanation seemed to be valid. The clusters are believed to have shapes of fully or partly formed icosahedra. With this it is possible for them to orient their top facts, which are usually parallel to their bottom facets, parallel to the surface. The fact that the facets have an (111) orientation could be reflected in the subsequent UPS spectrum.

After annealing, cluster sizes that range from Ag_{309} to Ag_{923} had a strong resemblance to polycrystalline bulk silver independent of coverage, with Ag_{561} at 63 *pAmin* coverage being the only exception. This has been attributed to random movements during annealing, which placed them unevenly at kinks, step edges or surface defects in combination with a possible deformation or destruction of the cluster. Ag_{561}/63 *pAmin*, on the other hand, strongly resembled bulk Ag(111). This has been attributed to the high cluster coverage and the subsequent formation of uniform islands, which are (111) oriented.

A special case among all cluster sizes was Ag_{923}. It showed a slightly different spectrum for all produced coverages. In the spectrum, the flank of the peak at -4.5 *eV* below the Fermi level is more rounded than those of other cluster sizes, which can be attributed to the dynamic final state effect. The cluster gains a positive charge due to the UPS measurement process so that an emitted electron is decelerated. This reduces its energy, which is reflected in the spectrum. It is conceivable that Ag_{923} experiences a different coupling to the surface in direct comparison to smaller sizes, which causes the dynamic final state effect to be more prominent.

5.4 Cluster-Surface Interaction in General

The distinction between moderate, strong and weak cluster-surface interaction is of course an artificial one. It has been useful in this thesis because of the experimental constraints we had to deal with. However, the interaction of nano particle and surface is more complex than that and very individual for varying sample systems.

Previous findings have already defined many types of clusters, either in free beam or on a surface. Some of them have been confirmed or have been at least shown to be plausible in this thesis. However, it has been demonstrated that the size evolution of clusters on surfaces is more complex for noble metals like silver than anticipated. Sudden height changes and inter-

mediate stable sizes have been shown to exist. In addition to that there are hints that the orientation of clusters heavily depends on the surface and even slight disturbances might cause very different outcomes. The thermal stability of clusters depends on many factors, some of which being the surface structure, cluster or island size. In some cases a high mobility of clusters has been observed, which lead to coalescence. In other cases decay processes, which are very specific to the environment, have been studied. As measurements indicated, a strong cluster size dependence of the electronic structure was present, partly confirming previous findings.

The initial approach of this thesis, which was a very thorough investigation of a well defined sample system with reproducible environmental conditions, has been vindicated as our findings demonstrate. As of now many problems remain and still better devices and experimental setups are necessary. Some of these will be discussed in the next section.

5.5 Outlook

This section will present future plans for new devices or experimental setups. Note that during the course of this thesis a lot more improvements were thought out that have not been realized yet. However, the next sections will focus on already started projects or the most promising ideas.

5.5.1 Devices

There is room for improvement of the Preparation Chamber's **manipulator**. It is quite close to many sensitive components. Because it is moved constantly back and forth, detrimental collisions can occur. To prevent this, a circuit could be built that would instantly stop the electric motor of the manipulator if it touches other devices. Because nearly every component is metallic and firmly grounded, this could be done by detecting a short circuit as soon as the manipulator touches another part of the machine.

Working with the most important new device, the **Movable Focus Lens**, has demonstrated that the functionality can be expanded. It is probable that the UPS focus is still larger than the deposition spot of the MFL. This is unfortunate because this way less clusters can be detected for a coverage below the coalescence limit on the surface and more unwanted surface material, in our case HOPG, is measured. Consequently the overall intensity of a cluster signal is reduced. To solve this problem, the MFL has been retracted from the sample in order to allow a greater scattering of the clusters and thus widen the deposition spot. The results are still inconclusive and it must be investigated if such an action compromises the positioning of the spot. Another possibility to increase the spot diameter is the widening of the borehole of the MFL. Furthermore an array of lenses with varying boreholes could be constructed, which would allow a greater choice in the selection of a fitting diameter.

Another device that facilitates UPS measurements is an already built but as yet untested **argon gas-discharge lamp**, which shall serve as photon source for UPS. The current helium

gas-discharge lamp delivers a photon energy of 21.22 *eV*. In addition to that two satellites are produced at 23.09 *eV* and 23.74 *eV* with 0.5% and 2% intensity of the main line, respectively [202]. Consequently echos of the main spectrum are produced, which deteriorate the measurement to a certain degree [203]. Argon encounters this problem with much more intense satellites so that it is normally not used as a photon source. However, a new stainless steel jacket has been constructed for the actual gas-discharge lamp. This is thought to prevent argon gas from entering the Preparation Chamber, otherwise the gas would adsorb on cooled samples and thus hamper the measurement tremendously. In order to allow the photons to get into the chamber, a window consisting of a lithium fluoride crystal has been constructed. In addition to that it has the ability to absorb photons above a certain energy. When heated to 370 *K*, all unwanted lines are cut off so that only the desired 11.62 *eV* line remains. Note that with a thickness of 1 *mm* the intensity of the desired line is reduced by a factor of *5* [203]. In our case the window has a thickness of 0.3 *nm*.

Figure 5.1 shows several argon lines, which are cut off by heating the window. Figure 5.2 provides an illustration of the jacket. The actual gas-discharge lamp is located inside. Heating and temperature detection of the window as well as first leak tests proved to be successful. In a next step the performance under vacuum conditions has to be tested.

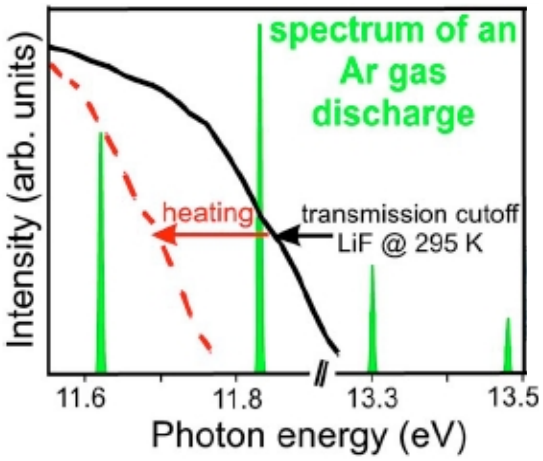

Figure 5.1: Vacuum ultraviolet spectrum of an Ar gas-discharge lamp. The black line shows the transmission threshold at room temperature. The cutoff is shifted to lower energies by heating [204].

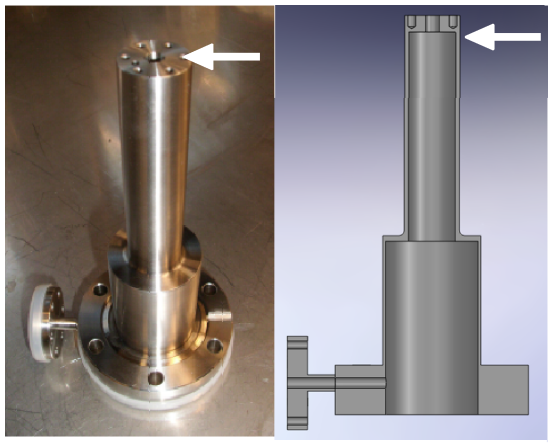

Figure 5.2: Photograph of the new stainless steel jacket for the Ar gas-discharge lamp (left). The position of the lithium fluoride window is marked by white arrows. A schematic profile of the same device is depicted on the right.

As mentioned in section 2.3 on page 100, STS experiments encountered numerous problems. It is suspected that a digital **lock-in amplifier and a new compensator electronics** would be able to reduce this effect. With the modulation of the tunneling voltage by an alternating reference and the use of a lock-in amplifier, disturbances unrelated to the tunneling current can be identified and filtered. However, the STM apparatus encompasses wires with close proximity, which tend to influence each other. As soon as a bias is applied and thus an electrical current is flowing, the other one serves as capacitor which leads to the measurement of a non-existing tunneling current.

To solve this problem a compensator electronics is to be built. It basically works as an inverse amplifier, so it is able to erase the disturbance current. Both the digital lock-in amplifier and the compensator electronics have been tested by other groups and were found to work in the desired fashion [205].

5.5.2 Experiments

Up until now UPS experiments are in an early stage. It was aimed to understand the behavior of copper and silver clusters of different sizes under varying environmental conditions. With this achieved the long term goal of the experiments can come into focus again. As discussed in section 1.1.1.2 on page 6, noble metal clusters can be described by a shell model. Photoelectron spectra can provide a "fingerprint" that reflects the **electronic structure** [118]. It is hoped that future experiments are able to visualize quantized states of small clusters and thus provide a much more detailed picture of the transition to bulk properties.

With an intensive investigation of silver as a cluster material, future experiments will be more focused on **copper**. This is done for two reasons: First, the height distribution as well as thermal stability of copper clusters on varying substrates, like C_{60} or bare Au(111), enables a direct comparison with silver under identical conditions. This way the influence of the material on the observed effects can be isolated. Second, in UPS experiments prominent band structure effects are expected to be represented by peaks closer to the Fermi level compared to silver. This coincides well with the reduced photon energy of the new Ar gas-discharge lamp.

As yet very early experiments have been conducted using copper clusters. Cu_{34}, Cu_{55}, Cu_{58}, Cu_{71} and Cu_{92} have been **deposited onto an HOPG** surface using similar methods and deposition pattern to those described in section 4.1.3.1 on page 137. Spectra have been gathered for *125 K* before and after annealing the sample at higher temperatures. Because only low d-band intensities could be detected, it is aimed to find out at which cluster coverage density coalescence occurs so that the amount of deposited material can be maximized accordingly. One way to achieve this is to lower the temperature as much as possible. However, 125 *K* was the minimum temperature possible before foreign material adsorbed. As mentioned before, the new Ar gas-discharge lamp may be an important asset for that reason. This is because most of the foreign material most probably stems from the gas of the discharge lamp that floods the Preparation Chamber. By sealing off the connection of lamp and chamber, this problem is hopefully solved.

Furthermore the measurement and **subtraction of bare HOPG** has to be optimized. First experiments measuring HOPG before deposition at the same position as the following cluster spot proved successful. The succeeding subtraction process produces less errors than the usual method of choosing a nearby HOPG spectrum as reference. For that, however, the positioning of the sample relative to the manipulator must be highly precise. Thus a thorough comparison of deposition coordinates with measurement coordinates must be conducted in order to get them as close as possible in future experiments.

In earlier experiments **angle-resolved UPS** has been tested. It is suspected that deviations in the electronic band structure of silver or copper, which are angle dependent due to the deviating momentum of the electrons, can be visualized. While differences in the spectra could

not be identified at this point, similar experiments shall be repeated with copper clusters at lower temperatures.

Furthermore measurement of **Cu clusters on C_{60}/Au(111)** have been conducted. Setup and deposition pattern resemble those described in section 2.2.4 on page 90. This experiment aims at gathering height information on copper clusters on a C_{60} surface. For example the existence of changes in the cluster height at a certain number of atoms, identified in the section mentioned above, is to be validated or refuted for copper. While first results point to such an effect, further evaluation is needed. Additional experiments might be able to map a wider range of heights and produce a large picture of the size evolution of copper, which can than be directly compared to that of silver. Note that copper atoms are similar in electronic properties to silver atoms but smaller in size. Thus the resulting clusters are also smaller so that they may be positioned differently on a C_{60} surface while possibly displaying a comparable electronic behavior. This may help to differentiate electronic and geometric effects, which can only be distinguished with difficulties in an STM measurement.

Another idea for the investigation of a **size dependent cluster height** revolves around the compensation of tip-induced changes in measured cluster height. In addition to depositing 9 sizes in a row, each size shall be mixed with an additional always identical cluster size. That way each height measurement has a reference so that a correction of the results is possible.

Of similar interest is the **thermal stability of Cu cluster** on one or multiple monolayers of C_{60} on Au(111). For once observed decay processes computed and measured with silver clusters, can be repeated with copper. Differences and similarities can help to further characterize the sample system. This includes energy and diffusion barriers as well as possible effects of the deviating geometries of silver and copper.

Another experiment that can be repeated using copper as a cluster material is the deposition of **clusters directly onto Au(111)**. Similar data could be collected and directly compared to the results for silver. MD and DFT simulations could be conducted for this material and further validate previous results. It is also possible to exchange the substrate material. Silver clusters on a silver substrate or copper clusters on a copper substrate would have the benefit of simplifying the system for molecular dynamic analyses.

Future **STS** measurements using the new digital lock-in amplifier and compensation electronics shall be conducted on silver as well as copper clusters. The experiments of this work illustrate the existing difficulties in distinguishing geometric and electronic effects on the cluster in combination with a surface. More complex interactions prevent an easy separation of the mentioned effects while simulations have general difficulties with manifold systems. This is probably one reason why until now mainly simple systems involving clusters and surfaces are understood by the scientific community. STS is potentially able to fixate many geometric parameters of a highly complex system while simultaneously mapping the electronic structure of the object of interest. Note that exactly this fixating of parameters requires a high precision, which makes this method susceptible to experimental sources of errors like vibrations, thermal drift effects and tip-cluster interaction.

It is hoped that future experiments will be able to **combine many of the experimental methods** and thus help to get a more general view on cluster-surface interactions without the need to separate the experimental techniques according to the strength of interaction. We have tried this several times in the past with mixed results. For example, noble gas films have been created on top of HOPG, which enabled measurements using STM. They were later desorbed so that UPS measurement on a slightly altered system could be conducted. Another approach used nano pits on HOPG, which fixated clusters so that STM experiments were possible. However, each of these approaches has the downside of restricting the freedom of the experimenter in choosing a well defined sample system. The importance of that has been highlighted in this thesis. In general a greater sensitivity of the devices in use must be achieved so that masked spectra in UPS for moderate cluster-surface interaction or weakly bound clusters can be analyzed in STM. In addition to that new surface and cluster materials can be considered that are of special use in the mentioned applications.

The **general goal** of our experiments is the investigation of nanoscopic systems on an atomic level. Despite our limited capacities today, we were already able to investigate certain mass selected clusters atom by atom. It would be a great enhancement to not only be able to measure geometric properties but simultaneously investigate changes of the electronic structure for few atom changes in cluster size. For clusters in a free beam this is demonstrated for a number of systems in the literature. However, for clusters on surfaces there are still no fully fledged methods so that this field is still in the stage of pioneering work.

6 Appendix

6.1 STS Spectra of Ag_{55}, Ag_{88}, Ag_{138} on 1 ML C_{60}/Au(111)

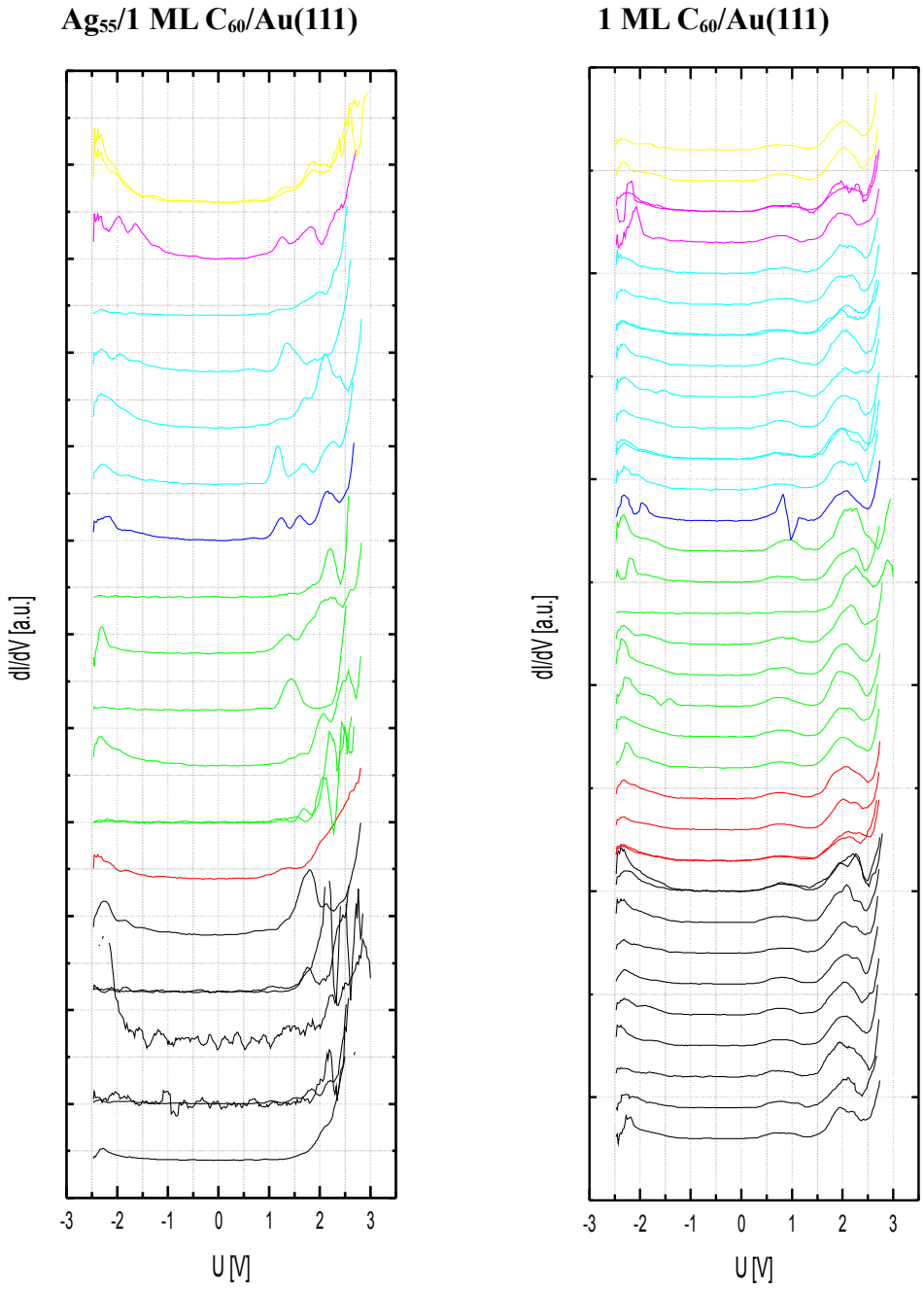

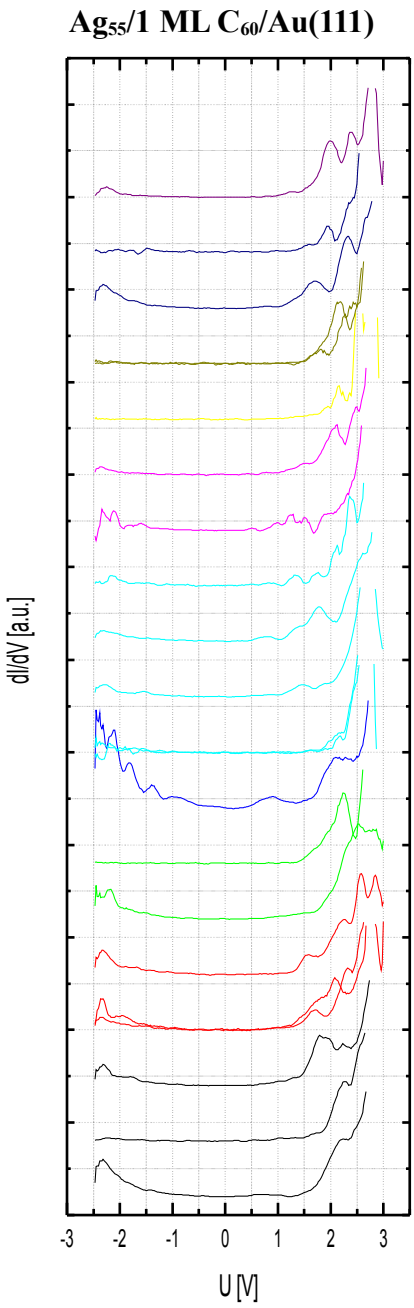
Ag55/1 ML C60/Au(111)
dI/dV [a.u.]
-3
-2
-1
0
1
2
3
U [V]

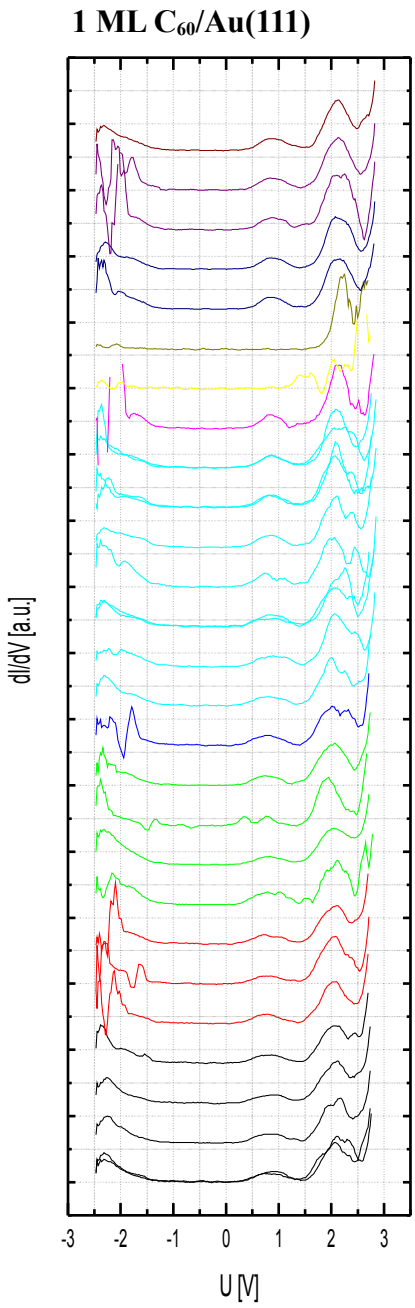
1 ML C60/Au(111)
dI/dV [a.u.]
-3
-2
-1
0
1
2
3
U [V]

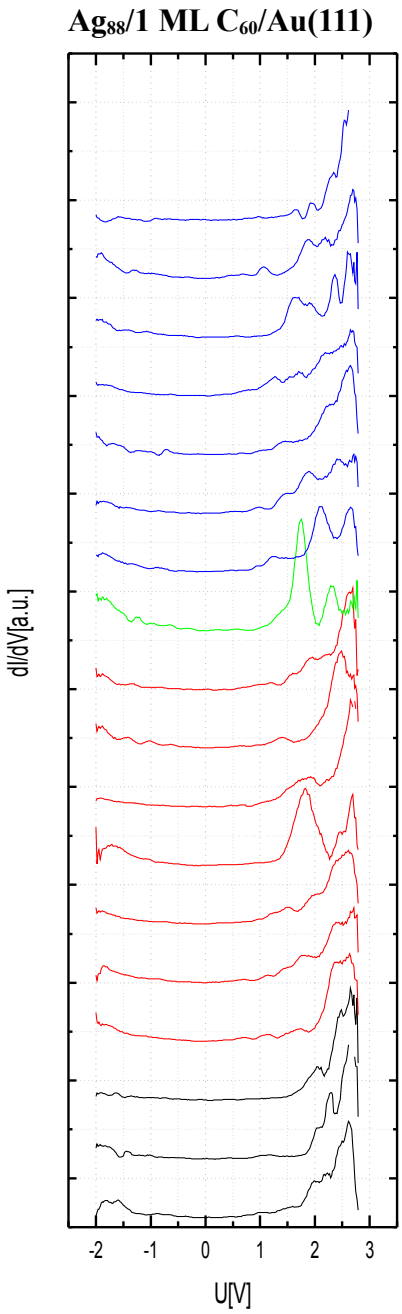
Ag88/1 ML C60/Au(111)
dI/dV[a.u.]
-2
-1
0
1
2
3
U[V]

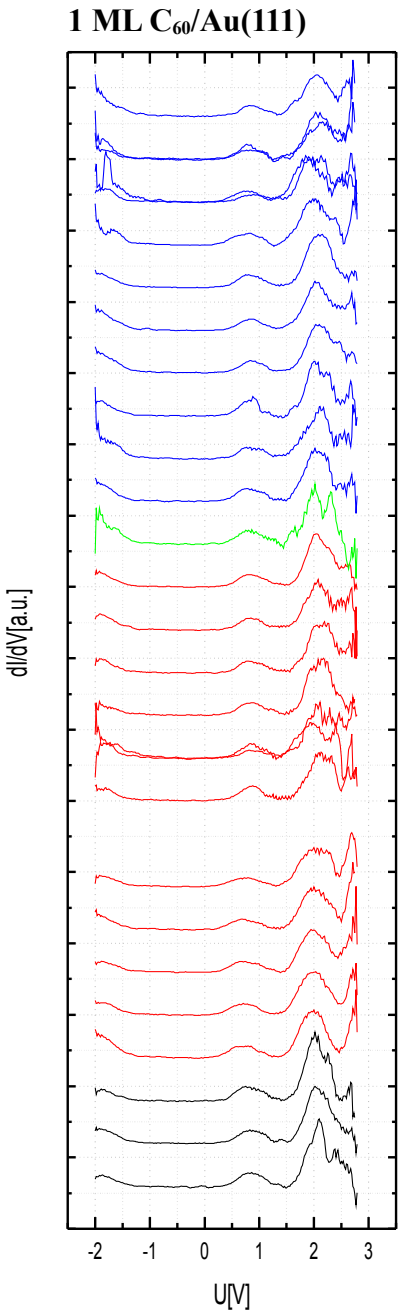
1 ML C60/Au(111)
dI/dV[a.u.]
-2
-1
0
1
2
3
U[V]

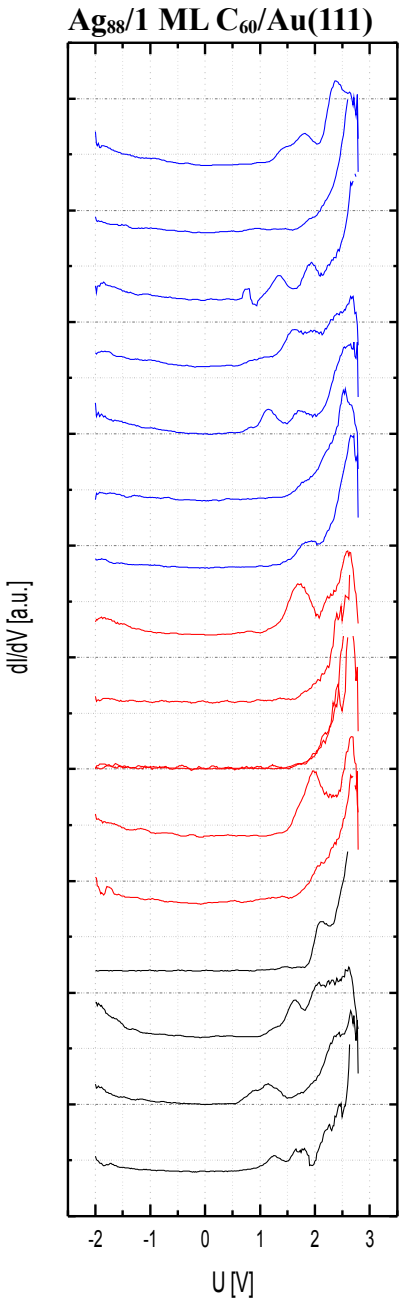
Ag88/1 ML C60/Au(111)
dI/dV [a.u.]
-2
-1
0
1
2
3
U [V]

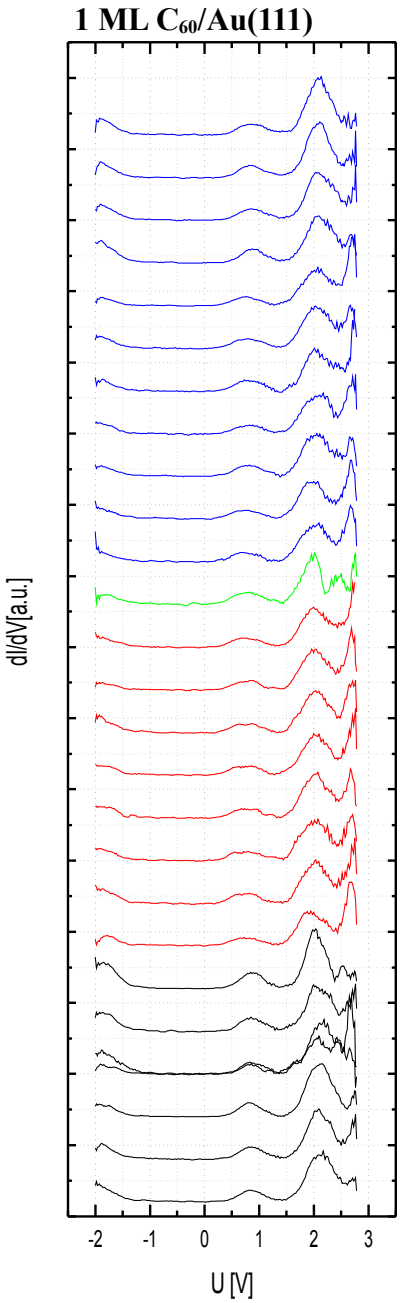
1 ML C60/Au(111)
dI/dV[a.u.]
-2
-1
0
1
2
3
U [V]

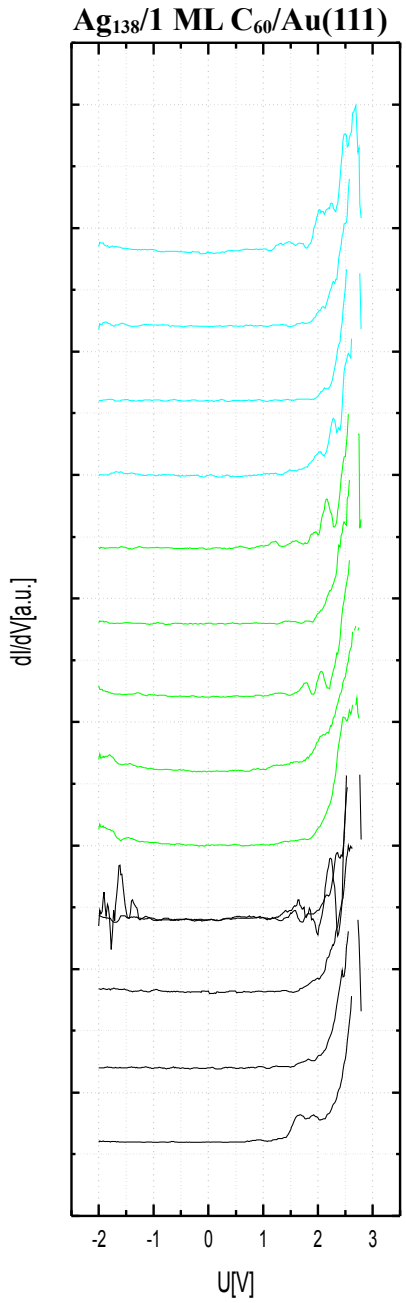
Ag138/1 ML C60/Au(111)
dI/dV[a.u.]
-2
-1
0
1
2
3
U[V]

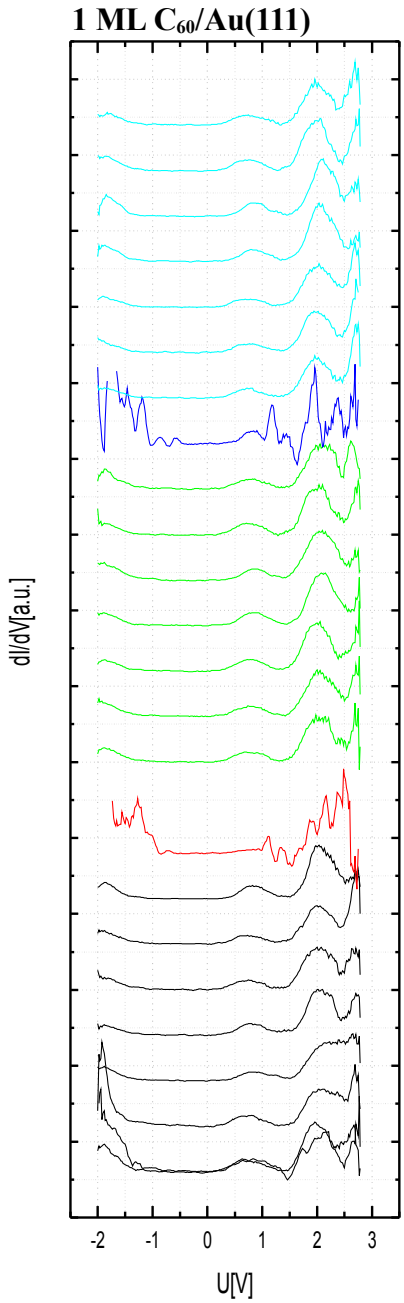
1 ML C60/Au(111)
dI/dV[a.u.]
-2
-1
0
1
2
3
U[V]

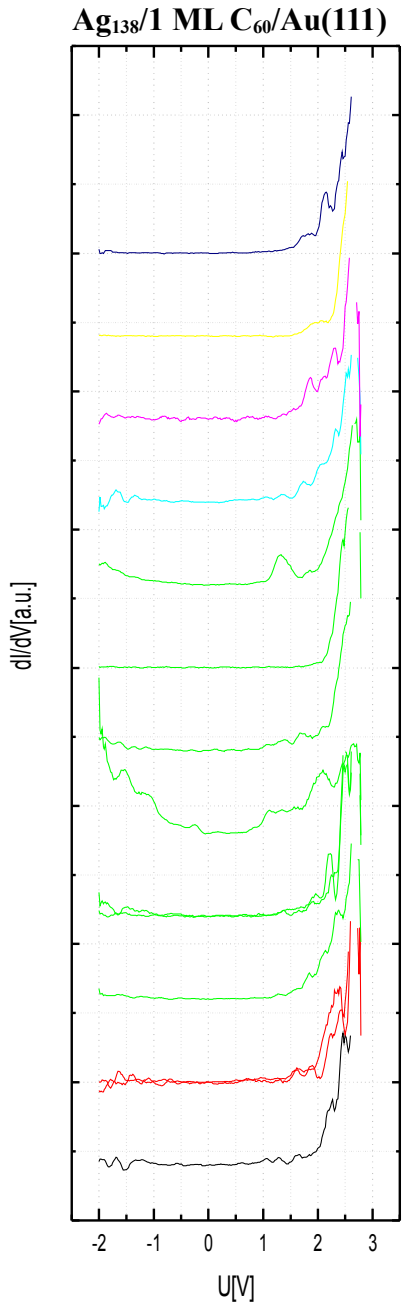
Ag138/1 ML C60/Au(111)
dI/dV[a.u.]
-2
-1
0
1
2
3
U[V]

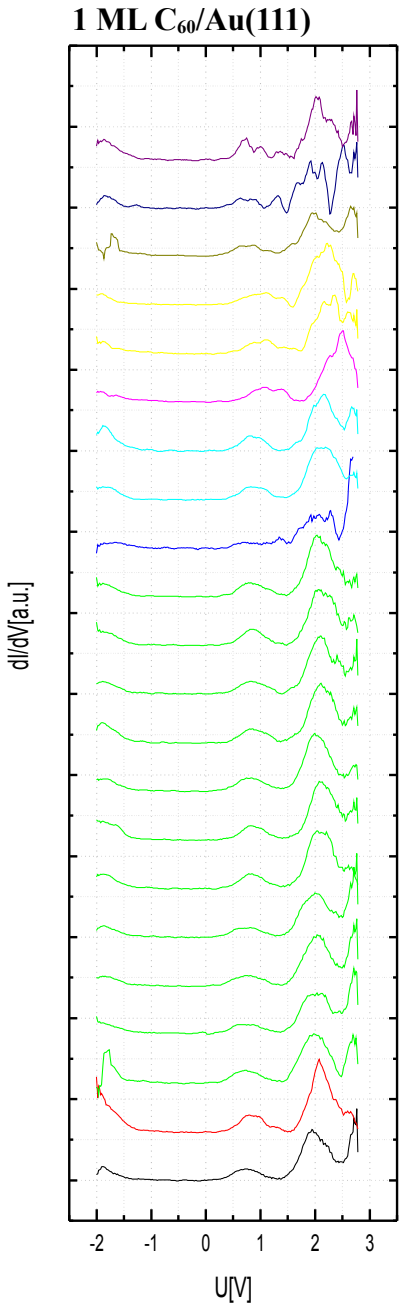
1 ML C60/Au(111)
dI/dV[a.u.]
-2
-1
0
1
2
3
U[V]

7 References

[1] G. Binnig and H. Rohrer,
Scanning tunneling microscopy,
Surface Science **126**, 236-244 (1983)

[2] G. Binnig, H. Rohrer, C. Gerber, and E. Weibel,
Tunneling through a controllable vacuum gap,
Applied Physics Letters **40**, 178-180 (1982)

[3] G. Binnig, H. Rohrer, C. Gerber, and E. Weibel,
Surface Studies by Scanning Tunneling Microscopy,
Phys. Rev. Lett. **49**, 57 (1982)

[4] H. Haberland,
Cluster. In *Lehrbuch Der Experimentalphysik*,
de Gruyter (1992)

[5] W. Lu and C. M. Lieber,
Nanoelectronics from the bottom up,
Nature Materials **6**, 841-850 (2007)

[6] J. Bansmann, S. H. Baker, C. Binns, J. A. Blackman, J.-P. Bucher, J. Dorantes-Dávilae, V. Dupuis, L. Favre, D. Kechrakos, A. Kleibert, et al,
Magnetic and structural properties of isolated and assembled clusters,
Surface Science Reports **56**, 189-275 (2005)

[7] D. Suter and K. Lim,
Scalable architecture for spin-based quantum computers with a single type of gate,
Phys. Rev. A **65**, 052309 (2002)

[8] S. Vajda, M. J. Pellin, J. P. Greeley, C. L. Marshall, L. A. Curtiss, G. A. Ballentine, J. W. Elam, S. Catillon-Mucherie, P. C. Redfern, F. Mehmood, et al,
Subnanometre platinum clusters as highly active and selective catalysts for the oxidative dehydrogenation of propane,
Nature Materials **8**, 213-216 (2009)

[9] A. Sanchez, S. Abbet, U. Heiz, W.-D. Schneider, H. Häkkinen, R. N. Barnett, and U. Landman,
When Gold Is Not Noble: Nanoscale Gold Catalysts,
J. Phys. Chem. A **103**, 9573-9578 (1999)

[10] B. Salisbury, W. Wallace, and R. Whetten,
Low-temperature activation of molecular oxygen by gold clusters: a stoichiometric process correlated to electron affinity,
Chemical Physics **262**, 131-141 (2000)

[11] U. Heiz and E. L. Bullock,
Fundamental aspects of catalysis on supported metal clusters,
Journal of Materials Chemistry **14**, 564-577 (2004)

[12] J. van Lith, A. Lassesson, S. A. Brown, M. Schulze, J. G. Partridge, and A. Ayesh,
A hydrogen sensor based on tunneling between palladium clusters,
Applied Physics Letters **91**, 181910-181910-3 (2007)

[13] L. Shang and S. Dong,
Silver nanocluster-based fluorescent sensors for sensitive detection of Cu(II),
Journal of Materials Chemistry **18**, 4636-4640 (2008)

[14] R. S. Niranjan, V. A. Chaudhary, I. S. Mulla, and K. Vijayamohanan,
A novel hydrogen sulfide room temperature sensor based on copper nanocluster functionalized tin oxide thin films,
Sensors and Actuators B: Chemical **85**, 26-32 (2002)

[15] C. Hrelescu, J. Stehr, M. Ringler, R. A. Sperling, W. J. Parak, T. A. Klar,
and J. Feldmann,
DNA Melting in Gold Nanostove Clusters†,
J. Phys. Chem. C **114**, 7401-7411 (2011)

[16] V. P. Zharov, E. N. Galitovskaya, C. Johnson, and T. Kelly,
Synergistic enhancement of selective nanophotothermolysis with gold nanoclusters: Potential for cancer therapy,
Lasers in Surgery and Medicine **37**, 219-226 (2005)

[17] S. Johnson, H. J. Todd, A. Chalmers, and J. Walker,
English dictionary,
Nathan Hale (1835)

[18] J. Daintith,
A dictionary of chemistry,
Oxford University Press (2008)

[19] K. Kopitzki,
Einführung in die Festkörperphysik,
Teubner Taschenbücher Physik (1993)

[20] M. D. Morse,
Clusters of transition-metal atoms,
Chemical Reviews **86**, 1049-1109 (1986)

[21] A. L. Mackay,
A dense non-crystallographic packing of equal spheres,
Acta Crystallographica **15**, 916-918 (1962)

[22] O. Echt, K. Sattler, and E. Recknagel,
Magic Numbers for Sphere Packings: Experimental Verification in Free Xenon Clusters,
Phys. Rev. Lett. **47**, 1121-1124 (1981)

[23] G. Czycholl,
Theoretische Festkörperphysik,
Springer (2008)

[24] W. D. Knight, K. Clemenger, W. A. de Heer, W. A. Saunders, M. Y. Chou, and M. L. Cohen,
Electronic Shell Structure and Abundances of Sodium Clusters,
Phys. Rev. Lett. **52**, 2141-2143 (1984)

[25] W. A. de Heer,
Confinement and Size Effects in Free Metal Clusters. In *Metal Clusters at Surfaces*,
Springer Berlin Heidelberg, Berlin, Heidelberg (2000), pp. 1-35

[26] W. A. de Heer,
The physics of simple metal clusters: experimental aspects and simple models,
Rev. Mod. Phys. **65**, 611-676 (1993)

[27] U. Heiz and W.-D. Schneider,
Physical Chemistry of Supported Clusters. In *Metal Clusters at Surfaces*
Springer Berlin Heidelberg, Berlin, Heidelberg (2000), pp. 237-273

[28] C. Mortimer,
Chemie,
Thieme Verlag (2003)

[29] W. A. de Heer, W. D. Knight, M. Y. Chou, and M. L. Cohen,
Electronic Shell Structure and Metal Clusters. In *Advances in Research and Applications*
Academic Press (1987), pp. 93-181

[30] M. Moseler, B. Huber, H. Häkkinen, U. Landman, G. Wrigge, M. A. Hoffmann, and B. v. Issendorff,
Thermal effects in the photoelectron spectra of Na_N^- clusters (N=4-19),
Phys. Rev. B **68**, 165413 (2003)

[31] B. Huber and M. Moseler,
Structural evolution of the sodium cluster anions Na_{20}^--Na_{57}^-,
Phys. Rev. B **80**, 235425 (2009)

[32] J. A. Alonso,
Structure and properties of atomic nanoclusters,
Imperial College Press (2005)

[33] J. P. K. Doye and S. C. Hendy,
On the structure of small lead clusters,
The European Physical Journal D - Atomic, Molecular and Optical Physics **22**, 99-107 (2003)

[34] H.S. Lim, C.K. Ong, and F. Ercolessi,
Stability of face-centered cubic and icosahedral lead clusters,
Surface Science **269-270**, 1109-1115 (1992)

[35] R. Kelting, R. Otterstätter, P. Weis, N. Drebov, R. Ahlrichs, and M. M. Kappes,
Structures and energetics of small lead cluster ions,
J. Chem. Phys. **134**, 024311 (2011)

[36] K.-M. Ho, A. A. Shvartsburg, B. Pan, Z.-Y. Lu, C.-Z. Wang, J. G. Wacker,
J. L. Fye, and M. F. Jarrold,
Structures of medium-sized silicon clusters,
Nature **392**, 582-585 (1998)

[37] A. A. Shvartsburg and M. F. Jarrold,
Tin clusters adopt prolate geometries,
Phys. Rev. A **60**, 1235-1239 (1999)

[38] L.-F. Cui, X. Huang, L.-M. Wang, D. Y. Zubarev, A. I. Boldyrev, J. Li, and L.-S. Wang,
Sn_{122}^{-}: Stannaspherene,
Journal of the American Chemical Society **128**, 8390-8391 (2006)

[39] G. A. Breaux, C. M. Neal, B. Cao, and M. F. Jarrold,
Tin clusters that do not melt: Calorimetry measurements up to 650 K,
Phys. Rev. B **71**, 073410 (2005)

[40] A. A. Shvartsburg and M. F. Jarrold,
Solid Clusters above the Bulk Melting Point,
Phys. Rev. Lett. **85**, 2530-2532 (2000)

[41] P. Jackson, I. G. Dance, K. J. Fisher, G. D. Willett, and G. E. Gadd,
Mass spectrometry and density functional studies of neutral and anionic tin clusters,
International Journal of Mass Spectrometry and Ion Processes **157-158**, 329-343 (1996)

[42] C. Majumder, V. Kumar, H. Mizuseki, and Y. Kawazoe,
Small clusters of tin: Atomic structures, energetics, and fragmentation behavior,
Phys. Rev. B **64**, 233405 (2001)

[43] A. Lechtken, N. Drebov, R. Ahlrichs, M. M. Kappes, and D. Schooss,
Communications: Tin cluster anions (Sn_n^-, n=18, 20, 23, and 25) comprise dimers of stable subunits,
J. Chem. Phys. **132**, 211102 (2010)

[44] R. M. Olson, S. Varganov, M. S. Gordon, H. Metiu, S. Chretien, P. Piecuch, K. Kowalski, S. A. Kucharski, and M. Musial,
Where Does the Planar-to-Nonplanar Turnover Occur in Small Gold Clusters?,
Journal of the American Chemical Society **127**, 1049-1052 (2005)

[45] X. Xing, B. Yoon, U. Landman, and J. H. Parks,
Structural evolution of Au nanoclusters: From planar to cage to tubular motifs,
Phys. Rev. B **74**, 165423 (2006)

[46] W. Fa, C. Luo, and J. Dong,
Bulk fragment and tubelike structures of Au_N (N=2-26),
Phys. Rev. B **72**, 205428 (2005)

[47] S. Bulusu and X. C. Zeng,
Structures and relative stability of neutral gold clusters: Au_n (n=15–19),
J. Chem. Phys. **125**, 154303 (2006)

[48] D. Tian and J. Zhao,
Competition Among fcc-Like, Double-Layered Flat, Tubular Cage, and Close-Packed Structural Motifs for Medium-Sized Au_n (n = 21−28) Clusters,
J. Phys. Chem. A **112**, 3141-3144 (2008)

[49] M. P. Johansson, D. Sundholm, and J. Vaara,
Au_{32}: A 24-Carat Golden Fullerene,
Angewandte Chemie International Edition **43**, 2678-2681 (2004)

[50] J. Wang, J. Jellinek, J. Zhao, Z. Chen, R. B. King, and P. von Ragué Schleyer,
Hollow Cages versus Space-Filling Structures for Medium-Sized Gold Clusters: The Spherical Aromaticity of the Au_{50} Cage,
J. Phys. Chem. A **109**, 9265-9269 (2005)

[51] I. L. Garzón, K. Michaelian, M. R. Beltrán, A. Posada-Amarillas, P. Ordejón, E. Artacho, D. Sánchez-Portal, and J. M. Soler,
Lowest Energy Structures of Gold Nanoclusters,
Phys. Rev. Lett. **81**, 1600-1603 (1998)

[52] D. Tian, J. Li, Y. Zhao, J. Zhao, and X. Guo,
Structural evolution of Au_n (n=29–35) clusters: A transition from hollow cage to amorphous packing,
Computational Materials Science **50**, 2359-2362 (2011)

[53] G. A. Eiceman and Z. Karpas,
Ion mobility spectrometry,
CRC Press (2005)

[54] Y. A. Zolotov,
Ion mobility spectrometry,
Journal of Analytical Chemistry **61**, 519-519 (2006)

[55] A. Kiyani, M. Abdollahzadeh, S. M. Sadat Kiai, and A. R. Zirak,
Designing of a Quadrupole Paul Ion Trap,
Journal of Fusion Energy **30**, 291-293 (2011)

[56] M. Maier-Borst, D. B. Cameron, M. Rokni, and J. H. Parks,
Electron diffraction of trapped cluster ions,
Phys. Rev. A **59**, R3162-R3165 (1999)

[57] Y. Negishi, H. Kawamata, A. Nakajima, and K. Kaya,
Photoelectron spectroscopy of tin and lead cluster anions: application of halogen-doping method,
Journal of Electron Spectroscopy and Related Phenomena **106**, 117-125 (2000)

[58] G. Ganteför, M. Gausa, K. H. Meiwes-Broer, and H. O. Lutz,
Photoemission from tin and lead cluster anions,
Zeitschrift für Physik D Atoms, Molecules and Clusters **12**, 405-409 (1989)

[59] H.R. Hertz,
Über den Einfluß des ultravioletten Lichtes auf die elektrische Entladung,
Ann. Phys. u. Chem. **31**, 983-1000 (1887)

[60] A. Einstein,
Über einen die Erzeugung und Verwandlung des Lichtes betreffenden heuristischen Gesichtspunkt,
Annalen der Physik **322**, 132-148 (1905)

[61] P. J. Mohr, B. N. Taylor, and D. B. Newell,
CODATA recommended values of the fundamental physical constants: 2006,
Reviews of Modern Physics **80**, 633-730 (2008)

[62] H. Hövel and I. Barke,
Morphology and electronic structure of gold clusters on graphite: Scanning-tunneling techniques and photoemission,
Progress in Surface Science **81**, 53-111 (2006)

[63] C. Westphal,
Meßmethoden in der Oberflächenphysik: Von reinen Kristalloberflächen zu biologisch relevanten Molekülen,
Vorlesungsskript, TU Dortmund (2008/09)

[64] S. Hüfner,
Photoelectron spectroscopy: principles and applications,
Springer (2003)

[65] W. Harbich,
Collision of Clusters with Surfaces
Springer Berlin Heidelberg, Berlin, Heidelberg (2000), pp. 107-145

[66] F. Ding, A. Rosen, S. Curtarolo, and K. Bolton,
Modeling the melting of supported clusters,
Applied Physics Letters **88**, 133110-133110-3 (2006)

[67] T. Castro, R. Reifenberger, E. Choi, and R. P. Andres,
Size-dependent melting temperature of individual nanometer-sized metallic clusters,
Phys. Rev. B **42**, 8548-8556 (1990)

[68] Y. Joo Lee, E.-K. Lee, S. Kim, and R. M. Nieminen,
Effect of Potential Energy Distribution on the Melting of Clusters,
Phys. Rev. Lett. **86**, 999-1002 (2001)

[69] F. Ghaleh, R. Köster, H. Hövel, L. Bruchhaus, S. Bauerdick, J. Thiel, and R. Jede,
Controlled fabrication of nanopit patterns on a graphite surface using focused ion beams and oxidation,
J. Appl. Phys. **101**, 044301 (2007)

[70] H. Cercellier, C. Didiot, Y. Fagot-Revurat, B. Kierren, L. Moreau, D. Malterre, and F. Reinert,
Interplay between structural, chemical, and spectroscopic properties of Ag/Au(111) epitaxial ultrathin films: A way to tune the Rashba coupling,
Phys. Rev. B **73**, 195413 (2006)

[71] P. Melinon, B. Prevel, V. Dupuis, A. Perez, B. Champagnon, Y. Guyot, M. Boudeulle, M. Pellarin, P. Dugourd, and M. Broyer,
New phases of amorphous carbon and silicon films obtained by low energy cluster beam deposition,
Materials Science and Engineering A **217-218**, 69-73 (1996)

[72] P. Melinon, V. Paillard, V. Dupuis, A. Perez, and P. Jensen,
From free clusters to cluster-assembled materials,
International journal of modern physics B **9**, 339-397 (1995)

[73] H. Haberland, Z. Insepov, and M. Moseler,
Molecular-dynamics simulation of thin-film growth by energetic cluster impact,
Phys. Rev. B **51**, 11061-11067 (1995)

[74] G. Kleer, E. Schäffer, M. Bodmann, J. Kraft, Y. Qiang, and H. Haberland,
Hartstoffschichten für das Pressen und Prägen von Gläsern bei hohen Temperaturen,
Materialwissenschaft und Werkstofftechnik **29**, 545-554 (1998)

[75] J. Nordiek, M. Moseler, and H. Haberland,
Energetic impact of Cu-clusters on Cu-surfaces,
Radiation Effects & Defects in Solids **142**, 27-38 (1997)

[76] H.-P. Cheng and U. Landman,
Controlled Deposition, Soft Landing, and Glass Formation in Nanocluster-Surface Collisions,
Science **260**, 1304-1307 (1993)

[77] H.-P. Cheng and U. Landman,
Controlled Deposition and Classification of Copper Nanoclusters,
J. Phys. Chem. **98**, 3527-3537 (1994)

[78] C. L. Cleveland and U. Landman,
Dynamics of Cluster-Surface Collisions,
Science **257**, 355-361 (1992)

[79] T. Raz, I. Schek, M. Ben-Nun, U. Even, J. Jortner, and R. D. Levine,
Dissociation dynamics of diatomic molecules embedded in impact heated rare gas clusters,
J. Chem. Phys. **101**, 8606 (1994)

[80] S. F. Belykh, I. S. Bitensky, D. Mullajanov, and U. K. Rasulev,
Nonlinear effects in cluster emission from solids induced by molecular ion impact,
Nuclear Instruments and Methods in Physics Research Section B: Beam Interactions with Materials and Atoms **129**, 451-458 (1997)

[81] C. Tomaschko, K.-H. Herrmann, J. Käshammer, R. Kügler, C. Schoppmann, and H. Voit,
Enhanced emission of secondary ions from solid surfaces bombarded with MeV polyatomic ions,
Nuclear Instruments and Methods in Physics Research Section B: Beam Interactions with Materials and Atoms **132**, 371-376 (1997)

[82] H. Fernas, H. Bernas, A. Kusnetsov, C. Clerc, L. Dumoulin, and J. Chaumont,
Giant sputtering rates from SiO (SiO_2) irradiated by carbon clusters,
Nuclear Instruments and Methods in Physics Research Section B: Beam Interactions with Materials and Atoms **129**, 436-438 (1997)

[83] G. Betz and W. Husinsky,
Cluster bombardment of solids: A molecular dynamics study,
Nuclear Instruments and Methods in Physics Research Section B: Beam Interactions with Materials and Atoms **122**, 311-317 (1997)

[84] H. Hsieh, R. S. Averback, H. Sellers, and C. P. Flynn,
Molecular-dynamics simulations of collisions between energetic clusters of atoms and metal substrates,
Phys. Rev. B **45**, 4417-4430 (1992)

[85] G. L. Kellogg,
Oscillatory behavior in the size dependence of cluster mobility on metal surfaces: Rh on Rh(100),
Phys. Rev. Lett. **73**, 1833-1836 (1994)

[86] S. Liu, L. Bönig, and H. Metiu,
Effect of small-cluster mobility and dissociation on the island density in epitaxial growth,
Phys. Rev. B, Condensed Matter **52**, 2907-2913 (1995)

[87] S. Khare, N. Bartelt, and T. Einstein,
Diffusion of monolayer adatom and vacancy clusters: Langevin analysis and Monte Carlo simulations of their Brownian motion,
Phys. Rev. Lett. **75**, 2148-2151 (1995)

[88] J. Wen, J. W. Evans, M. C. Bartelt, J. W. Burnett, and P. A. Thiel,
Coarsening mechanisms in a metal film: From cluster diffusion to vacancy ripening,
Phys. Rev. Lett. **76**, 652-655 (1996)

[89] R. Guerra, U. Tartaglino, A. Vanossi, and E. Tosatti,
Ballistic nanofriction,
Nature Materials **9**, 634-637 (2010)

[90] V. N. Popok, I. Barke, E. E. B. Campbell, and K.-H. Meiwes-Broer,
Cluster–surface interaction: From soft landing to implantation,
Surface Science Reports **66**, 347-377 (2011)

[91] V. Bonačić-Koutecký, L. Češpiva, P. Fantucci, and J. Koutecký,
Effective core potential-configuration interaction study of electronic structure and geometry of small neutral and cationic Ag_n clusters: Predictions and interpretation of measured properties,
J. Chem. Phys. **98**, 7981 (1993)

[92] B. Nacer, C. Massobrio, and C. Félix,
Deposition of metallic clusters on a metallic surface at zero initial kinetic energy: Evidence for implantation and site exchanges,
Phys. Rev. B **56**, 10590-10595 (1997)

[93] V. A. Ukraintsev,
Data evaluation technique for electron-tunneling spectroscopy,
Phys. Rev. B **53**, 11176-11185 (1996)

[94] R. Staub, D. Alliata, and C. Nicolini,
Drift elimination in the calibration of scanning probe microscopes,
Review of Scientific Instruments **66**, 2513-2516 (1995)

[95] J. T. Woodward and D. K. Schwartz,
Removing drift from scanning probe microscope images of periodic samples,
Journal of Vacuum Science & Technology B: Microelectronics and Nanometer Structures **16**, 51-53 (1998)

[96] V. Y. Yurov and A. N. Klimov,
Scanning tunneling microscope calibration and reconstruction of real image: Drift and slope elimination,
Review of Scientific Instruments **65**, 1551-1557 (1994)

[97] I. S. Tilinin, M. K. Rose, J. C. Dunphy, M. Salmeron, and M. A. Van Hove,
Identification of adatoms on metal surfaces by STM: experiment and theory,
Surface Science **418**, 511-520 (1998)

[98] M. D. Graef,
Introduction to conventional transmission electron microscopy,
Cambridge University Press (2003)

[99] D. B. Williams and C. B. Carter,
The Transmission Electron Microscope. In *Transmission Electron Microscopy*,
Springer US, Boston, MA (2009), pp. 3-22

[100] D. C. Rapaport,
The art of molecular dynamics simulation,
Cambridge University Press (2004)

[101] E. K. U. Gross and R. M. Dreizler,
Density functional theory,
Springer (1995)

[102] J. J. Sáenz, J. M. Soler, and N. García,
Evaporation of small clusters of noble gases by ionization,
Surface Science **156**, 121-125 (1985)

[103] G. Chalasinski and M. M. Szczesniak,
Origins of Structure and Energetics of van der Waals Clusters from ab Initio Calculations,
Chemical Reviews **94**, 1723-1765 (1994)

[104] V. A. Parsegian,
Van der Waals forces: a handbook for biologists, chemists, engineers, and physicists,
Cambridge University Press (2006)

[105] P. C. Kelires and J. Tersoff,
Equilibrium alloy properties by direct simulation: Oscillatory segregation at the Si-Ge(100) 2×1 surface,
Phys. Rev. Lett. **63**, 1164-1167 (1989)

[106] Ercolessi, Tosatti, and Parrinello,
Au(100) surface reconstruction,
Phys. Rev. Lett. **57**, 719-722 (1986)

[107] Brommer, Needels, Larson, and Joannopoulos,
Ab initio theory of the Si(111)-(7 x 7) surface reconstruction: A challenge for massively parallel computation,
Phys. Rev. Lett. **68**, 1355-1358 (1992)

[108] M. Amarouche, G. Durand, and J. P. Malrieu,
Structure and stability of Xe^{+}_{n} clusters,
Journal of Chemical Physics **88**, 1010-1018 (1988)

[109] T. D. Märk and P. Scheier,
Production and stability of neon cluster ions up to Ne^{+}_{90},
Chemical Physics Letters **137**, 245-249 (1987)

[110] I. A. Harris, R. S. Kidwell, and J. A. Northby,
Structure of Charged Argon Clusters Formed in a Free Jet Expansion,
Phys. Rev. Lett. **53**, 2390-2393 (1984)

[111] Mark, Leiter, Ritter, and Stamatovic,
Low-energy-electron attachment to oxygen clusters produced by nozzle expansion,
Phys. Rev. Lett. **55**, 2559-2562 (1985)

[112] I. Boustani,
Systematic ab initio investigation of bare boron clusters: Determination of the geometry and electronic structures of B_n (n=2-14),
Phys. Rev. B **55**, 16426-16438 (1997)

[113] E. Hering, R. Martin, and M. Stohrer,
Taschenbuch der Mathematik und Physik,
Springer (2009)

[114] B. I. Rickett and J. H. Payer,
Composition of Copper Tarnish Products Formed in Moist Air with Trace Levels of Pollutant Gas: Hydrogen Sulfide and Sulfur Dioxide/Hydrogen Sulfide,
Journal of The Electrochemical Society **142**, 3723-3728 (1995)

[115] D. C. Frost, A. Ishitani, and C. A. McDowell,
X-ray photoelectron spectroscopy of copper compounds,
Molecular Physics **24**, 861-877 (1972)

[116] C. L. Pettiette, S. H. Yang, M. J. Craycraft, J. Conceicao, R. T. Laaksonen, O. Cheshnovsky, and R. E. Smalley,
Ultraviolet photoelectron spectroscopy of copper clusters,
Journal of Chemical Physics **88**, 5377-5382 (1988)

[117] D. G. Leopold, J. Ho, and W. C. Lineberger,
Photoelectron spectroscopy of mass-selected metal cluster anions. I. Cu_n^-, n=1-10,
Journal of Chemical Physics **86**, 1715-1726 (1987)

[118] O. Cheshnovsky, K. J. Taylor, J. Conceicao, and R. E. Smalley,
Ultraviolet photoelectron spectra of mass-selected copper clusters: Evolution of the 3d band,
Phys. Rev. Lett. **64**, 1785-1788 (1990)

[119] L. Ley and M. Cardona,
Photoemission in Solids II: Case Studies,
Springer (1979)

[120] G. Audi, O. Bersillon, J. Blachot, and A. H. Wapstra,
The Nubase evaluation of nuclear and decay properties,
Nuclear Physics A **729**, 3-128 (2003)

[121] A. N. Nesmeĭanov,
Vapor pressure of the chemical elements,
Elsevier Pub. Co. (1963)

[122] C. Kittel,
Einführung in die Festkörperphysik,
Oldenbourg Wissenschaftsverlag (2005)

[123] S. Duffe,
Thermally activated processes and electronic properties of size selected Ag clusters and grown metal islands on C_{60} functionalized surfaces,
Dissertation, Technische Universität Dortmund (2009)

[124] W. T. Read and W. Shockley,
Dislocation Models of Crystal Grain Boundaries,
Phys. Rev. **78**, 275-289 (1950)

[125] C. Wöll, S. Chiang, R. J. Wilson, and P. H. Lippel,
Determination of atom positions at stacking-fault dislocations on Au(111) by scanning tunneling microscopy,
Phys. Rev. B **39**, 7988-7991 (1989)

[126] J. A. DeRose, T. Thundat, L. A. Nagahara, and S. M. Lindsay,
Gold grown epitaxially on mica: conditions for large area flat faces,
Surface Science **256**, 102-108 (1991)

[127] J. V. Barth, H. Brune, G. Ertl, and R. J. Behm,
Scanning tunneling microscopy observations on the reconstructed Au(111) surface: Atomic structure, long-range superstructure, rotational domains, and surface defects,
Phys. Rev. B **42**, 9307-9318 (1990)

[128] H.-J. Güntherodt and R. Wiesendanger,
Scanning tunneling microscopy I: general principles and applications to clean and adsorbate-covered surfaces,
Springer (1994)

[129] O. El-Shazly, S. G. Tawfik, A. K. Ibrahim, I. H. Ibrahim, and E. F. El-Wahidy,
Electrical resistivity and Hall effect of K-$FeCl_3$ graphite intercalation compounds,
Journal of Materials Science **28**, 5040-5044 (1993)

[130] H. S. Nalwa,
Handbook of Organic Conductive Molecules and Polymers: Charge-transfer salts, fullerenes, and photoconductors,
Wiley (1997)

[131] N. Watanabe, T. Nakajimȧ, and H. Touhara,
Graphite fluorides,
Elsevier (1988)

[132] G. Lolli,
Relationship between the micro-structure of cobalt-molybdenum catalysts supported on silica and the selectivity towards single-walled carbon nanotubes,
ProQuest (2007)

[133] E. Osawa,
Superaromaticity,
Kagaku **25**, 854-863 (1970)

[134] H. W. Kroto, J. R. Heath, S. C. O'Brien, R. F. Curl, and R. E. Smalley,
C_{60}: Buckminsterfullerene,
Nature **318**, 162-163 (1985)

[135] W. Krätschmer, L. D. Lamb, K. Fostiropoulos, and D. R. Huffman,
C_{60}: A new form of carbon,
Nature **347**, 354-358 (1990)

[136] G. Schull and R. Berndt,
Orientationally Ordered (7 x 7) Superstructure of C_{60} on Au(111),
Phys. Rev. Lett. **99**, 226105 (2007)

[137] H. Hövel, T. Becker, D. Funnemann, B. Grimm, C. Quitmann, and B. Reihl,
High-resolution photoemission combined with low-temperature STM,
Journal of Electron Spectroscopy and Related Phenomena **88-91**, 1015-1020 (1998)

[138] Karl Jousten,
Wutz Handbuch Vakuumtechnik,
Vieweg +Teubner (2009)

[139] T. Richter,
Untersuchung von deponierten und gewachsenen Silberclustern auf Fullerenschichten mittels Rastertunnelmikroskopie,
Diplomarbeit, Technische Universität Dortmund (2007)

[140] H. Haberland, M. Mall, M. Moseler, Y. Qiang, T. Reiners, and Y. Thurner,
Filling of micron-sized contact holes with copper by energetic cluster impact,
Journal of Vacuum Science & Technology A: Vacuum, Surfaces, and Films **12**, 2925-2930 (1994)

[141] N. Yoshimura,
Vacuum technology: practice for scientific instruments,
Springer (2008)

[142] B. von Issendorff and R. E. Palmer,
A new high transmission infinite range mass selector for cluster and nanoparticle beams,
Review of Scientific Instruments **70**, 4497 (1999)

[143] L. Partyarcha,
Massenselektierte Silbercluster und aufgedampftes Silber auf C_{60}/HOPG und C_{60}/Au(111),
Diplomarbeit, Technische Universität Dortmund (2008)

[144] R. Bitter, T. Mohiuddin, and M. Nawrocki,
LabView advanced programming techniques,
CRC Press/Taylor & Francis Group (2007)

[145] J. J. Berman,
Perl: The Programming Language,
Jones & Bartlett Learning (2008)

[146] A. Krause,
Foundations of GTK+ Development,
Apress (2007)

[147] J. Suzanne, J. P. Coulomb, and M. Bienfait,
Thermodynamics and kinetics of the first monolayer adsorption of xenon on the (0001) graphite face,
Journal of Crystal Growth **31**, 87-91 (1975)

[148] I. Horcas, R. Fernández, J. M. Gómez-Rodríguez, J. Colchero, J. Gómez-Herrero, and A. M. Baro,
WSXM: A software for scanning probe microscopy and a tool for nanotechnology,
Review of Scientific Instruments **78**, 013705 (2007)

[149] S. Duffe, N. Grönhagen, L. Patryarcha, B. Sieben, C. Yin, B. von Issendorff, M. Moseler, and H. Hövel,
Penetration of thin C_{60} films by metal nanoparticles,
Nature Nanotech **5**, 335-339 (2010)

[150] P. Blandin and C. Massobrio,
Diffusion properties and collisional dynamics of Ag adatoms and dimers on Pt(111),
Surface Science **279**, L219-L224 (1992)

[151] A. J. Logsdail and J. Akola,
Interaction of Au_{16} Nanocluster with Defects in Supporting Graphite: A Density-Functional Study,
J. Phys. Chem. C **115**, 15240-15250 (2011)

[152] J. Akola and H. Häkkinen,
Density functional study of gold atoms and clusters on a graphite (0001) surface with defects,
Phys. Rev. B **74**, 165404 (2006)

[153] P. Jensen, X. Blase, and P. Ordejón,
First principles study of gold adsorption and diffusion on graphite,
Surface Science **564**, 173-178 (2004)

[154] N. Miroslawski,
Geometrisch und elektronisch magische Cluster,
Diplomarbeit, Technische Universität Dortmund (2010)

[155] W. Ostwald,
Über die vermeintliche Isomerie des roten und gelben Quecksilberoxyd,
Z. Phys. Chem. **34**, 495 (1900)

[156] K. Morgenstern, G. Rosenfeld, E. Lægsgaard, F. Besenbacher, and G. Comsa,
Measurement of Energies Controlling Ripening and Annealing on Metal Surfaces,
Phys. Rev. Lett. **80**, 556-559 (1998)

[157] K. Morgenstern, G. Rosenfeld, and G. Comsa,
Decay of Two-Dimensional Ag Islands on Ag(111),
Phys. Rev. Lett. **76**, 2113-2116 (1996)

[158] M. Bowker,
Surface science: The going rate for catalysts,
Nature Materials **1**, 205-206 (2002)

[159] T. Irawan, I. Barke, and H. Hövel,
Size-dependent morphology of gold clusters grown on nanostructured graphite,
Appl. Phys. A **80**, 929-935 (2005)

[160] K. Mende,
Geometrische Form und Stabilität von Silberclustern auf Oberflächen untersucht mit Rastertunnelmikroskopie und Photoelektronenspektroskopie,
Diplomarbeit, Technische Universität Dortmund (2010)

[161] J.-G. Lee, J. Lee, T. Tanaka, and H. Mori,
In Situ HREM Observation of Crystalline-to-Gas Transition in Nanometer-Sized Ag Particles,
Phys. Rev. Lett. **96**, 075504 (2006)

[162] H. Hövel, T. Becker, A. Bettac, B. Reihl, M. Tschudy, and E. J. Williams,
Crystalline structure and orientation of gold clusters grown in preformed nanometer-sized pits,
Applied Surface Science **115**, 124-127 (1997)

[163] H. Hövel, B. Grimm, M. Pollmann, and B. Reihl,
Cluster-Substrate Interaction on a Femtosecond Time Scale Revealed by a High-Resolution Photoemission Study of the Fermi-Level Onset,
Phys. Rev. Lett. **81**, 4608-4611 (1998)

[164] J. H. Dil, J. W. Kim, S. Gokhale, M. Tallarida, and K. Horn,
Self-organization of Pb thin films on Cu(111) induced by quantum size effects,
Phys. Rev. B **70**, 045405 (2004)

[165] T. Miller, A. Samsavar, G. E. Franklin, and T.-C. Chiang,
Quantum-Well States in a Metallic System: Ag on Au(111),
Phys. Rev. Lett. **61**, 1404-1407 (1988)

[166] F. J. Himpsel,
Fe on Au(100): Quantum-well states down to a monolayer,
Phys. Rev. B **44**, 5966-5969 (1991)

[167] R. K. Kawakami, E. Rotenberg, H. J. Choi, E. J. Escorcia-Aparicio, M. O. Bowen, J. H. Wolfe, E. Arenholz, Z. D. Zhang, N. V. Smith, and Z. Q. Qiu,
Quantum-well states in copper thin films,
Nature **398**, 132-134 (1999)

[168] T.-C Chiang,
Photoemission studies of quantum well states in thin films,
Surface Science Reports **39**, 181-235 (2000)

[169] P. Segovia, E. G. Michel, and J. E. Ortega,
Quantum Well States and Short Period Oscillations of the Density of States at the Fermi Level in Cu Films Grown on fcc Co(100),
Phys. Rev. Lett. **77**, 3455-3458 (1996)

[170] Y.-F. Zhang, J.-F. Jia, T.-Z. Han, Z. Tang, Q.-T. Shen, Y. Guo, Z. Q. Qiu, and Q.-K. Xue,
Band Structure and Oscillatory Electron-Phonon Coupling of Pb Thin Films Determined by Atomic-Layer-Resolved Quantum-Well States,
Phys. Rev. Lett. **95**, 096802 (2005)

[171] F. Ghaleh,
Characterization of surface defects produced with focused ion beams and exploration of applications for controlled growth of nanostructures,
Dissertation, Technische Universität Dortmund (2009)

[172] R. Otero, A. L. Vázquez de Parga, and R. Miranda,
Observation of preferred heights in Pb nanoislands: A quantum size effect,
Phys. Rev. B **66**, 115401 (2002)

[173] C. M. Wei and M. Y. Chou,
Theory of quantum size effects in thin Pb(111) films,
Phys. Rev. B **66**, 233408 (2002)

[174] A. Arranz, J. F. Sánchez-Royo, J. Avila, V. Pérez-Dieste, P. Dumas, and M. C. Asensio,
Quantum-well states in ultrathin Ag(111) films deposited onto H-passivated Si(111)-(1×1) surfaces,
Phys. Rev. B **65**, 195410 (2002)

[175] R. A. Johnson and G. K. Bhattacharyya,
Statistics: Principles and Methods,
John Wiley and Sons (2009)

[176] G. E. P. Box and M. E. Muller,
A Note on the Generation of Random Normal Deviates,
Ann. Math. Statist. **29**, 610-611 (1958)

[177] F. Furche, R. Ahlrichs, P. Weis, C. Jacob, S. Gilb, T. Bierweiler, and M. M. Kappes,
The structures of small gold cluster anions as determined by a combination of ion mobility measurements and density functional calculations,
J. Chem. Phys. **117**, 6982 (2002)

[178] M. P. Johansson, A. Lechtken, D. Schooss, M. M. Kappes, and F. Furche,
2D-3D transition of gold cluster anions resolved,
Phys. Rev. A **77**, 053202 (2008)

[179] S. Cammelli, D. Lützenkirchen-Hecht, C. Degueldre, J. Bertsch, and R. Frahm,
Polydispersity and EXAFS simulations,
Journal of Physics: Conference Series **190**, 012027 (2009)

[180] O. Kostko, B. Huber, M. Moseler, and B. von Issendorff,
Structure Determination of Medium-Sized Sodium Clusters,
Phys. Rev. Lett. **98**, 043401 (2007)

[181] K. Clemenger,
Ellipsoidal shell structure in free-electron metal clusters,
Phys. Rev. B **32**, 1359-1362 (1985)

[182] H. A. Jahn and E. Teller,
Stability of Polyatomic Molecules in Degenerate Electronic States. I. Orbital Degeneracy,
Proceedings of the Royal Society of London. Series A, Mathematical and Physical Sciences **161**, 220-235 (1937)

[183] S. Duffe, T. Irawan, M. Bieletzki, T. Richter, B. Sieben, C. Yin, B. von Issendorff, M. Moseler, and H. Hövel,
Softlanding and STM imaging of Ag_{561} clusters on a C_{60} monolayer,
The European Physical Journal D **45**, 401-408 (2007)

[184] M. De Menech, U. Saalmann, and M. E. Garcia,
Recovering hidden electronic states using energy-resolved imaging of metal clusters at surfaces,
New J. Phys. **9**, 340 (2007)

[185] P. Davis,
The GIMP for Linux and Unix,
Harold Davis (2000)

[186] J. Jones,
GIMP User's Manual,
Lulu.com (2008)

[187] R. G. Mortimer,
Physical chemistry,
Academic Press (2008)

[188] D. J. Wales, J. P. K. Doye, A. Dullweber, M. P. Hodges, F. Y. Naumkin, F. Calvo, J. Hernández-Rojas, and T. F. a Middleton,
Cambridge Cluster Database,
available at http://www-wales.ch.cam.ac.uk/CCD.html

[189] H. J. C. Berendsen, J. P. M. Postma, W. F. van Gunsteren, A. DiNola, and J. R. Haak,
Molecular dynamics with coupling to an external bath,
J. Chem. Phys. **81**, 3684-3690 (1984)

[190] A. P. Sutton and J. Chen,
Long-range Finnis-Sinclair potentials,
Phil. Mag. Lett. **61**, 139-146 (1990)

[191] H. Rafii-Tabar and A. P. Sulton,
Long-range Finnis-Sinclair potentials for f.c.c. metallic alloys,
Phil. Mag. Lett. **63**, 217-224 (1991)

[192] A. Nakano,
A space-time-ensemble parallel nudged elastic band algorithm for molecular kinetics simulation,
Computer Physics Communications **178**, 280-289 (2008)

[193] G. Henkelman, B. P. Uberuaga, and H. Jónsson,
A climbing image nudged elastic band method for finding saddle points and minimum energy paths,
J. Chem. Phys. **113**, 9901-9904 (2000)

[194] G. Henkelman and H. Jónsson,
Improved tangent estimate in the nudged elastic band method for finding minimum energy paths and saddle points,
J. Chem. Phys. **113**, 9978-9985 (2000)

[195] N. Grönhagen, T. T. Järvi, N. Miroslawski, H. Hövel, and M. Moseler,
in preparation

[196] J. Kliewer, R. Berndt, J. Minár, and H. Ebert,
Scanning tunnelling microscopy and electronic structure of Mn clusters on Ag(111),
Appl. Phys. A **82**, 63-66 (2005)

[197] H. Brune, K. Bromann, H. Röder, K. Kern, J. Jacobsen, P. Stoltze, K. Jacobsen, and J. Nørskov,
Effect of strain on surface diffusion and nucleation,
Phys. Rev. B **52**, R14380-R14383 (1995)

[198] M. P. Seah and W. A. Dench,
Compilation of experimental data determined with various electron energies for a large variety of materials,
Surf. Interface. Anal. I (1979)

[199] B. Wortmann, K. Mende, S. Duffe, N. Grönhagen, B. von Issendorff, and H. Hövel,
Ultraviolet photoelectron spectroscopy of supported mass selected silver clusters,
Phys. Stat. Sol. (b) **247**, 1116–1121 (2010)

[200] H. Hövel,
Clusters on surfaces: high-resolution spectroscopy at low temperatures,
Appl. Phys. A **72**, 295-302 (2001)

[201] H. Hövel, B. Grimm, M. Pollmann, and B. Reihl,
Femtosecond dynamics of final-state effects in the valence band photoemission of silver clusters on a graphite substrate,
The European Physical Journal D **9**, 595-599 (1999)

[202] R. Matzdorf,
Investigation of line shapes and line intensities by high-resolution UV-photoemission spectroscopy - Some case studies on noble-metal surfaces,
Surface Science Reports **30**, 153-206 (1998)

[203] M. Budke and M. Donath,
Ar gas discharge lamp with heated LiF window: A monochromatized light source for photoemission,
Applied Physics Letters **92**, 231918-231918-3 (2008)

[204] A. H. Laufer, J. A. Pirog, and J. R. McNesby,
Effect of Temperature on the Vacuum Ultraviolet Transmittance of Lithium Fluoride, Calcium Fluoride, Barium Fluoride, and Sapphire,
J. Opt. Soc. Am. **55**, 64-66 (1965)

[205] K. Sell, I. Barke, S. Polei, C. Schumann, V. von Oeynhausen, and K. Meiwes-Broer,
Surface photovoltage of Ag nanoparticles and Au chains on Si(111),
Phys. Stat. Sol. (b) **247**, 1087-1094 (2010)

8 Picture Credits

Figure 1.16
http://upload.wikimedia.org/wikipedia/commons/5/50/Graphit_gitter.png
(18.04.11)

Figure 1.17
http://upload.wikimedia.org/wikipedia/commons/5/54/GraphitGitter4.png
(18.04.11)

Figure 1.2
http://upload.wikimedia.org/wikipedia/commons/thumb/9/9c/Icosahedron-golden-rectangles.svg/2000px-Icosahedron-golden-rectangles.svg.png
(28.04.11)

Figure 1.8
http://upload.wikimedia.org/wikipedia/commons/f/f9/ScanningTunnelingMicroscope_schematic.png,
Michael Schmid (29.07.11)

Figure 1.9
http://upload.wikimedia.org/wikipedia/commons/d/d1/Constant_current.svg
(29.07.11)

Figure 1.24
http://www.tulving.com/bullion/2009%201oz%20Silver%20Eagle%20Obv.jpg
(29.07.11)

Acknowledgment

An dieser Stelle möchte ich meinen Dank an all diejenigen richten, die zum Gelingen dieser Arbeit beigetragen haben.

Ich danke Herrn Prof. Dr. Metin Tolan für die Möglichkeit meine Dissertation an diesem Lehrstuhl anfertigen zu können.

Ein besonderer Dank gilt Herrn Dr. Heinz Hövel, der durch seinen unermüdlichen Einsatz, seine fachliche Kompetenz und seiner menschlichen Art die Arbeit an diesem Lehrstuhl für mich sehr angenehm gestaltet hat.

Ich bedanke mich bei Herrn Prof. Dr. Markus Betz für die Bereitschaft das Zweitgutachten anzufertigen und dafür, dass er Interesse an meiner Arbeit zeigt.

Frau Dipl. Phys. Natalie Miroslawski danke ich für ich die angenehme und produktive Zusammenarbeit. Erst durch ihren fachlichen Durchblick und ihre Engagement konnten viele Experimente zum Erfolg geführt werden. Des Weiteren bedanke ich mich dafür, dass sie mit ihrer Freundlichkeit und Offenheit immer für eine angenehme Arbeitsatmosphäre gesorgt hat.

Herrn. Dipl. Phys. Kolja Mende danke ich für die Zusammenarbeit in der problematischsten Phase meiner Dissertation. Obwohl wir mit vielen technischen Schwierigkeiten zu kämpfen hatten, half er durch seine Kompetenz und seinen Ideenreichtum die Probleme zu lösen.

Herrn Dipl. Phys. Ben Wortmann danke ich ebenfalls für die Zusammenarbeit. Dadurch, dass er sich vor Herausforderungen nicht scheute und immer neue Ideen einbrachte, konnten einige Experimente erfolgreich abgeschlossen werden.

Ein Dank geht auch an Herrn Kand. Phys. David Engemann, der den Bau einiger wesentlicher Komponenten der Anlage vorangetrieben hat und noch immer wichtige Verbesserungen an den Auswertungswerkzeugen vornimmt.

Einen entscheidenden Beitrag für diese Arbeit leistete auch Herr Dr. Tommi Järvi, sowie Herr Prof. Dr. Michael Moseler, die mit Hilfe von MD und DFT Simulationen halfen experimentelle Ergebnisse zu bestätigen.

Herrn Prof. Dr. Bernd v. Issendorff möchte ich für all die Hilfe danken, die nicht nur zum Bau der Fokussierungslinse beigetragen hat, sondern auch zum Lösen der technischen Probleme mit der Clusterstrahlanlage.

Weiterer Dank gilt all den Diplomanden, Doktoranden und Mitarbeitern des Lehrstuhls bedanken. Wesentliche Impulse und Hilfen für meine Arbeiten gingen von den Zahlreichen hier nicht namentliche genannten Personen aus.

Herrn Widynski danke ich für die Bereitstellung des flüssigen Stickstoffs und Heliums. Beide Substanzen waren essentiell für die in dieser Arbeit geschilderten Experimente.

Allen Mitarbeitern der mechanischen Werkstatt möchte ich dafür danken, dass sie wichtige apparative Komponenten angefertigt haben.

Abschließend möchte ich mich bei meiner gesamten Familie bedanken, allen voran meinen Eltern und Brüdern. So angenehm und menschlich die Arbeit am Lehrstuhl auch gewesen sein mag, benötigte ich doch immer, gerade in schwierigen Zeiten, die Nähe meiner Familie.